

**A Distributed Biosphere–Hydrological Model
for Continental Scale River Basins**

**大陸河川のための分布型生物圏水文モデルに
関する研究**

Qihong Tang

Copyright

by

Qihong Tang

2006

The Dissertation Committee for Qihong Tang
certifies that this is the approved version of the following dissertation:

**A Distributed Biosphere–Hydrological Model
for Continental Scale River Basins**

**大陸河川のための分布型生物圏水文モデルに
関する研究**

Committee:

Taikan Oki, Supervisor

Toshio Koike

Ryosuke Shibasaki

Shinjiro Kanae

Kun Yang

Takeyoshi Chibana

**A Distributed Biosphere–Hydrological Model
for Continental Scale River Basins**
**大陸河川のための分布型生物圏水文モデルに
関する研究**

by

Qihong Tang

Dissertation

Presented to the Faculty of the Graduate School of

The University of Tokyo

in Partial Fulfillment

of the Requirements

for the Degree of

Doctor of Philosophy

The University of Tokyo

Sep. 2006

Faith of Truth

Acknowledgments

It is a pleasure to thank the many people who made this dissertation possible.

I would like to express my sincere gratitude and appreciation to my Ph.D. supervisor, Dr. Taikan Oki for his attention, guidance, insight, and support during this research and the preparation of this dissertation. With his enthusiasm, his inspiration, and his great efforts to explain things clearly and simply, he helped to make hydrology desired for me. Throughout my dissertation-writing period, he provided encouragement, sound advice, good teaching, and lots of good ideas. I would also like to thank Professors Toshio Koike, Ryosuke Shibasaki, Shinjiro Kanae, Kun Yang and Takeyoshi Chibana for reading this dissertation and offering constructive comments. Professor Dawen Yang at Tsinghua University offered much appreciated advice, support and thought-provoking ideas throughout the model development period. I would like to express my thanks to Dr. Shinjiro Kanae for his guidance and support during the research time.

I would like to thank Masahiro Koike for the demonstrations of experiment, Kei Yoshimura, Shin Miyazaki, Shinta Seto, Sirajul Md. Islam, Yokoo Yoshiyuki, Hikaru Komatsu, Yanjun Shen, Magnus Bengtsson, Daisuke Komori, Goro Mouri, Thanh Ngo Duc, Hyungjun Kim, and Naota Hanasaki for their generous help in research, and other colleagues, including Yukiko Hirabayashi, Chusit Apirmanekul, Farzin Nasiri Saleh, Tomohito Yamada, Yoshito Suga, Yasuhiro Ishizaki, Meiyun Lin, Tsuyoshi Okazawa, Takeshi Kokubo, Kaeko Takagaki, Kenichi Kubo, Yuki Koiwa, Jeil Cho, Daisuke Ikari, Toshiyuki Inuzuka, Takahito Sakimura, Yuko Arai, Nobuyuki Utsumi, Ken Kodama and all past and present members of the Musiake/Oki/Kanae Laboratory for their friendship and companionship. Also, I will wish to acknowledge my appreciation to Ayako Kurosawa, Yuki Tsukada, Fumiko Shimizu for their kindness.

The research has been supported by the Japanese Government (MONBUKAGAKUSHO: MEXT) Scholarship. I have appreciated the support of the Department of Civil Engineering, the University of Tokyo during the years of my Ph.D. study.

I am grateful to all the members of the Institute of Hydrology and Water Resources,

Tsinghua University. My sincere thanks go to Professors Zhidong Lei and Heping Hu for their mental and moral support regarding my weltanschauung, philosophy and value system. I thank all the classmates of SG71, Tsinghua University for our nice common experience in Qinghua Yuan and for their encouragements after I came to Tokyo. I mention with thanks schoolfellows Hui Lu, Lei Wang and all the friends in Tokyo for their friendship.

Finally, I would like to thank my family for their life-long love and support. I especially owe much to my parents for offering their invaluable love, encouragement and understanding. Without them, this work could not have been completed.

QIUHONG TANG

The University of Tokyo

Sep. 2006

**A Distributed Biosphere–Hydrological Model
for Continental Scale River Basins**
大陸河川のための分布型生物圏水文モデルに
関する研究

Publication No. _____

Qihong Tang, Ph.D.
The University of Tokyo, 2006

Supervisor: Taikan Oki

Abstract

Water cycle is essential substance move for human survival. Mathematical modeling of hydrology is the key tool to meet the more and more critical societal needs for improved water management and hazards prediction. The development of hydrological modeling has been in the direction from the first generation empirical and lumped models, to the second generation distributed hydrological models, and then to the third generation distributed biosphere-hydrological model. The new generation models incorporate the advanced schemes to understand the response of hydrological cycle to the change of biosphere, human society and climate system. The advances of methods for translating satellite data into global surface parameter sets have driven the development of the third generation models. With the new generation model, many of the merging advances in monitoring, computation, and telecommunications are brought to bear on disaster prevention, food supply, health, security and development issues facing Earth's growing population.

Multidisciplinary developments have prompted hydrological simulation. These advances include the new insights into mass/heat flux in the Soil-Vegetation-Atmosphere Transfer (SVAT) processes, progress in getting reliable land surface information from satellite remote sensing (RS), and developments of Geographic Information System (GIS) technique to extract topographic variables from digital elevation models (DEMs). This study has aimed at developing a new generation distributed biosphere-hydrological model accounting for the merging multidisciplinary advances. The main objectives include: extraction of hydrology related information from nontraditional datasets, development of a time-continuous distributed process-based land surface hydrological model accounting for the representations of the terrains, soil, vegetation, and hydrological response, model evaluation of the new generation model, and model application to evaluate the effects of human activity and natural climate variability on hydrology cycle.

The credibility of extraction of hydrology related information from nontraditional datasets is examined with a distributed biosphere-hydrological (DBH) model system. The nontraditional datasets to address water resource problems are largely from satellite remote sensing. The DBH model system is applied to the Yellow River basin, a continental scale river basin in semi-arid area, to compare the satellite remote sensing data with in situ observations. The relationship between nontraditional dataset and traditional in situ observation on cloud cover, which is characterized by large spatial and temporal variations, shows strong correlations, implying

the credibility of use of nontraditional datasets in hydrological simulation. The DBH model system is then used to analyze hydro-climatic change and stream flow change, exploring the possible connections between hydrology, vegetation, climate and human activity in the Yellow River basin. The analysis, using station, satellite metadata and interpolated coverage, indicates that the precipitation decreases in most part of the Yellow River basin, climatic factors such as temperature and evaporative demand of the atmosphere have large trend in special part of the basin, and that human activities have changed the vegetation condition in the irrigation districts. The Loess Plateau, the Tibetan Plateau, and the irrigation districts are suggested as precipitation, temperature, and human activities "hot spots" of the Yellow River drying up, respectively.

A realistic distributed biosphere-hydrological (DBH) model has been developed for representing the role of both topography and land cover characteristics in hydrological cycle. The model is designed for use in a continental scale river basin and coupling with atmospheric models. The vegetated surface is calculated by a realistic land surface model SiB2. The vegetation phenology is described by satellite data, and the transfer of energy, mass and momentum between the atmosphere and land surface. The hydrological part estimates the surface runoff and calculates the interlayer exchanges within the soil profile and interaction between soil water and groundwater. The geomorphologic properties are abstracted from Digital Elevation Model using a distributed hydrological sub-model. Realistic watershed map and river way map are used to delineate sub-river basins and river network. The sub-river basins are coded following a natural numbering scheme which is self-replicating and is possible to provide identification numbers to the level of the smallest sub-basins. The river network routing order of the sub-basins is implicated in the numbering scheme. The runoff is then accumulated and routed to outlet using kinematic wave approach. The parameters and forcing data are obtained from various ways, including remote sensing, ground observation, and statistical surveys. The hydrology-related information was digitized into the model system in order to diminish the uncertainty in the hydrological simulation.

The model evaluation processes, such as model verification, validation and credibility, are preformed in the Yellow River basin, China. The effects of natural and anthropogenic heterogeneity on hydrological simulation were evaluated using the DBH model system. The model system embeds a biosphere model into distributed hydrological scheme, representing both topography and vegetation conditions in mesoscale hydrological simulation. An irrigation scheme has been included in the model system. The effects on hydrological processes of two kinds of variability, precipitation variability and the variability on irrigation redistributing runoff, was

investigated in this study, representing the natural and anthropogenic heterogeneity, respectively. Runoff is underestimated if the rainfall is spatially uniformly put over large grid cell. And runoff simulation could be improved by taking into account the precipitation heterogeneity. However, the negative runoff contribution cannot be simulated by only considering the natural heterogeneity. This constructive model shortcoming can be eliminated by taking into account anthropogenic heterogeneity, irrigation water withdrawals. Irrigation leads to increased evapotranspiration and decreased runoff. Surface soil moisture in the irrigated area increases because of irrigation. Simulations performed for the Yellow River basin indicates that stream flow decrease of 41% by irrigation. The latent heat flux increase in peak irrigation season (June, July, August: JJA) is 3.3 W m^{-2} with a decrease in ground surface temperature of 0.1 K of the river basin. The maximum simulated increase in latent heat flux is 43 W m^{-2} and ground temperature decrease is 1.6 K in peak irrigation season (JJA).

A comprehensive application of the DBH model system is performed in the Yellow River basin with the use of data analysis results to evaluate the effects of human activity and natural climate variability on hydrology cycle. Scenario simulations are performed from 1960 to 2000 to quantify the effects of human activity on hydrology, and to distinguish it from the effects from natural climate variability. The linear tendency of the forcing data is removed to provide input for non-change scenarios. The model results from six scenarios, i.e. most realistic control scenario, non-climate change scenario, non-vegetation change scenario, non-irrigated area change scenario, stable scenario without linear tendency and stable scenario without climate pattern change, are compared. The results show that climate change is dominated in the upper and middle reaches, but human activities are dominated in the lower reaches of the Yellow River basin. The runoff and evapotranspiration decrease over the Loess Plateau is dominated by the contribution of climate change. The intensively affected area by irrigation and vegetation change is the irrigation districts especial in the Weihe irrigation district and lower reaches irrigation districts. The river discharge at the river mouth nearly half is affected by climate change and half by human activities. The linear climate change contributes to the water consumption, but the climate pattern change is more important than the linear climate change. The river channel flow is more significant affected by the direct irrigation water withdrawals than by the climate change, which dominantly contributes to the annual water resources change. The reservoirs are believed to make more stream flow consumption for irrigation, at the same time, our results demonstrate the reservoirs help to keep environment flow and counter zero-flow in the river channel.

Contents

Acknowledgments	vii
Abstract	ix
List of Tables	vi
List of Figures	viii
Chapter 1 Introduction	1
1.1 General Introduction	1
1.2 Challenges in Hydrology	2
1.3 Research Objectives	3
1.4 Outline of the Dissertation	4
Chapter 2 Evolution of Hydrological Modeling	7
2.1 Introduction	7
2.2 Hydrological Modeling	8
2.3 Land Surface Modeling	13
2.4 Land Surface Hydrology with Biospheric Aspects	16
2.5 Summary	17
Chapter 3 Analyses on Observed Data	19
3.1 Introduction	19
3.1.1 Geography in the Yellow River Basin	20
3.1.2 Available Data in the Yellow River Basin	22
3.2 Remote Sensing Data Analysis	27
3.2.1 Introduction	27
3.2.2 Methodology	28

3.2.3	Results and Conclusions	32
3.2.4	Discussion	39
3.3	Ground Observations Analysis	41
3.3.1	Data Sources	41
3.3.2	Methods	42
3.3.3	Results and Discussion	43
3.3.4	Conclusion Remarks	47
3.4	Summary	48
Chapter 4 Development of a Distributed Biosphere–Hydrological Model		51
4.1	Introduction	51
4.2	Modeling Strategy	52
4.3	The Model Structure	53
4.3.1	Land Surface Model	53
4.3.2	Hydrological Model	56
4.3.3	River Routing Scheme	65
4.3.4	Irrigation Scheme	69
4.4	Parameters and Forcing Data	71
4.4.1	Remote Sensing Data	71
4.4.2	Ground-Observations	74
4.4.3	Statistical Survey Data	79
4.5	Summary	80
Chapter 5 Evaluation of the DBH Model System		83
5.1	Model Evaluation Processes	83
5.1.1	Model Verification	84
5.1.2	Model Validation	86
5.1.3	Model Credibility	89
5.2	Introduction of Subgrid Heterogeneity	90
5.3	Model Description	94
5.4	Approach	96
5.4.1	Study Area	96
5.4.2	Input Data	97
5.5	Model Validation	98
5.6	Analyses and Results	100

5.7	Discussions	105
5.8	Summary	108
Chapter 6 Long Term Change of Hydrological Cycles in the Yellow River Basin		109
6.1	Introduction	109
6.2	Data and Methodology	113
6.2.1	Data Analysis	113
6.2.2	Methodology	113
6.3	Results and Analysis	117
6.4	Conclusions and Discussions	126
6.5	Summary	127
Chapter 7 Conclusions and Recommendations		129
7.1	Summary of the Research	130
7.1.1	Information from Nontraditional Data	130
7.1.2	Distributed Biosphere-Hydrological Model	130
7.1.3	Effects of Heterogeneity on Hydrological Response	131
7.1.4	Comprehensive Model Application	131
7.2	Conclusions	132
7.3	Suggestions for Future Research	133
Appendix A Green-Ampt Model		135
A.1	Derivation of Green-Ampt Model	135
A.2	Green-Ampt Infiltration	136
Appendix B Numeric Solutions		139
B.1	Water Fluxes Underground	139
B.2	River Flow	141
Appendix C Data Processing		144
C.1	Map Projections	144
C.1.1	Geographic	144
C.1.2	Lambert Azimuthal Equal Area Projection	145
C.1.3	Interrupted Goode Homolosine Projection	146
C.1.4	Data Resampling	147
C.2	Point-Surface Interpolation	147

C.2.1	Thiessen Polygons	149
C.2.2	Thin Plate Splines	149
C.2.3	Inverse Distance Weighted Method	150
C.2.4	Comparison of Interpolation Methods	150
C.3	Extract Geomorphological Properties	151
C.3.1	DEM Derivative Map	153
C.3.2	Topologically Coding System Based on DEM	154
C.4	Time Series Analysis	157
C.4.1	Trend Detection	157
C.4.2	Remove Trend Method	159
	Bibliography	160
	Vita	179

List of Tables

3.1	Daily NCI, CLAVR values, and ground observations	35
3.2	Daily NCI values and cloud indices derived from observations	38
3.3	Observed annual discharge change at gauges	44
3.4	Change in climate and vegetation condition	44
5.1	Annual largest flood peak validation (Flood peak: m^3/s , Time: date)	89
5.2	Simulated and reported annual irrigation water consumption (10^9m^3)	100
5.3	Mean annual runoff (R), evaporation (E) for the various case (mm year^{-1}) . . .	101
5.4	Changes in energy components in peak irrigation season JJA	106
6.1	Simulation contributions of annual discharge change along river main stem (m^3/s)	125

List of Figures

1.1	Distributed Biosphere-Hydrological (DBH) Model System.	5
2.1	Development of hydrological models. (a) first generation empirical and lumped models, (b) second generation distributed hydrological models, (c) third generation distributed biosphere-hydrological model.	10
2.2	Development of LSMs: (a) first generation "bucket" model, (b) second generation model with separated vegetation canopy and soil, (c) third generation model with carbon flux pathway. [The figure is reproduced from Sellers et al. (1997)]	14
3.1	The Yellow River basin.	20
3.2	Geography of the Yellow River basin.	21
3.3	Profiles along the riverway (upper) and along the line (lower) from outlet to headwater.	22
3.4	Forcing variables in the study area (1982-2000).	24
3.5	Time series of monthly forcing variables (1982-2000).	25
3.6	Averaged LAI and FPAR (1982-2000).	26
3.7	Soil parameters.	26
3.8	Study area.	29
3.9	NDVI Cloud Index (NCI).	30
3.10	Time series of NCI, SCI, CLAVR, and ground-observed cloud amounts.	32
3.11	Cloud amount, NCI, SCI, and CLAVR values. (a) NCI values versus SCI; (b) CLAVR versus cloud amount; (c) NCI versus cloud amount; (d) SCI versus cloud amount.	33
3.12	Histogram of cloud distributions at the ground-observation stations.	34
3.13	R^2 for (a) daily NCI values and the observed cloud amount, (b) daily NCI values and the observed SCI, (c) CLAVR values and the observed cloud amount, (d) and CLAVR values and the observed SCI.	36

3.14	Cumulative distribution of R^2 associated with (a) NCI-cloudiness and CLAVR-cloudiness, (b) and NCI-SCI and CLAVR-SCI.	37
3.15	R^2 values for (a) the NCI and cloud amount, (b) and the NCI and SCI as a function of altitude.	38
3.16	Seasonal variation in R^2 values for (a) the NCI and cloud amount, (b) and the NCI and SCI.	39
3.17	R^2 values for (a) the NCI and cloud amount in January and September, (b) and the NCI and SCI in January and September as a function of altitude.	40
3.18	Relative trend magnitude of precipitation (a), reference evapotranspiration (b), relative humidity (c), sunshine duration (d), cloud amount (e) from 1960 to 2000 and LAI value (f) from 1981 to 2000.	46
3.19	Trend magnitude of mean temperature (a), minimum temperature (b), maximum temperature (c) and diurnal temperature range (d) from 1960 to 2000.	47
4.1	Structure of the DBH model.	54
4.2	Area-amount relationship: (a) exponential area-amount relationships, (b) and effective precipitation area-amount relationships used in DBH model.	58
4.3	Wetting front of the Green-Ampt model.	58
4.4	Empirical soil moisture characteristic curve.	61
4.5	Wetness-hydraulic conductivity relationship and b.	62
4.6	Wetness-hydraulic conductivity relationship and saturated hydraulic conductivity.	63
4.7	Conceptual representation of river-groundwater exchange.	63
4.8	Revise hydro-DEM with realistic river way map.	66
4.9	Real riverway and derived river way with revised DEM.	67
4.10	Methodology adopted to determine flow intervals with a numeric example.	69
4.11	Flow intervals with a threshold value of 1.5 (left) and 6.0 (right) times of grid size.	70
4.12	HYDRO1k dataset for Asia.	73
4.13	SiB2 land cover for Eurasia.	75
4.14	Ground observation stations in GSSDD dataset.	76
4.15	Diurnal temperature curve with TM model.	78
4.16	South Asia and Near East Soil Map of the World Soil Map.	80
4.17	Global Map of Irrigated Areas.	81
5.1	Relationship between model verification, validation and credibility.	84
5.2	Model verification on the river routing scheme subroutine.	86

5.3	Model validation with ground observations: (a) daily discharge, (b) monthly discharge, (c) and mean monthly discharge comparisons.	88
5.4	Simulated and observed discharge at Lanzhou station: (a) daily, (b) monthly, (c) and mean monthly comparisons.	91
5.5	Precipitation area-amount relationships.	95
5.6	(a) Mean annual precipitation and (b) irrigated area (%) in the Yellow River basin.	98
5.7	Simulated and observed mean monthly stream flow at Tangnaihai station.	99
5.8	Simulated and observed daily stream flow at Tangnaihai station.	100
5.9	Effects of precipitation heterogeneity on runoff simulation from 1983 to 2000; (a) total runoff and (b) surface runoff in the Yellow River Basin.	102
5.10	Effects of natural and anthropogenic heterogeneities on annual stream flow along the Yellow River from upstream to downstream.	103
5.11	Spatial effects of irrigation on water balance components in the Yellow River basin; (a) water shortage in a grid cell with an irrigated area, (b) irrigation water withdrawal, (c) evaporation change, (d) runoff change.	104
5.12	Simulated surface soil wetness (top 2 cm) without irrigation in the Yellow River basin (a), and simulated surface soil wetness change (%) with irrigation (b).	104
5.13	Spatial effects of irrigation on energy balance components (a) changes in ground surface temperature dT_g , (b) changes in canopy temperature dT_c , (c) changes in latent heat fluxes ra_{et} , and (d) changes in sensible heat fluxes ra_{ht} in the peak irrigation season (JJA).	106
6.1	Irrigated area in the Yellow River basin.	114
6.2	Climate data with and without linear tendency.	115
6.3	Vegetation data extension and the data with/without linear tendency.	116
6.4	Observed and simulated discharge in S1, control simulation at main stem gauges.	118
6.5	Reported and simulated water withdrawals in S1, control simulation at upper, middle, and lower reaches of the Yellow River.	119
6.6	Simulated changes from 1960 to 2000 with S1, control simulation: a) Runoff change, b) Evapotranspiration change, c) Water withdrawals change, and d) Ground surface temperature change.	120
6.7	Simulated a) sensible heating and b) canopy assimilation flux changes from 1960 to 2000 with S1, control simulation.	120

6.8	Simulated changes contributed from climate linear change: a) Runoff change, b) Evapotranspiration change, c) Water withdrawals change, and d) Ground surface temperature change.	121
6.9	Simulated changes contributed from vegetation change: a) Runoff change, b) Evapotranspiration change, c) Water withdrawals change, and d) Ground surface temperature change.	122
6.10	Simulated changes contributed from irrigation area change: a) Runoff change, b) Evapotranspiration change, c) Water withdrawals change, and d) Ground surface temperature change.	123
6.11	Simulated changes contributed from climate linear change, vegetation and irrigation change: a) Runoff change, b) Evapotranspiration change, c) Water withdrawals change, and d) Ground surface temperature change.	124
6.12	Simulated and observed drying days at the Lijin station.	126
A.1	Use Green-Ampt model to estimate infiltration.	137
B.1	Flow speed estimated from the Manning's equation.	142
B.2	Discharge estimated from the Manning's equation with a rectangular river section.	142
C.1	Global AVHRR data with the Interrupted Goode Homolosine projection.	146
C.2	Data resampling process.	148
C.3	Interpolation results with IDW (upper), TPS (middle), and TS (lower) method.	152
C.4	Sample subdivisions of a sub-basin and an interbasin.	155
C.5	Sample subdivisions of Pfafstetter Level 2.	156
C.6	Sample subdivisions of Pfafstetter Level 3.	156
C.7	Trend detection with annual precipitation in the Yellow River basin, 1960-2000.	158
C.8	Remove trend with daily precipitation.	160

Chapter 1

Introduction

1.1 General Introduction

Water is the most widespread substance to be found in the natural environment. It forms the following reservoirs: oceans, lakes, rivers, glaciers, snowfields and the underground waters. Water moves from one reservoir to another by way of processes like evaporation, condensation, precipitation, deposition, runoff, infiltration, sublimation, transpiration, melting, and groundwater flow. The planetary water supply is dominated by the oceans, which hold about 97% of the earth's water. The remaining 3% is the freshwater so important to our survival, but about 68% of that is stored in ice in Antarctica and Greenland and about 32% of that is groundwater (Alley et al., 2002). The freshwater that we see in rivers, lakes, and rain is less than 1% of the freshwater. The terrestrial freshwater cycle, i.e. groundwater and surface water, is of great importance in the global hydrological cycle and for the supply of water to humankind. Water at the land surface is a vital resource, both for human needs and for natural ecosystems. Desertification and drought affects more than 900 million people in 100 countries. Irrigation already accounts for more than 70% of freshwater withdrawn from lakes, rivers, and groundwater aquifers, and perhaps 80% of the additional food supplies required to feed the world's population in the next 30 years will depend on irrigation (UN-SWI, 1997). Study on terrestrial freshwater cycle is a dramatic challenge in focus, driven by the societal priorities, emerging technologies, and better understanding of the earth system.

The terrestrial freshwater cycle is affected by many factors such as land-atmosphere exchanges, plant physiology, land use and anthropogenic disturbance (Entekhabi et al., 1999; Hutjes et al., 1998; Vitousek et al., 1997; Vörösmarty and Sahagian, 2000). The energy and moisture budgets at the land surface are mainly linked by evaporation, which is an expenditure

of both energy and water mass. Local positive feedbacks in the land-atmosphere system are believed to contribute to the observed persistence and intensification of droughts (Brubaker and Entekhabi, 1996). Earth's vegetation cover has a profound influence on a lateral redistribution of water and transported constituents, such as nutrients and sediments, and acts therefore as an important moderator of Earth's biogeochemical cycles. Evidences show that local land use practices influence regional climate, vegetation and then stream flow patterns (Stohlgren et al., 1998). The terrestrial surface water system is dominated directly by humanity. Even very little water is directly usable by human; humanity has extensively altered river systems through diversions and impoundments to meet their water, energy, and transportation needs. Over half of world large river systems are affected by dams. Dam-impacted catchments experience higher irrigation pressure and about 25 times more economic activity per unit of water than do unaffected catchments (Nilsson et al., 2005). Adequate flows no longer reach the deltas of many rivers in average years, including the Nile, Huang He (Yellow), Amu Darya and Syr Darya, and Colorado (Gleick, 2003). Groundwater is a crucial source of fresh water throughout the world. More than 1.5 billion people worldwide rely on groundwater for their primary source of drinking water. The dynamic aspects of groundwater flow systems, their recharge, and interactions with surface water and the land surface are numerous and extend over many different time scales (Zektser and Loaiciga, 1993; Alley et al., 2002).

1.2 Challenges in Hydrology

The traditional hydrology has only focused on the river basin, although hydrology, as a geophysical science, has a universal coverage. Recently, there has been worldwide recognition of the need for global observations and studies of the water cycle and hydrological processes. hydrological research is undergoing an important, fundamental change in the direction of the science. Nontraditional datasets, new tools, and a better understanding of the connection between hydrology and the rest of the climate system are being developed to meet the more and more critical societal needs for improved water management and hazards prediction.

The nontraditional datasets to address water resource problems are largely from satellite remote sensing. Remote sensing provides the potential for global coverage of hydrology related data such as vegetation data that can be used to improve hydrological simulation. Such data are logistically and economically impossible to obtain through traditional in situ measurement. The advances in computer capacity made it possible to develop new data processing techniques and make complex simulation. The research on biospheric aspects of the hydrological cycle is

initiated by International Geosphere Biosphere Programme (IGBP) through experiments and modeling of energy, water, carbon dioxide and sediment fluxes over the land surface (Hutjes et al., 1998). New insights into water and heat flux in the soil-vegetation-atmosphere system at a variety of spatial and temporal scales provide scientific base for using the remote sensing data to improve hydrological simulation. Hydrologists are encountering a new intellectual paradigm that emphasizes connections between hydrology and land surface processes together with other components of the earth system (NRC, 1991). This coupling is now widely considered to be essential. Land surface hydrology is a discipline through which many of the merging advances in monitoring, computation, and telecommunications may be brought to bear on disaster prevention, food supply, health, security and development issues facing Earth's growing population (Entekhabi et al., 1999).

There are several new challenges in hydrology science:

1. to determine the exchanges of moisture and energy between soil, vegetation, snow pack and the overlying atmospheric boundary layer, and to provide a pathway to couple surface hydrological systems and the overlying atmospheric systems;
2. to develop process-based tools to investigate the interaction mechanisms between the terrains, soil, vegetation of the land surface, and hydrological response;
3. to represent the spatial and temporal heterogeneity in the natural system with time-continuous distributed models;
4. to model the spatial interactions and lateral redistribution of moisture over complex terrain, which significantly influences the partitioning of precipitation into runoff and large scale soil-vegetation-atmosphere exchange processes and cannot be constructed, captured by spatially lumped or one-dimensional soil hydrology models;
5. and to quantify the effects of human activity on the landscape, ecology, and hydrology, and to distinguish them from natural climate variability.

1.3 Research Objectives

Realizing the current challenges in hydrology science, this research has aimed at developing a time-continuous distributed process-based land surface hydrological approach, which can represent the land surface exchanges of moisture/energy, model the spatial interactions and lateral

redistribution of moisture over complex terrain, and assess the effects of human activity on the hydrology cycle. The main objectives of the research include:

1. to extract hydrology related information from nontraditional datasets and to analyze the vegetation, climate, human activity and the potential effects on the hydrology cycle;
2. to develop and validate a time-continuous distributed process-based land surface hydrological model on the basis of the representations of the terrains, soil, vegetation of the land surface, and hydrological response;
3. to study the effects of heterogeneity in both the nature system and anthropogenic disturbance on the hydrological simulations;
4. to study the spatial interactions and lateral redistribution of runoff forced by human activities;
5. and to apply the land surface hydrological model to evaluate the effects of human activity and natural climate variability on hydrology cycle.

1.4 Outline of the Dissertation

Chapter 2 reviews literatures on hydrological modeling, land surface modeling, and land surface hydrology research with biospheric aspects. hydrological modeling section emphasizes on the development of hydrological modeling and current physically based distributed hydrological models. In the land surface modeling section, review is made on a universal coverage related hydrology cycle, including vegetation model, land surface scheme, remote sensing technique used in biosphere and ecology simulation. The land surface hydrology research with biospheric aspects was surveyed.

The remaining chapters give a full description of a Distributed Biosphere-Hydrological (DBH) Model system (Figure 1.1). The DBH model system includes a distributed biosphere-hydrological model, forcing data and parameter processing module, and results analysis module.

Chapter 3 presents the performance of the DBH model system to extract hydrology related information from nontraditional datasets and to analyze the vegetation, climate, human activity and the potential effects on the hydrology cycle. The DBH model system is applied to the Yellow River basin, a continental scale river basin in semi-arid area, to compare the satellite remote sensing data with in situ observations, confirming that the new global forcing

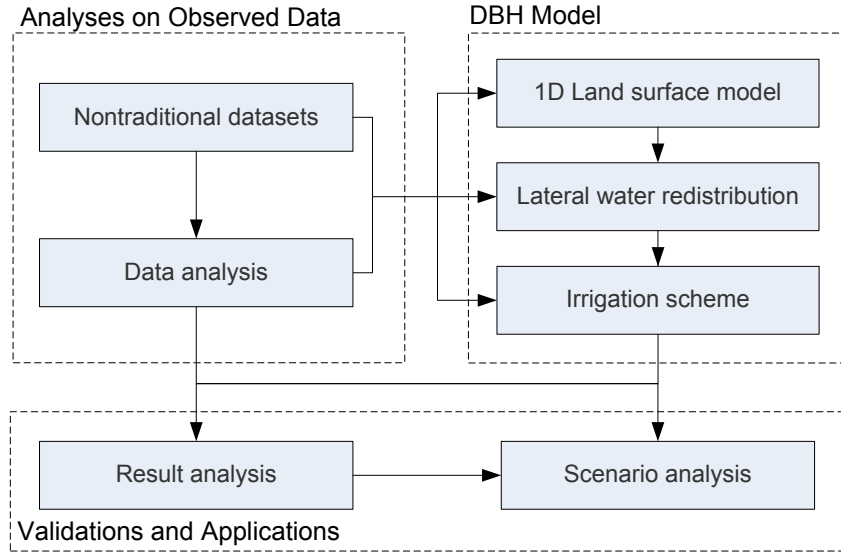


Figure 1.1: Distributed Biosphere-Hydrological (DBH) Model System.

data is valid for hydrological simulation. The DBH model system is then used to analyze hydroclimatic change and stream flow change, exploring the possible connections between hydrology, vegetation, climate and human activity in the Yellow River basin.

Chapter 4 describes development of a Distributed Biosphere-Hydrological (DBH) Model system for continental scale river basins. The surface flow, subsurface flow, channel network flow, groundwater-river interaction, and irrigation scheme is newly developed and then, coupled with a realistic land surface model SiB2. The parameter use and analysis of nontraditional dataset are important parts of the model system. The datasets include satellite remote sensing data, ground observations, and statistical survey data.

Chapter 5 evaluates with model verification, validation, and credibility processes, as well as represents the effects of heterogeneity in both the nature system and anthropogenic disturbance on the hydrological simulations with the DBH model system. The precipitation variability and partial irrigation within grid cells were used to demonstrate the effects of natural and anthropogenic heterogeneities in the hydrological cycle, respectively. The spatial interactions and lateral redistribution of runoff forced by human activities is simulated with an irrigation scheme. The effects on the river flow pattern, i.e. discharge along river main stem, were investigated.

Chapter 6 describes a comprehensive application with the use of data analysis results to evaluate the effects of human activity and natural climate variability on hydrology cycle. With the assistance of the nontraditional datasets, long term simulation is performed in the Yellow River basin to quantify the effects of human activity on hydrology, and to distinguish it from the effects from natural climate variability. The explicit representation of the relationships between

hydrology, vegetation and climate is used to interpret the Yellow River drying up phenomenon, which attracts focus from both hydrologist and society.

Chapter 7 summarizes the entire research with findings and conclusions. Suggestions for future research are given in broad perspectives of terrestrial fresh water research with connections with oceans, atmospheres, biosphere and geosphere.

Chapter 2

Evolution of Hydrological Modeling

2.1 Introduction

Hydrology is the study of the movement, distribution, and quality of water throughout the Earth. The hydrological cycle is mainly driven by solar radiation. It includes water movement among the atmosphere, land, surface water and groundwater. hydrological models are simplified, conceptual representations of a part of the hydrological cycle. They are primarily used for hydrological prediction and for understanding hydrological processes. Mathematical modeling of hydrology is employed to address a wide spectrum of environmental and water resources problem. It is essential for understanding dynamic interactions amongst climatic, terrestrial, petrologic, lithologic and hydrospheric systems (Singh and Frevert, 2002a).

Hydrological modeling began in the nineteenth century for the design of roads, canal, dam, bridges and water supply systems. It primarily involved the development of concepts, theories and models of individual components of the hydrological cycle, such as overland flow, channel flow, infiltration, depression storage, evaporation, interception, subsurface flow and base flow until the middle of the 1960s (Singh and Woolhiser, 2002). The integration of the individual components of the hydrological cycle and hydrological simulation of the entire watershed were made possible in the later 1960s (Crawford and Linsley, 1966). A number of these models appeared such as SHE (Abbott et al., 1986a,b; Bathurst et al., 1995), TOPMODEL (Beven, 1995), GBHM (Yang et al., 1998, 2000), which differently represented the interconnected subsystems. Many of the advances after the 1970s were due to improves in computational facilities or new measurement techniques. The role of distributed hydrological models increased because of the availability of digit maps as well as the increase in satellite remote sensing, allowing for the preparation of large data banks which will include many physical characteristics

and the advances of more powerful computers, allowing for the solution of the differential equations. The important advances in hydrological modeling in the 1990s were the employment of geographical information system (GIS), remotely sensed data, and environmental tracers. The use of digital elevation models (DEMs), remote sensing data and GIS raised the questions of subgrid variability, the effect of pixel size on model calibration, and the role of the use of topographic indices (Hornberger and Boyer, 1995; Ambroise et al., 1996).

Recently, new challenge of hydrological modeling is issued to the use of nontraditional dataset, new tools, and a better model of the connection between hydrology and the rest of the earth system (Entekhabi et al., 1999). With the advances in biosphere, atmosphere, and environmental monitoring and computation, especially the connection between land surface hydrology, biosphere and climate system, the hydrology is not limited on the rainfall-runoff and the effect of topography. The scope of hydrologist has broadened to climatology, terrestrial biosphere, ecosystem, geosphere, biogeochemistry, remote sensing etc. The hydrology has come to stress on the natural and altered biosphere as well as interactions with the engineering and social sciences in complex landscapes.

2.2 Hydrological Modeling

A hydrology model is an assemblage of mathematical descriptions of components of the hydrological cycle. The hydrological modeling in broad sense was combined of two basic components. The first one expresses all the rational knowledge that one has on the phenomenon to be represented and can be referred to as the physical component. The second is the stochastic component, expressing in statistical terms what cannot be explained by the degree of rational knowledge already introduced in the physical components (Todini, 1988). Most watershed hydrology models are deterministic, but some consist of one or more stochastic components.

Until the early 1980s, hydrological models use lumped rainfall-runoff relationship to describe hydrological cycle on the land. Three generations of hydrological models have taken us from the early empirical model to where we stand now. The first, developed before the 1980s, was based on statistical relationship between rainfall and runoff, or integrated different components of the hydrological cycle in a lumped or fake-distributed way (Figure 2.1a). The surface parameters often were uniform over the watershed. In the 1980s, a second generation of models recognized the effects of spatial heterogeneity in the calculations of the overall hydrological behaviors (Figure 2.1b). At the same time, powerful computer occurred, making it possible to solve the differential equation on extremely large discretized grids. And regional, spatially vary-

ing data of land surface properties were assembled from geographical surveys. The latest new (third) generation models used modern theories relating biosphere to provide a more realistic description of land surface hydrology (Figure 2.1c). The new generation models incorporate the advanced schemes to understand the response of hydrological cycle to the change of biosphere, human society and climate system. The advances of methods for translating satellite data into global surface parameter sets have driven the development of the third generation models.

Todini (1988) took the level of a priori knowledge on the system as the basis for model classification and gave four classes of model structures with increasing level of a priori knowledge: 1) purely stochastic, 2) lumped integral, 3) distributed integral, 4) and distributed differential. The purely stochastic model does not imply a cause and effect relationship between the input variables and output variables. The level of information introduced in stochastic model is minimal and the results are valid on average. If the spatial derivatives are ignored, the model is "lumped", otherwise, it is "distributed". All aspects of the model must be distributed including parameters, initial and boundary conditions must be distributed if a model is truly distributed. A fully distributed characterization is impossible at that time because of the practical limitations of data and discrete descriptions of geometry and parameters. The purely stochastic, lumped integral and distributed integral models are the first generation model because of the inadequate computation of internal fluxes. The distributed differential models are the second generation model. The difficulty for the second generation model is to acquire the distributed parameters. Todini (1988) foresaw that the new information system based on remote sensing technologies will provide the means for acquisition of distributed data.

The typical second generation model is SHE model (Abbott et al., 1986a,b), which emphasizes on physically based model. SHE has been extended to include sediment transport and is applicable at the scale of a river basin (Bathurst et al., 1995). TOPMODEL (Beven and Kirkby, 1979) uses surface topographic and soil information to simulate the lateral redistribution of soil water over a catchment by saturated throughflow. The model is based on demonstrated principles of hillslope hydrology in which locations with large upslope contributing areas and low surface gradients maintain higher soil moisture levels than locations that are steep or have low upslope contributing areas. TOPMODEL has been extended to contain increased catchment information, more physically based processes, and improved parameter estimation. TOPMODEL and SHE are well accepted as the standard models for traditional hydrological analysis.

Hornberger and Boyer (1995) reviewed advances in watershed modeling and emphasized the need to deal with spatial variability and scaling and the need to explicitly consider linkages

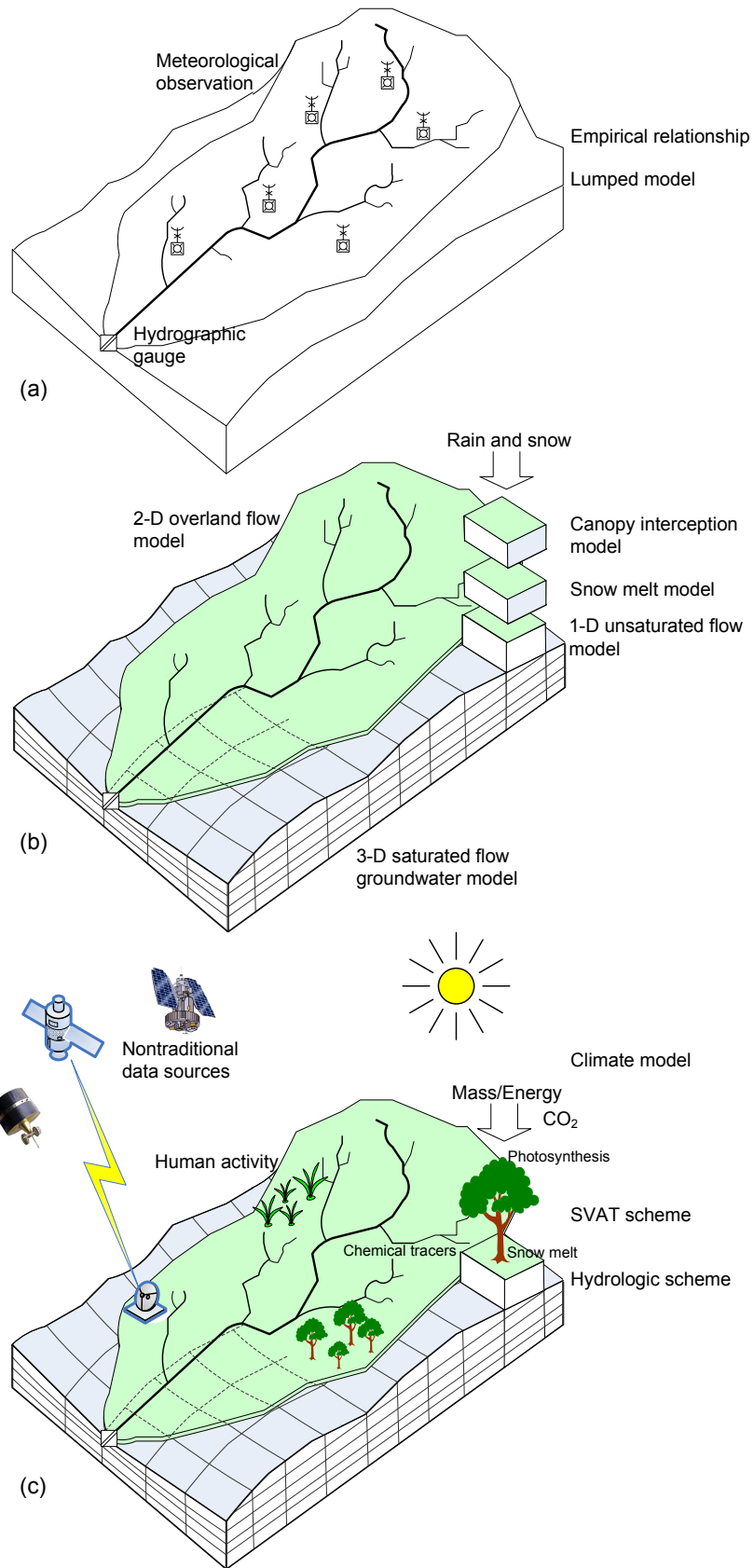


Figure 2.1: Development of hydrological models. (a) first generation empirical and lumped models, (b) second generation distributed hydrological models, (c) third generation distributed biosphere-hydrological model.

among hydrology, geochemistry, environmental biology, meteorology, and climatology. To make progress with the issues of heterogeneity and scaling, hydrologists will have to come to terms with the need to pay closer attention to gathering appropriate, high-quality data. There is much to be learned about complex flow paths within catchments, and models based on our best representation of physical processes will remain an essential part of studies designed to understand catchment processes. They foresaw the increasing role of the acquisition of more data and more experimentation in the future progress of hydrology.

Singh and Woolhiser (2002) provided a historical perspective of hydrological modeling and discussed the new developments and challenges in watershed models. They listed a sample of popular hydrological models from around the globe in chronological order. Singh (1995) edited a book that summarized 26 popular models. After that, global and regional models have received increasing attention. Singh and Frevert (2002a) and Singh and Frevert (2002b) edited other books which selected 15 models of large watershed hydrology and 23 models of small watershed hydrology and applications. They suggested hydrology models would have to embrace rapid advances occurring in remote sensing and satellite technology, geographical information systems, database management systems, error analysis, risk and reliability analysis, and expert systems. With the use of remote sensing technology, our ability to observe data over large and inaccessible areas and to map these areas spatially is improved, making it possible to develop truly distributed models for both gauged and ungauged watersheds. With the use of GIS, the large quantities of data can be stored, retrieved, managed, and manipulated in distributed models.

Creative research on distributed hydrological models has been done in the Hydrology Laboratory of the Institute of Industrial Science, the University of Tokyo. These works include several distributed hydrological models developed in the 1990s (Ni, 1994; Jia, 1997; Yang, 1998; Dutta, 1999). Basically, the models reflect the frontier of hydrological modeling of the end of 1980s. The models, following SHE, belongs to the distributed differential type, representing the catchment behavior in terms of all the differential equations discretized in time and space, expressing mass and momentum balance for each subsystem and linking together the subsystems by matching at each step in time their mutual boundary conditions. The model develop strategy is somehow improved by Yang (1998) who tried to extract geomorphologic information from DEMs. Dutta (1999) made an attempt to develop a flood inundation and damage estimation model to meet the increasing societal demand.

Although much progress has been achieved in hydrology, there is a greater road ahead. It is well recognized that topography, soil characteristics, vegetation, and climate interact in a

complex manner to determine the types, intensities, and the locations of runoff production in a landscape. Hydrological response of a river basin will be altered by natural or human-induced changes to one or more of these forcing variables. However, the scope of current hydrological models are mainly limited in rainfall-runoff processes with the emphasis on topography, while biologists devote to coupling vegetation models with boundary layer micrometeorology theory with simplified resistance representations of plant physiology, remote sensing scientists focus on the land cover change or other earth surface observations, and climatologists concentrate on the climate change and the related dynamic mechanisms. Hydrological models concern with runoff production and lateral redistribution of soil moisture, and the representation of vegetation and the use of more "realistic" distributed nontraditional data are absent. It is necessary to accurately, explicitly represent the relationships between hydrology, vegetation, and climate for the prediction of the changes in vegetation patterns, water quality, and runoff production. The third generation hydrological model is urgently required.

It is difficult to quantify the hydrology cycle through in situ observations over large spatial domains and over long time periods. Satellite remote sensing provides a methodology to overcome these issues with a broad spatial coverage and a repeat temporal coverage. Many attempts had been done to use remote sensing data for the estimation of parameters of hydrological models or to use such data as model input. Otlé et al. (1989) presented a hydrological model to simulate both the hydraulic and energy budgets at the soil surface and compared simulated water budgets to the water deficit from satellite data. Schultz (1993) discussed hydrological modeling based on remote sensing information. Su (2000) propose methods for mapping land use changes and vegetation parameters using remote sensing data in the context of hydrological studies. The hydrology applications of remote sensing, especially in Canada, were reviewed by Pietroniro and Prowse (2002); Pietroniro and Leconte (2000, 2005). In hydrology, soil moisture, precipitation, runoff, evaporation, transpiration, surface temperature, incoming short and long wave radiation etc. can be observed/inferred directly or indirectly via remote sensing. Lakshmi (2004) commented on the role of satellite remote sensing in the Prediction of Ungauged Basins. It is apparent that the use of remotely sensed data is severely limited for most small-size basins with areas less than a few square kilometers because of the coarse spatial resolution of the current generation of satellite or radar data. Medium-sized and large basins can use most of the satellite and radar data sets. In large basin, remotely sensed data will help in assisting the existing ground observations.

2.3 Land Surface Modeling

The land surface is a key component of climate and hydrological models. It controls the partitioning of available energy at the surface between sensible and latent heat, and the partitioning of available water between evaporation and runoff. The land surface is also the location of the terrestrial carbon sink. The land surface is essential to the exchanges of energy, heat, momentum, and carbon to the atmosphere. Land surface can influence weather and climate at a range of time scales, from seconds to millions of years (Pielke, 2001). Land surface parameterizations (LSPs) or land surface models (LSMs) are required for climate models.

There are many LSPs from the simple ones to realistic schemes describing a comprehensive range of land-atmosphere interactions. Sellers et al. (1997) summarized the LSPs into three generations (Figure 2.2). The first was based on simple aerodynamic bulk transfer formulas and often uniform prescriptions of surface parameters over continents in the later 1960s and 1970s. The first LSP was implemented into a climate model by Manabe (1969). This parameterization of hydrology is commonly called the "Manabe bucket model". A second generation of models was based from Deardorff (1978) in the early 1980s, who introduced a method for simulating soil temperature and moisture in two layers and vegetation as a single bulk layer. In terms of vegetation, vegetation layer(s) that shielded a fraction of the ground from solar radiation was proposed in the second generation models. Second-generation models usually represent the vegetation-soil system such that the surface interacts with the atmosphere, rather than being passive as in the first-generation models (Sellers et al., 1986). Second generation models estimate interception by the canopy, although it is possible to include this process in a first generation scheme. The model canopy conductance empirically, taking into account plant and environmental conditions, but they only use this conductance to model transpiration in the second generation models. The third generation models (Sellers et al., 1996) use modern theories relating photosynthesis and plant water relations to provide a consistent description of energy exchange, evapotranspiration, and carbon exchange by plants. The addition of an explicit canopy conductance improves the simulation of the evapotranspiration pathway, as well as to address the issue of carbon uptake by plants.

The ecological models parallelly developed by a different community as the development of land surface models. These ecological models tended to focus on carbon and other biogeochemical cycles, use plant functional relationships to categorize the vegetation such as Bonan et al. (2002). Running and Coughlan (1988) presented a ecological model that calculates key process involved in the carbon, water and nitrogen cycles for forests. The model was designed

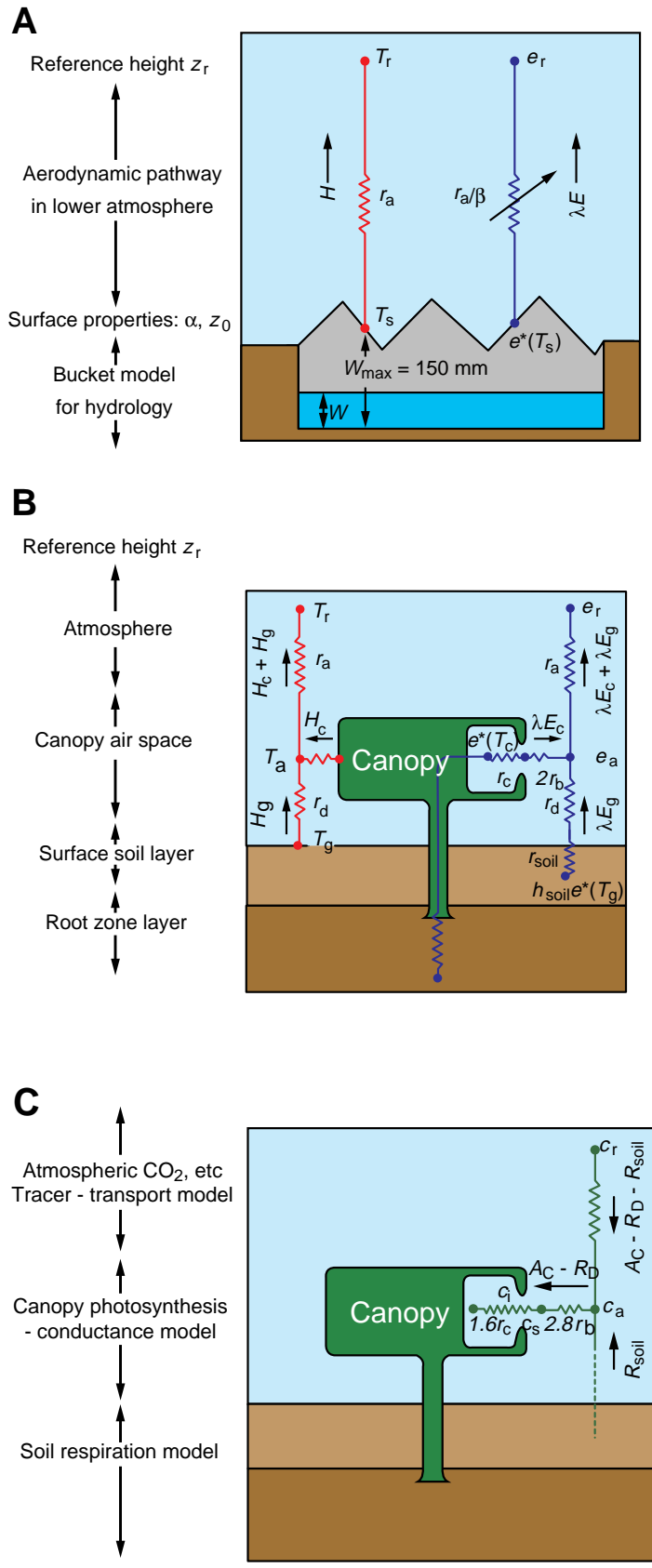


Figure 2.2: Development of LSMs: (a) first generation "bucket" model, (b) second generation model with separated vegetation canopy and soil, (c) third generation model with carbon flux pathway. [The figure is reproduced from Sellers et al. (1997)]

to be driven ultimately by remote sensing inputs of surface climate and vegetation structure, in the framework of a geographic information system containing topographic and physical site characteristics. These ecological models tended to focus on how the terrestrial biosphere responded to the atmosphere rather than how the land surface partitioned energy and water as a boundary condition for the atmosphere.

Pitman (2003) reviewed the evidences showing the influence of the land surface is significant on climate and that changes in the land surface can influence regional to global scale climate on time scales from days to millennia. Pitman (2003) provides evidence from climate model experiments that the land surface is of central importance. It is pointed out that significant problems remain to be addressed, including the difficulties in parameterization of hydrological processes, root processes, sub-grid-scale heterogeneity and biogeochemical cycles.

Both Sellers et al. (1997) and Pitman (2003) suggested that the way forward for land surface modeling is to use third generation LSMs and to improve the representation of hydrological processes in parallel. Advanced understanding of soil temperature physics, soil moisture processes, large-scale hydrology, snow physics, radiative transfer, photosynthesis-level biochemistry and large-scale ecology, boundary-layer processes, biogeochemical cycling and advanced computer science are required.

Many efforts have been done to develop remote sensing algorithms for inferring surface state characteristics. Sellers et al. (1995) reported the achievements of the ISLSCP (International Satellite Land Surface Climatology Project) workshop. The workshop reviewed progress in the area of land science, examine the role of remote sensing and set future research directions. The remote sensing techniques are widely used in water-energy-carbon, biogeochemistry and ecosystem modeling. The data priorities for land science were recommended by the workshop. The consolidated, prioritized data need were: 1) vegetation data such as cover type, phenology, disturbance, leaf area index (LAI), the Fraction of Photosynthetically Active Radiation absorbed by green vegetation canopy (FPAR), 2) Near-surface meteorology data, 3) Precipitation data, 4) Radiation fluxes, 5) Soils physics such as texture, depth, porosity and chemistry data, 6) Topography data, 7) Runoff data, and 8) Snow and ice data. After the initiatives of the ISLSCP, many global datasets were made available by the scientist from different field. Most of the global datasets were obtained inferred directly or indirectly via satellite remote sensing, and some were through global ground observation network and surveys (FAO, 1995; Myneni et al., 1997; HYDRO1k Team, 2003; Zhang et al., 2004; Siebert et al., 2005). The advances in source data from satellites, meteorological analyses, and analyses of surface survey work drive the modeling community to make more realistic simulation and deeply understand the land

surface-biosphere-atmosphere interaction.

2.4 Land Surface Hydrology with Biospheric Aspects

Biosphere research emphasize on plant physiology and phenology to simulate ecosystem productivity and biogeochemical cycling. Hydrology oriented biosphere research are similar in their emphasis of energy and water exchange, but require a detailed understanding of soil moisture and runoff dynamics to predict correctly the hydrological routing and river discharges. Attempts had been made to reconcile the differences between biospheric and hydrological research in some second generation hydrological models. The role of vegetation is very simply represented with Penman-Monteith equation (Allen et al., 1998) to estimate evapotranspiration. For instance, the SHE model tried to simulate the complete hydrological cycle, including a Penman-Monteith for evapotranspiration (Abbott et al., 1986a,b).

In order to make the current generation of hydrological models to be more integrated description of surface energy balance, photosynthesis, soil moisture and nutrient status, incorporation of carbon dynamics and vegetation physiology is motivated. Band et al. (1991) have utilized geographic information processing, remote sensing, and the ecosystem model FOREST-BGC to simulate the patterns of forest evaporation. Band et al. (1993) extended the work by coupling FOREST-BGC with TOPMODEL to account for the effects of lateral soil moisture redistribution on ecological processes. Liang et al. (1994) used an aerodynamic representation of the latent and sensible heat fluxes at the land surface and estimated water/energy components over multiple land surface cover types (VIC model). Wigmosta et al. (1994) proposed a distributed soil-hydrology-vegetation model (DHSVM) to dynamic represent the spatial distribution of soil moisture, snow cover, evapotranspiration and runoff production with a two-layer canopy representation for evapotranspiration. Evaporation of intercepted water from the surface of wet vegetation is assumed to occur at the potential rate. Transpiration from dry vegetative surfaces is calculated using a Penman-Monteith approach. The original works of Band et al. (1993); Liang et al. (1994); Wigmosta et al. (1994) were widely used in case application studies.

Mackay and Band (1997) presented a dynamic coupling of distributed hydrology and canopy growth with carbon and nitrogen processes with the coupling model of FOREST-BGC and TOPMODEL. The transpiration is computed daily using the Penman-Monteith combination equations. Storck et al. (1998) performed an application of the DHSVM to assess the hydrological effects of logging in the Pacific Northwest. Matheussen et al. (2000) used the VIC model to assess the effects of land cover change on stream flow in the interior Columbia River

basin. The evapotranspiration from each vegetation type within the grid cell is characterized by its potential evapotranspiration, aerodynamic resistance to the transfer of water and architectural resistance. Vanshaar et al. (2002) used the DHSVM to simulate hydrological effects of changes in land cover for four small and medium forested catchments of interior Columbia River basin.

In the above cases, the hydrological models typically employ empirical, rather than mechanistic formulations to predict stomata conductance and canopy fluxes. Engel et al. (2002) established the relationships between stomata conductance, leaf water potential, hydraulic conductance, soil moisture distribution and site water balance in an experimental catchment dominated by mesic and xeric ecotypes of *Quercus rubra*. The hydrology model is based on TOPMODEL formulations and uses topographic data and the averaged water table depth in the catchment to predict stream discharge. Chen et al. (2005) further developed the DHSVM to simulate the detailed spatial and temporal variation patterns of evapotranspiration around a flux tower site. The model utilized optical remote sensing data to characterize the distributions of vegetation types and LAI, in addition to meteorological, topographical and soil data. The water table and soil moisture fields were initialized using the TOPMODEL principle. Although a few works have been done to target on biospheric aspects in land surface hydrology, there is still gap between the biosphere and hydrology community. These works are suffered either inadequate representation of lateral water redistribution such as river routing or inadequate representation of plant physiology and phenology such as photosynthesis. The interdisciplinary achievements such as global datasets from satellite remote sensing were not fully used, limiting the models from a wider scope. Especially, the effect of human activities, which directly acts on the surface hydrological cycle, is not considered for most of the new generation distributed biosphere-hydrological models. Further research to bridge atmosphere-biosphere-land surface hydrology, to use the available nontraditional data, and to incorporate the human activity is needed in the land surface hydrology research.

2.5 Summary

In this chapter, existing hydrological models, land surface models and land surface hydrological models with biospheric aspects are reviewed. The three generations of hydrological models are summarized. The development of surface hydrology clearly shows the need of research on development of the new generation distributed biosphere-hydrological model. The three generations of land surface models are described. The advances in the techniques of data acquisition

made it possible to extract surface state characteristics and improved the understanding to land surface hydrology-biosphere-atmosphere interactions. The third generation distributed biosphere-hydrological model is interdisciplinary research, which should integrate the contributions from ecology, plant physiology and phenology, climatology, remote sensing, and traditional hydrology. The efforts from different scientific communities have given a great perspective of the land surface hydrology research.

The present research is addressed on the challenge of land surface hydrology research – bridging land surface hydrology to biosphere and atmosphere with use of current available nontraditional data and with the consideration of effects from human society. Full coupling of the third generation land surface biosphere model and a second generation distributed hydrological model would solidly advance the development of the new generation hydrological model and improve our understanding to land surface.

Chapter 3

Analyses on Observed Data

3.1 Introduction

The distributed biosphere-hydrological model system is applied to describe the hydrological cycle in the real world. The DBH model system gives a universe framework for the hydrological simulation over the Earth's land with the use of the global data sets. The applications of DBH model will not be limited by the location of the river basin over most land surface. However, it is clear that we live on a human dominated planet. Impounding and impeding the flow of rivers provides reservoirs of water that can be used for energy generation as well as for agriculture. Waterways also are managed for transport and for flood control. These anthropogenic activities have altered Earth's freshwater ecosystems profoundly. It is difficult to identify anthropogenic activity effects for traditional hydrological model because the land transformations by human activities are not represented. The DBH model system, which intensively uses remote sensing data, makes it possible to analyze anthropogenic effects on the hydrological cycle. The remote sensing observations can present land transformation such as vegetation condition and land cover change, which should account for the strong, often dominant influence of humanity, rather than directly represent the human activity. In this sense, the DBH model can be used to estimate human effects rather than simulate human activity. The local hydro-climatic data analysis is essential to investigate hydrological phenomena in a specific river basin. Data analysis is also part of the DBH model system.

A continental scale river basin, the Yellow River of China, with various topographic and climatic conditions is selected to perform the data analysis application. This chapter includes a detailed description of the study area, the remote sensing data analysis, and the ground observations analysis results. The application of remote sensing data analysis is described in

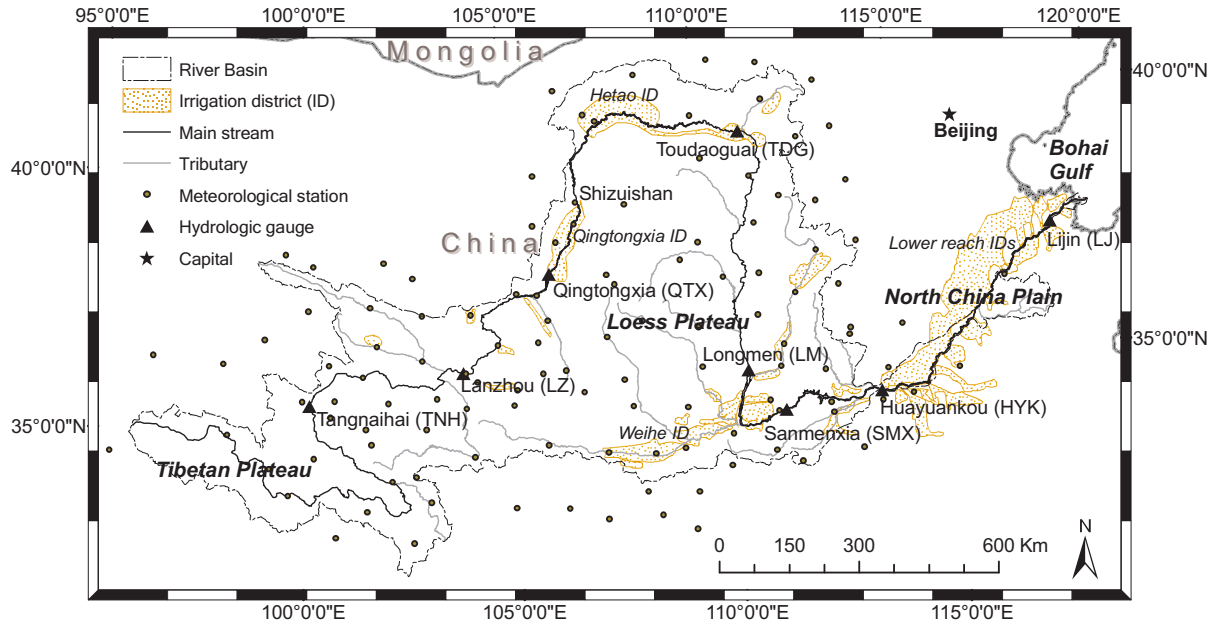


Figure 3.1: The Yellow River basin.

Section 3.2. The application of ground observations analysis is presented in Section 3.3.

The Yellow River is the second longest river in China. The headwaters of the Yellow River begin on the Tibetan Plateau and the river flows eastward, passing through the Loess Plateau and the North China Plain before emptying into the Bohai Gulf (Figure 3.1). The river flows 5464 km in distance in the main course and has a drainage area of 752,443 km². The watershed area is as large as 794,712 km² if the endorhic inner flow area is included. Most of the basin's area is arid or semi-arid. The Yellow River has been facing serious water problems, such as water shortage and eco-environmental degradation (Xu et al., 2002; Feng et al., 2005). In particular, the lower Yellow River has suffered from drying up phenomenon, i.e., zero-flow in sections of the river channel, since the 1970s. The water crisis in the Yellow River has raised a critical question: what contributes to the river drying up? The Yellow River drying up has been a hot topic in hydrology in China, attracting focus from many researches (Liu and Zheng, 2004; Fu et al., 2004; Xia et al., 2004; Yang et al., 2004a; Xu, 2005b).

3.1.1 Geography in the Yellow River Basin

The upper reach of the Yellow River drains over half of the total basin area and extends from the river's origin to the Hekouzhen (where is around Toudaoguai station). The headwater of the Yellow River stands more than 4,000 m above sea level. The middle reach, covering 46 percent of basin area and providing an additional 43 percent of the total runoff, begins at Hekouzhen.

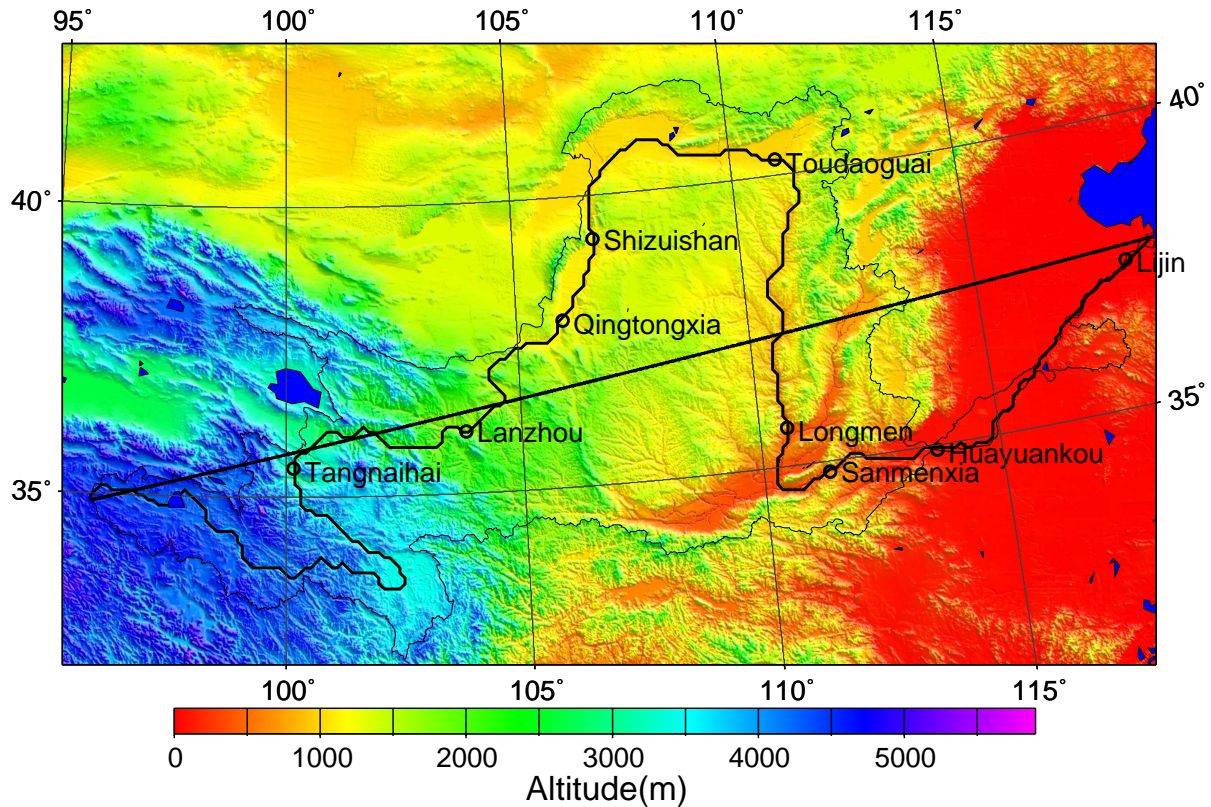


Figure 3.2: Geography of the Yellow River basin.

From there the river begins its great bend to the south into and through the Loess Plateau. The altitude in middle reaches is 1,000-2,000 m. The lower reach of the Yellow River starts at Huayuankou station and forms one of the most unique river segments in the world. The sediment transported from the middle reach begins to settle as the river spills onto the flat North China Plain, producing a consistently aggrading bed and a naturally meandering and unstable channel. The averaged altitude in the plain area is lower than 100. The altitude of the Yellow River basin is shown in figure 3.2.

The altitude profiles along the river way and the direct line from outlet to headwater are shown in figure 3.3. The altitude profile is directly abstracted from DEM map, showing the rough tendency of elevation change. The three ladders from Tibetan Plateau, the Loess Plateau to the North China Plain is obvious. The Yellow river is a meandering river with a meander ratio of 2.7. Meander ratio is a means of quantifying how much a river meanders. It is calculated as the length of the stream divided by the distance from river outlet to the headwater. A perfectly straight river would have a meander ratio of 1, and the higher this ratio is above 1, the more the river meanders. Oki and Sud (1998) used a definition of meandering ratio (r_M) as the ratio of actual (published) river length to the idealized river length. They

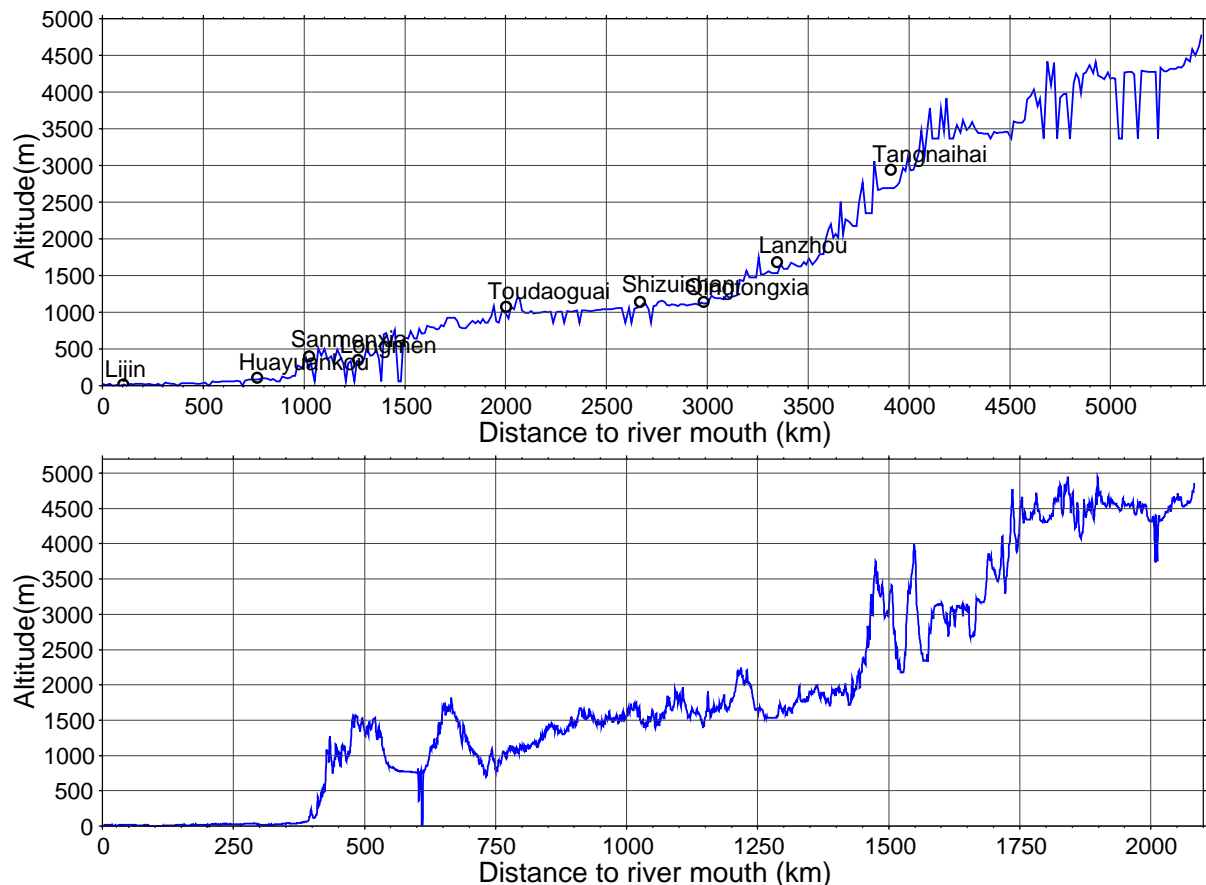


Figure 3.3: Profiles along the riverway (upper) and along the line (lower) from outlet to head-water.

recommended globally for all available data, r_M is 1.4, and it is 1.3 for rivers with areas larger than 500,000 km² in the 1×1 degree Total Runoff Integrating Pathways (TRIP). Abstracting the river network of the Yellow River from 10 km DEM grid meshes, the r_M is 1.24.

3.1.2 Available Data in the Yellow River Basin

Land surface models should be driven with reliable meteorological forcing variables such as temperature, precipitation, wind, vapor pressure, and downward longwave and shortwave radiation. The temperature, precipitation, wind speed are measured routinely at many meteorological stations. Unfortunately, downward longwave and shortwave radiation are usually unavailable for large river basins. A possible radiation data source is the output from atmospheric GCMs. But the biases in GCMs are generally still too large for hydrological models (Lau et al., 1996; Gadgil and Sajani, 1998; Boyle, 1998). One approach to obtaining radiation data is to calculate the missing data as a function of available observations.

In this study, the routine meteorological data from 120 meteorological stations inside and

closed to the study basin were obtained from the China Meteorological Administration (CMA). The data set is available from 1950s to 2000 with the daily precipitation, mean temperature, maximum and minimum temperatures, surface relative humidity and sunshine duration. The hourly meteorological data offers the greater accuracy for estimating energy flux in land surface model. Several techniques are available for approximating the diurnal temperature curve through the use of daily maximum and minimum temperatures. From the simplest to the most complex, these are averaging, single triangulation, double triangulation, single sine, double sine, and mixed curve (Baskerville and Emin, 1969; Allen, 1976; Zalom et al., 1983). These curves are often used by ecologists and biologists. Cesaraccio et al. (2001) gave a mixed sine and square-root curve (TM model) and compared it with published models. The TM model was used in this study to estimate the hourly mean temperature. The vapor pressure was then estimated from observed relative humidity and temperature (Allen et al., 1998).

The grided precipitation and temperature data is produced from station observations. The IDW method was selected for this study. In estimating each grid point using IDW method, eight nearest stations regardless direction and distance are used to contribute to grid point estimation and form the distance weighting function (Piper and Stewart, 1996). Weights for the eight stations were determined in a two-stage process following New et al. (2000). All stations were first weighted by distance from the grid point. The second component of the distance weight was determined by the directional (angular) isolation of each the eight selected stations (Jones et al., 1997; New et al., 2000). Figure 3.4 displays the patterns of the variables in the forcing dataset (precipitation, mean, minimum and maximum temperature, relative humidity, vapor pressure, wind speed, sunshine duration, downward shortwave radiation, and downward longwave radiation). Figure 3.5 shows the time series of monthly averaged forcing variables from 1982 to 2000.

SiB2 land cover, LAI, and FPAR are obtained from global data sets. Soil texture is taken from FAO global soil map. And soil parameters soil water potential at saturation, soil hydraulic conductivity at saturation, soil wetness parameter, porosity and averaged slope are estimated from the soil texture (Cosby et al., 1984). Figure 3.6 gives the averaged LAI and FPAR values in the study area. Figure 3.7 shows the soil parameters (soil water potential at saturation, hydraulic conductivity at saturation, soil wetness parameter, and porosity) in the study area.

On the basis of previous studies, the present study will focus on the climatic change and vegetation condition change in the basin. Forty years of hydro-climatic data and twenty years of vegetation condition data have been collected. The spatial climatic change and vegetation

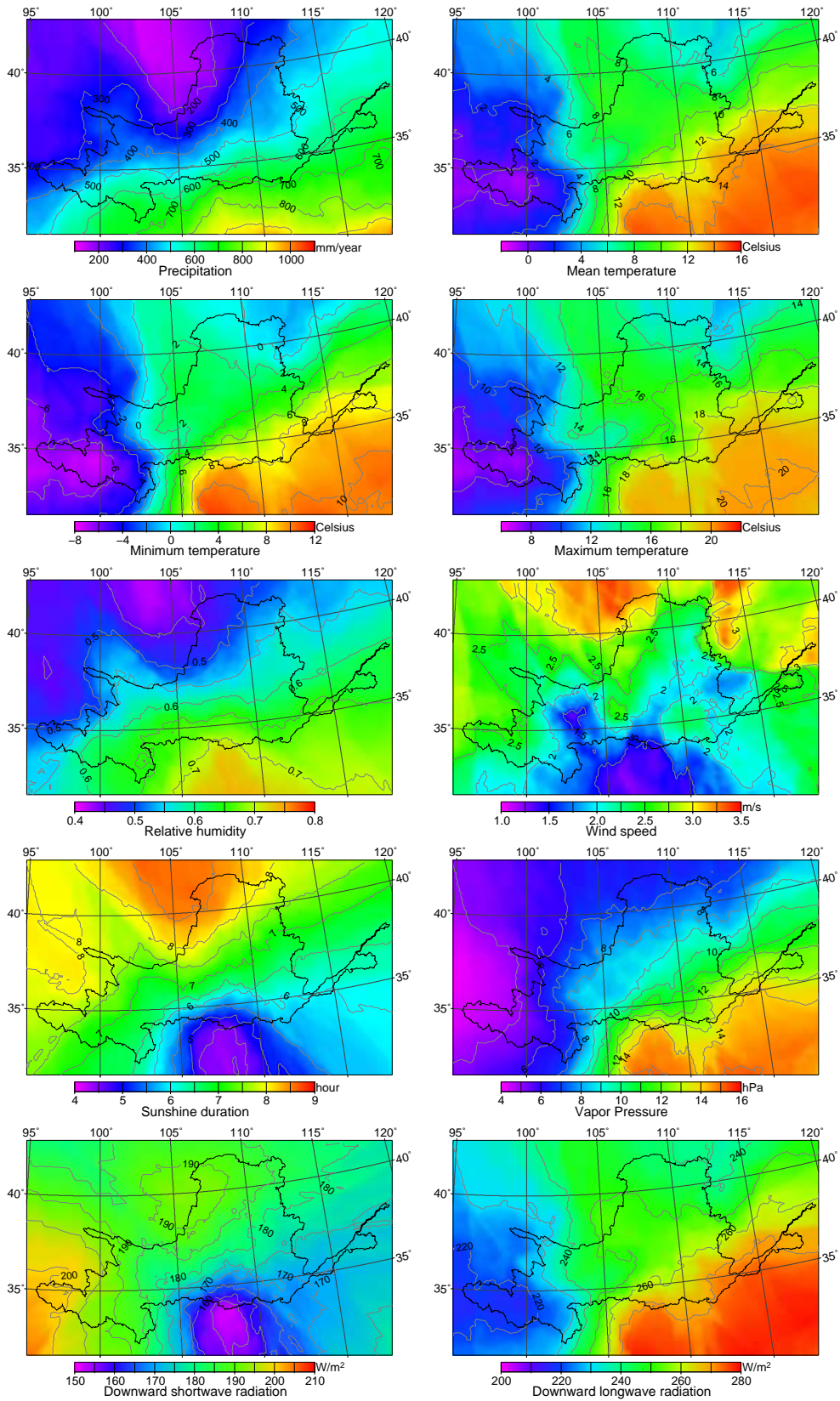


Figure 3.4: Forcing variables in the study area (1982-2000).

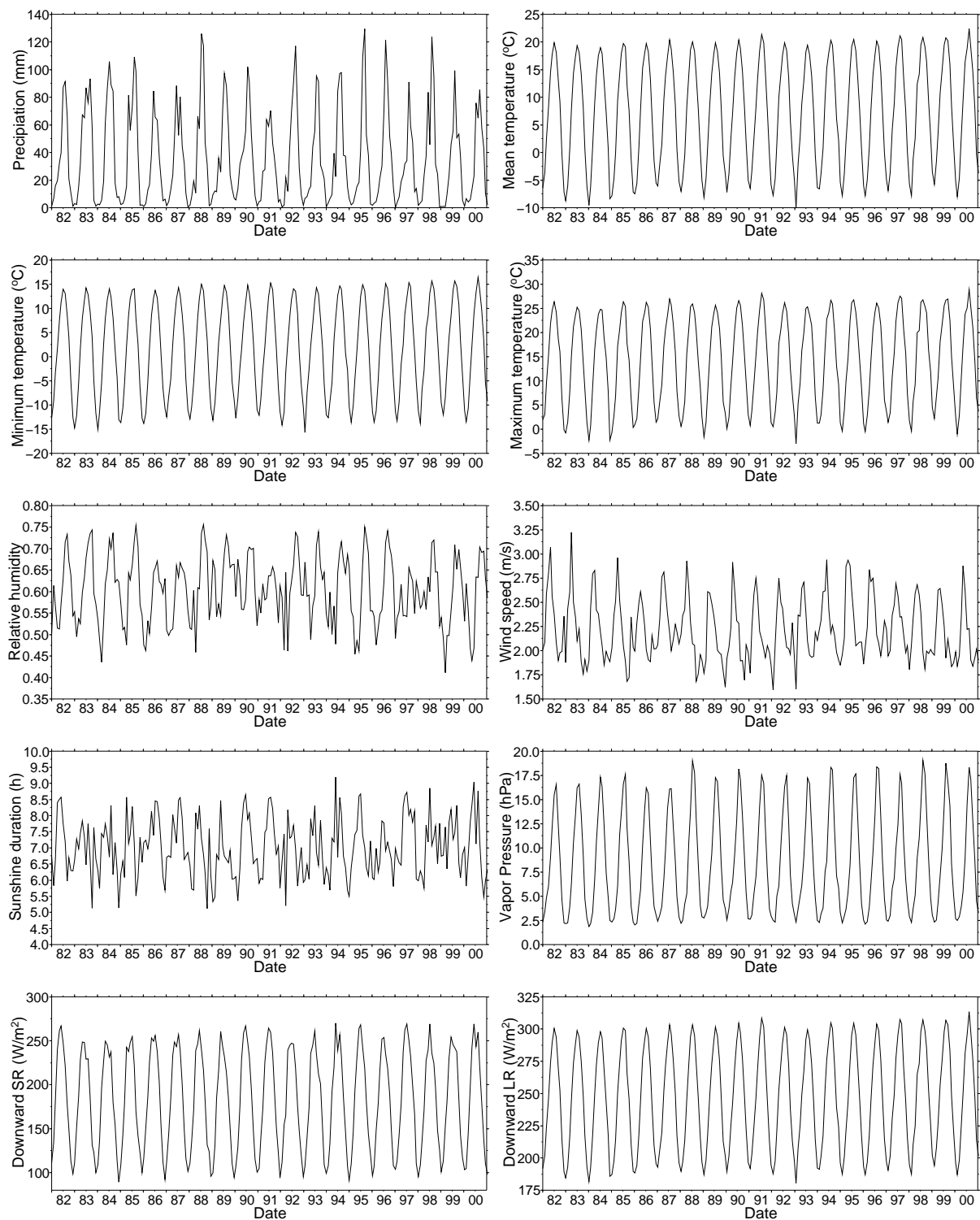


Figure 3.5: Time series of monthly forcing variables (1982-2000).

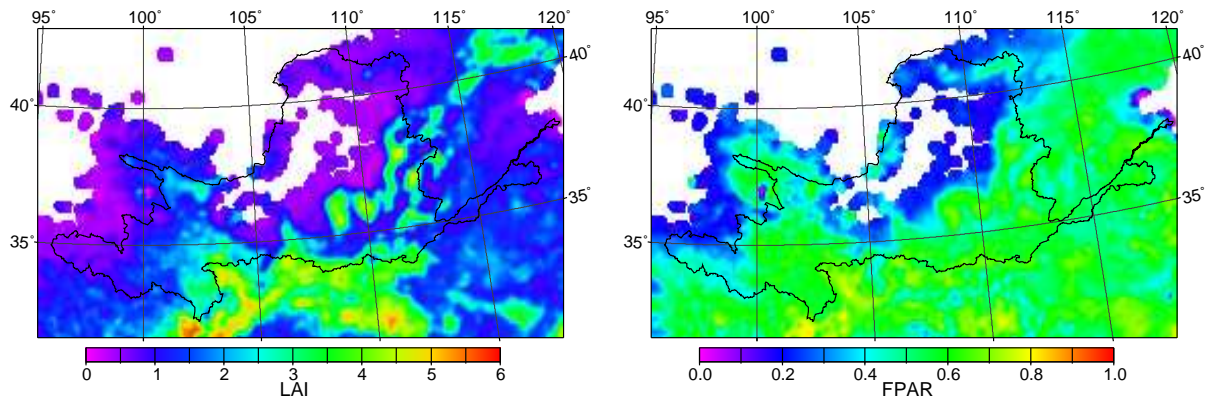


Figure 3.6: Averaged LAI and FPAR (1982-2000).

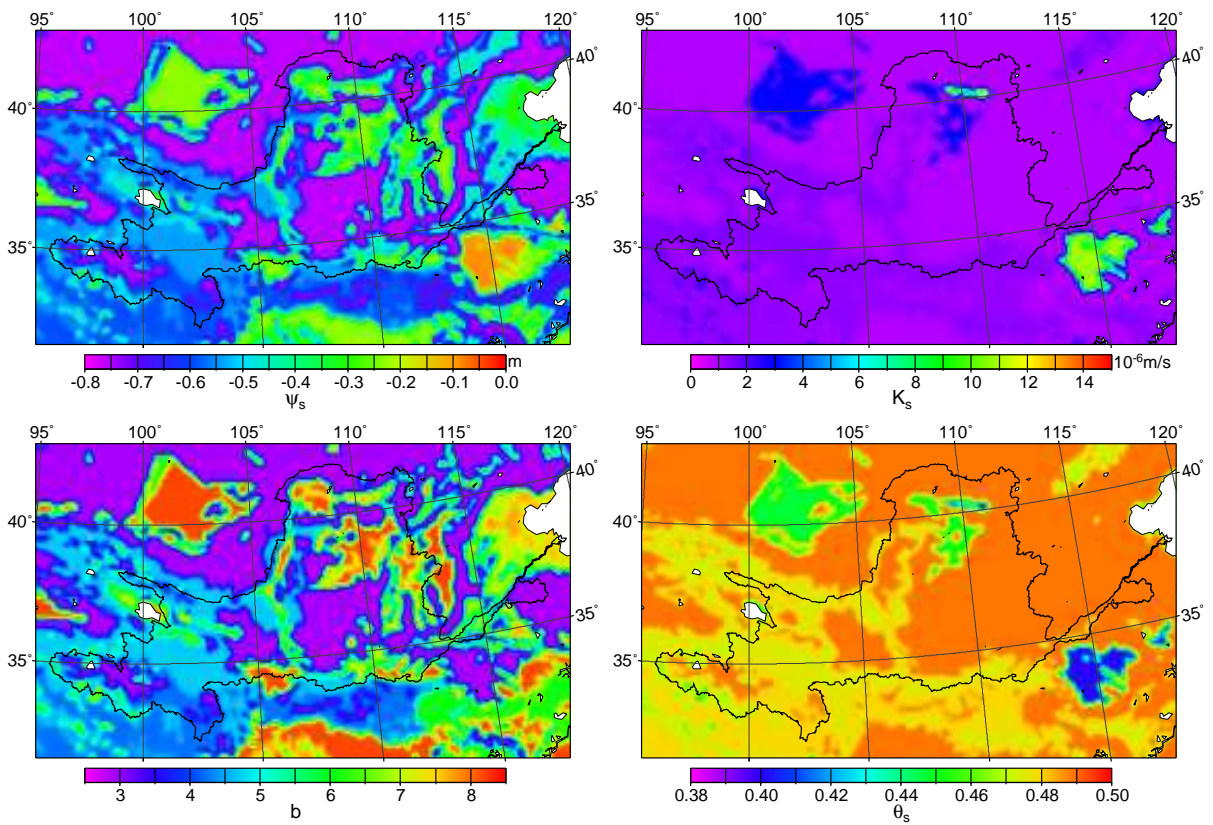


Figure 3.7: Soil parameters.

condition change will be examined to describe trends in different parts of the basin.

3.2 Remote Sensing Data Analysis

Several remote sensing data sources are used in the DBH model system. However, most of them are derived from the imagery of NOAA/NASA satellite (Pathfinder AVHRR Land Database, PAL). While more advanced imagers are already flying, AVHRR remains an important source of remote sensing data. In addition, only the AVHRR offers a data-record that spans over twenty years making it a critical data set for decadal climate studies. The DBH model system provides a tool to detect the time series of remote sensing data change in each pixel. And the remote sensing data can be compared with ground station observations and data coverage interpolated from ground observations. The tool could be used to check the consistence between remote sensing products and the spatial data estimated from conventional interpolation methods. It provide a new way to evaluate the algorithm used in remote sensing data processing, and hopefully bridge the gap between remote sensing and ground observations in the large scale. The tool is designed for the AVHRR data format and could be used with remote sensing products from other sources. The tool is applied to analyze the relationship between NDVI data and ground observed cloud indices in this section (Tang and Oki, 2006).

3.2.1 Introduction

The normalized difference vegetation index (NDVI) is a non-linear transformation of the visible (red) and near-infrared bands of remotely sensed imagery. The NDVI is defined as the ratio of $(\text{NIR} - \text{Red})$ to $(\text{NIR} + \text{Red})$, where NIR is the spectral response in the near-infrared band, and Red is the spectral response in the red band (Tarpley et al., 1984). The NDVI obtained using visible and near infrared data from channels 1 (0.58-0.681 μm) and 2 (0.725-1.11 μm) (i.e., $[\text{CH } 2 - \text{CH } 1]/[\text{CH } 2 + \text{CH } 1]$) of the Advanced Very High Resolution Radiometer (AVHRR) is commonly used to monitor vegetation (Tucker, 1979; Jackson et al., 1983; Justice et al., 1985; Tucker et al., 1991). As an index of relative seasonal changes in vegetation rather than the vegetation amount, the NDVI cannot be used directly as a parameter in numerical models. Various studies have correlated the NDVI with physical properties of the vegetation canopy, such as the leaf area index (LAI), fractional vegetation cover, vegetation condition, and biomass (Wiegand et al., 1979; Zhang and Williams, 1997; Carlson and Ripley, 1997). Previous studies have also related the NDVI to components of the water balance equation, such as soil moisture, precipitation, and evaporation (Choudhury and Golus, 1988; Grist et al., 1997; Szilagyi et al.,

2000). However, clouds can block satellite observations, and numerous studies have explored methods to yield a "cloud free" NDVI, as would be measured at the ground surface. Maximum-value composite images from temporal satellite data have been used to remove errors caused by clouds (Holben, 1986). This compositing process provides the most cloud-free image possible.

Although clouds can be considered obstacles to satellite-derived observations, cloud distortions in satellite data can also allow for cloud estimates. The NOAA National Environmental Satellite, Data and Information Service (NESDIS) developed an experimental satellite-derived cloud dataset to provide cloud parameterization schemes in real time (Stowe et al., 1999). This "cloud from AVHRR" (CLAVR) dataset is retrieved by a sequential, multispectral, decision-tree threshold algorithm that uses information from NOAA satellites (Stowe, 1991; Stowe et al., 1991). Preliminary analysis has compared the CLAVR cloud product to other satellite-derived cloud analyses, such as data from the U.S. Air Force Real-Time Nephanalysis (RTNEPH) and the International Satellite Cloud Climatology Project (ISCCP) (Hou et al., 1993). However, no direct comparisons between CLAVR and a ground-observed cloud index have been made over a large region.

This study used daily NDVI images derived from NOAA AVHRR data. Monthly composite NDVI values were compared to daily NDVI data to create a daily NDVI Cloud Index (NCI). Daily NCI values were related to observed cloud amounts and sunshine duration indices from 120 meteorological stations over a 6-year period. The NCI and CLAVR cloud values were then compared to the observed cloud amounts and sunshine index over a 776,900 km² study area with diverse land cover. Relationships between the NCI and CLAVR and ground-observed cloud cover are presented and analyzed.

3.2.2 Methodology

Daily time series of NDVI between 1995 and 2000 over the Yellow River Basin in China (Figure 3.8) were obtained from the NOAA/NASA Pathfinder AVHRR Land Database (PAL; 8 km resolution; available at <http://daac.gsfc.nasa.gov/>; (Goward et al., 1991)). The study area contains three main landforms: the Qinghai-Tibet Plateau, the Loess Plateau, and an alluvial plain (Yang et al., 2004a). Daily NDVI values, which had been corrected for Rayleigh scattering and ozone absorption but not for atmospheric water vapor (James and Kalluri, 1994), were the basis of the NDVI dataset. Although the PAL dataset is not sufficiently stable to represent cloud variations within one day, it can represent daily variations in cloud status. More advanced imagers are now in operation, but the AVHRR remains an important source of remotely sensed data. Only the AVHRR offers a data record longer than 20 years, which is critical for decadal

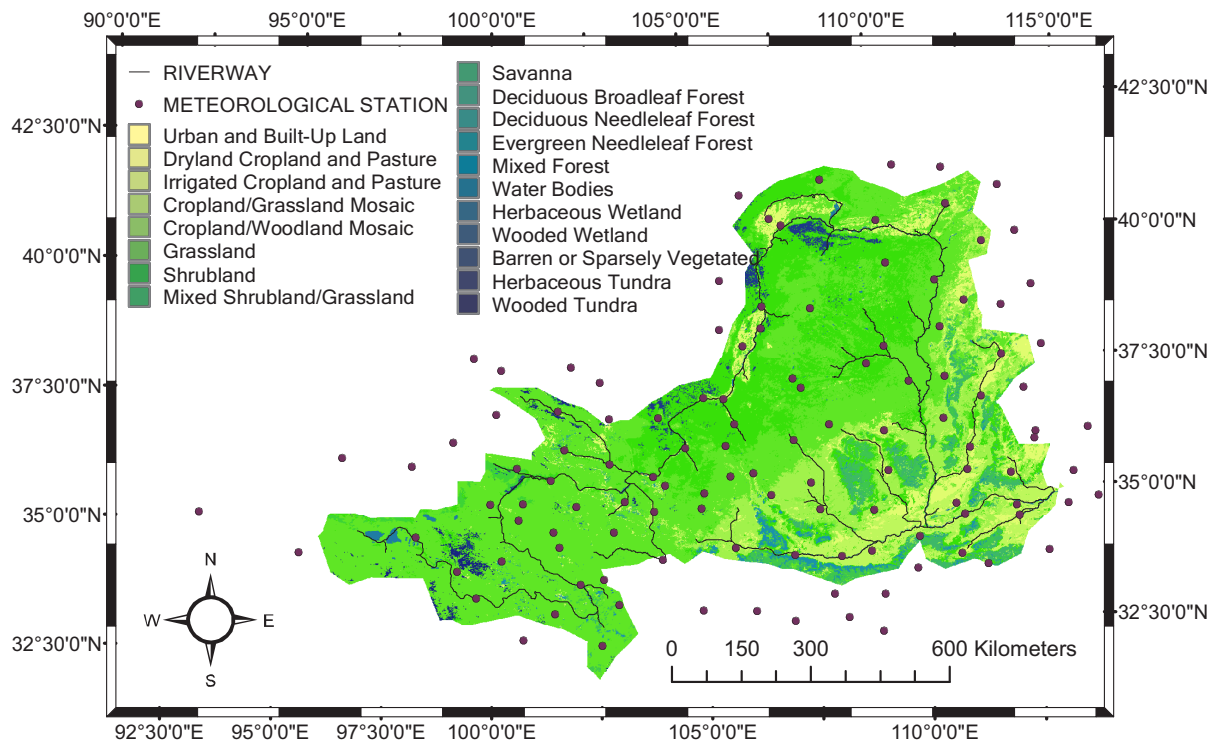


Figure 3.8: Study area.

climate studies. Daily CLAVR flag data from the PAL dataset were also used in this study. Land use data were obtained from the U.S. Geological Survey Land Use dataset based on 1-km AVHRR data between April 1992 and March 1993 (Anderson et al., 1976; Loveland et al., 1999). Elevation data were derived from HYDRO1k, a geographic database developed at the U.S. Geological Survey's (USGS) Earth Resources Observation and Science (EROS) Data Center that provides comprehensive and consistent global coverage of topographically derived datasets (HYDRO1k Team, 2003).

Numerous methods allow the production of a cloud-free NDVI (Holben, 1986; Verhoef et al., 1996; Roerink et al., 2000). The maximum composite method used in this study simplifies calculations. Daily NDVI values are composited at each grid point in the study area based on comparison of NDVI values on consecutive days in each month. The pixel with the highest NDVI value for the month is chosen as the date for inclusion in the composite. NDVI values for each day in the study period are then interpolated from the composite monthly data using a cubic spline method. The estimated daily NDVI is considered a "cloud free" NDVI.

The ratio of the NDVI value directly derived from instantaneous satellite observations to the "cloud free" NDVI value represents the cloud influence. For clear sky, the NDVI derived directly from satellite observations matches the "cloud free" NDVI. For an overcast sky, the NDVI directly derived from satellite observations is the same as the minimum NDVI for the

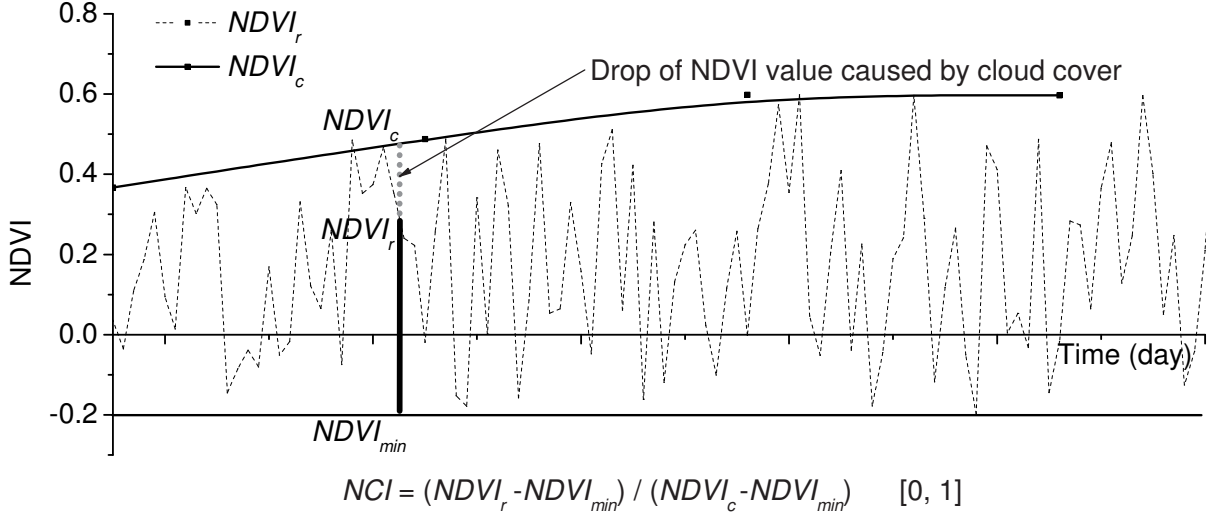


Figure 3.9: NDVI Cloud Index (NCI).

entire study period. A partially cloudy sky is indicated when the NDVI directly derived from satellite observations falls between the "cloud free" NDVI value and the minimum NDVI. The NCI ranges from 0 for overcast to 1 for clear and is defined as (Figure 3.9)

$$NCI = (NDVI_r - NDVI_{min}) / (NDVI_c - NDVI_{min}) \quad (3.1)$$

where $NDVI_r$ is the NDVI value directly derived from instantaneous satellite observations; $NDVI_c$ is the "cloud free" NDVI value, and $NDVI_{min}$ is the minimum value of NDVI. Note that the NCI is bounded so that it is less than 1.0.

The China Meteorological Administration (CMA) provided daily observed cloud amount and actual duration of sunshine data from 120 meteorological stations within or close to the study area (Figure 3.8). Solar radiation, R_s , was calculated with the Angstrom formula that relates solar radiation to extraterrestrial radiation and relative sunshine duration (Allen et al., 1998):

$$R_s = (a_s + b_s \times n/N)R_a \quad (3.2)$$

where n is the actual duration of sunshine (hour), N is the maximum possible duration of sunshine or daylight hours (hour), a_s is a regression constant that is the fraction of extraterrestrial radiation reaching the Earth on overcast days, $(a_s + b_s)$ is the fraction of extraterrestrial radiation reaching the Earth on clear days, and R_a is extraterrestrial radiation. The ratio of actual sunshine duration to daylight hours n/N describes the influence of clouds on solar radiation and is defined as the Sunshine-Cloud Index (SCI).

Daily NCI and CLAVR values were related to ground observations of cloud amount and

the SCI from the 120 meteorological stations. A linear least-squares best fit method was used, and the overall quality of the fit was then parameterized in terms of the correlation coefficient R defined by

$$R = \frac{N \sum x_s x_g - \sum x_s \sum x_g}{\sqrt{[N \sum x_s^2 - (\sum x_s)^2][N \sum x_g^2 - (\sum x_g)^2]}} \quad (3.3)$$

where N is the total number of time series being compared, x_s represents the satellite-derived cloud indices (i.e., NCI or CLAVR values), and x_g represents ground-observed cloud indices (i.e., the observed cloud amount or SCI). The R^2 value is the square of the correlation coefficient. The linear least-squares fitting method requires that ground-observed cloud indices be predicted by satellite-derived cloud indices as follows:

$$x'_g = a + bx_s \quad (3.4)$$

where x'_g is the cloud index predicted by the satellite data,

$$b = \frac{N \sum x_s x_g - \sum x_s \sum x_g}{N \sum x_s^2 - (\sum x_s)^2} \quad (3.5)$$

and

$$a = \frac{\sum x_g - b \sum x_s}{N} \quad (3.6)$$

The root-mean-square error (RMSE) and mean absolute error (MAE) between the predicted cloud index x'_g and the ground-observed cloud indices are given as

$$RMSE = \sqrt{\frac{1}{N} \sum (x'_g - x_g)^2} \quad (3.7)$$

and

$$MAE = \frac{1}{N} \sum |x'_g - x_g| \quad (3.8)$$

The NCI values can be estimated over the entire study area, but ground stations provide only point observations. Surface climate data from station observations are thus usually interpolated to gridded data (New et al., 1999). Similarly, the observed cloud amount and SCI values for the stations were interpolated to a grid over the study area using a thin-plate spline algorithm. Daily NCI values over the study area were then compared to the gridded cloud amount and SCI data for the same period (1995 to 2000). The relationship as a function of land cover was analyzed using U.S. Geological Survey Land Use data. HYDRO1k digital elevation model (DEM) data were used to derive variation with elevation.

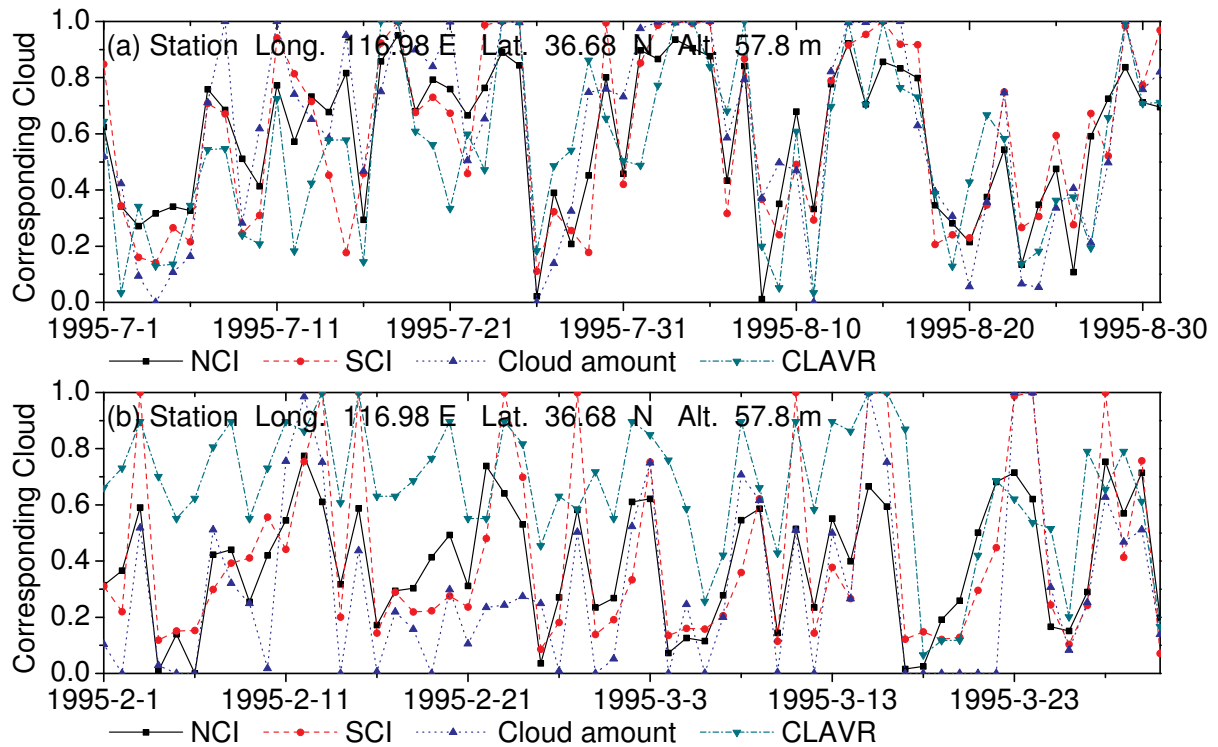


Figure 3.10: Time series of NCI, SCI, CLAVR, and ground-observed cloud amounts.

Comparisons for each month yielded seasonal variations in the relationship. Daily NCI values of one month were selected and related to the cloud amount and SCI from 1995-2000. The monthly variation of the relationship was demonstrated.

3.2.3 Results and Conclusions

Figure 3.10 shows time series of NCI, SCI, CLAVR, and ground-observed cloud amounts. Values of NCI, SCI, and CLAVR are scaled from [0, 1], while observed cloud amount value is from [1, 0]. Figure 3.10a compares July and August, and Fig. 3.10b compares February and March. Both CLAVR and the NCI capture the daily cloud variance in summer. The NCI cloud estimates do not agree with the ground-observed cloud amount or the SCI in winter. In winter, the cloud amount estimated by CLAVR poorly matches the ground observations.

Figure 3.11 shows the relationships of the cloud amount, NCI, SCI, and CLAVR at the observation stations. Valid data observed during the study period were cataloged into ten categories, and the distributions are presented. The linear fit line for the data points is shown with the squared correlation coefficient. Figure 3.11a shows NCI values and SCI ($R^2 = 0.506$). Figures 3.11b, 3.11c, and 3.11d show the relationship between ground-observed cloud amount and the CLAVR, NCI, and SCI values, respectively. The CLAVR values and cloud amount have the poorest correlation ($R^2 = 0.169$). CLAVR values range mainly from 1-15. The NCI

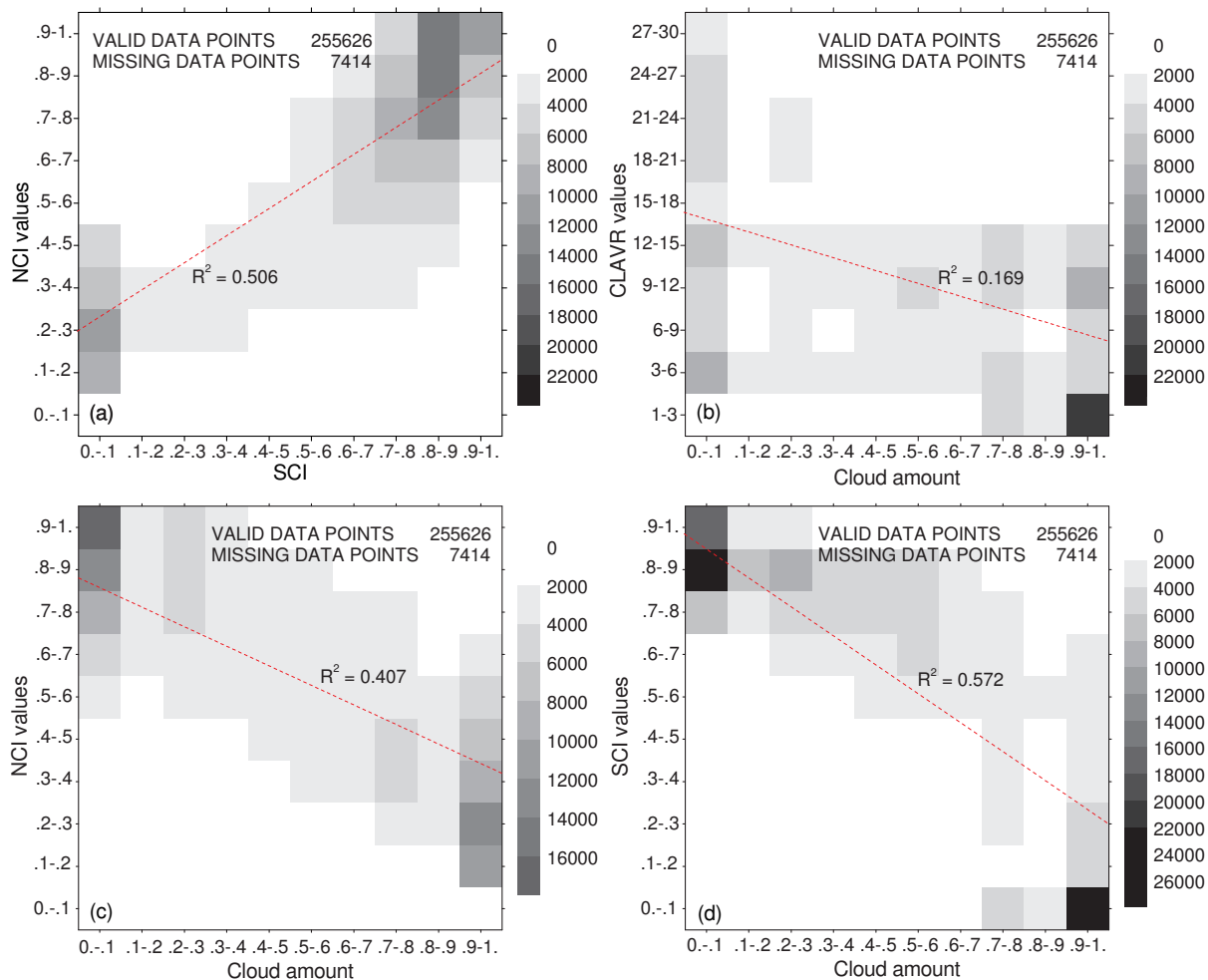


Figure 3.11: Cloud amount, NCI, SCI, and CLAVR values. (a) NCI values versus SCI; (b) CLAVR versus cloud amount; (c) NCI versus cloud amount; (d) SCI versus cloud amount.

and SCI both had higher correlations with ground-observed cloud amount with R^2 values of 0.407 and 0.572, respectively. The NCI results are more consistent with the ground-observed cloud index. The direct relationship between CLAVR values and the ground-observed cloud amount is not as robust.

Figure 3.12 shows histograms of cloud distributions at the ground-observation stations during the study period. More than 20% of the points have cloud fractions between 0.55 and 0.65 for the CLAVR cloud estimates because "mixed cloudy" is the predominant classification from the CLAVR algorithm. Less than 1% of the points have cloud fractions ranging from 0.95-1.0 for the NCI clouds because $NDVI_{min}$ was derived from the minimum NDVI value for the entire study period. For the SCI clouds, more than 20% of the points have cloud fractions between 0.05 and 0.25. The ground-observed cloud amount is relatively uniformly distributed in each cloud category, with higher occurrences in the nearly clear and cloudy categories.

Table 3.1 shows the R^2 value for satellite remotely sensed data and ground observations.

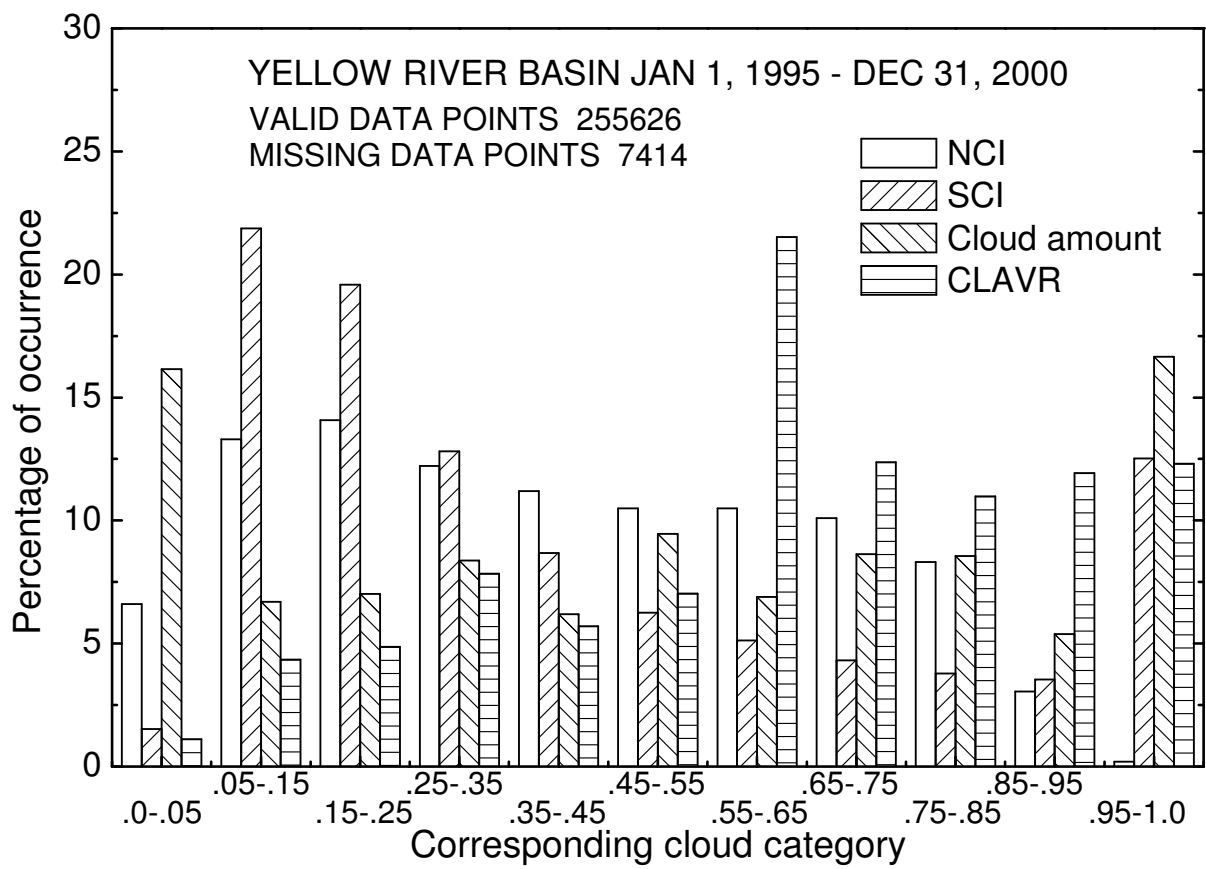


Figure 3.12: Histogram of cloud distributions at the ground-observation stations.

Table 3.1: Daily NCI, CLAVR values, and ground observations

USGS Land Use	NCI/Cloud		NCI/SCI		CLAVR/Cloud		CLAVR/SCI	
	R^2	SD	R^2	SD	R^2	SD	R^2	SD
Urban and Built-Up Land	0.42	0.05	0.53	0.07	0.18	0.10	0.25	0.11
Dryland Cropland and Pasture	0.42	0.06	0.51	0.07	0.17	0.08	0.23	0.10
Irrigated Cropland and Pasture	0.45	0.04	0.58	0.04	0.26	0.07	0.33	0.09
Cropland/Grassland Mosaic	0.45	0.04	0.53	0.03	0.20	0.07	0.28	0.09
Cropland/Woodland Mosaic	0.47	0.07	0.58	0.04	0.32	0.07	0.28	0.09
Grassland	0.38	0.08	0.48	0.07	0.11	0.07	0.16	0.08
Shrubland	0.40	0.07	0.49	0.07	0.20	0.11	0.26	0.15
Mixed Forest	0.39	0.02	0.45	0.09	0.14	0.02	0.21	0.06
Grand summary	0.41	0.07	0.50	0.07	0.16	0.09	0.22	0.11

The R^2 values for the NCI and cloud amount range from 0.38 to 0.47, with an average value of 0.41 for the 120 stations representing diverse land covers. The averaged standard deviation (SD) of R^2 is 0.07. For the NCI and SCI, R^2 values range from 0.45 to 0.58, with an average value of 0.50. The averaged standard deviation of the R^2 values is 0.07. Results show that the correlation coefficients for NCI and the observed cloud amount or SCI have high values across diverse land cover types. The R^2 associated with CLAVR values and the observed cloud amount or SCI are 0.16 and 0.22, respectively. Correlation coefficients for CLAVR values and the observed cloud amount or SCI show lower values than the correlation coefficients between the NCI values and ground-observed indices.

The RMSE associated with the NCI and observed cloud amount ranges from 0.21 to 0.30, with an average value of 0.25. The MAE ranges from 0.17 to 0.25 with an average value of 0.20. Figure 3.13a shows the R^2 value for the daily NCI values and observed cloud amount in each pixel of the study area. Figure 3.14a shows the cumulative distribution function of R^2 values in the study area. For less than 20% of the pixels, R^2 is less than 0.36 (i.e., the correlation coefficient equals 0.6). In the study area, 87% of the pixels have R^2 values of less than 0.49 (i.e., the correlation coefficient equals 0.7). The RMSE associated with NCI and SCI ranges from 0.16 to 0.26 with an average value of 0.20, and the MAE ranges from 0.12 to 0.22, with an average value of 0.16. Figure 3.13b shows the correlation coefficients between daily NCI values and observed SCI for each pixel. Figure 3.14b shows the distribution of R^2 values in the study area. The R^2 values are less than 0.36 (i.e., the correlation coefficient equals 0.6) at fewer than 10% of the pixels. Pixels where the R^2 value is less than 0.49 (i.e., the correlation coefficient equals 0.7) cover 41% of the study area. For CLAVR data, the RMSE associated with the cloud amount ranges from 0.26 to 0.34, with an average value of 0.30, and the averaged MAE is 0.25. The RMSE associated with the SCI ranges from 0.21 to 0.30, with an average of

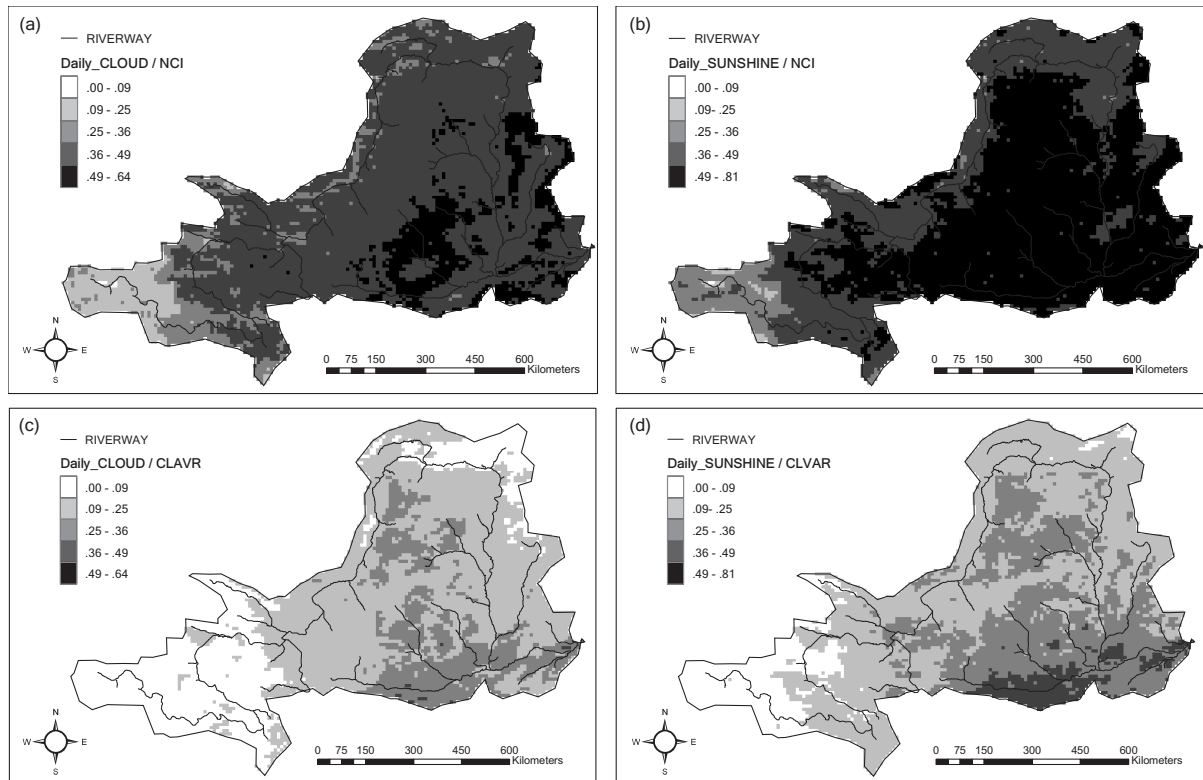


Figure 3.13: R^2 for (a) daily NCI values and the observed cloud amount, (b) daily NCI values and the observed SCI, (c) CLAVR values and the observed cloud amount, (d) and CLAVR values and the observed SCI.

0.25 and average MAE of 0.20. The error in CLAVR estimates is larger than that for the NCI. Figures 3.13c and 3.13d show the R^2 associated with daily CLAVR values and ground-observed cloud indices. The R^2 values in most of grid boxes are less than those associated with daily NCI values. Pixels where R^2 is less than 0.36 occupy 99.8% and 94.9% of the study area for the cloud amount and SCI, respectively (Figure 3.14).

The NDVI is sensitive to and influenced by land cover. Comparison of Figures 3.13 and 3.8 indicates a close relationship between the NCI and observed cloud indices over most of the well vegetated land covers. Table 3.2 shows the R^2 associated with the cloud indices calculated from satellite-derived data and from ground observations. The R^2 values associated with the NCI and cloud amount range from 0.26 to 0.49, with an average value of 0.42 for all the pixels in the study area. Pixels classified by the USGS to have wooded tundra, mixed shrubland/grassland, and water bodies have the lowest R^2 , with average values of 0.26, 0.27, and 0.35, respectively. Standard deviations of R^2 are substantially larger, and the relationships more uncertain, over water bodies and over wooded tundra than over other land types. R^2 values exceeding 0.4 occur for relatively well vegetated land uses including deciduous broadleaf forest, cropland/woodland mosaics, cropland/grassland mosaics, savanna, mixed forest, irri-

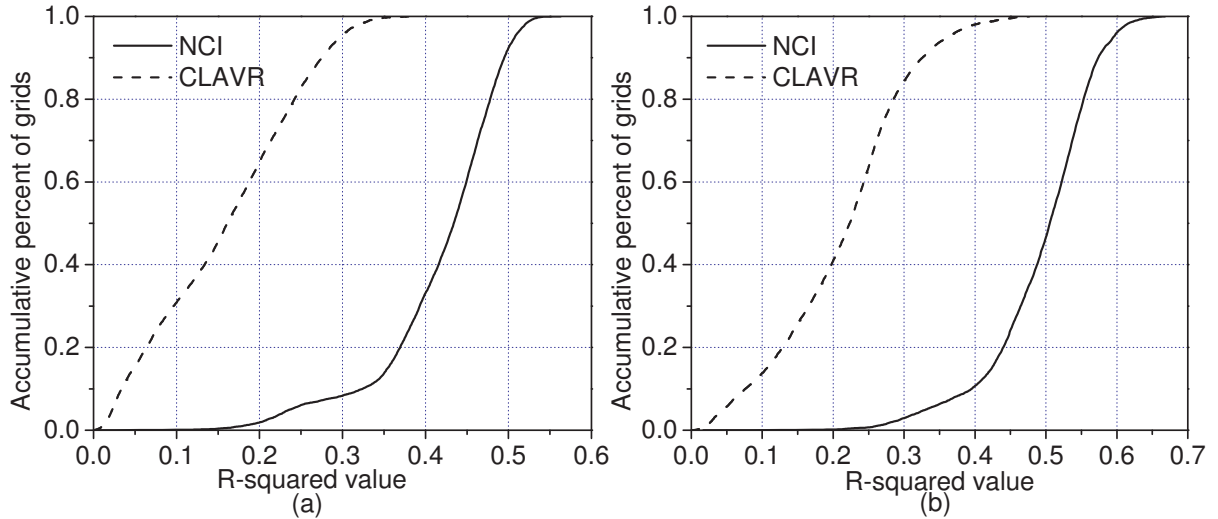


Figure 3.14: Cumulative distribution of R^2 associated with (a) NCI-cloudiness and CLAVR-cloudiness, (b) and NCI-SCI and CLAVR-SCI.

gated cropland and pasture, dryland cropland and pasture, deciduous needleleaf forest, and shrubland. The R^2 associated with the NCI and SCI range from 0.33 to 0.57, with an average value of 0.49 in the study area. The smallest R^2 values again occur over regions classified by the USGS as having wooded tundra. The standard deviations of R^2 values are the largest, indicating uncertainty, over water bodies and wooded tundra. The R^2 values remain higher than 0.5 over the well vegetated land uses mentioned above. The lower R^2 values over wooded tundra suggest that frozen surface soil and snow cover may disturb the relationships between the NCI and observed cloud indices.

Figure 3.13 shows that the weakest relationships for both the cloud amount and SCI occur at the Qinghai-Tibet Plateau, where the land use is classified as wooded tundra. Figure 3.15 shows R^2 values versus altitude for all the pixels in the study area. Figure 3.15a provides R^2 values relating the NCI and SCI; these values are approximately 0.45 for altitudes less than 500 m, near 0.40 for altitudes between 500 and 3,500 m, and near 0.20 for altitudes around 4,500 m. Figure 3.15b shows that the R^2 values for the NCI and cloud amount vary between 0.40 and 0.65 for altitudes below 3,500 m, decreasing sharply to 0.20 at higher altitudes. The relationship at low elevations is more robust than at high elevations. Because frozen surface soil and snow cover are more common at higher elevations, this result further confirms the hypothesis that frozen surface soil and snow cover may disturb the relationship between the NCI and observed cloud indices.

Figure 3.16 shows seasonal variations in R^2 values in the study area. The mean R^2 value for all the pixels is shown by the curve; standard deviations are shown by error bars. The R^2

Table 3.2: Daily NCI values and cloud indices derived from observations

USGS Land Use	Cloud R^2	Cloud SD	SCI R^2	SCI SD
Urban and Built-Up Land	0.37	0.06	0.49	0.06
Dryland Cropland and Pasture	0.44	0.05	0.51	0.07
Irrigated Cropland and Pasture	0.46	0.04	0.57	0.05
Cropland/Grassland Mosaic	0.47	0.04	0.55	0.05
Cropland/Woodland Mosaic	0.48	0.04	0.54	0.04
Grassland	0.39	0.08	0.47	0.08
Shrubland	0.43	0.05	0.50	0.06
Mixed Shrubland/Grassland	0.27	0.06	0.38	0.08
Savanna	0.47	0.05	0.51	0.04
Deciduous Broadleaf Forest	0.49	0.03	0.52	0.04
Deciduous Needleleaf Forest	0.43	0.05	0.51	0.02
Mixed Forest	0.46	0.05	0.52	0.05
Water Bodies	0.35	0.13	0.43	0.14
Barren or Sparsely Vegetated	0.37	0.05	0.45	0.06
Wooded Tundra	0.26	0.10	0.33	0.10
Grand summary	0.42	0.08	0.49	0.08

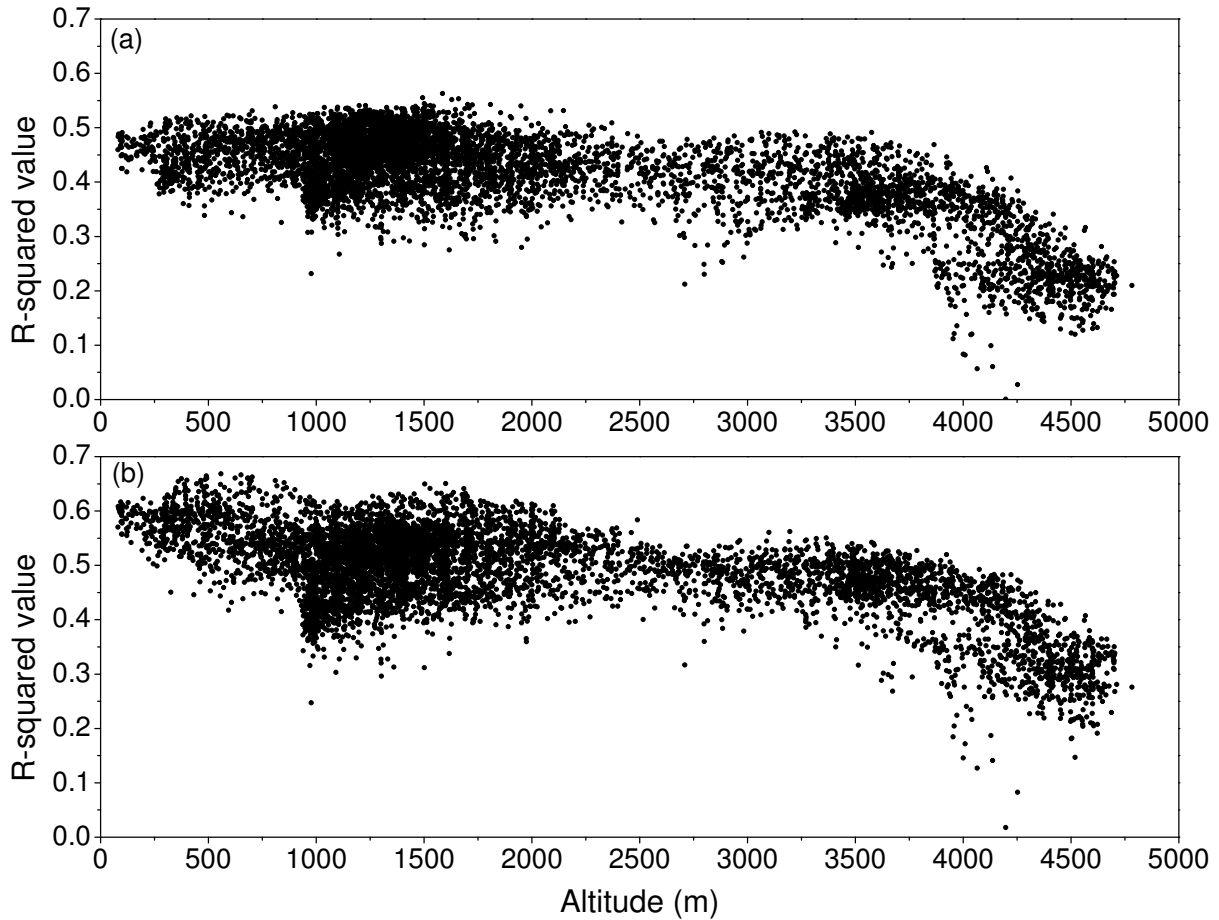


Figure 3.15: R^2 values for (a) the NCI and cloud amount, (b) and the NCI and SCI as a function of altitude.

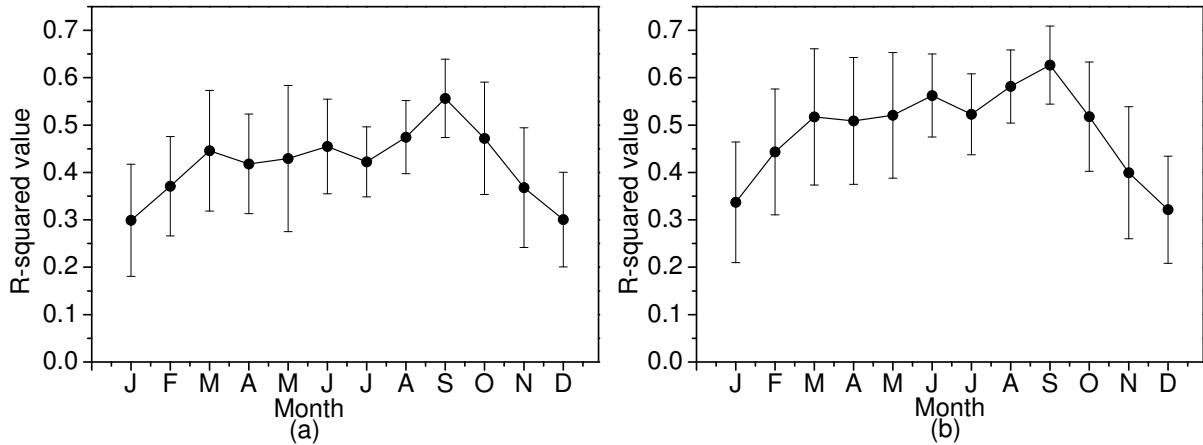


Figure 3.16: Seasonal variation in R^2 values for (a) the NCI and cloud amount, (b) and the NCI and SCI.

values are small in January during boreal winter. Values increase in March, April, and May as spring arrives. Peaks occur in September when snow and frozen surface soil melt on the Qinghai-Tibet Plateau. The R^2 values decrease starting in October as snow begins to cover the Qinghai-Tibet Plateau. Standard deviations in summer are significantly smaller than in winter. The NDVI is a more reliable estimate of cloudiness in summer. The relatively poor relationship in winter occurs because of snow and frozen surface soil.

Figure 3.17 compares the R^2 values in January and September. The R^2 values are large in September for the relationship for both cloud amount and SCI. Smallest values in September occur at high elevations where permanently frozen soil and snow cover exist. The R^2 values are lower in January over the entire study area. Smallest values persist at altitudes above 3,500 m, the elevation of the Qinghai-Tibet Plateau. Values in January at altitudes of 1,000-2,000 m corresponding to the Loess Plateau decrease to the values found at high elevations in September. The R^2 values remain high over the alluvial plain where altitudes are less than 500 m.

The relationships between NCI and observed cloud amount and the SCI are robust over most well-vegetated regions. The strongest relationships occur at low elevations in summer, and the weakest relationships occur at high elevations in winter. Frozen surface soil and snow cover may preclude the NDVI index from correctly determining cloudiness in the latter area. Nevertheless, the daily NDVI index is a useful tool for estimating the influence of clouds and solar radiation over a large area.

3.2.4 Discussion

Cloud cover is characterized by large spatial and temporal variations. Only cloud cover estimated at the time of the afternoon satellite overpass was used in this study, so diurnal variations

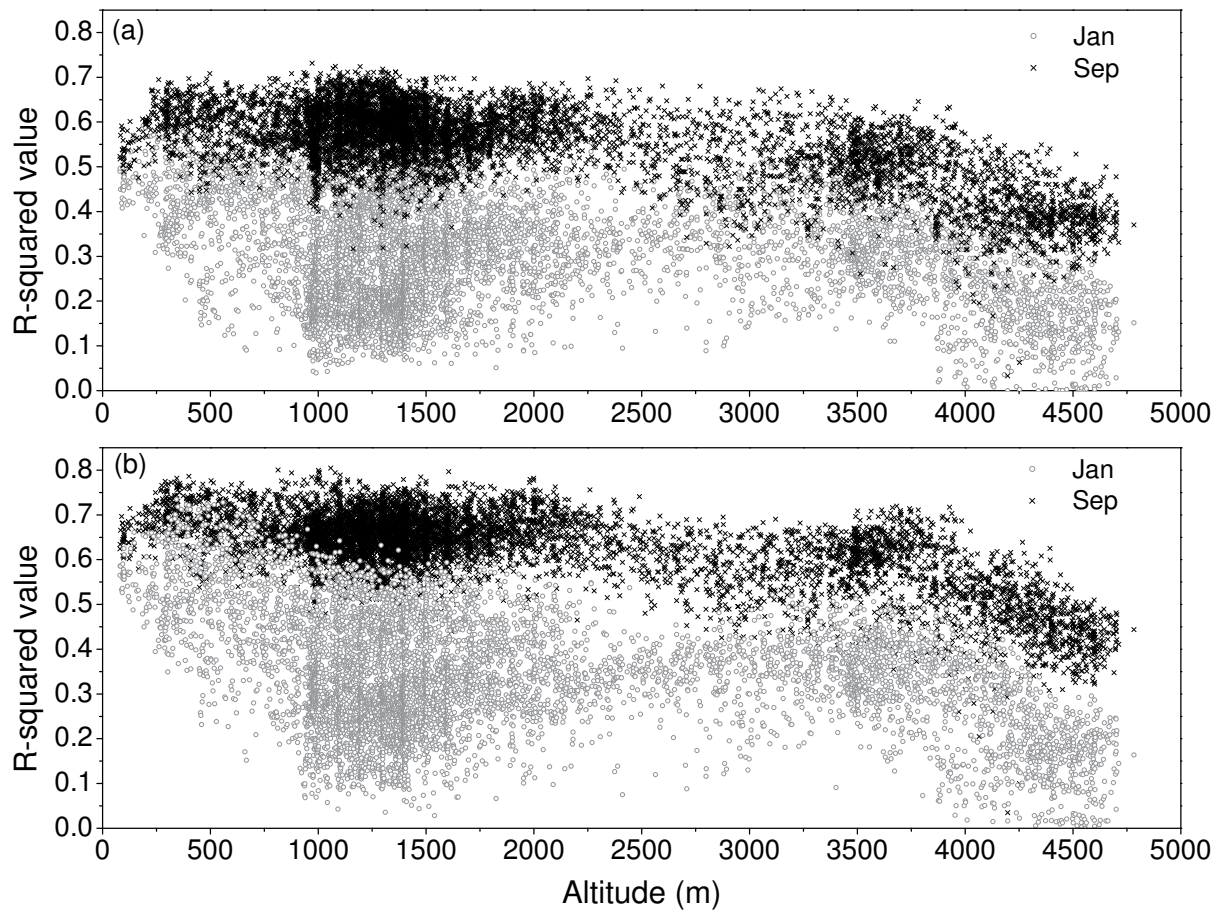


Figure 3.17: R^2 values for (a) the NCI and cloud amount in January and September, (b) and the NCI and SCI in January and September as a function of altitude.

in cloud cover were not considered. However, results show a robust relationship between the daily NDVI cloud index and ground-observed cloud indices; the R^2 values in summer were large, around 0.6 (i.e., the correlation coefficient equals 0.8), suggesting that day-to-day cloud variations are captured by the daily NDVI indicator. The NCI is a simple method for estimating clouds and showed good agreement with a ground-observed cloud index. NCI values were more consistent with the ground-observed cloud indices than the CLAVR values were. The agreement between the NDVI index and ground-observed cloudiness suggests that spatial distributions in cloud cover are captured by NDVI values. Correlations between the NCI and ground observations were better in summer than in winter, better over cropland than over wooded tundra, mixed shrubland/grassland, or water bodies, and better over low elevations than over high elevations.

3.3 Ground Observations Analysis

3.3.1 Data Sources

The climate data from 120 meteorological stations inside and closed to the study basin (Figure 3.1) were obtained from the China Meteorological Administration (CMA). The data set is available from 1960 to 2000 with the daily precipitation, daily mean temperature, daily maximum and minimum temperatures, daily mean surface relative humidity, daily sunshine duration, and daily cloud amount. Several stations on the Qinghai-Tibet Plateau were established from the end of 1950s, limiting the study period from 1960 to 2000 (Liu and Chen, 2000).

Six major hydrological gauges at the main stream of the Yellow River, Tangnaihai, Lanzhou, Toudaoguai, Sanmenxia, Huayuankou and Lijin stations (Figure 3.1) were collected from Hydrological Year Book by the Hydrological Bureau of the Ministry of Water Resources of China (Information Center of Water Resources, 1950-1990).

The watershed above the Tangnaihai station is the source region of the Yellow River. The water withdrawals from the river are limited in this region. The Toudaoguai station is after two large irrigation districts (Qingtongxia and Hetao IDs). The Lanzhou-Toudaoguai section is a "net" water consumption zone of the Yellow River, i.e. the annual discharge at the Toudaoguai station is less than the discharge at the Lanzhou station. The drainage area between Toudaoguai and Sanmenxia station is located on the Loess Plateau and is in a transitional zone from semi-arid to semi-humid climate. The Huayuankou station is another key station at the main stream. The annual discharge at this station reaches its maximum value. The Lijin station is the last hydrological station before the river emptying into the Baohai Gulf. Between

Huayuankou and Lijin station, the runoff into the river channel is slight because the elevation of the riverbed is higher than the land surface behind artificial levees. In addition, there are large irrigation districts in the lower reach, which are located outside the watershed and channeled river water (Fu et al., 2004; Chen et al., 2002). It is another "net" water consumption zone of the Yellow River.

The data related to irrigation was collected from the Yellow River Conservancy Commission (YRCC (Yellow River Conservancy Commission), 1986, 1991-2000) and publications from previous researches (Liu and Zhang, 2002; Yang et al., 2004a; Xia et al., 2004). The data included annual or decadal irrigation area and river water consumption in upper, middle, and lower reach of the Yellow River.

The vegetation condition index leaf area index (LAI) was obtained from Myneni et al. (1997). The LAI data set is available with monthly temporal frequency and 16×16 km spatial resolution from 1981 to 2000.

3.3.2 Methods

The meteorological data at the stations was interpolated to 10×10 km gridded data set to observe spatial distribution of the climatic change. Several methods were investigated to interpolate the daily station observations. These included surface-fitting procedure thin-plate splines (Hutchinson, 1995), Thiessen polygon area averaging (Thiessen, 1911), and angular distance weighted (ADW) averaging (New et al., 2000). The thin-plate splines interpolation was found to be unsuitable because there were considerable undershoot and overshoot in the edge of the study area. Thiessen polygon interpolation employ a limited number of data points in the estimation of grid point values. The ADW method was selected for this study.

In estimating each grid point using ADW method, eight nearest stations regardless direction and distance are used to contribute to grid point estimation and form the distance weighting function (Piper and Stewart, 1996). Weights for the eight stations were determined in a two-stage process following New et al. (2000). All stations were first weighted by distance from the grid point (Jones et al., 1997; New et al., 2000):

$$w_k = (e^{-x/x_0})^m \quad (3.9)$$

where x is the distance from the grid point of interest, x_0 is the correlation decay distance, m is parameters between 1 and 8. A value of 4 for m was suggested by New et al. (2000). The second component of the distance weight was determined by the directional (angular) isolation

of each the eight selected stations:

$$\alpha_k = \frac{\sum_{l=1}^8 w_l [1 - \cos \theta(k, l)]}{\sum_{l=1}^8 w_l} \quad : \quad l \neq k \quad (3.10)$$

where $\cos \theta(k, l)$ is the angular separation of station k and l , and w_l is the distance weight at station l . The angular-distance weight is then calculated from:

$$W_k = w_k(1 + \alpha_k) \quad (3.11)$$

Based on the interpolated data, the linear regression model was used to estimate the trend magnitude in each grid point. The regression weight was calculated as:

$$\beta = \frac{n \sum_{i=1}^n t_i y_i - \sum_{i=1}^n t_i \sum_{i=1}^n y_i}{n \sum_{i=1}^n (t_i)^2 - (\sum_{i=1}^n t_i)^2} \quad (3.12)$$

where n is the time series number, t_i is the time number, and y_i is the data value at the time t_i . The statistical significance of the annual trends is evaluated using the Student's t-test (Haan, 1977). The trend magnitude during the study period was then estimated from the regression weight:

$$\Delta Y = \beta \cdot T \quad (3.13)$$

where T is the span of time during the study period. The relative trend magnitude was represented as:

$$\Delta Y' = 100 \cdot n \cdot \Delta Y \bigg/ \sum_{i=1}^n y_i \quad (3.14)$$

A detail description on the trend detection is in Appendix C.4.1.

The trend of precipitation (P), mean relative humidity (U_m), sunshine duration (D_s), mean cloud amount (C_a) and LAI data was presented using relative trend magnitude. The trend of mean temperature (T_m), minimum temperature (T_{min}), maximum temperature (T_{max}) and diurnal temperature range (DTR) data was presented using trend magnitude. The relative trend magnitude of reference evapotranspiration (ET) was calculated to watch the change in evaporative demand of the atmosphere (Allen et al., 1998).

3.3.3 Results and Discussion

Observed annual discharge changes at the six gauges during the study period are shown in Table 3.3. There are significant decreasing trends for all the gauges except for Tangnaihahi gauge. The

Table 3.3: Observed annual discharge change at gauges

Stations	Discharge (10^9m^3)	Averaged ^a (mm)	Trend ^b (mm)	Relative (%)
Tangnaihai	20.8	171	-	-
Lanzhou	31.5	141	-48	-34
Toudaoguai	22.1	60	-35	-58
Sanmenxia	34.2	50	-35	-71
Huayuankou	38.4	53	-40	-77
Lijin	29.8	40	-59	-149

^aAnnual discharge is presented as the water depth over the control area of each gauge.

^bA significance level of 5% is used to detect the trend.

Table 3.4: Change in climate and vegetation condition

Items	Averaged	Trend	Relative trend (%)	Significance (%)
P (mm/year)	443	-46	-10	6
ET (mm/year)	1040	-6	-1	47
U_m	0.58	0.00	0	18
D_s (hour/day)	7.16	-0.43	-6	1
C_a	0.52	-0.07	-13	0
T_m ($^{\circ}\text{C}$)	7.00	1.44	-	0
T_{min} ($^{\circ}\text{C}$)	1.23	1.68	-	0
T_{max} ($^{\circ}\text{C}$)	14.01	1.25	-	0
DTR	12.78	-0.43	-3	0
LAI	1.50	0.24	16	32
LAI in IDs	1.09	0.53	48	13

annual discharge at the Toudaoguai gauge is less than that at Lanzhou gauge and the discharge at Lijin gauge is less than that at Huayuankou gauge, suggesting the runoff absorbing is more than runoff generating in the Lanzhou-Toudaoguai and Huayuankou-Lijin sections.

Table 3.4 lists the climatic change in the Yellow River basin from 1960 to 2000 and the vegetation condition change from 1981 to 2000. The precipitation shows a decreasing trend with a significance level of 6%. Taking a significance level of 0.1, there is no significant trend in reference evapotranspiration. The decreasing in the river discharge possibly responds to the decrease in precipitation. There are no significant trends in relative humidity. Decreasing sunshine duration and cloud amount trends are found. The cloud amount decrease trend was also reported over much of China by Kaiser (1998). The Yellow River did become warmer according to the increasing trends in temperatures. The averaged LAI value over the Yellow River basin shows no significant trend, but the LAI value in irrigation districts (IDs) increases with a significance level of 13%. This indicates vegetation condition in the IDs became better from 1981 to 2000. The water consumptions and irrigation area increase from 1980 to 1995 confirms the vegetation condition change (Liu and Zhang, 2002).

Figure 3.18(a-e) shows the spatial distribution of relative trend magnitudes in precip-

itation, reference evapotranspiration, relative humidity, sunshine duration, and cloud amount over the Yellow River basin with a significant level of 5%. Figure 3.18(f) shows relative trend magnitude in LAI value over the basin and the lower reach IDs, with the marked zone of 20% significant level. The grid cell where the LAI data are unavailable, displays blank in the figure 3.18. The spatial pattern of precipitation trend shows increase in part region before the Tangnaihai gauge and decrease over the Loess Plateau. It can explain why there is no discharge decreasing trend at Tangnaihai gauge but decreasing trends at the other gauges. Reference evapotranspiration increases in the eastern Tibetan Plateau and Qingtongxia district, suggesting the evaporative demand of the atmosphere becomes larger in these regions. The relative humidity decreasing trend is obvious in the Qingtongxia-Hetao district, showing that region might become drier. Reduction in sunshine duration is observed in the lower reaches. There is decreasing cloud amount trend over the basin as mentioned before. LAI values show decreasing trends on the Tibetan Plateau and headwaters of tributaries at middle reaches. The vegetation degradation in the source region was also reported by Feng et al. (2005). And they indicated the degradation was enhanced by human activities. The LAI values in Qingtongxia-Hetao and lower reach IDs show obvious increasing trends, which are consistent with the irrigation area increase. The large discharge decreasing trends at the Toudaoguai and Lijin gauges should respond to the vegetation improvement and consequential water consumption in the Qingtongxia-Hetao and lower reach IDs.

The trend magnitudes of temperatures and DTR are shown in Figure 3.19 with a significant level of 5%. The grid cell where is out of the significant level, i.e. no trend is detected, displays blank in the figure 3.19. There are grand increasing trends in temperatures over the whole basin, except for the Sanmenxia-Huayuankou section. The mean temperature increase magnitude is large in the Tibetan Plateau and Qingtongxia-Hetao district. Minimum temperature shows increasing trends in the Tibetan Plateau and Qingtongxia-Hetao district, where cloud amount shows decreasing trends. Increases in cloud amount have been offered as a possible explanation for increasing minimum temperatures in other parts of the world (Kaiser, 1998). However, it seems other mechanisms should be considered in the Yellow River. Maximum temperature shows increasing trend over most of the basin except for one part of the lower reach district. In the Tibetan Plateau and Qingtongxia-Hetao district, the maximum temperature increasing magnitudes are obviously less than that of minimum temperature. A narrowing of the DTR is found in the Tibetan Plateau, Qingtongxia-Hetao district and lower reach district. The narrowing DTR in the Tibetan Plateau and Qingtongxia-Hetao district is due to differential changes in daily maximum and minimum temperatures. This is consistent with the global DTR

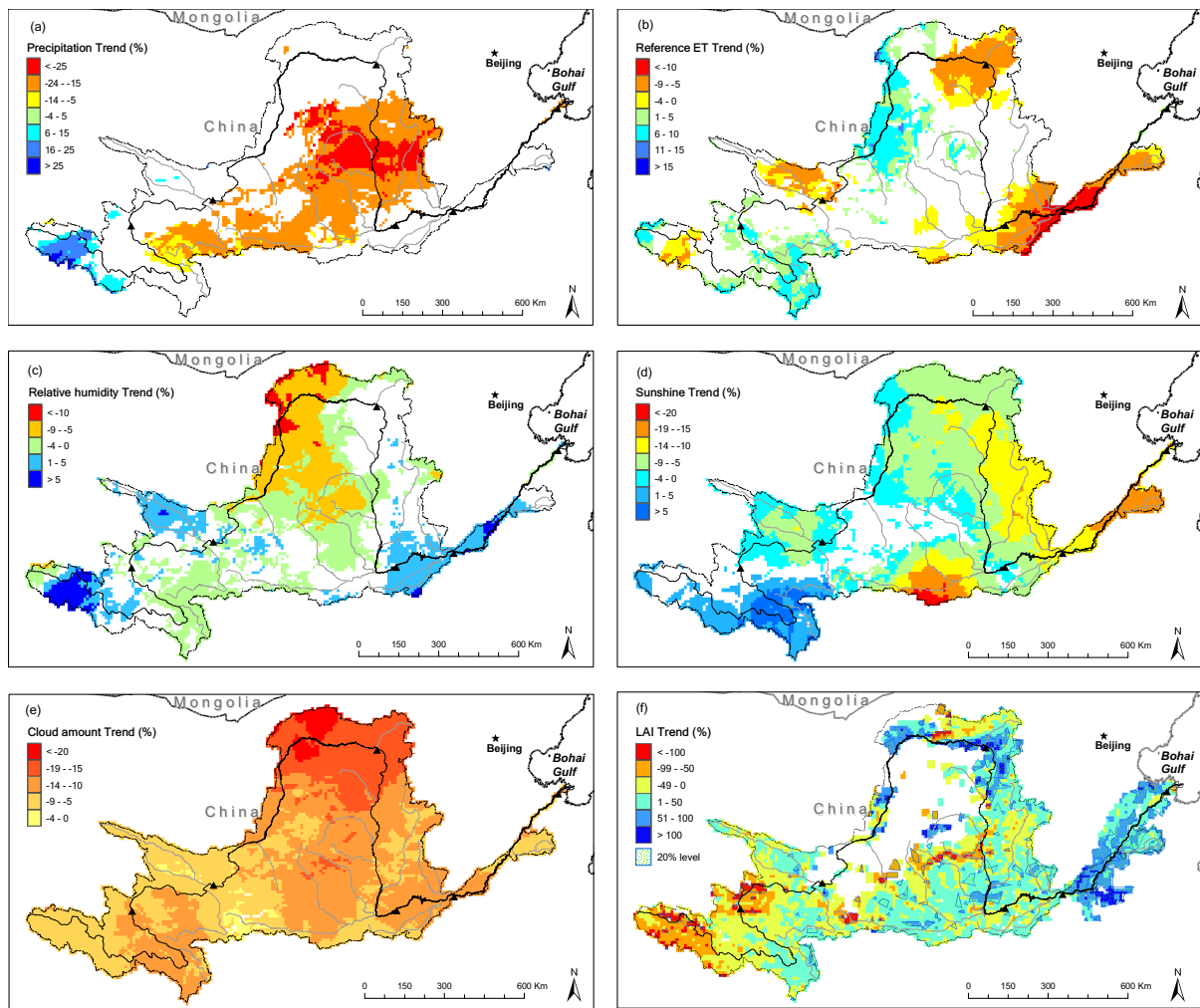


Figure 3.18: Relative trend magnitude of precipitation (a), reference evapotranspiration (b), relative humidity (c), sunshine duration (d), cloud amount (e) from 1960 to 2000 and LAI value (f) from 1981 to 2000.

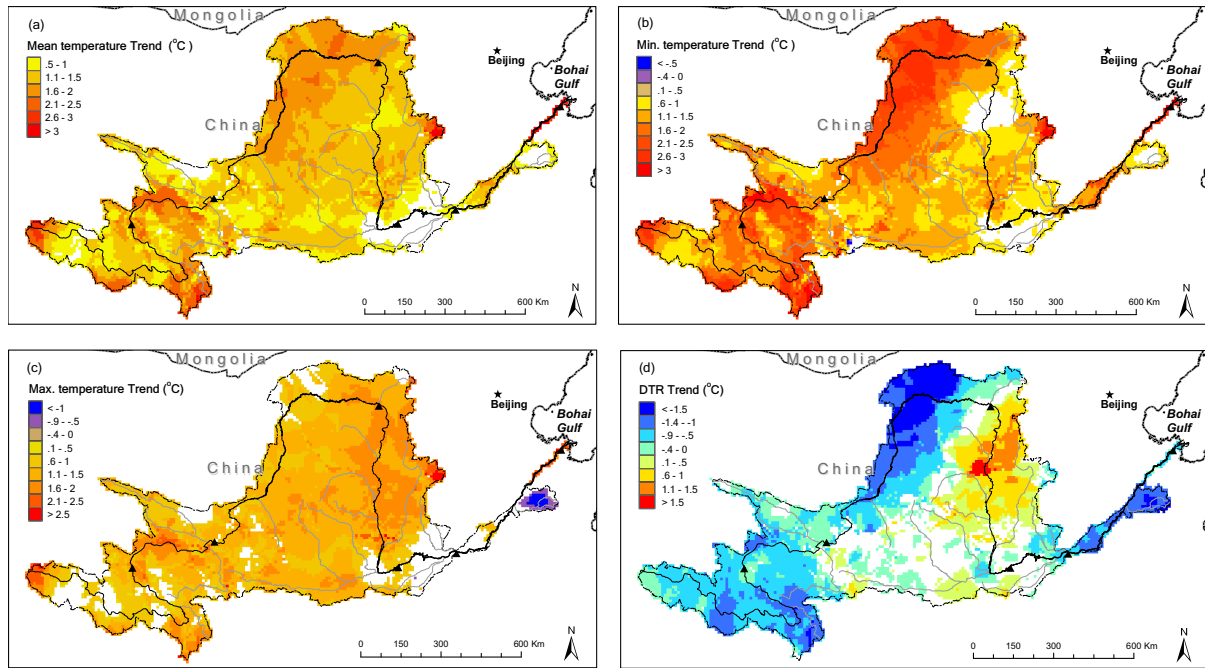


Figure 3.19: Trend magnitude of mean temperature (a), minimum temperature (b), maximum temperature (c) and diurnal temperature range (d) from 1960 to 2000.

trend (Easterling et al., 1997). The widening DTR is observed in the northern Loess Plateau, where has increasing trend in maximum temperature but not in minimum temperature.

3.3.4 Conclusion Remarks

Four decades data of ground hydro-climate observations and two decades data of remote sensing vegetation condition observations were used to analyze climate and land surface spatial variability and explore the reason for the drying up of the Yellow River.

There are high spatial variabilities in climate from the upstream to the downstream. It is found that the precipitation decreased much in the region between the Lanzhou and Huayuankou gauge, which implies that the reductions of discharge are due, at least in part, to less precipitation. The precipitation decreasing region concentrates in the Loess Plateau, suggesting that it is a precipitation "hot spot" of the Yellow River drying up.

The mean air temperature shows increasing trend over the whole basin, and the largest increase regions are the Tibetan Plateau and Qingtongxia-Hetao district. The large increase in minimum temperature in the Tibetan Plateau and Qingtongxia-Hetao district contributes to the mean temperature increase and the reduction of DTR in these regions. The evaporative demand of the atmosphere in eastern Tibetan Plateau and Hetao district shows a significant increasing trend. The Tibetan Plateau and Qingtongxia-Hetao district could be a temperature

”hot spot” of the basin drying up.

The Qingtongxia-Hetao IDs show an obvious increasing trend in LAI values, indicating intensive human activities have changed the vegetation condition in that region. The vegetation improvement and water consumption in the Qingtongxia-Hetao IDs might affect the regional hydro-climatic regimen and contribute to the discharge reduction at downstream gauges. The vegetation improvement is also observed in the lower reach IDs. The Qingtongxia-Hetao and the lower reach IDs would be human activities ”hot spot” of the Yellow River drying up.

3.4 Summary

The DBH model system is used to perform hydrological, climatological analysis. Applications of remote sensing data analysis and ground observations analysis are presented in the Yellow River basin.

An NDVI Cloud Index (NCI) was derived from Pathfinder AVHRR daily NDVI data and compared to observed cloud amounts and a sunshine duration cloud index (SCI) over an area of diverse land cover. Ground observations from 120 meteorological stations were significantly related to the daily NCI and the SCI, with R^2 values of 0.41 and 0.50, respectively. The daily NCI and interpolated cloud indices derived from ground observations over the 776,900 km² study area were compared. The correlation coefficient between the NCI and the observed cloud amount was less than 0.6 for less than 20% of the area. The correlation coefficient between the NCI and the observed sunshine duration index was less than 0.6 for less than 10% of the area and less than 0.7 for 41% of the area. There were strong correlations for high elevations in summer, while correlations for low elevations in winter were weaker. A frozen soil surface or snow cover degrades the NDVI relationship to clouds. The NCI and observed cloud indices had high correlation coefficients in areas with diverse land uses, suggesting that the NCI may be useful in estimating cloudiness over a large region.

Analysis of hydro-climatic observations and vegetation data in the Yellow River basin has shown that the Yellow River drying up is due, at least in part, to the less precipitation in the middle reaches during the last four decades. The vegetation improvement in the Qingtongxia-Hetao and lower reach irrigation districts appear to contribute to the drying up of the river. The analysis, using station, satellite metadata and interpolated coverage, indicates that the precipitation decreases in most part of the Yellow River basin, that climatic factors such as temperature and evaporative demand of the atmosphere have large trend in special part of the basin, and that human activities have changed the vegetation condition in the irrigation

districts. The Loess Plateau, the Tibetan Plateau and Qingtongxia-Hetao district, and the Qingtongxia-Hetao and lower reach irrigation districts are suggested as precipitation, temperature, and human activities "hot spots" of the Yellow River drying up, respectively.

Chapter 4

Development of a Distributed Biosphere–Hydrological Model

4.1 Introduction

The formation of a distributed biosphere-hydrological (DBH) model for use in the large river basins is presented. The DBH model system is a spatially distributed model, integrating hydrological processes and soil-vegetation-atmosphere transfer processes at the river basin scale. The DBH model system incorporates a previously developed land surface model SiB2 (Sellers et al., 1996) and a distributed hydrological sub-model, including the use of satellite data to describe vegetation state and phenology and the use of Digital Elevation Model (DEM) data to describe geomorphological characteristics. The principle motivation for formulating DBH model was to provide more realistic estimates of evapotranspiration and runoff over a continental scale river basin. The model can be used to investigate runoff change according to land cover change and to assess water resource in large basin.

Hydrological models with a spatial structure are being increasingly based on DEM or Digital Terrain Model (DTM) (Moore et al., 1988a,b). DEMs automatically extract topographic variables, such as basin geometry, stream networks, slope, aspect, and flow direction, etc. from raster elevation data. Many of the existing models, such as SHE (Bathurst et al., 1995), TOPMODEL (Beven, 1995), GBHM (Yang et al., 1998, 2000), etc., use DEMs to represent geographical characteristics of a watershed. The adaptation of DEM improved the representation of runoff accumulation processes. However, the conceptual prescription of land surface and empirical evaporation calculation were recognized weaknesses of most distributed hydrological models. Distributed representation of land surface is still a challenge for large scale model-

ing because of the limitations of global observations. Satellite data gives a chance to describe the vegetation phenology. Vegetation index data acquired from meteorological satellites were processed to derive time series fields of the Fraction of Photosynthetically Active Radiation absorbed by green vegetation canopy (FPAR), the total Leaf Area Index (LAI), and the canopy greenness fraction (N). The remotely sensed data can be integrated into hydrological model and enhance the accuracy of evaporation calculation. Several scientific developments prompted a radical improvement of DBH model. First, meteorologists provided new insights into heat flux in the Soil-Vegetation-Atmosphere Transformation (SVAT) processes (Sellers, 1985; Sellers et al., 1986). Second, remote sensing became matured as a tool to get reliable land surface information. Third, topographic variables extracted from DEMs provided a plausible way to describe runoff accumulation on ground and in subsurface (Verdin and Greenlee, 1996; Yang et al., 1998). As more and more data have been collected in computerized database, in particular, in Geographical Information Systems (GIS), the data availability has improved significantly (Andersen et al., 2001). Readily accessible data is used in construction of large scale distributed models (Vörösmarty et al., 1989; Abdulla and Lettenmaier, 1997; Yang and Musiak, 2003).

The advantages of the DBH model can be summarized as follows:

1. The calculation of evaporation is more reliable by using a physical land surface scheme for simulation of heat flux in the SVAT processes.
2. Satellite data is used to describe time series land cover change. It becomes possible to estimate hydrological responses in ungauged basin by using readily accessible data.
3. The meteorological observations from hydro- meteorological stations, such as precipitation, temperature, humidity, vapor pressure, sunshine duration, and wind speed, are used in the model. The model could be coupled with atmospheric model by using the outputs from atmospheric models instead of observations.

4.2 Modeling Strategy

The land surface sub-model is based on a biophysical approach to model the surface energy and moisture balance, in large part using methodologies developed by micrometeorologist and agricultural scientist (Sellers et al., 1996; Allen et al., 1998).

SiB2 of Sellers et al. (1996) is used in the land surface sub-model. In SiB2, satellite data was used to describe the vegetation phenology of a given DBH model grid area. A realistic canopy photosynthesis- conductance model was incorporated to describe the simultaneous

transfer of CO₂ and water vapor into and out of the vegetation. The hydrological part of the SiB2 simulated the surface runoff of the given DBH model grid area and calculated the interlayer exchanges within the soil profile and interaction between soil water and groundwater.

The hydrological sub-model is based on geomorphological characteristics of the river basin to simulate the surface and subsurface flow, mainly using DEM-based methodologies developed by hydrologists (Verdin and Verdin, 1999; Yang et al., 1998).

The surface runoff flowing to a river system was described by one dimensional kinematic wave model (Lighthill and Whitham, 1955; Chow, 1959). An approach from Rushton and Tomlinson (1979) was used to estimate groundwater and river water interaction. Realistic watershed map and river way map were used to delineate sub-river basins and river network. The sub-river basins were coded following Pfafstetter method (Pfafstetter, 1989; Verdin and Verdin, 1999). The runoff was then accumulated and routed to outlet using kinematic wave approach.

The incorporation of land surface model SiB2 with its most critical processes, evapotranspiration, derived from satellite observations and heat flux simulation in the SVAT processes represents the major improvement in DBH model over other distributed hydrological models. Subsequent sections provide the details of the DBH model.

4.3 The Model Structure

This section briefly reviews the atmospheric boundary conditions, physical parameters and prognostic variables of land surface sub-model SiB2 and describes the soil layer and groundwater layer interaction, runoff conduction to river network, river basin delineation, river routing and the governing equations of the distributed hydrological sub-model. The overall model structure is shown in Fig. 4.1.

4.3.1 Land Surface Model

The land surface model SiB2 is used to estimate the transfer of energy, mass and momentum between the atmosphere and the vegetated surface. The atmospheric boundary conditions necessary to force SiB2 include air temperature T_m , vapor pressure e_m , wind speed u_m , precipitation P , shortwave downward radiation R_{sd} , incoming longwave radiation R_{ld} , and CO₂ and O₂ concentration c_m and o_m at a reference level, z_m , within the atmospheric boundary layer. In practice, mean values of c_m and o_m be defined (35 and 2090 Pa, respectively) for current atmospheric conditions. Daily air temperature, vapor pressure, wind speed and precipitation

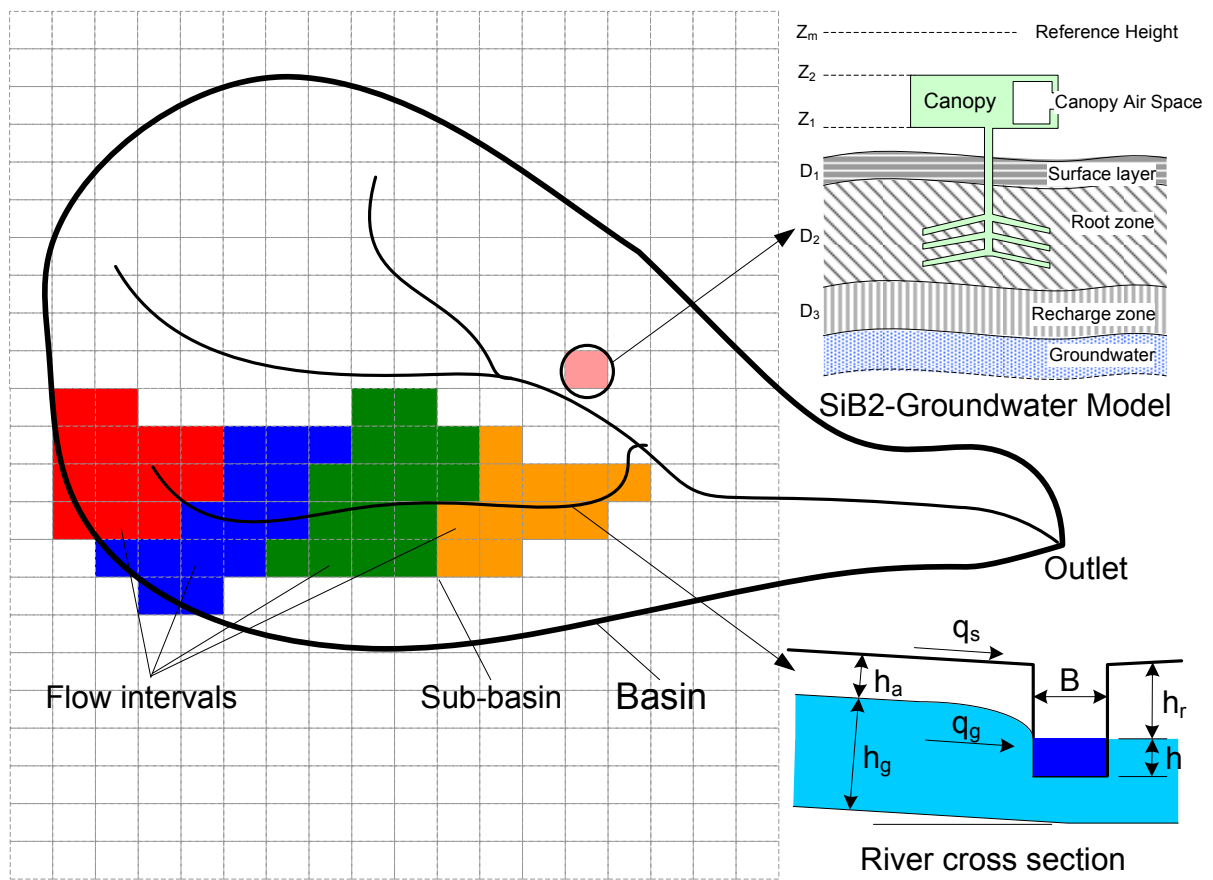


Figure 4.1: Structure of the DBH model.

data from over 8000 worldwide stations was available at Global Surface Summary of Day Data Version 6 (GSSDD). The station observation data was interpolated to ten kilometers grids for DBH model with thin plate splines. The shortwave downward radiation was estimated from meteorological observations following Revfeim (1997) and Yang et al. (2001). The incoming longwave radiation was estimated as (Brunt, 1932; Jiménez et al., 1987):

$$R_{ld} = \varepsilon_a \sigma T_a^4 \quad (4.1)$$

where ε_a is the atmospheric emissivity, $\sigma = 5.6704 \times 10^{-8}$ is the Stefan-Boltzmann constant ($\text{W}\cdot\text{m}^{-2}\cdot\text{K}^{-4}$), and T_a is the air temperature (K). The atmospheric emissivity ε_a is presented as a function of water vapor pressure:

$$\varepsilon_a = 0.66 + 0.039\sqrt{e_a} \quad (4.2)$$

where e_a is the vapor pressure (kPa).

Time invariant vegetation and ground parameters and time varying vegetation parameters of SiB2 were obtained from satellite data or assigned following Sellers et al. (1996). SiB2 land cover is available at USGS Global Land Cover Characterization data (GLCC). Global LAI and FPAR based on Pathfinder Version 3 Normalized Difference Vegetation Index (NDVI) with spatial resolution 16 kilometers mesh could be obtained from Myneni et al. (1997). The Food and Agriculture Organization (FAO) global soil type map (Source: Land and Water Development Division, FAO, Rome) was used to produce the DBH model grid soil properties such as soil water potential at saturation ψ_s (m), soil hydraulic conductivity at saturation K_s (m/s), soil wetness parameter b , porosity θ_s and averaged slope S_s . Serval empirical formulas are suggested to estimate the soil hydraulic and thermal parameters (Cosby et al., 1984):

$$\psi_s = -0.01 \times 10^{(1.88 - 0.0131 \cdot P_{sand})} \quad (4.3)$$

$$K_s = 7.0556 \times 10^{(-6.884 + 0.0153 \cdot P_{sand})} \quad (4.4)$$

$$b = 2.91 + 0.159 \cdot P_{clay} \quad (4.5)$$

$$\theta_s = 0.489 - 0.00126 \cdot P_{sand} \quad (4.6)$$

where P_{sand} and P_{clay} are percentages of sand and clay in a dry soil, respectively. Soil optical properties are assigned by vegetation type following Sellers et al. (1996).

4.3.2 Hydrological Model

The DBH model has fifteen prognostic physical state variables: twelve variables of land surface sub-model SiB2 and three water depth variables (groundwater depth h_a , surface overland flow depth h_s and river water depth h_r). The surface runoff, infiltration, water exchange between groundwater and soil layers, groundwater-river water exchange and flow in river channel will be described in this subsection.

Surface runoff

Surface runoff is the portion of runoff that occurs on unchannelized surfaces, and is also referred to as overland flow. Surface runoff may be generated in three ways:

1. When the rate of rainfall on a surface exceeds the rate at which water can infiltrate the ground, and the depression storage has been filled. This is called infiltration excess overland flow, Hortonian overland flow (Horton, 1939), or unsaturated overland flow. This more commonly occurs in arid and semi-arid regions, where rainfall intensities are high and the soil infiltration capacity is reduced because of surface sealing, or in paved areas.
2. When the soil is saturated and the depression storage filled, and rain continues to fall, the rainfall will immediately produce surface runoff. This is saturation excess overland flow or saturated overland flow.
3. After water infiltrates the soil on an up-slope portion of a hill, the water may flow laterally through the soil, and exfiltrate (flow out of the soil) closer to a channel. This is called subsurface return flow or interflow.

The unsaturated and saturated overland flows are considered. The effective precipitation, i.e. canopy through-fall to ground, is estimated following SiB2. The ground is assumed to have a surface storage with a maximum liquid capacity. With very heavy rainfall, the local infiltration capacity of the soil is less than the rainfall rate and overland flow can be generated. The area-amount relationship for the effective precipitation is used to estimate overland flow. The area-amount relationship is shown in figure 4.2. The horizontal axis refers to fraction of the grid area, and the vertical axis refers to the relative amount of effective precipitation. The exponential relationship in figure 4.2a is:

$$I(x) = ae^{-bx} + c \quad (4.7)$$

where, a , b , and c are constants. The function $I(x)$ is normalized to 1. Then, $\int_0^1 I(x) = 1$. When $a = 0.0001$, $b = 20$, $c = 0.9999$, $I(x) \approx 1.0$, representing grid uniform distributed precipitation. If setting $a = b$, we have $c = e^{-a}$, representing non-uniform distributed precipitation within one grid cell. Figure 4.2a gives the non-uniform distributed curve with $a = 4$ and $a = 20$, respectively. If the effective precipitation is assumed to be consisted of a grid uniform distributed component and a non-uniform distributed component, the effective precipitation distribution is:

$$PI(x) = (P_c a_c + P_l a_l) e^{-bx} + (P_c c_c + P_l c_l) \quad (4.8)$$

where, P is total effective precipitation during the time step (m), $P = P_c + P_l$, P_c and P_l is non-uniform and uniform distributed precipitation component during a time step, respectively (m). Figure 4.2b shows the area-amount relationship and the soil hydraulic conductivity. The soil hydraulic conductivity for the surface layer is used to calculate a water absorption rate for the top soil layer. The proportion of the grid area for which the effective precipitation exceeds the soil infiltration capacity x_s is given by the solution to:

$$P_{w1}(max) = K \quad (4.9)$$

where $P_{w1}(max)$ is the effective precipitation that soil can absorb during the time step (m/s), K is soil hydraulic conductivity (m/s). Combining equation 4.9 with equation 4.8, we have:

$$x_s = \frac{-1}{b} \log \left[\frac{K}{P_c a_c + P_l a_l} - \frac{c_p}{a_p} \right] \quad (4.10)$$

The unsaturated overland flow R_{uo} then is calculated as:

$$R_{uo} = \int_0^{x_s} PI(x) dx - K x_s = P \frac{a_p}{b} (1 - e^{-b x_s}) + c_p x_s - K x_s \quad (4.11)$$

Infiltration

The unsaturated infiltration is estimated using the Green-Ampt model. When the soil is saturated and the depression storage filled, and rain continues to fall, the rainfall will become saturated surface runoff. The Green-Ampt model is a widely-known analytic model of unsaturated infiltration.

The assumptions of the Green-Ampt model are:

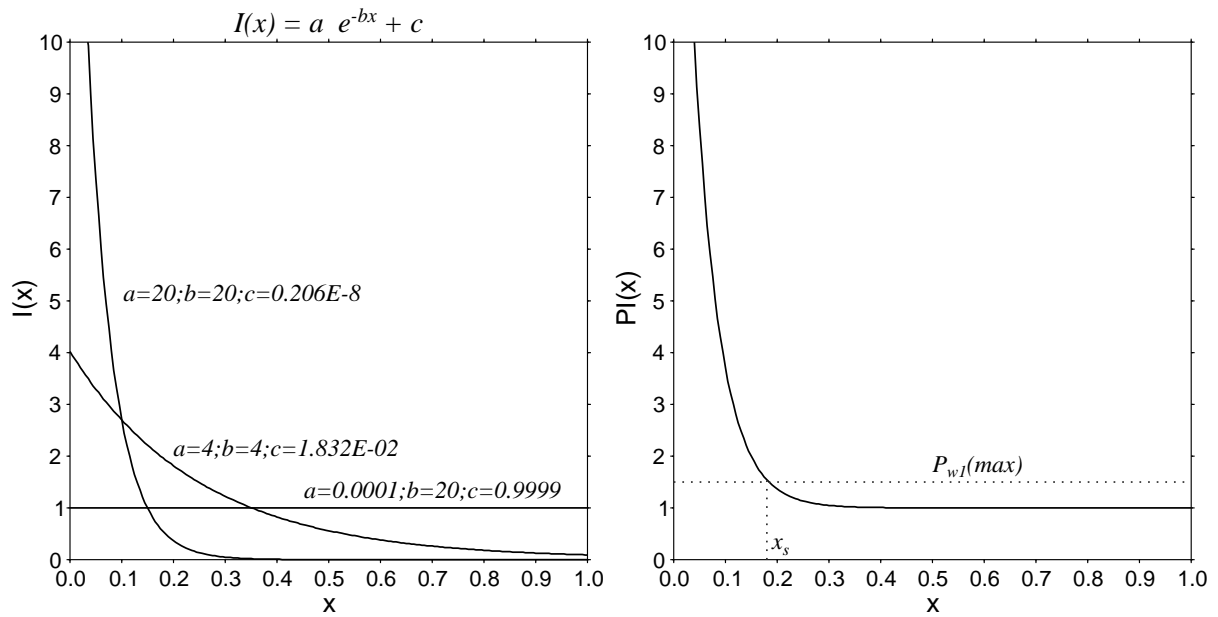


Figure 4.2: Area-amount relationship: (a) exponential area-amount relationships, (b) and effective precipitation area-amount relationships used in DBH model.

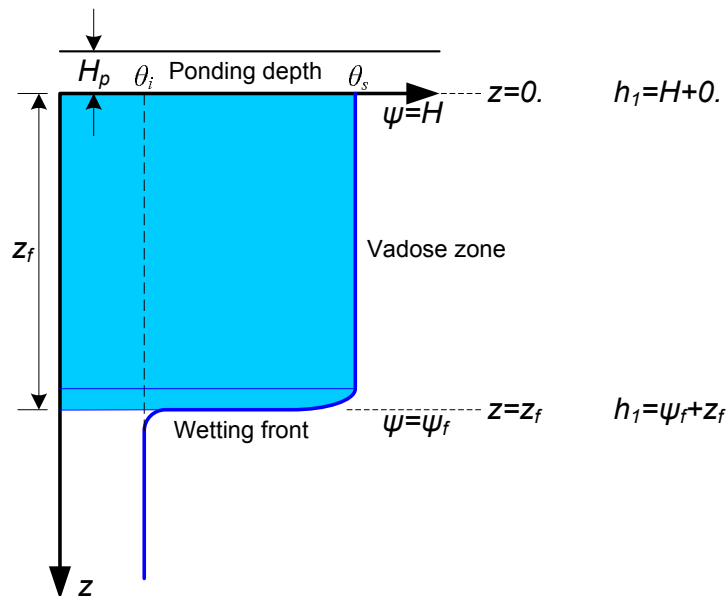


Figure 4.3: Wetting front of the Green-Ampt model.

- a) As rain continues to fall and water infiltrates, the wetting front advances at the same rate with depth, which produces a well-defined wetting front.
- b) The volumetric water contents remain constant above and below the wetting front as it advances.
- c) The soil-water suction immediately below the wetting front remains constant with both time and location as the wetting front advances.

The "well-defined" wetting front means that the water content is uniform behind and before the front, and changes value only at the point of the front, across an infinitely small distance. This is also called "plug flow" because the entering water is seen as a uniform plug with a sharp front that fills the pores completely as soon as it reaches them. Figure 4.3 illustrates the variation in moisture content θ with depth z direction below the surface, at a point in time when the front has progressed a distance z_f . The θ_s is usually considered as the porosity. However, the entering water does not have to saturate the pores. It can be an unsaturated plug flow that fills the pores to the inflow saturation, which is less than the porosity and is called effective porosity. The θ_i is initial moisture content.

The derivation of Green-Ampt model and the Green-Ampt infiltration is described in Appendix B.1.

Overland Flow on the Hillslope

The surface overland flow is described by the one-dimensional kinematic wave model that includes the continuity equation (Lighthill and Whitham, 1955; Hager, 1984):

$$\frac{\partial h_s}{\partial t} + \frac{\partial q_s}{\partial x} = i \quad (4.12)$$

and momentum equation:

$$q_s = \frac{1}{n} S_0^{1/2} h_s^{5/3} \quad (4.13)$$

where h_s is the surface overland flow depth (m), q_s is the overland discharge per unit width (m^2/s), t is time (s), x is the distance along the overland flow (m), i is surface runoff in water depth (m), S_0 is the friction slope gradient, and n is Manning's roughness parameter.

Water Fluxes Underground

When soil is not saturated, there are air phase and water phase in the soil. In unsaturated soil, water is partially bounded by the soil particle, and partially by an interface with the air phase.

Soil water energy in unsaturated zone is affected by gravity, attraction by the solid matrix, pressure (in water saturated soil), and presence of solutes. Soil water potential is defined with respect to reference pure water at the same temperature, under atmospheric pressure and at a specified elevation. Generally, soil water potential Ψ_t is:

$$\Psi_t = \Psi_g + \Psi_m + \Psi_p + \Psi_o \quad (4.14)$$

where, Ψ_g is gravitational potential, Ψ_m is matric potential, Ψ_p is pressure potential, Ψ_o is osmotic potential. Gravitational potential is caused by the force of gravity pulling on the water; matric potential is because attraction by the solid matrix reduces soil water potential relative to pure water so pressure is negative. Depth below a free water surface leads only to positive values of pressure potential. The presence of solutes reduces soil water potential relative to pure water. Osmotic potential has negligible effect on water movement except where a semi permeable membrane exists and when movement is in the vapor phase. The osmotic potential is neglected in the DBH model. Relationship between soil moisture content and matric potential is the soil moisture characteristic curve. The shape of the soil moisture characteristic curve depends on soil structure and texture.

Assuming the soil moisture characteristic curve fits the empirical relationship of Clapp and Hornberger (1978), there is:

$$\Psi_m = \psi_s W^{-b} \quad (4.15)$$

where, W is soil moisture wetness fraction. The empirical soil moisture characteristic curve is shown in figure 4.4. The parameter b will change much the shape of the soil moisture characteristic curve.

A three-layer isothermal model was used to calculate the hydraulic diffusion and gravitational drainage of water in the soil, the equation used to describe vertical exchanges between soil layers is:

$$Q = K \left[\frac{\partial \psi}{\partial z} + 1 \right] \quad (4.16)$$

where Q is vertical water exchange between soil layers (m/s), K is estimated effective hydraulic conductivity between soil layers (m/s), ψ soil moisture potential (m), and z is vertical distance. For the three soil layers, the water balance equation is used, together with momentum equation 4.16. The ground water table is assumed to constant to calculate water transfer between groundwater and soil water. So the boundary condition of the top soil layer is water flux and the lower boundary condition is the ground water table. The transfer of water between

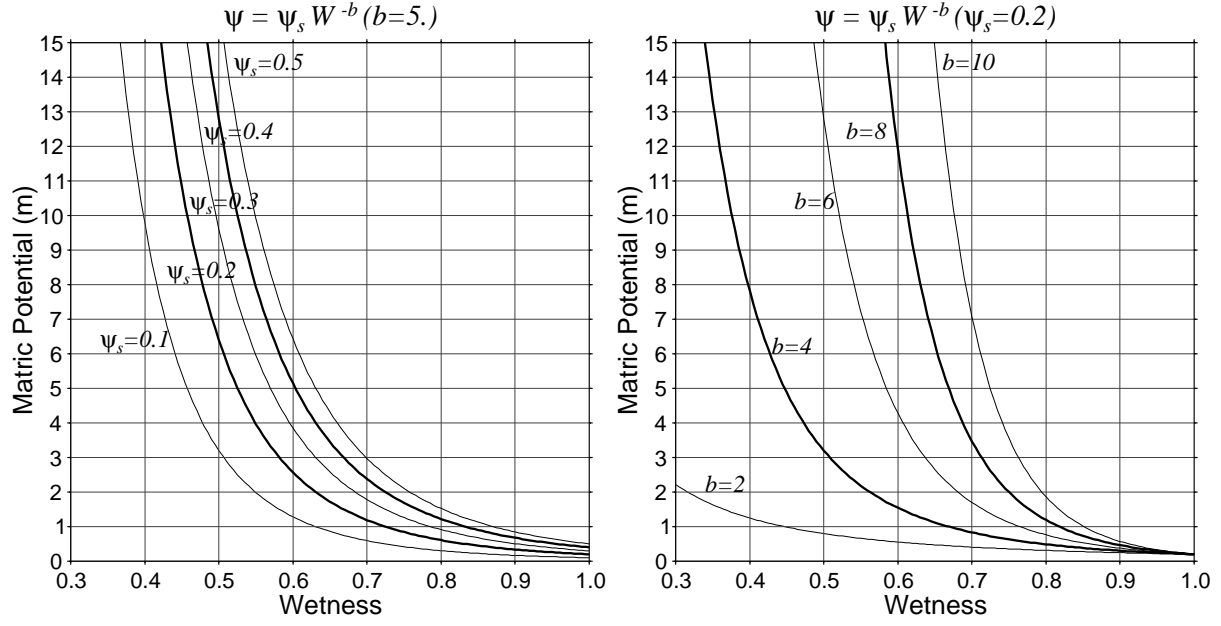


Figure 4.4: Empirical soil moisture characteristic curve.

groundwater and soil water is given by :

$$Q_{3g} = K_{3g} \left[\frac{\partial \psi_{3g}}{\partial z_{3g}} + 1 \right] \quad (4.17)$$

where Q_{3g} is vertical water exchange between soil recharge zone (the third soil layer) and groundwater layer (m/s), K_{3g} is estimated effective hydraulic conductivity between soil layer and groundwater layer (m/s), ψ_{3g} soil moisture potential (m), and z_{3g} is vertical distance. The soil moisture potential ψ_3 of soil recharge zone is taken from the empirical relationship of Clapp and Hornberger (1978):

$$\psi_3 = \psi_s W_3^{-b} \quad (4.18)$$

where W_3 is soil moisture wetness fraction in the soil recharge zone, equals to volumetric soil moisture to saturation soil moisture, B is empirical parameter. The soil hydraulic conductivity of soil recharge zone K_3 is obtained from the saturation hydraulic conductivity K_s (Clapp and Hornberger, 1978):

$$K_3 = K_s \left[\frac{\psi_s}{\psi_3} \right]^{(2b+3)/b} \quad (4.19)$$

Combining the equation 4.18 into equation 4.19, we have:

$$K_3 = K_s W_3^{(2b+3)} \quad (4.20)$$

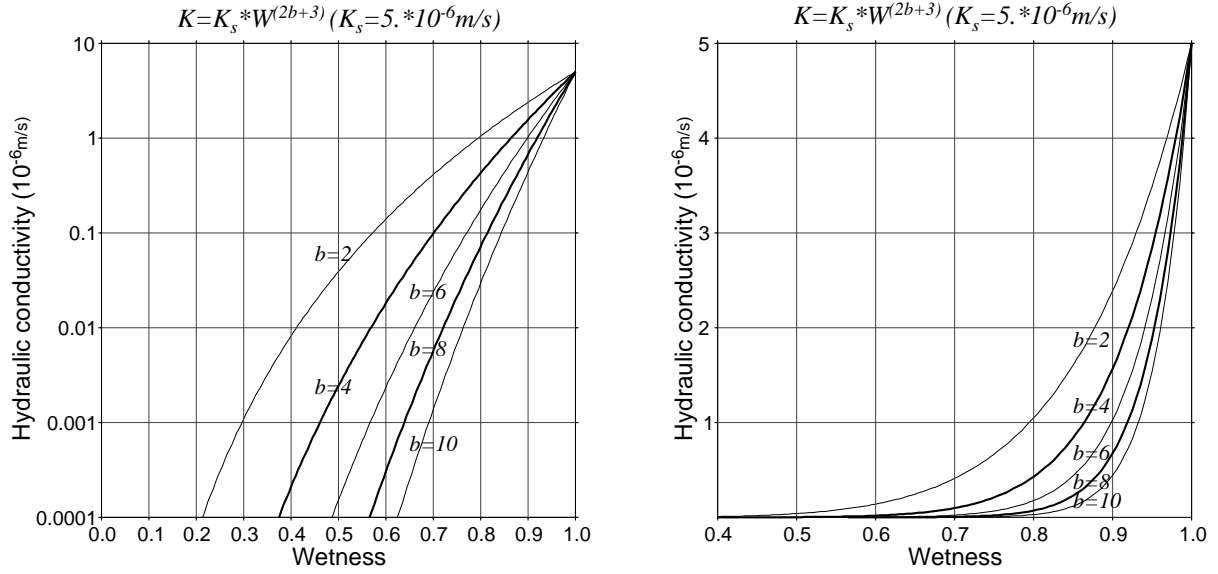


Figure 4.5: Wetness-hydraulic conductivity relationship and b .

Figure 4.5 shows the soil wetness-hydraulic conductivity relationship with the same saturated hydraulic conductivity of $5 \times 10^{-6} \text{m/s}$. The hydraulic conductivity decreases sharply if the parameter b is large. Figure 4.6 shows the soil wetness-hydraulic conductivity relationship with the same parameter b of 4. With the parameter $b = 4$, the hydraulic conductivity will decrease to very small value if the soil wetness is less than 0.35. The effective hydraulic conductivity K_{3g} then is estimated as:

$$K_{3g} = f_{ice} \left[\frac{K_3 \psi_3 - K_s \psi_s}{\psi_s - \psi_3} \right] \left[\frac{b}{b+3} \right] \quad (4.21)$$

where the soil freeze factor f_{ice} is a function of temperature defined in SiB2 (Sellers et al., 1996).

The numeric solution of water exchange inter-soil layers and water flux between soil and groundwater is described in Appendix B.1.

Groundwater-River Water Exchange

The flow between the river network and the groundwater is considered to be groundwater flow to a ditch over a sloping impermeable bed (Childs, 1971; Towner, 1975). This conceptual representation of river-groundwater exchange is shown in Figure 4.7. Assuming that the flow lines are approximately parallel to the bed, according to the Dupuit-Forchheimer approximation, the flow of water per unit width of the river can be written in terms of the hydraulic conductivity and the absolute slope of the water table:

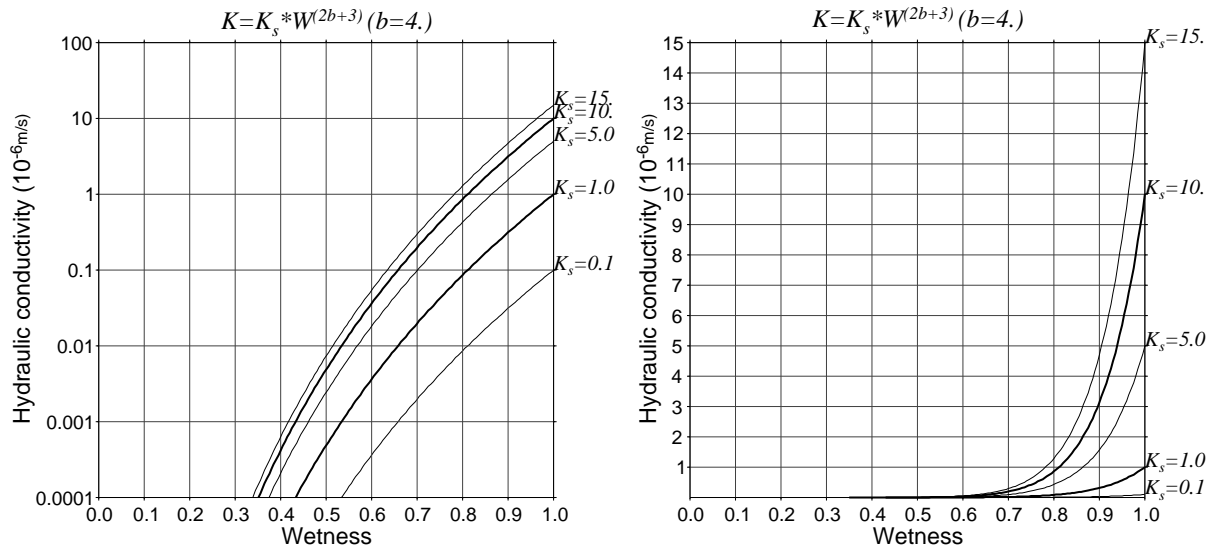


Figure 4.6: Wetness-hydraulic conductivity relationship and saturated hydraulic conductivity.

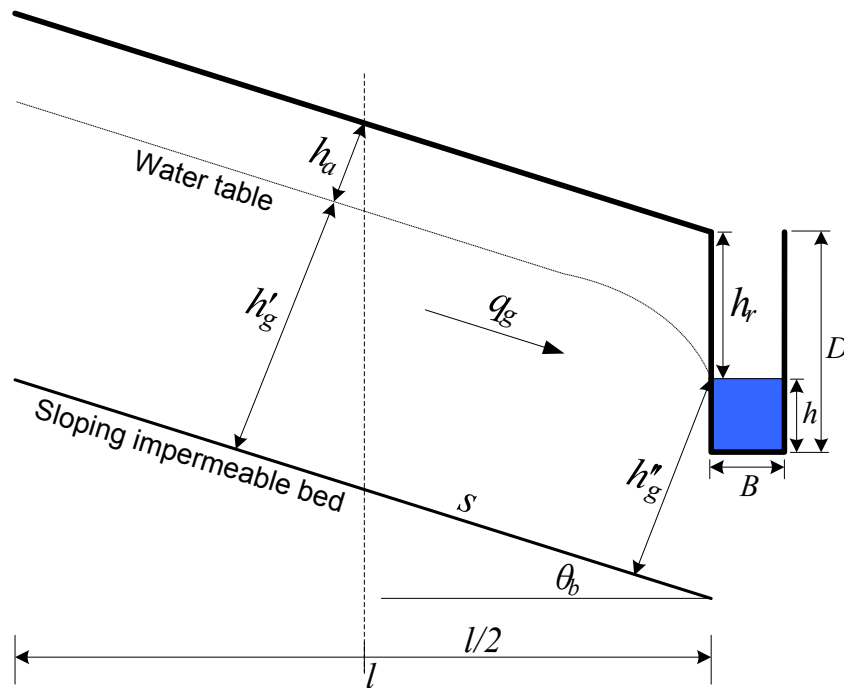


Figure 4.7: Conceptual representation of river-groundwater exchange.

$$q_g = K_s h_g \left[\frac{dh_g}{ds} \cos \theta_b + \sin \theta_b \right] \quad (4.22)$$

where q_g is the flow between the groundwater and river water (m^2/s), θ_b is the bed slope (rad.), s is the distance along the riverbed (m), and h_g is the aquifer thickness (m). If q_g is positive, it is base flow for water-gaining streams. If q_g is negative, it is river recharge for water-losing streams. The equation 4.22 could be written as:

$$q_g = K_s \frac{h'_g + h''_g}{2} \left[\frac{h'_g - h''_g}{l/(2 \cos \theta_b) + h_r \sin \theta_b} \cos \theta_b + \sin \theta_b \right] \quad (4.23)$$

where h'_g is the averaged aquifer thickness, and $h''_g = h_a + h'_g - h_r \cos \theta_b$ is the aquifer thickness at the river, l is the width of hillslope which is set as half of the value of grid area to river length in the grid cell.

The groundwater depth change Δh_a is estimated from the water reservoir storage change.

$$\frac{\Delta h_a}{\Delta t} = - \frac{(Q_{3g} - q_g/l - leak)}{\mu_s} \quad (4.24)$$

where μ_s is the specific yield, the item *leak* is groundwater discharge in water depth by other reasons such as human use groundwater from aquifer (m/s). The $\mu_s = 0.1$ is used as the DBH model default setting.

Flow in River Channel

The river flow is governed by the following continuity equation (Lighthill and Whitham, 1955; Chow, 1959):

$$\frac{\partial Q}{\partial x} + \frac{\partial(B \cdot h)}{\partial t} = q_s + q_g \quad (4.25)$$

and momentum equation:

$$Q = \frac{1}{n(B + 2h)^{2/3}} S_r^{1/2} (B \cdot h)^{5/3} \quad (4.26)$$

where Q is the river discharge (m^3/s), B is the river width (m), h is the flow depth (m), and S_r is the riverbed slope. Estimation of the Manning's roughness parameter n for natural streams was based on field observations guided by Chow (1959) and Acrement and Schneider (1989). $n = 0.12$ is recommended for natural river if the surveyed data is unavailable. The river width B is specified along the river network, using the geomorphological relationship between river

width and mean annual discharge (Arora and Boer, 1999):

$$B = \max(25, Z \cdot Q_m^\beta) \quad (4.27)$$

$$Z = 6 + Q_{m,mouth} \times 10^{-4} \quad (4.28)$$

where Q_m is the mean annual discharge (m^3/s) passing through a given river section, and $Q_{m,mouth}$ is the mean annual discharge at the mouth of the river, β is empirical parameter. A value of β equal to 0.5 is used following Arora and Boer (1999). The river bed depth D (m) is assigned as the below implicit equation:

$$\frac{D^5}{(B + 2D)^2} = \left[\frac{nQ_{max}}{\sqrt{S_r}} \right]^3 \frac{1}{B^5} \quad (4.29)$$

where Q_{max} is the maximum discharge (m^3/s) passing through the given river section.

The momentum equation 4.26 can be expressed in the form:

$$B \cdot h = \left[n \frac{P^{2/3}}{\sqrt{S_r}} \right]^{3/5} \cdot Q^{3/5} \quad (4.30)$$

If setting $\alpha = [nP^{2/3}/\sqrt{S_r}]^{3/5}$, $\beta = 3/5$, and the total lateral inflow $q = q_s + q_g$ and substitueing the equation 4.30 in to continuity equation 4.25, we have:

$$\frac{\partial Q}{\partial x} + \alpha\beta Q^{\beta-1} \frac{\partial Q}{\partial t} = q \quad (4.31)$$

The numeric solution of river flow in the river channel is described in Appendix B.2.

4.3.3 River Routing Scheme

The topographic structure is extracted from DEM in Geographic Information System (Jenson and Domingue, 1988). If the realistic river way and watershed border are available, they can be used to revise the DEM and help to produce river network and river basin. First, find the grids on the river network according to the realistic river way map. Then "burn into" the river network by changing the elevation value of these grids to some units (e.g. 100 units) less or assign a low value. For all the grids out of the realistic watershed border, modify the elevation value of these grids to some units (e.g. 100 units) larger or assign a large value. Figure 4.8 shows the original DEM map and revised DEM map with realistic river way and watershed map. The right side of figure 4.8 gives the revision of hydro-DEM in which the grids outside of

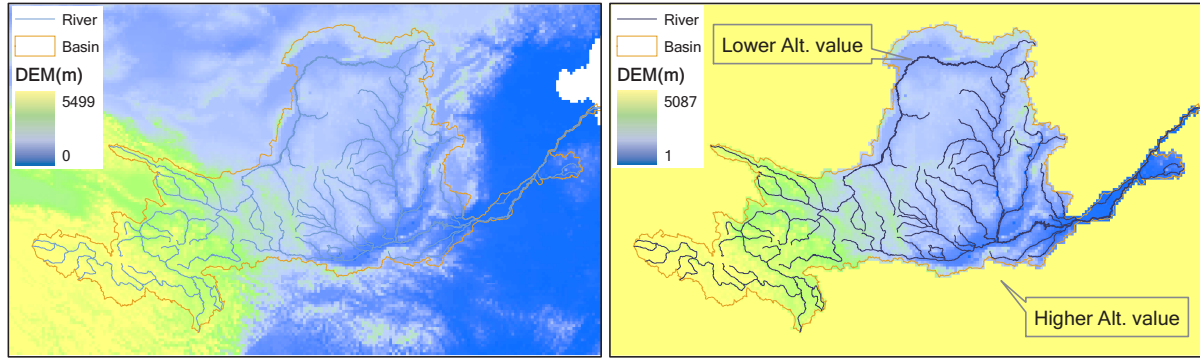


Figure 4.8: Revise hydro-DEM with realistic river way map.

the watershed border is set to a large value and the grids on the riverway are assigned to a low value. The revised hydro-DEM will be used for further processing.

The flow direction and downstream distance to the outlet along the flow direction is calculated from the modified DEM (Jenson and Domingue, 1988). The river network produced from the modified DEM will fit the realistic river way map. Figure 4.9 gives a comparison result of real riverway and derived river way with revised DEM. The derived river way closely agrees with realistic river way, indicating the methodology works well. For the grids over the watershed border, the area fraction, which means the area fraction inside the realistic watershed, is considered. The modeled river basin area will fit the realistic watershed area. The way to get flow direction and to extract other geomorphological properties from DEM is presented in Appendix C.3.1.

Identification of sub-river basins is an indispensable step in river basin modeling to route the river network and support water resource management. The Pfafstetter numbering scheme for delineation and codification of river basin is used which is based on topographic control and the topology of the river network. The system is founded upon concepts first articulated by Pfafstetter (1989) and detailed documented by Verdin and Verdin (1999). The numbering scheme is self-replicating, making it possible to provide identification numbers to the level of the smallest sub-basins extractable from DEM. The routing order of the sub-basins is implicated in the Pfafstetter code. The method to extract the watershed topology is described in in Appendix C.3.2.

Within a given smallest sub-basin, flow intervals, or hydrotopes, are specified to represent the time lag and accumulating processes in river network according to the distance to outlet of the sub-basin. The approach to determine flow interval is illustrated in Figure 4.10. The numbers in the grids show the downstream distance to the outlet of the sub-basin along the

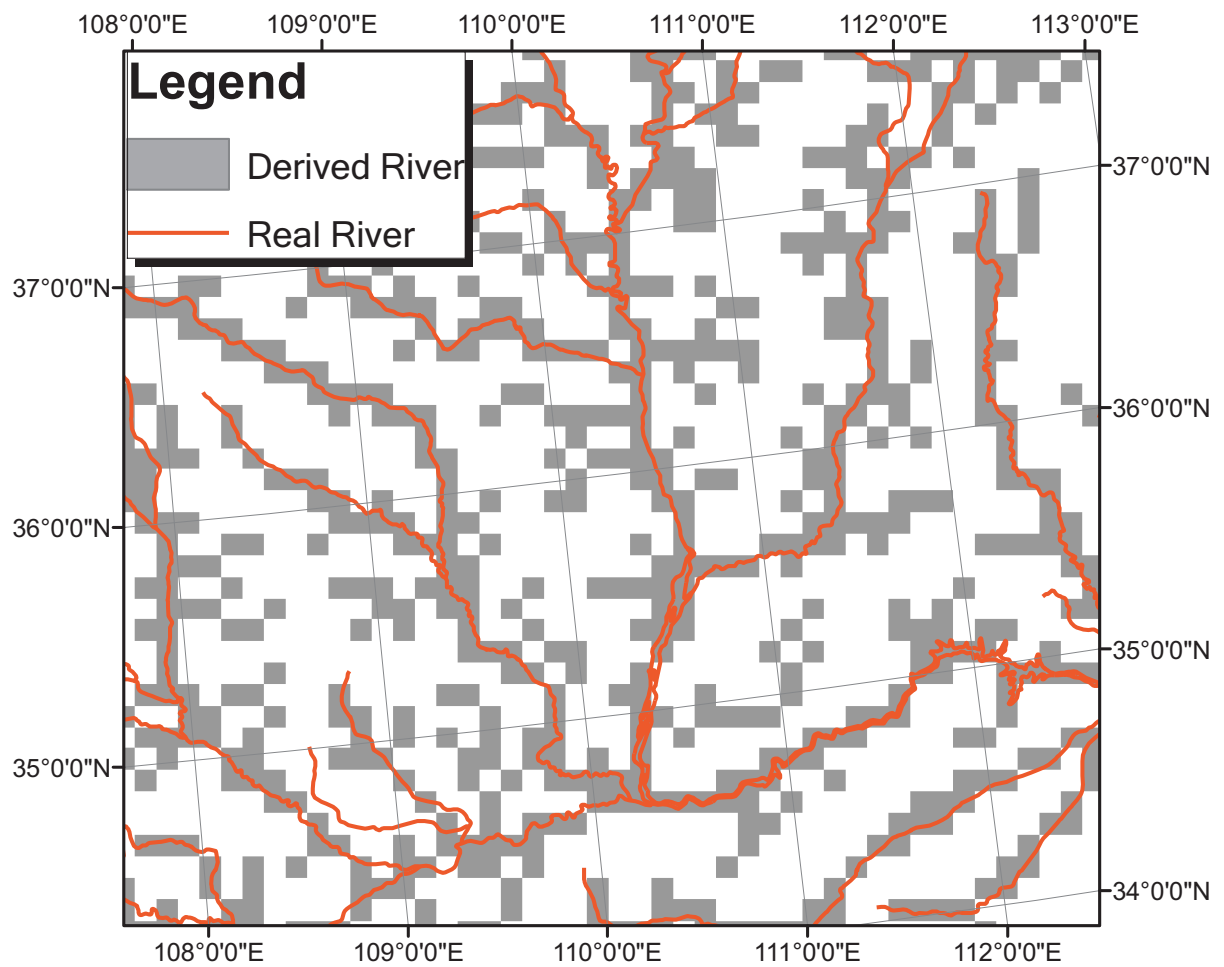


Figure 4.9: Real riverway and derived river way with revised DEM.

flow direction. The grids are assembled into flow interval j :

$$j = 1 + \text{Truncate}(L'/T_v) \quad (4.32)$$

where L' is the downstream distance to the outlet of the sub-basin along the flow direction in times of grid size, T_v is a threshold value to determine flow intervals. The T_v should be larger than $\sqrt{2}$ times of grid size to guarantee there are grids in the first flow interval. The flow interval threshold value decides the flow interval length. Figure 4.11 shows the flow intervals in a sub-basin with different flow interval threshold value. The left side of figure 4.11 gives the hydrotopes with a threshold value of 1.5 times of grid size, and the right side figure gives that of six times of grid size. The grids in the same flow interval have similar distance to the outlet of the sub basin following the flow direction map. The grids might be disjunct from each other even they are in the same hydrotope. The function *Truncate* is used to drop all the digits after the decimal point. For each flow interval, a river section is allocated. The river channel length L_j of flow interval j is then estimated as:

$$L_j = k \cdot L'_j = \begin{cases} k \cdot (\overline{L'_j} - \overline{L'_{j-1}}) & : j > 1 \\ k \cdot \overline{L'_j} & : j = 1 \end{cases} \quad (4.33)$$

$$k = \frac{L_r}{\sum_m L'_m} \quad (4.34)$$

where L_r is the river length of the main stream and m denotes all the flow intervals along the main stream.

One river section is assigned to each flow interval. The slope of each grid is calculated from the 3×3 neighborhood grids using the average maximum technique (Burrough, 1986). Slope identifies the maximum rate of change in value from each cell to its neighbors. Conceptually, the slope function fits a plane to the z values of a 3×3 cell neighborhood around the processing or center cell. The direction the plane faces is the aspect for the processing cell. The slope at a target grid is:

$$\text{Slope}_s = \sqrt{\left(\frac{dz}{dx}\right)^2 + \left(\frac{dz}{dy}\right)^2} \quad (4.35)$$

where dx , dy , and dz are calculated using a 3×3 roving window. Considering the 3×3 window

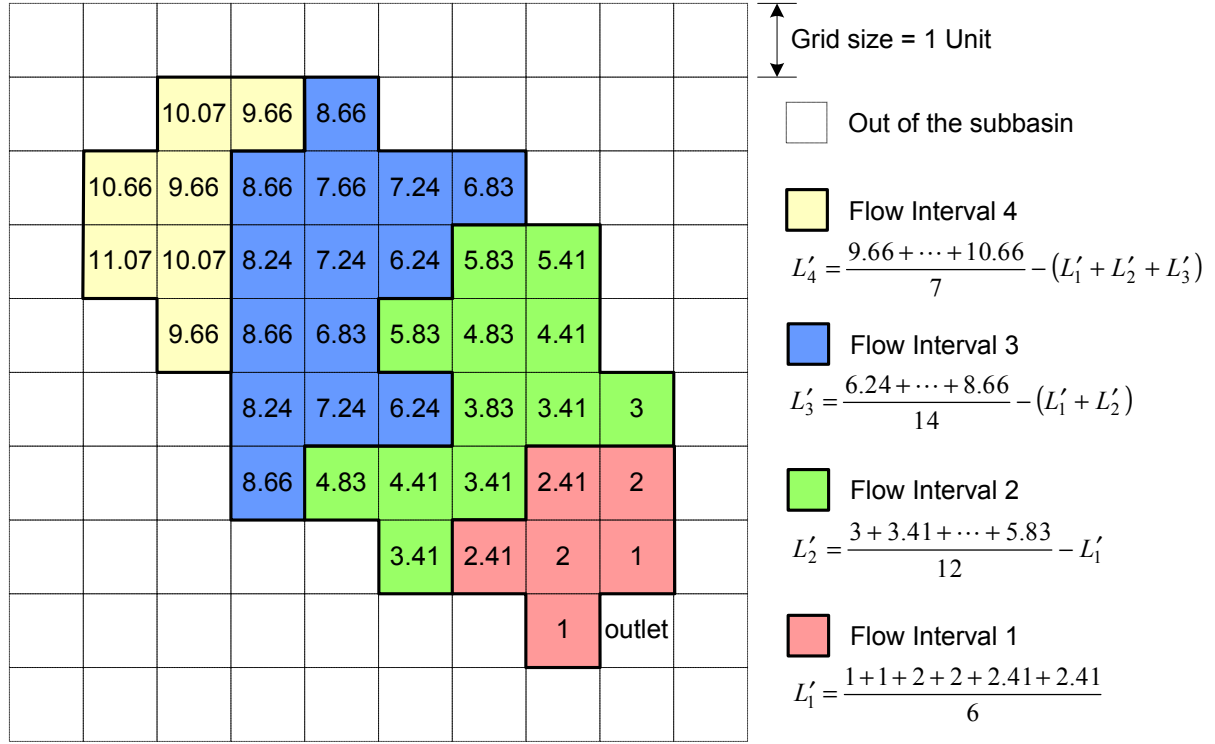


Figure 4.10: Methodology adopted to determine flow intervals with a numeric example.

with below z values

$$\begin{bmatrix} a & b & c \\ d & e & f \\ g & h & i \end{bmatrix}$$

we have:

$$\frac{dz}{dx} = \frac{(a + 2d + g) - (c + 2f + i)}{8 \times Gridsize} \quad (4.36)$$

and

$$\frac{dz}{dy} = \frac{(a + 2b + c) - (g + 2h + i)}{8 \times Gridsize} \quad (4.37)$$

The river bed slope S_r is then estimated as the averaged slope of all the grids in the given flow interval. All the river water recharge in the grids of the flow interval is accumulated to the river section and led to the outlet of the river basin following the river network.

4.3.4 Irrigation Scheme

In each grid cell, land use was partitioned into an irrigation part and nonirrigation part, based on the Global Map of Irrigated Areas (Siebert et al., 2005) dataset. The irrigation part of the land use was set as the SiB2 land use of "Agriculture or C3 Grassland." The nonirrigation part

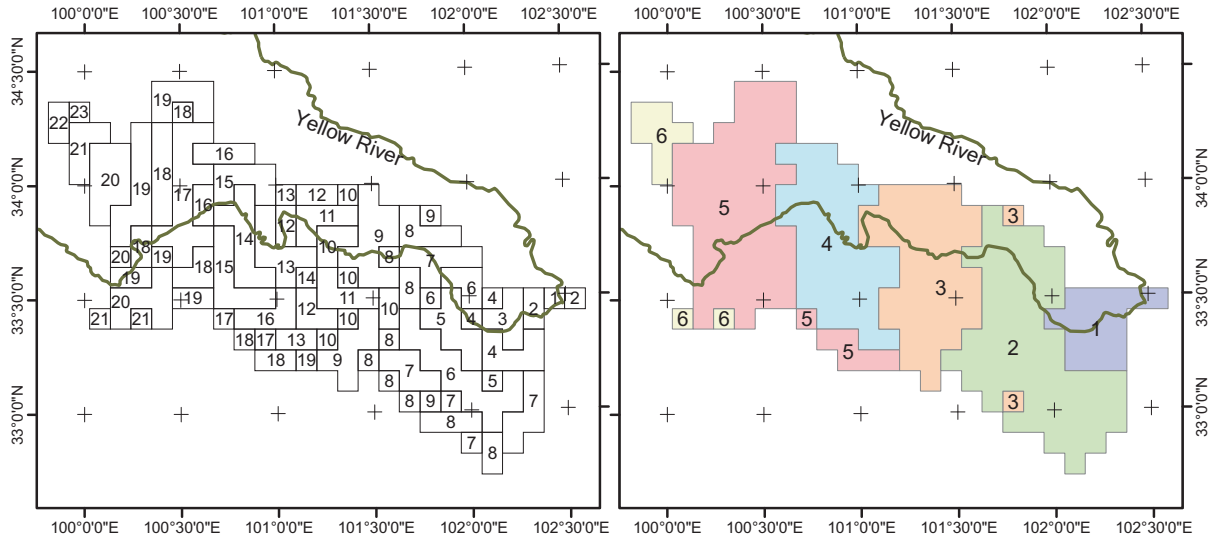


Figure 4.11: Flow intervals with a threshold value of 1.5 (left) and 6.0 (right) times of grid size.

was obtained from the Global Land Cover Characterization dataset (Loveland et al., 2000). For the calculation of water and energy fluxes between the atmosphere and land surface, the mosaic strategy was used. The SiB2 model was performed at irrigation and nonirrigation tiles, respectively, and each tile interacted with the atmosphere independently. The runoff from irrigation and nonirrigation tiles was mixed homogeneously throughout the grid square and routed to the river channel.

The irrigation scheme was based on simulated soil moisture in the irrigation tiles and available water for irrigation. The main purpose of irrigation was to keep the soil moisture in the irrigation tiles above the wilting point level. The SiB2 model was modified to consider irrigation water use, based on the predicted soil moisture. Irrigation started when the soil moisture was below the wilting point level and continued until soil moisture reached the field capacity level. During the irrigation time, if precipitation charged the soil water and soil moisture reached the field capacity level, irrigation would stop. The water loss in the irrigation channel was not considered in this approach, so the simulated irrigation requirement was the net irrigation consumption. The available water for irrigation was estimated based on the predicted river flow by the river routing module. Irrigation water can be extracted from two possible sources, local river runoff or river runoff at an assigned river channel. Basically, the irrigation water was extracted from river runoff locally. For the central irrigation area, the grid clusters were recognized as irrigation districts. Irrigation districts usually extract irrigation water from specific river channels. If an irrigation district is outside the river basin, the irrigation water is taken from specific river channels, usually the nearest main stem of the river network for a

water supply that is as steady as possible. No reservoir operation was taken into account in this study, although irrigation water availability might be affected by reservoir management. Considering this realistic situation, the irrigation water withdrawal capacity was set for each water diversion gap.

4.4 Parameters and Forcing Data

The DBH model system provides a useful tool for studying the interrelationships of upstream and downstream hydrological regime and of managing water and land resources. It is a comprehensive, distributed, and physically based modeling system capable of simulating all major hydrological processes in the land phase of hydrological cycle. A major problem in hydrological modeling is the inadequate gauged data to describe the hydrological processes. Various methods are used to get the hydrology-related information and digitize the information into distributed biosphere-hydrological model. Three sources of data, remote sensing data, ground station gauge, and statistical survey data are used in the DBH model system. Remote sensing techniques can produce high spatial coverage of important terms in water balance for large area, but at the cost of a rather sparse temporal resolution. Ground observation can produce all the terms of weather observations at a high temporal, but low spatial resolution. Statistical survey data produce irrigated area, soil type data at a low temporal, low spatial resolution, but it is the only way we can get for hydrological simulation. The use of various sources data, in combination within DBH model system, provides new possibilities for deriving spatially distributed time series of input variables, as well as new means for calibration and validation of the hydrological model.

4.4.1 Remote Sensing Data

The data derived from remote sensing data includes Digital Elevation Model (DEM) data, land use data, land cover data, and solar radiation data.

The DEM dataset HYDRO1k is used (HYDRO1k Team, 2003). HYDRO1k, developed at the U.S. Geological Survey's (USGS) EROS Data Center, is a geographic database providing comprehensive and consistent global coverage of topographically derived data sets. Developed from the USGS' recently released 30 arc-second digital elevation model (DEM) of the world (GTOPO30), HYDRO1k provides a standard suite of geo-referenced data sets (at a resolution of 1 km) that will be of value for all users who need to organize, evaluate, or process hydrological information on a continental scale. HYDRO1k data are projected into an equal area projection.

The the Lambert Azimuthal Equal Area projection was selected for this database. (Steinwand et al., 1995). The introduction of the Lambert Azimuthal Equal Area projection is presented in Appendix C.1.2. Projection parameters vary by continent. The Asian projection parameters is $100^{\circ} 00' 00''$ E for longitude of origin, $45^{\circ} 00' 00''$ N for latitude of origin, respectively. The HYDRO1k data set for Asia is shown in figure 4.12. The cell size for all continents is 1,000 meters and the radius of the sphere of influence is 6,370,997 meters for all continents except Africa. Along with the hydrologically correct DEM, the flow directions, flow accumulations, slope raster data layers are developed using standard GIS techniques. All derivative raster data layers were produced using ARC/INFO's GRID module (ESRI, 1992).

The NOAA/NASA Pathfinder AVHRR Land Data Sets are used (Agbu and James, 1994). These data sets include Clouds from AVHRR (CLAVR) data, Normalized Difference Vegetation Index (NDVI) data, LAI data, FPAR data. Clouds from AVHRR (CLAVR) uses the five-channel multispectral information in a series of sequential decision-tree type tests to identify the cloud-free, mixed (variably cloudy), and cloudy pixels in Pathfinder AVHRR Land data. The Clouds from AVHRR (CLAVR) series of algorithms are designed to serve two roles in the NOAA/NESDIS AVHRR processing. First, it serves as the pixel level cloud mask for a number of AVHRR applications. Second, it provides estimates of cloud properties for use by numerical weather prediction (NWP). Normalised Difference Vegetation Index (NDVI) products are produced using measurements from the Advanced Very High Resolution Radiometer (AVHRR) on board the NOAA polar orbiting meteorological satellites. The reflectance measured from Channel 1 (visible: $0.58 - 0.68 \mu\text{m}$) and Channel 2 (near infrared: $0.73 - 1.0 \mu\text{m}$) are used to calculate the index:

$$NDVI = (Ch2 - Ch1)/(Ch2 + Ch1) \quad (4.38)$$

The leaf area index (LAI), generally defined as one-sided green leaf area per unit ground area, is a key variable to present vegetation condition. A multi-year global monthly LAI and related fraction of photosynthetically active radiation absorbed by vegetation (FPAR) data set was derived from satellite based NDVI data with corrections for residual artifacts, with an algorithm that used global land cover and a three-dimensional radiative transfer model (Myneni et al., 1997). The data sets have a native spatial resolution of 8 km by 8 km with the Interrupted Goode Homolosine projection. The introduction of the Interrupted Goode Homolosine projection and the data conversion between the Goode's projection and Lambert projection is presented in Appendix C.1.3.

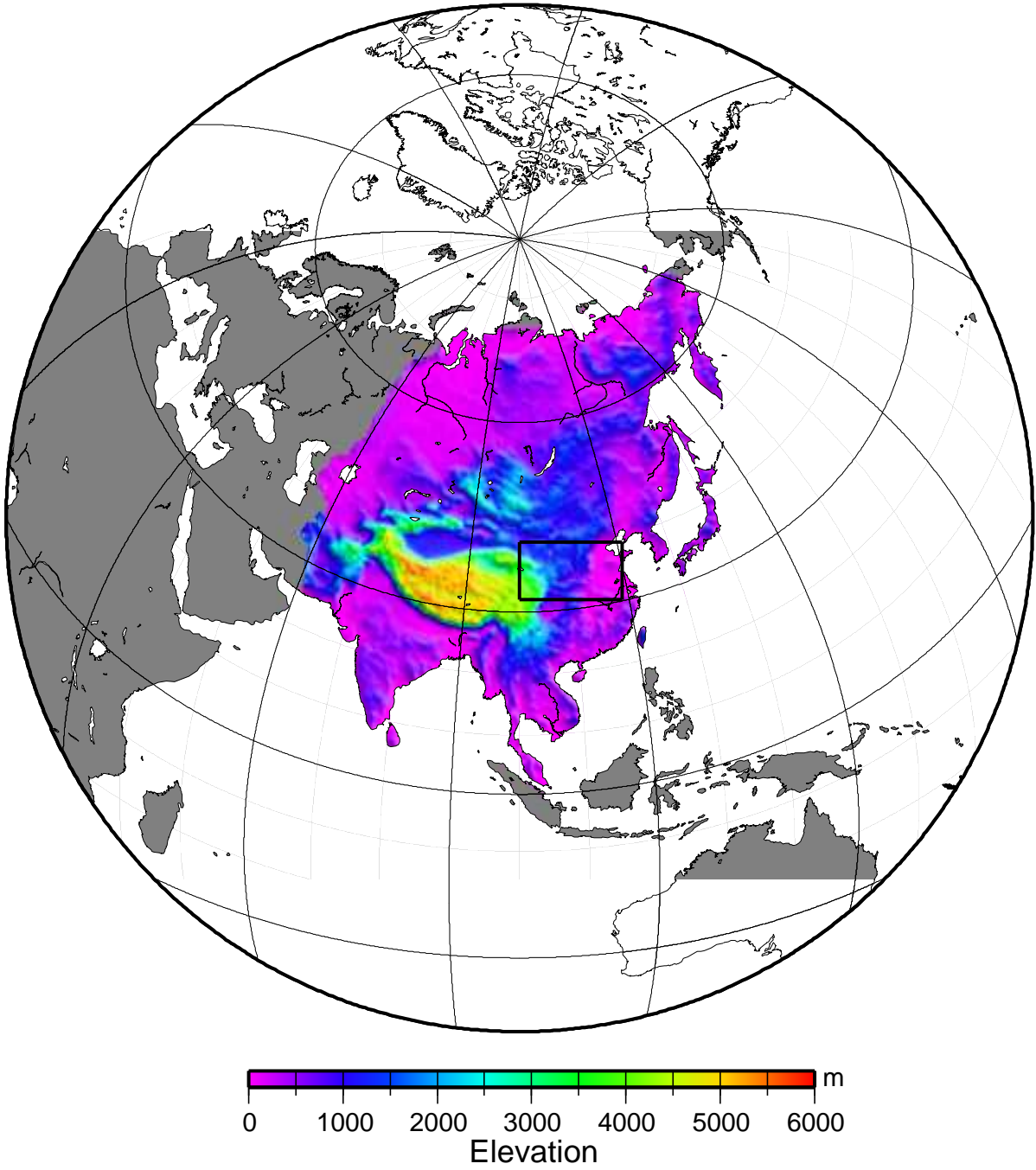


Figure 4.12: HYDRO1k dataset for Asia.

Land cover data is taken from 1-km resolution global land cover characteristics data base by the U.S. Geological Survey's (USGS) Earth Resources Observation System (EROS) Data Center, the University of Nebraska-Lincoln (UNL) and the Joint Research Centre of the European Commission. The data set is derived from 1-km Advanced Very High Resolution Radiometer (AVHRR) data spanning a 12-month period (April 1992-March 1993) and is based on a flexible data base structure and seasonal land cover regions concepts. A core set of derived thematic maps produced through the aggregation of seasonal land cover regions are included in the dataset. These are Global Ecosystems, IGBP Land Cover Classification, U.S. Geological Survey Land Use/Land Cover System, Simple Biosphere Model (Sellers et al., 1986), revised Simple Biosphere Model (Sellers et al., 1996), Biosphere-Atmosphere Transfer Scheme, and Vegetation Lifeforms. The SiB2 land cover from Eurasia land cover of the global land cover data base is used in the DBH model. The SiB2 land cover from Eurasia data base is shown in figure 4.13.

The upwelling and downwelling, shortwave and longwave radiative fluxes are recommended to be derived from ground station observed data, such as conventional meteorological observations sunshine time, cloudiness. Satellite remote sensing makes it possible to estimate the radiative fluxes with large spatial extendence. The International Satellite Cloud Climatology Project (ISCCP) data sets are incorporated in DBH model and provide an optional radiative fluxes source when the ground observations are unavailable. ISCCP was established in 1982 as part of the World Climate Research Programme (WCRP) to collect and analyze satellite radiance measurements to infer the global distribution of clouds, their properties, and their diurnal, seasonal, and interannual variations. Data collection began on 1 July 1983 and is currently planned to continue through 30 June 2010. The upwelling and downwelling, shortwave and longwave radiative fluxes has been calculated at the top of the atmosphere, in the atmosphere, and at the surface using a complete radiative transfer model with improved observations of the physical properties of the surface, atmosphere, and clouds based on the International Satellite Cloud Climatology Project (ISCCP) data sets (Zhang et al., 2004). The radiative transfer model is from the NASA Goddard Institute for Space Studies (GISS) GCM.

4.4.2 Ground-Observations

The term 'ground-observation' refers to observations made near the ground surface. Conventional meteorological data are generally observed by the instruments near the ground surface. For example, temperature and humidity instruments are generally located in instrument shelters about 2.0 meters above the ground. Precipitation measurements are made by a variety

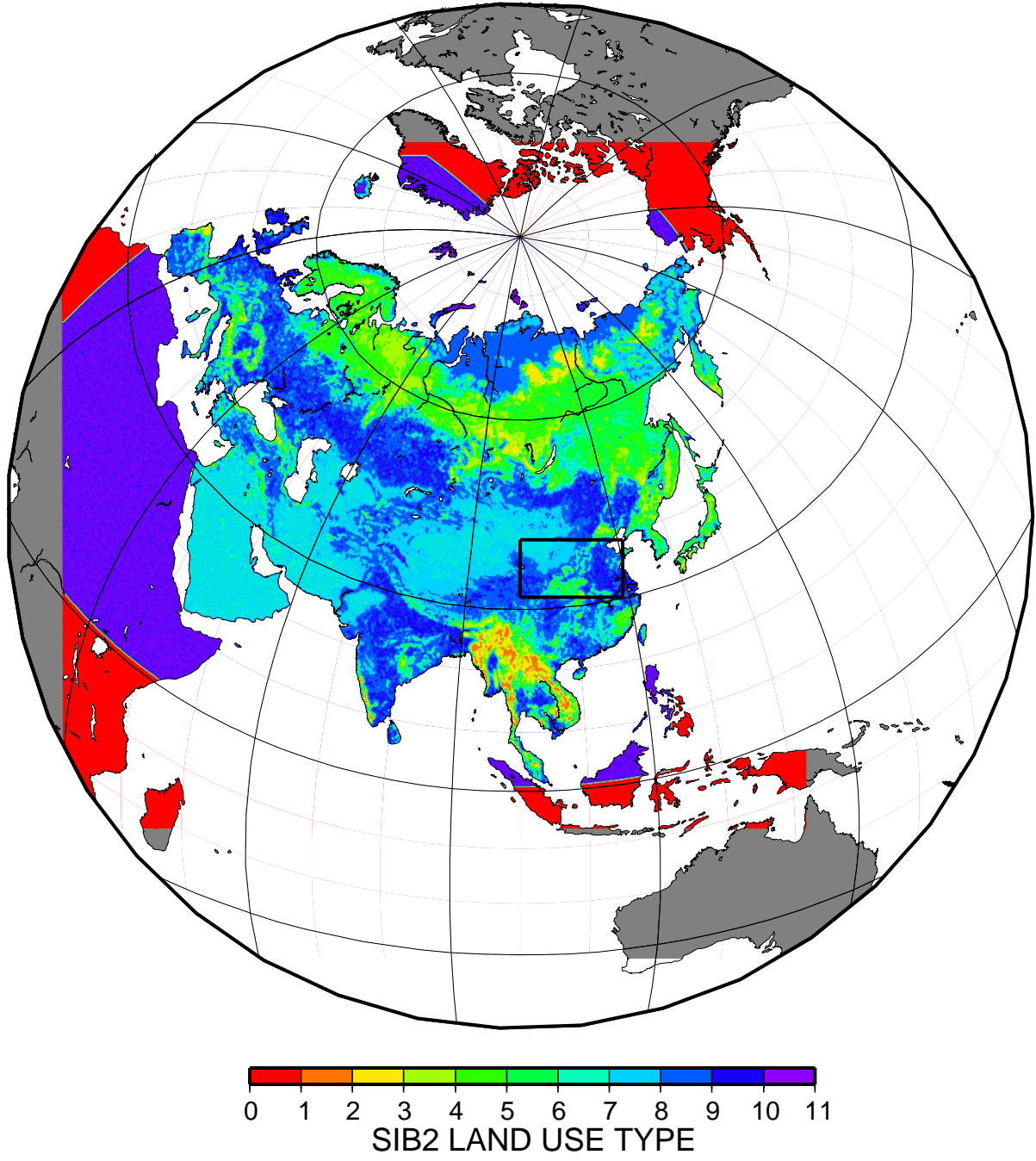


Figure 4.13: SiB2 land cover for Eurasia.

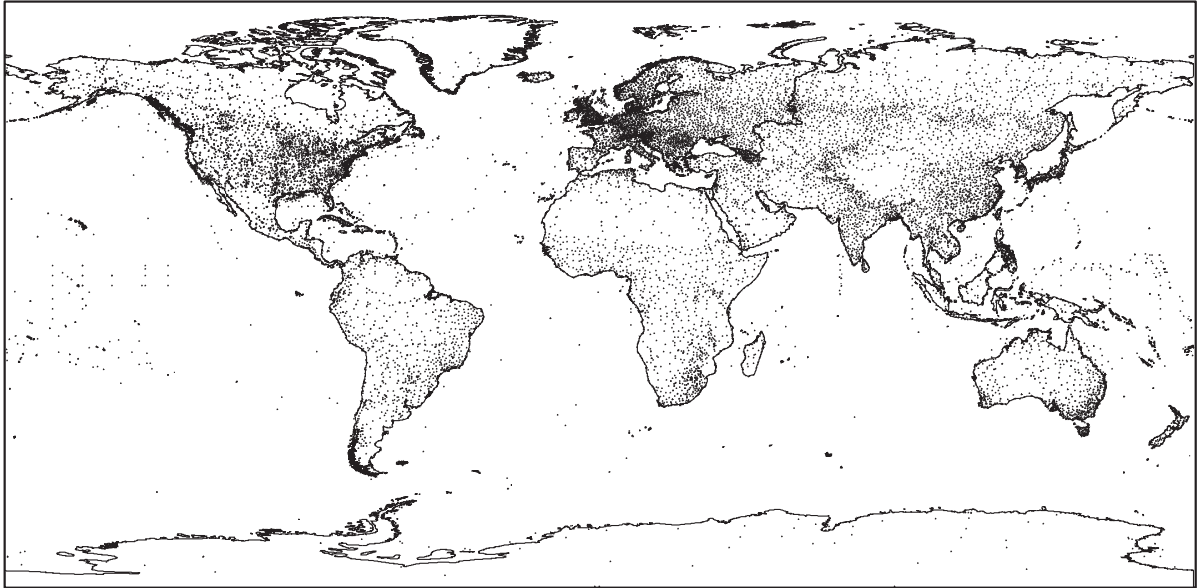


Figure 4.14: Ground observation stations in GSSDD dataset.

of devices and methods. The most common method is to measure the water depth within a container. The major advantage of ground station observations is that the observations span the longest time periods and are often used in climate studies. However, there are many limitations associated with these observations. These include missing data, spatial-temporal sampling problems, different instrument types, instrument bias, etc. The major limitation is the spatial problem. The ground observations are available at the point scale at the locations where the weather stations are, while spatial data is required for study over a large area. A number of studies (Luo et al., 1998; Hansen and Lebedeff, 1987; New et al., 1999) have used surface air temperature data at meteorological stations around the world to estimate changes over a large area (regional, zonal, or global averages, etc.). In these studies, interpolation methods are commonly used to get estimated surface data from the ground observations.

Spatial Distribution

The spatial distribution of stations making surface observations over the mid-latitudes of the northern hemisphere is uneven but adequate for many research projects interested in studying large-scale phenomena. Figure 4.14 shows the locations of the ground stations in the Global Surface Summary of Day Data Version 6 (GSSDD) dataset. The GSSDD data are based on data exchanged under the World Meteorological Organization (WMO) World Weather Watch Program according to WMO Resolution 40 (Cg-XII). About 8000 stations' data are typically included in the dataset.

Interpolation is the process of using known data values to estimate unknown data values. Except for surfaces created by Kriging, most of interpolation at locations which are exactly the same as one of the original sample points will return the same value of the original sample point. At non-original sample point locations, the value will be interpolated based on the known values of neighboring points. Various interpolation techniques are often used in the atmospheric sciences. Three interpolation methods, Thiessen-Polygon (TS) method (Thiessen, 1911), Thin Plate Splines (TPS) method (Hutchinson and Gessler, 1994; Hutchinson, 1995), and Inverse Distance Weighted (IDW) method (Willmott et al., 1985; New et al., 2000), could be selected in the DBH model. The IDW method is recommended for the point density with 40 km distance between two nearest station. The mathematics on the three interpolation method is in Appendix C.2.

Temporal Downscaling

The ground observation data sets are usually provided with daily temporal resolution. However, hourly meteorological data offers the greater accuracy for estimating energy flux and is required in most of land surface model. The daily meteorological data should downscale to hourly data for the DBH model. Several techniques are available for approximating the diurnal temperature curve through the use of daily maximum and minimum temperatures. From the simplest to the most complex, these are averaging, single triangulation, double triangulation, single sine, double sine, and mixed curve (Baskerville and Emin, 1969; Allen, 1976; Zalom et al., 1983). (de Wit et al., 1978) presented a WAVE model to approximate diurnal temperature curve. The WAVE method uses a cosine function for the period from the time of minimum temperature to the time of maximum temperature and another cosine function from the time of the maximum temperature to the time of minimum temperature the next day. The method fixes at 14:00 as the time of the maximum temperature, and at sunrise the time of the minimum temperature. No site-specific calibration is required. (Parton and Logan, 1981) describe the diurnal temperature curve by a truncated sine function during day time and an exponential function at night. These curves are often used by ecologists and biologists. Cesaraccio et al. (2001) gave a mixed sine and square-root curve (TM model) and compared it with published models. The TM model was used in this study to estimate the hourly mean temperature.

The TM model divides the day into three segments (Figure 4.15): from the sunrise hour (H_n) to the time of maximum temperature (H_x), from H_x to the sunset hour (H_o), and from H_o to the sunrise hour for the next day (H_p). The model uses two sine-wave functions in the daylight and a square-root decrease in temperature at night. H_n and H_o are determined as a

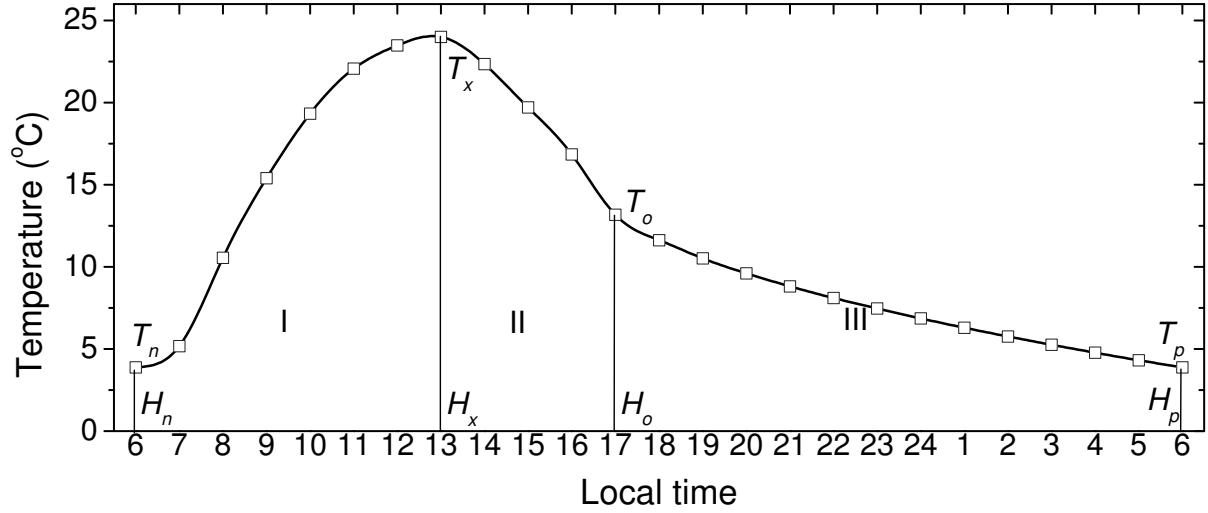


Figure 4.15: Diurnal temperature curve with TM model.

function of the site latitude and the day of the year. H_p is calculated as $H_p = H_n + 24$. The time of the maximum temperature is set 4 hours before sunset, i.e. $H_x = H_o - 4$. Temperature at H_n (T_n), H_x (T_x) and H_p (T_p) are the observed minimum, maximum temperature on the current day and minimum temperature on the following day, respectively. For the facility to use the daily data, the minimum temperature on the current day is used for T_p in the default setting of DBH model system, so that $T_p = T_n$. The temperature at time H_o (T_o) is calculated with an empirical equation:

$$T_o = T_x - 0.39(T_x - T_p) \quad (4.39)$$

The diurnal temperature curve $T(t)$ is:

$$T(t) = \begin{cases} T_n + \alpha_t \frac{t - H_n}{H_x - H_n} \frac{\pi}{2} & : H_n < t \leq H_x \\ T_o + R_t \sin \left[\frac{\pi}{2} + \left(\frac{t - H_x}{4} \right) \frac{\pi}{2} \right] & : H_x < t \leq H_o \\ T_o + b_t \sqrt{t - H_o} & : H_o < t \leq H_p \end{cases} \quad (4.40)$$

where t is the hour of the day in local time, $\alpha_t = T_x - T_n$, $R_t = T_x - T_o$, and $b_t = (T_p - T_o) / \sqrt{H_p - H_o}$.

The minimum daily air temperature (T_n) is often used as a surrogate for mean daily dew point ($T_{d,day}$) to estimate near-surface humidity. This method is unreliable under arid conditions where nightly minimum temperatures may remain well above the dew point. An empirical model was developed by Kimball1 et al. (1997) using daily air temperature data,

potential evapotranspiration ($l_{E_p,day}$, m) and annual precipitation ($l_{P,ann}$, m), to predict $T_{d,day}$:

$$T_{d,est} = T_n \left[-0.127 + 1.121(1.003 - 1.444EF + 12.312EF^2 - 32.766EF^3) + 0.0006(T_x - T_n) \right] \quad (4.41)$$

where $T_{d,est}$ is mean daily dew point (K), T_n is the minimum daily air temperature (K), T_x is the maximum daily air temperature (K), and $EF = l_{E_p,day}/l_{P,ann}$. Equation 4.41 is used to estimate daily dew point and vapor pressure in the DBH model when the potential evapotranspiration is available. If the potential evapotranspiration is not available, $T_{d,est} = T_n$ is set.

The downward shortwave radiation was estimated from sunshine duration. The widely-used FAO Angström-type model (Angström, 1924; Doorenbos and Pruitt, 1977) may underestimate shortwave radiation in high elevation area. Therefore, we adopted a new and widely validated radiation model (Yang et al., 2001; Yang and Koike, 2005) to estimate the radiation, with hourly sunshine data interpolated from daily data following Revfeim (1997). The downward longwave radiation at the Earth's surface was calculated using the Stefan-Boltzmann relationship. There are many parameterization schemes to estimate the atmospheric emissivity with the effect of clouds (Brunt, 1932; Brutsaert, 1975; Jiménez et al., 1987). Niemelä et al. (2001) presented a comparison of several downward longwave radiation flux parameterizations with hourly averaged surface-radiation observations in Finland. They found all the longwave radiation schemes usually underestimated the downward clear-sky flux. Although the method has shortcomings, it allows the development of forcing datasets for historic periods. The downward longwave radiation flux parameterization was used in this study following Jiménez et al. (1987).

4.4.3 Statistical Survey Data

Soil structure and texture is important parameters in hydrological simulation. Currently the best source of this information is the World Soil Map, which was produced by the Food and Agriculture Organization (FAO) of the United Nations Educational, Scientific, and Cultural Organization (UNESCO) in 10 volumes between 1970 and 1978. It provides the most detailed, globally consistent soil data. The FAO soil map is shown in figure 4.16.

Human alteration of Earth is substantial and growing. Between one-third and one-half of the land surface has been transformed by human action. Irrigation increases atmospheric humidity in semiarid areas, often increasing precipitation and thunderstorm frequency (Milly and Dunne, 1994; Vitousek et al., 1997). Irrigation area data is required to assess the anthropic

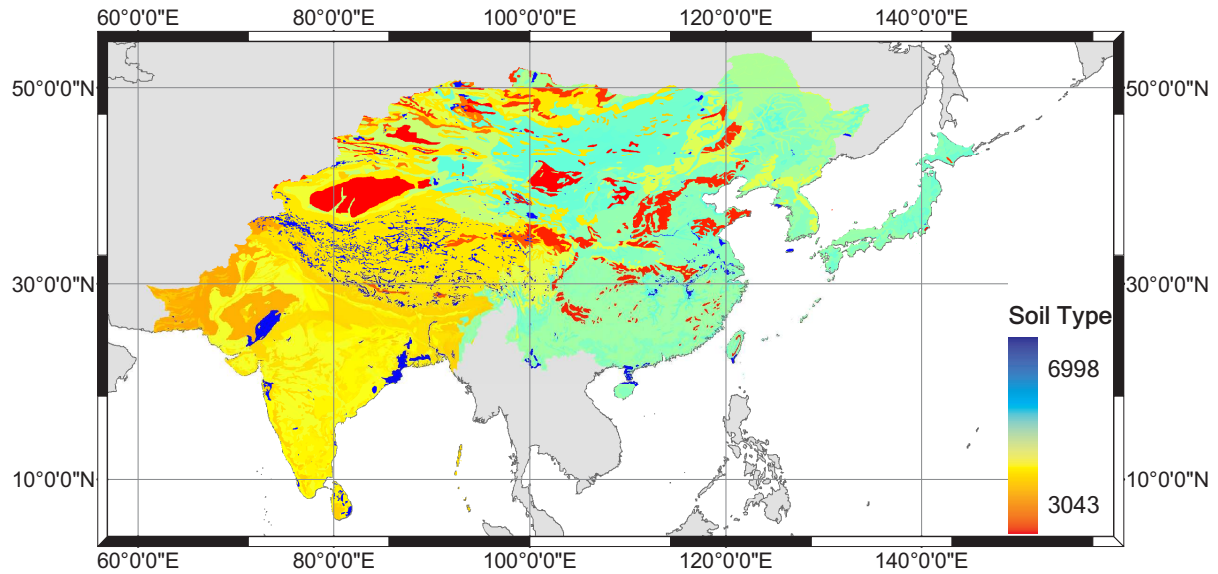


Figure 4.16: South Asia and Near East Soil Map of the World Soil Map.

activity affects on hydrological cycle. Information about fraction of area irrigated within each grid cell is obtained from digital global map of irrigated areas (Siebert et al., 2005). The map shows the amount of area equipped for irrigation around 1995 as a percentage of the total area on a raster with a resolution of 5 minutes. The area actually irrigated in 1995 was smaller, but is unknown for most countries. A special note has to be made for Australia where the map shows the total area actually irrigated. This is due to the fact that statistics collected in Australia refer to actually irrigated area as opposed to statistics with area equipped for irrigation which are collected in most other countries. The global map of irrigated areas is shown in figure 4.17.

4.5 Summary

In this chapter, development of a distributed biosphere-hydrological (DBH) model for continental scale river basins is described. The DBH model solves the flow processes in all the main hydrological processes based on physical governing equations and is designed to consider spatial heterogeneity of physical characteristics of a river basin. The DBH model also physically represents the roles of vegetation in the energy and mass transfer between atmosphere and land surface. The DBH model incorporates a previously developed land surface model SiB2 and a distributed hydrological sub-model, including the use of satellite data to describe vegetation state and phenology, and the use of Digital Elevation Model (DEM) data to describe geomorphological characteristics. Global datasets, e.g. HYDRO1K, AQUASTAT, are used to extract

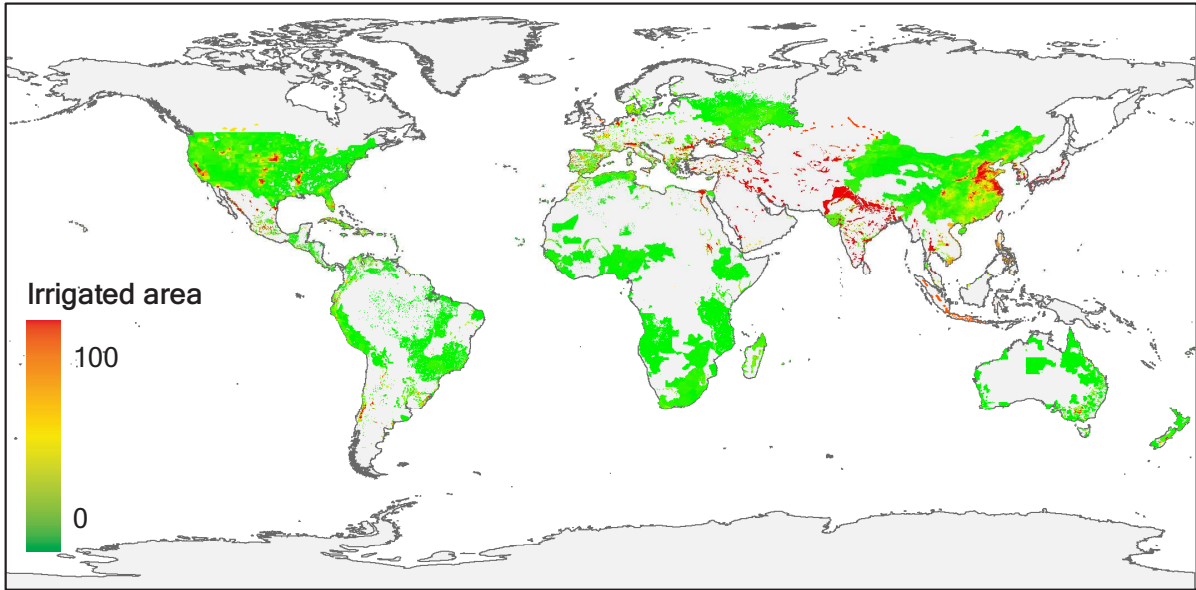


Figure 4.17: Global Map of Irrigated Areas.

spatially distributed parameters of elevation, land use, soil types, vegetation, and irrigation area. A three-level desegregations scheme plus a vertical subdivision into three soil layers and one groundwater layer are implemented in the DBH model system for macro scale basins. The model could be coupled with atmospheric model to estimate climate impacts on hydrology.

Chapter 5

Evaluation of the DBH Model System

5.1 Model Evaluation Processes

Oreskes et al. (1994) described the role of verification, validation, and confirmation of numerical models in the earth sciences. Verification and validation of numerical models of natural systems is impossible. This is because natural systems are never closed and because model results are always non-unique. Models can be confirmed by the demonstration of agreement between observation and prediction, but confirmation is inherently partial. Complete confirmation is logically precluded by the fallacy of affirming the consequent and by incomplete access to natural phenomena. Models can only be evaluated in relative terms, and their predictive value is always open to question. The primary value of models is heuristic.

In this section, the mechanism for validating DBH system is described. Important concepts needed to understand the model evaluation processes are verification, calibration, validation, credibility, and qualification (Rykiel, 1996). Verification is a demonstration that the modeling formalism is correct. Calibration is the estimation and adjustment of model parameters and constants to improve the agreement between model output and a data set. Validation is a demonstration that a model within its domain of applicability possesses a satisfactory range of accuracy consistent with the intended application of the model. Credibility is a sufficient degree of belief in the validity of a model to justify its use for research and decision making. Qualification is aimed at discovering the domain over which a validated model may properly be used, i.e., whether the model is acceptable for use in a more general context, and amounts to revalidating a model for new cases. The calibration and qualification of model system involves

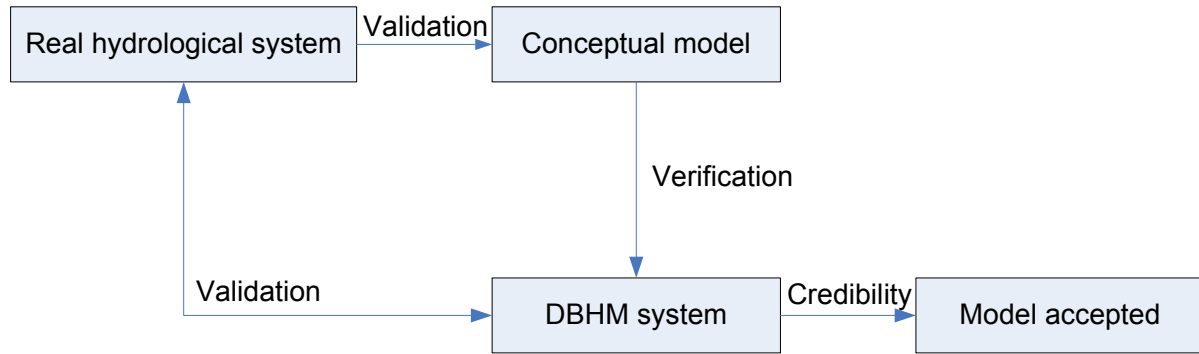


Figure 5.1: Relationship between model verification, validation and credibility.

detail case study of the model system and will be discussed in the application. The general model validation process for the DBH model system is described in this section.

There are three steps in deciding if a model system is an accurate representation of the actual systems considered. The first step is to verify the model that is to make sure that the model system acts as it is intended to against the numerical target that has been designed. This generally involves the code debugging and can be aided by testing each module of code rather than the entire program. It also includes detecting the model system under a number of input parameters. One of the methods is to check the model system against certain conditions occurring. The certain conditions usually are set to a simple condition so that the model performance could be checked easily with conceptual models such as water energy balance. Once the model simulation is verified then the computer simulation presents the intended system model. The next step is to validate the model so that the model system can be considered to be accurately representing the real system. This validation is done by comparing the models to what is generally accepted as the real system, or the model results that should agree with observations for validations. The final step in the simulation is to make sure that the model system is credible which is to see if the simulation is accepted as being accurate and useful. For the purpose of this research, this would be subjected to the simulation details, models and methods. The relationship of these steps can be seen in figure 5.1.

5.1.1 Model Verification

There are two types of verification errors: mechanical error and logical error. The mechanical error amounts to debugging a computer program and in mathematical models showing that the mathematics is mechanically correct. It is difficult to verify that the model entirely accurate under all circumstances. There are some minor coding errors were found in the original SiB2

model. It is hard to check the entire model and find the minor coding errors. The best way might be to check the modules of the model system one by one. Main subroutines of the DBH model system are verified with known processes or compared with the case study results using Microsoft Excel. These subroutines include the FAO Penman-Monteith formula to calculate reference evapotranspiration (Allen et al., 1998), the kinematic wave model to estimate river channel flow, the one dimensional SiB2 model to simulate land surface processes, etc. The mechanical error verification is an important technical matter that relates to how faithfully and accurately ideas are translated into computer code or mathematical formalisms. The DBH model is also verified under different operation system. It can work under Microsoft® Windows XP™, UNIX, and Linux with DIGITAL Visual FORTRAN 6.0 or Intel® FORTRAN compiler.

A more subtle and difficult verification problem is showing that the program logic is correct. One simplest method is to check the model system against certain conditions occurring. The certain conditions can be set as simple as possible and the conditions should be easily checked with conceptual models. A verification process has been done for the river channel routing scheme. The runoff flow of water per unit width to the river channel is assumed to be a constant. The discharge at the outlet of the river basin should start from zero before the runoff recharges to the river channel and increase as time passes and more runoff is recharged to the river channel before the river flow becomes steady. The discharge at the outlet should be the runoff flow rate times the total river channel length according to water balance theory after the discharge becomes steady. The simple certain condition is set and tested with an assumed river basin with the DBH model. The runoff flow rate is set to $0.1 \text{ m}^2/\text{s}$ and $0.0001 \text{ m}^2/\text{s}$, with the corresponding theoretic discharge of $2802.12 \times 10^3 \text{ m}^3/\text{s}$ and $2802.12 \text{ m}^3/\text{s}$, respectively. Figure 5.2 shows the model verification results on the river routing scheme subroutine. The discharge starts from zero and becomes theoretic values after the discharge is steady. The discharge becomes steady after 80 hours for the runoff flow rate of $0.1 \text{ m}^2/\text{s}$ and after 1200 hours for the runoff flow rate of $0.0001 \text{ m}^2/\text{s}$. It is expected the discharge becomes steady more quickly when the runoff flow rate is larger. It is worth to note that the case check of certain conditions is not sufficient conditions of model verification, i.e. the correct results under the certain conditions can not guarantee the model is correct. However, it is a necessary condition and can eliminate the suspicion on the model system.

A third way to verify the models is to check the range and distribution of input parameters and output results. The parameters should be in the reasonable range and have qualitative spatial distribution. The DBH model system can export distributed map of basin discretization, soil parameters, discharge station controlled area, river channel parameters, annual mean

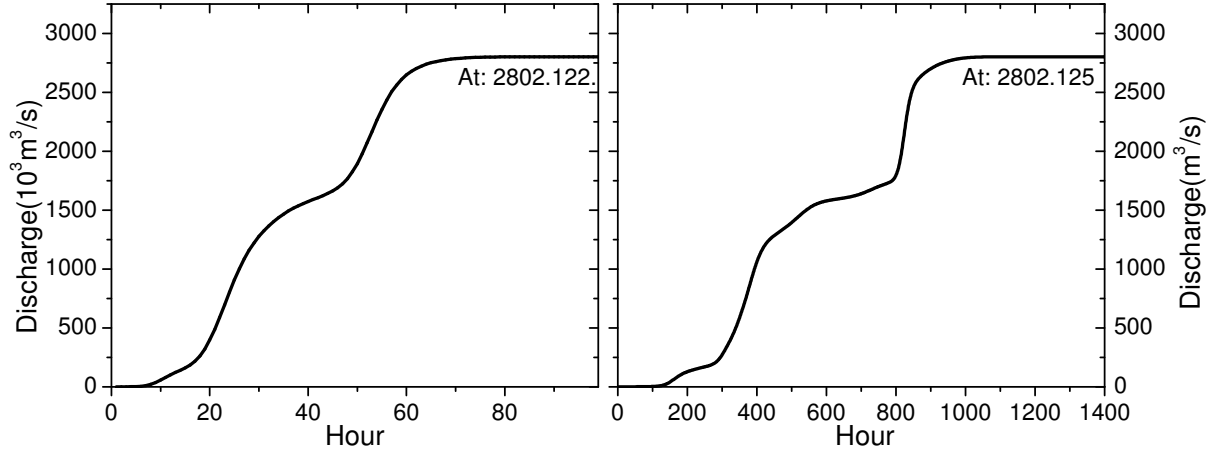


Figure 5.2: Model verification on the river routing scheme subroutine.

meteorological data, reference evapotranspiration, etc. These maps could help to check the range and qualitative spatial distributed characteristics of model input and output.

5.1.2 Model Validation

Validation shows that a model meets some specified performance standard under specified conditions. This indicates that the model is acceptable for use. It does not indicate that it embodies any 'absolute' truth, nor even that it is the best model available. Such a test cannot demonstrate the logical validity of the model's scientific content. The operational and data components can be validated, but the theoretical component cannot. Model validation of DBH model system is done with the comparisons of simulated results with data obtained by observation and measurement of the observations in real hydro-meteorological system.

Validation criteria or standards must be built to decide the acceptability of the model system. The simulation is evaluated in terms of the error variances for the observations. Let x_i and f_i ($i = 1, \dots, n$) denote time series of observations and simulated values. The averages are $\bar{x} = \sum_{i=1}^n x_i/n$ and $\bar{f} = \sum_{i=1}^n f_i/n$.

Several criteria are used and listed below. Mean error (ERR) is defined as:

$$ERR = \frac{1}{n} \sum_{i=1}^n (f_i - x_i) \quad (5.1)$$

The relative bias (BIAS) provides a measure of the magnitude of the mean error:

$$BIAS = \frac{1}{n} \sum_{i=1}^n (f_i - x_i)/\bar{x} \quad (5.2)$$

Mean absolute error (MAE) is given as:

$$MAE = \frac{1}{n} \sum_{i=1}^n |f_i - x_i| \quad (5.3)$$

The mean square error between model-simulated f_i and the observed x_i is:

$$e^2 = \frac{1}{n} \sum_{i=1}^n (f_i - x_i)^2 \quad (5.4)$$

Set

$$\sigma_x = \sqrt{\frac{\sum_{i=1}^n (x_i - \bar{x})^2}{n}} \quad (5.5)$$

and

$$\sigma_f = \sqrt{\frac{\sum_{i=1}^n (f_i - \bar{f})^2}{n}} \quad (5.6)$$

The mean square error can be written in a fraction equation (Murphy, 1988):

$$\frac{e_m^2}{e^2} + \frac{e_a^2}{e^2} + \frac{e_p^2}{e^2} = 1 \quad (5.7)$$

where

$$e_m^2 = (\bar{f} - \bar{x})^2 \quad (5.8)$$

$$e_a^2 = (\sigma_f - \sigma_x)^2 \quad (5.9)$$

$$e_p^2 = 2\sigma_f\sigma_x \left[1 - \frac{1}{n\sigma_f\sigma_x} \sum_{i=1}^n (f_i - \bar{f})(x_i - \bar{x}) \right] \quad (5.10)$$

The three terms in the equation (5.7) are related to overall bias error, amplitude error (through the ratio of the variances) and phase error (through the correlation). The root mean square error $RMSE = \sqrt{e^2}$, the relative root mean square error $RRMSE = rmse/\bar{x}$, and the mean square skill score $MSSS = 1 - e^2/\sigma_x^2$, are calculated.

The model validation was done in a continental scale river basin in North China. The simulation was performed in the test period from 1983 to 1993. The simulation time step is hourly and the results are summarized in daily, monthly, and annual data to validate with ground observations. The validation results are shown in figure 5.3. The model gives reasonable simulation results with a variety of validation criteria. The model performs the best with mean monthly comparison and works well with monthly comparison. The daily comparison is relatively worse but the validation criteria are still in acceptable range.

The simulated annual largest flood peak is compared with daily ground observation.

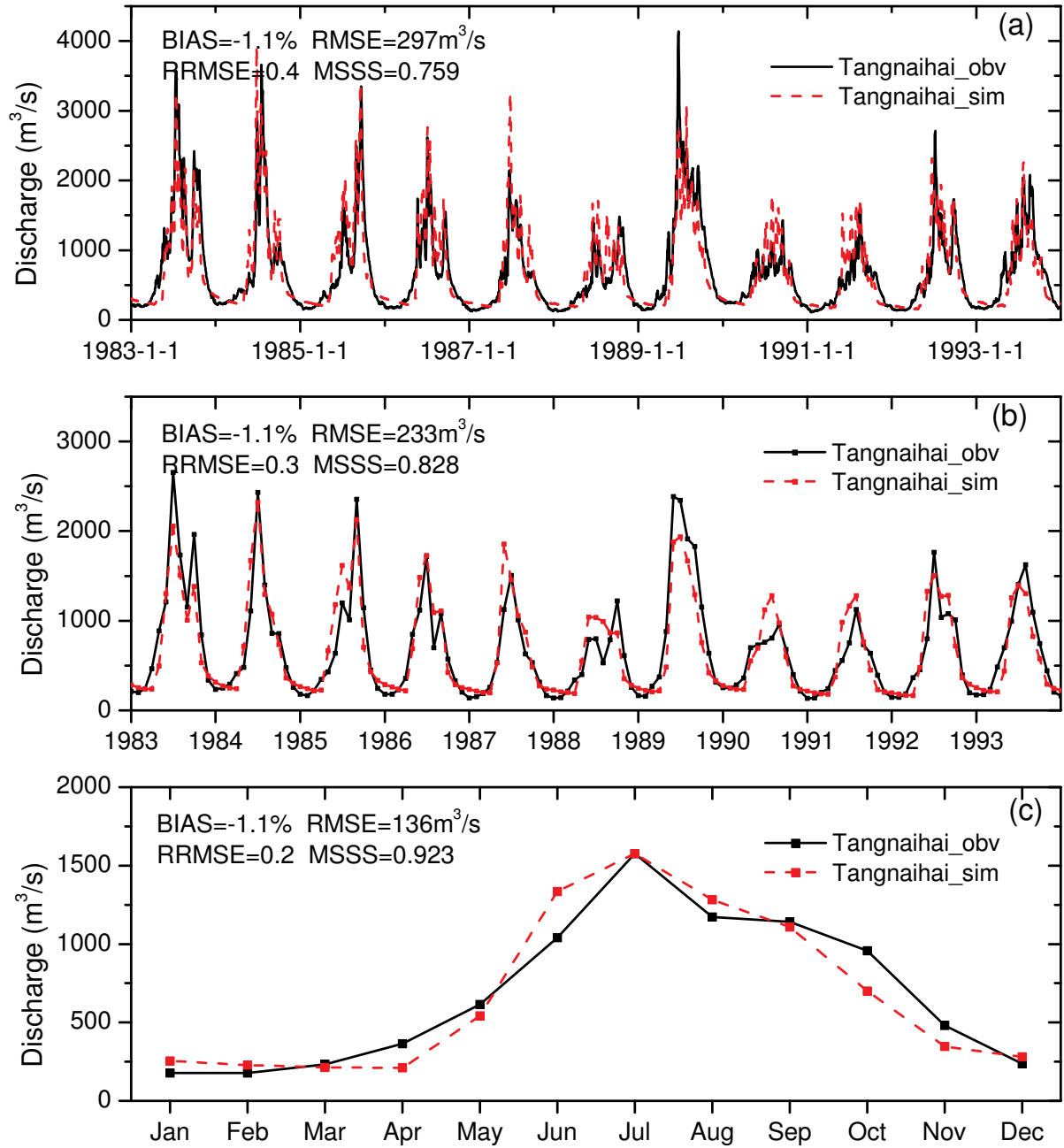


Figure 5.3: Model validation with ground observations: (a) daily discharge, (b) monthly discharge, (c) and mean monthly discharge comparisons.

Table 5.1: Annual largest flood peak validation (Flood peak: m³/s, Time: date)

Year	Obv.		Sim.		Diff.		Diff./Obv.
	Flood	Time	Flood	Time	Flood	Time	Flood (%)
1983	3560	14-Jul	3253	14-Jul	-307	0	-8.6
1984	3660	17-Jul	3099	15-Jul	-561	-2	-15.3
1985	3350	21-Sep	3389	18-Sep	39	-3	1.2
1986	2620	4-Jul	2766	5-Jul	146	1	5.6
1987	2150	25-Jun	3252	27-Jun	1102	2	51.3
1988	1480	10-Oct	1340	7-Oct	-140	-3	-9.5
1989	4140	23-Jun	2670	26-Jun	-1470	3	-35.5
1990	1430	17-Sep	1309	13-Sep	-121	-4	-8.5
1991	1590	18-Aug	1751	17-Aug	161	-1	10.1
1992	2710	7-Jul	2322	22-Jun	-388	-15	-14.3
1993	2040	21-Jul	2264	23-Jul	224	2	11.0

The validation results are shown in table 5.1. In most years of the simulation period, the flood peak discharge difference is less than 10% of the observation. The largest error occurs at the simulation of 1987 with an over 50% bias. The largest flood peak time is well simulated. All the time differences are less than 5 days except for the simulation in 1992 with a time difference of 15 days.

5.1.3 Model Credibility

The credibility of a model is related to the amount of knowledge available, the purpose of the model, and the consequences of any decisions based on it. A model with high operational credibility does not necessarily have high conceptual credibility. The conceptual hydrological models have used for a long time by many engineers over many parts of the world. Some of the concepts in the conceptual models have very weak physical meaning or give only a simple statistical relationship. These models could have high operational credibility and be used for a specific purpose. The DBH system gives much more detail description of the water and energy transfer processes in the river basin scale than the conceptual models. The model credibility could be proved by the checking the qualitative behavior of the system rather than quantitative accuracy. The distributed simulation makes it possible to check the model credibility with various physical parameters at different parts of the study area rather than the outlet discharge for most conceptual model. The simulation in DBH model system could be used to check the water and energy balance and uninterrupted observations, while many runoff-rainfall model targets in flood simulation and can be checked in the flood period. It should be noted that credibility is a subjective qualitative judgment, and cannot be quantified in any absolute sense.

A model credibility check on qualitative behavior was performed. The simulation was

tested in the continental scale river basin in North China in the test period from 1983 to 2000. The gauged river discharge at the hydrological station (Lanzhou station) after Longyangxia reservoir is checked. The reservoir started operation from October, 1986 and was thought to effectively affect the observed discharge from 1987. The reservoir has beneficial reservoir capacity of $24.7 \times 10^9 \text{ m}^3$. It is anticipative the big reservoir would affect the discharge at Lanzhou station. Since the reservoir operation, the discharge observations at the Lanzhou station are the results with the reservoir influence. The discharge without reservoir, i.e. natural flow, will not be gauged. The simulated discharge at Lanzhou station can give the natural flow. It should more significantly agree with the gauged discharge before the reservoir operation. Figure 5.4 gives the simulated and observed discharge at Lanzhou station. Comparing the daily discharge, the MSSS is 0.502 before the reservoir operation and -2.0 after the reservoir operation. The monthly discharge comparison map shows that the reservoir decreased the discharge in summer seasons and increased the discharge in winter seasons. The mean monthly discharge curve demonstrates the difference. The simulated discharge pattern is close to the observed one before 1987. The observed the discharge reached higher values than simulated one from November to May and kept a lower level from June to September. The grant model skill during the study period is not significant with a MSSS of -0.607. This is caused by the reservoir operation. The simulated results are as expected and can provide a qualitative assessment of the reservoir influence.

5.2 Introduction of Subgrid Heterogeneity

The land surface-atmosphere interface is a major component of the climate system, characterized by hydrological coupling between the atmosphere and the land biosphere. Several land surface models have been developed to describe land-atmosphere water and energy exchanges, including the bucket model (Manabe, 1969), Biosphere-Atmosphere Transfer Scheme (BATS) (Dickinson et al., 1986), the Simple Biosphere (SiB) model (Sellers et al., 1986), and the Bare Essentials of Surface Transfer (BEST) (Desborough and Pitman, 1998). These models emphasize the vertical structure, representing the land surface as one or two tiers of vegetation (i.e., canopy or groundcover, or both). However, one of the main shortcomings of these schemes is that they do not capture the pronounced heterogeneity of the Earth's land surface. This heterogeneity spans a wide range of scales and affects the surface energy and water budgets, as well as land-atmosphere exchanges of momentum, heat, and water through several nonlinear processes. Distributed representations of spatial information and physical descriptions of the

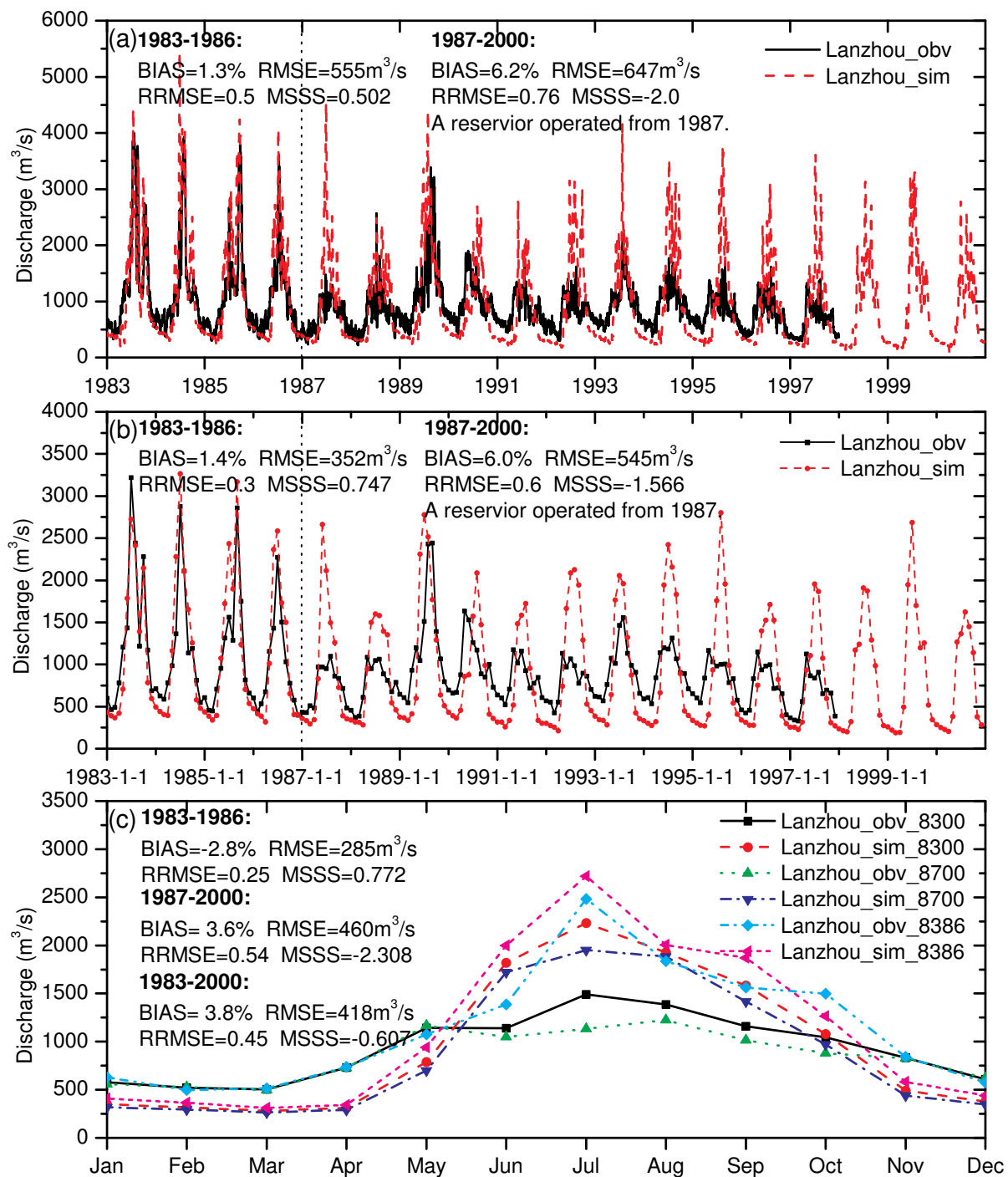


Figure 5.4: Simulated and observed discharge at Lanzhou station: (a) daily, (b) monthly, (c) and mean monthly comparisons.

land biosphere and hydrological processes are necessary because of their spatial heterogeneity and highly nonlinear form. The resolution of present-day general circulation models (GCMs) is still too coarse to explicitly capture the effects of surface heterogeneity, which must thus be parameterized within the framework of complex and nonlinear land surface process schemes. A realistic representation of subgrid-scale variability would markedly improve land surface modeling (Koster and Suarez, 1992a).

Numerous studies have investigated the subgrid-scale variability associated with terrain, soil, and vegetation heterogeneities. Milly and Eagleson (1988) found that surface runoff could be greatly underestimated if the areal variability of precipitation associated with various scales and types of storms were ignored. Entekhabi and Eagleson (1989) used analytic distributions of rainfall and soil moisture conditions to examine the sensitivity of runoff, bare soil evaporation efficiency, and transpiration efficiency to soil type and climatic forcing. Avissar and Pielke (1989) suggested a parameterization of subgrid-scale forcing for heterogeneous land surfaces in atmospheric numerical models and found that spatial heterogeneity in vegetation could have significant effects on temperature and precipitation. Pitman et al. (1990) used a surface hydrology model driven by meteorology simulated by a GCM to investigate the influence of the subgrid distribution of precipitation on the surface water balance. Their results indicated that improving the realism of the areal distribution of precipitation could alter the partitioning between runoff and evapotranspiration. Seth et al. (1994) divided one GCM grid into several subgrids to study the effects of subgrid-scale vegetation and climate specifications on surface fluxes and hydrology, and showed that energy partitioning at the surface, surface stress, and runoff could all be significantly affected by subgrid variability. Ghan et al. (1997) presented a preliminary evaluation of the relative importance of subgrid variations in parameters related to the surface hydrology. They found that subgrid variability in summertime precipitation would increase runoff, and subgrid variations in vegetation and soil properties would increase surface runoff and reduce evapotranspiration. Giorgi (1997a,b) described a theoretical framework for the representation of surface heterogeneity within complex biophysical surface schemes for use in climate models and assessed the sensitivity to relevant parameters.

Giorgi and Avissar (1997) reviewed methodologies for the representation of land surface subgrid-scale heterogeneity effects and grouped the effects of surface heterogeneity into two categories: "aggregation" and "dynamical" effects. Subgrid-scale aggregation has been shown to affect the simulated surface latent and sensible heat fluxes, snowpack, and dynamics of soil moisture and runoff. Dynamical heterogeneity effects are associated with microscale and mesoscale circulations induced by heterogeneous surfaces. Models of dynamical heterogeneity

processes attempt to describe the effects of atmospheric circulations induced by surface heterogeneities (Seth and Giorgi, 1996; Avissar and Schmidt, 1998). Models of aggregation effects attempt to calculate the contribution of different subgrid-scale surface types to the grid box average energy and water budgets and surface-atmosphere exchanges. Such models have been based on discrete approaches, whereby heterogeneity is described in terms of a finite number of subgrid "tiles" or "patches," and on continuous approaches, in which heterogeneity is described in terms of probability density functions. Many researchers have used probability density functions within continuous approaches to investigate the variability of precipitation and soil characteristics (Entekhabi and Eagleson, 1989; Gao and Sorooshian, 1994; Liang and Xie, 2001; Zeng et al., 2002; Yeh and Eltahir, 2005). Several studies have also represented land use and vegetation cover subgrid variability based on discrete approaches (Koster and Suarez, 1992b; Leung and Ghan, 1998). Koster and Suarez (1992b) considered two conceptually different strategies, the "mixture" and "mosaic" strategies, for dealing with subgrid variability in vegetation cover. The mixture strategy assumes that the different vegetation types are effectively mixed homogeneously throughout the grid square, so that the atmosphere interacts only with a set of near-surface atmospheric conditions pertaining to the mixture. With the mosaic strategy, the different vegetation types in a grid square are assumed to be geographically distinct. The different types are viewed as separate tiles of a square grid mosaic, and each tile interacts with the atmosphere independently. The effective differences between the strategies are small over a wide range of the condition. In particular, the strategies are effectively equivalent when the transpiration resistances of the different vegetation types are of the same order of magnitude.

Although the subgrid variability of natural factors, such as precipitation, soil infiltration capacity, and vegetation cover, has been extensively studied, few studies have investigated the subgrid-scale variability caused by human activities. Döll and Siebert (2002) modeled the global irrigation water requirements under present-day climate conditions and found that the annual irrigation water requirement in hot semiarid regions can be more than 1000 mm. Boucher et al. (2004) concluded that human activity through irrigation has a direct influence on the water vapor concentration, and estimated a global mean radiative forcing up to 0.1 W m^{-2} and a surface cooling of up to 0.8 K over an irrigated area. Gordon et al. (2005) showed that deforestation is as large a driving force as irrigation in terms of changes to the hydrological cycle. Haddeland et al. (2005) reported on an irrigation scheme in a macroscale hydrological simulation and evaluated the effects of irrigation on the water and energy balances of the Colorado and Mekong river basins. These studies indicated that the subgrid variability caused

by human activities has potentially important effects on the surface water and energy balances. However, few complete studies have described the effects of both the subgrid variability of natural factors and human activities on hydrological simulation. In particular, few studies have examined the influence of subgrid variability on large-scale distributed hydrological patterns within a continental scale river basin.

Among the subgrid heterogeneities affecting hydrological processes, we account for two heterogeneities: precipitation heterogeneity and the heterogeneity of irrigation redistributing runoff; these factors represent the natural subgrid variability and the variability caused by human activities, respectively. Precipitation heterogeneity is represented by a simple spatial exponential distribution. An irrigation scheme based on simulated soil moisture and available water was developed to represent subgrid variability related to irrigation. The study objective was to analyze the effects of anthropogenic heterogeneity on the water and energy balances of a large-scale basin in a semiarid river basin by comparing the effects of natural heterogeneity and anthropogenic heterogeneity (Tang et al., 2006).

5.3 Model Description

A modeling framework was developed to represent the effects of natural and anthropogenic heterogeneity on the water and energy balances of a continental scale river basin. The modeling framework, a distributed biosphere-hydrological (DBH) model, embeds a biosphere model into a distributed hydrological scheme, representing both topography and vegetation conditions in a mesoscale hydrological simulation (Tang et al., 2006).

In the DBH model system, the revised Simple Biosphere (SiB2) model (Sellers et al., 1996) is used to calculate the transfer of energy, mass, and momentum between the atmosphere and the surface of the Earth, and a river routing scheme is used to lead the runoff to the river basin outlet. The overall structure of DBH model system is shown in Fig. 4.1.

The Food and Agriculture Organization (FAO) Digital Soil Map of the World (FAO, 1995) was used to produce the DBH model grid soil properties, such as the soil water potential at saturation ψ_s (m), soil hydraulic conductivity at saturation K_s (m/s), soil wetness parameter b , and porosity θ_s (Cosby et al., 1984).

This subsection describes the modification of the SiB2 model to include a river-routing module and an irrigation scheme.

The SiB2 model is grid-based and designed for use in atmospheric general circulation models. It calculates the water and energy balance equations at the land surface. In the

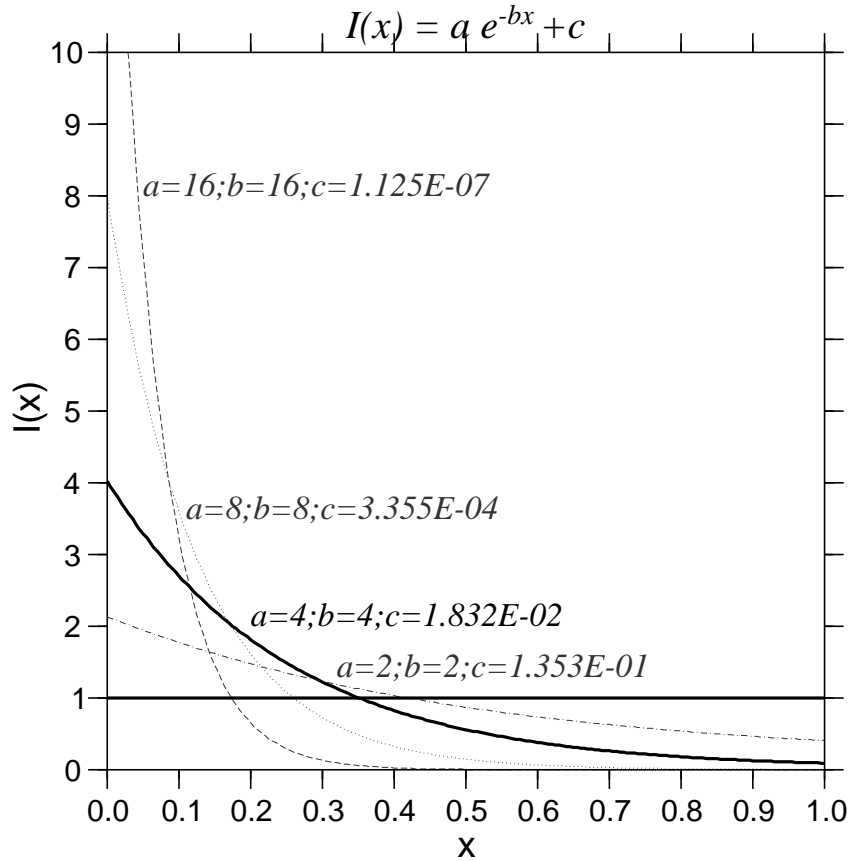


Figure 5.5: Precipitation area-amount relationships.

SiB2 model, precipitation consists of large-scale spatially uniform precipitation and convective spatially nonuniform precipitation. In most GCMs, a single (area-averaged) figure for convective precipitation is produced for each grid area for each time step. The SiB2 model can use GCM outputs of large-scale and convective precipitation. In this study, we evaluated the relative importance of subgrid variations in precipitation and in human activities. Observations were used to drive a physically based model of the land surface water and energy balances. Large-scale and convective precipitation could not be specified from the observed precipitation. We assumed that the observed rainfall was spatially distributed according to a simple exponential $I(x)$:

$$I(x) = ae^{-bx} + c \quad (5.11)$$

where $I(x)$ is the relative amount of rainfall as a function of the fractional area of the grid area x , ($0 < x < 1$), and a , b , and c are constants (Figure 5.5). The constants a , b , and c are normalized so that the integration of $I(x)$ over the whole grid is 1. If set $a = b$, then $c = e^a$.

Surface runoff and subsurface runoff were routed to the basin outlet through a channel network as described by Tang et al. (2006). The river basin and river network were abstracted

from a 10-km digital elevation model (DEM). The Pfafstetter numbering scheme for delineation and codification of the river basin was used and based on topographic controls and the river network topography. The system was founded on concepts first described by Pfafstetter (1989) and later detailed by Verdin and Verdin (1999). The numbering scheme was self-replicating, making it possible to provide identification numbers to the level of the smallest subbasins extractable from the DEM. The routing order of the subbasins was indicated in the Pfafstetter code. Within a given smallest subbasin, flow intervals were specified to represent the time lag and accumulating processes in the river network according to the distance to the subbasin outlet. The surface runoff flowed to the river channel following a hillslope, as governed by a one-dimensional kinematics wave model. The subsurface runoff connected the river channel to a groundwater reservoir. The river flow was governed by a kinematics wave model, taking into account the friction of the river channel.

The input data to the SiB2 model were hourly precipitation, temperature, vapor pressure, wind speed, shortwave downward radiation, and incoming longwave radiation. When the hourly input data were not supplied to the model, we partitioned these variables in the model time step based on daily precipitation and maximum and minimum temperatures, using standard algorithms or empirical relationships (Cesaraccio et al., 2001). The vapor pressure was estimated from observed relative humidity and temperature (Allen et al., 1998). The downward shortwave radiation was estimated from sunshine duration. Because elevation of the upper stream of Yellow Riverbasin is very high, the widely-used FAO Angstrom-type model (Angström, 1924; Doorenbos and Pruitt, 1977) may under-estimate shortwave radiation. Therefore, we adopted a new and widely validated radiation model (Yang et al., 2001; Yang and Koike, 2005) to estimate the radiation, with hourly sunshine data interpolated from daily data following Revfeim (1997). The daily wind speed was directly used as hourly wind speed. The irrigation scheme was incorporated. The irrigation scheme was based on simulated soil moisture in the irrigation tiles and available water for irrigation.

5.4 Approach

5.4.1 Study Area

The model was applied to the Yellow River basin of China. The Yellow River is the second-longest river in China. The headwaters of the Yellow River begin on the Tibetan Plateau, and the river flows eastward, passing through the Loess Plateau and the North China Plain before emptying into Bohai Gulf (Figure 3.1). The main course of the river flows 5464 km, and the

river basin area is 794,712 km². The Yellow River faces serious water problems, including water shortages and eco-environmental degradation (Xu et al., 2002; Feng et al., 2005). In particular, the lower Yellow River has suffered from a drying-up phenomenon since the 1970s, and many researchers have focused on the river's hydrology (Liu and Zheng, 2004; Fu et al., 2004; Xia et al., 2004; Yang et al., 2004a; Xu, 2005b).

There are several irrigation districts inside the river basin, such as the Qingtongxia and Hetao districts (Figure 3.1). Some large irrigation districts in the lower reaches are located outside the watershed but extract irrigation water from the Yellow River (Fu et al., 2004; Chen et al., 2002). Liu and Zhang (2002) have described the status of irrigation in the river basin.

To validate the model and analyze the impact of subgrid-scale variability on stream flow, we examined the discharges from the following eight major hydrological gauges on the main stream of the Yellow River: Tangnaihai (TNH), Lanzhou (LZ), Qingtongxia (QTX), Toudaoguai (TDG), Longmen (LM), Sanmenxia (SMX), Huayuankou (HYK), and Lijin (LJ) stations (Figure 3.1). The watershed above Tangnaihai station is the source region of the Yellow River, and water withdrawals from the river are limited. Qingtongxia station is downstream from a large irrigation district (the Qingtongxia irrigation district). Toudaoguai station is downstream from another large irrigation district (the Hetao irrigation district). The Lanzhou-Qingtongxia and Qingtongxia-Toudaoguai sections are "net" water consumption zones of the Yellow River, i.e., the annual discharge at Qingtongxia station is less than that at Lanzhou station, and the discharge at Toudaoguai station is less than that at Qingtongxia station. Huayuankou station is another key station on the main stream. The annual discharge at this station reaches the maximum value for the main river stem. Lijin is the last hydrological station before the river empties into Baohai Gulf. Between Huayuankou and Lijin stations, the runoff into the river channel is small because the elevation of the riverbed is higher than the land surface behind artificial levees. In addition, there are large irrigation districts in the lower reaches that are located outside the watershed and channeled river water (Fu et al., 2004; Chen et al., 2002). This area is another "net" water consumption zone of the Yellow River.

5.4.2 Input Data

Climate data from 120 meteorological stations inside and close to the study basin (Figure 3.1) were obtained from the China Meteorological Administration (CMA). The dataset is available from 1982 to 2000 and contains the daily precipitation, mean temperature, maximum and minimum temperatures, mean surface relative humidity, sunshine duration, and cloud amount. The vegetation condition index leaf area index (LAI) and fraction of photosynthetically active

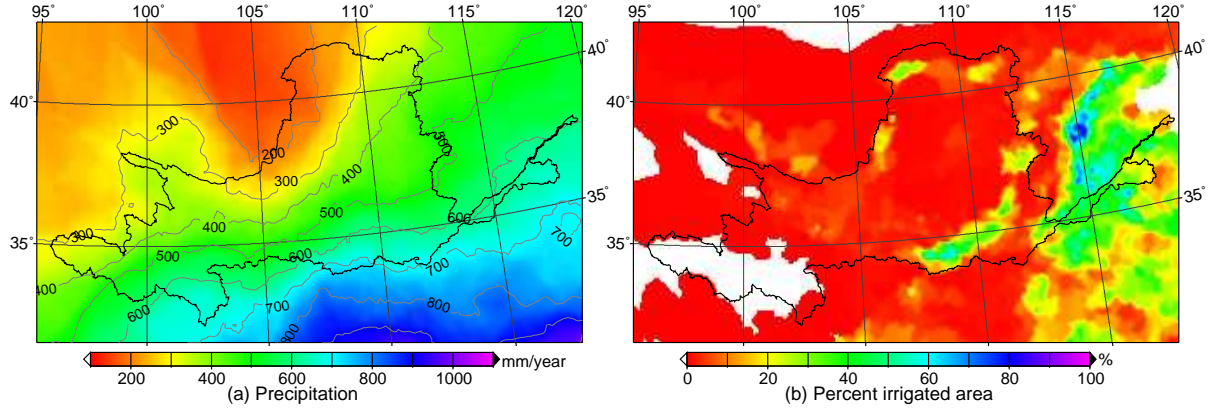


Figure 5.6: (a) Mean annual precipitation and (b) irrigated area (%) in the Yellow River basin.

radiation absorbed by the green vegetation canopy (FPAR) were obtained from Myneni et al. (1997). The LAI and FPAR datasets are available at monthly temporal frequencies from 1982 to 2000. Information about the percentage of irrigated area within each grid cell was obtained from Siebert et al. (2005). The meteorological data at the stations were interpolated to a 10-km gridded dataset using the angular distance weighted (ADW) averaging method (New et al., 2000). Figure 4 shows the mean annual precipitation within a 10×10 -km grid cell, and also the percentage of irrigated area within the grid cells.

The LAI and FPAR datasets were resampled to the same resolution for use in the model. SiB2 land cover data are available from the USGS Global Land Cover Characterization dataset. The FAO Digital Soil Map of the World was used to produce the grid soil properties such as the soil water potential at saturation, soil hydraulic conductivity at saturation, soil wetness parameter, porosity.

5.5 Model Validation

The model was tested for the Yellow River basin for the period 1983-2000 after initializing the model until equilibrium was reached. Initially the model was run without considering the precipitation subgrid-scale variability and the irrigation scheme. There are no large irrigation districts near the upstream Tangnaihai station. The discharge observations at Tangnaihai station were considered to be the natural flow and were compared with the simulated stream flow. The mean bias (BIAS), root mean square error (RMSE), relative root mean square error (RRMSE), and mean square skill score (MSSS) were used to evaluate the model performance. The BIAS is defined as

$$BIAS = \frac{1}{N} \sum (x_s - x_o) / \bar{x}_o \quad (5.12)$$

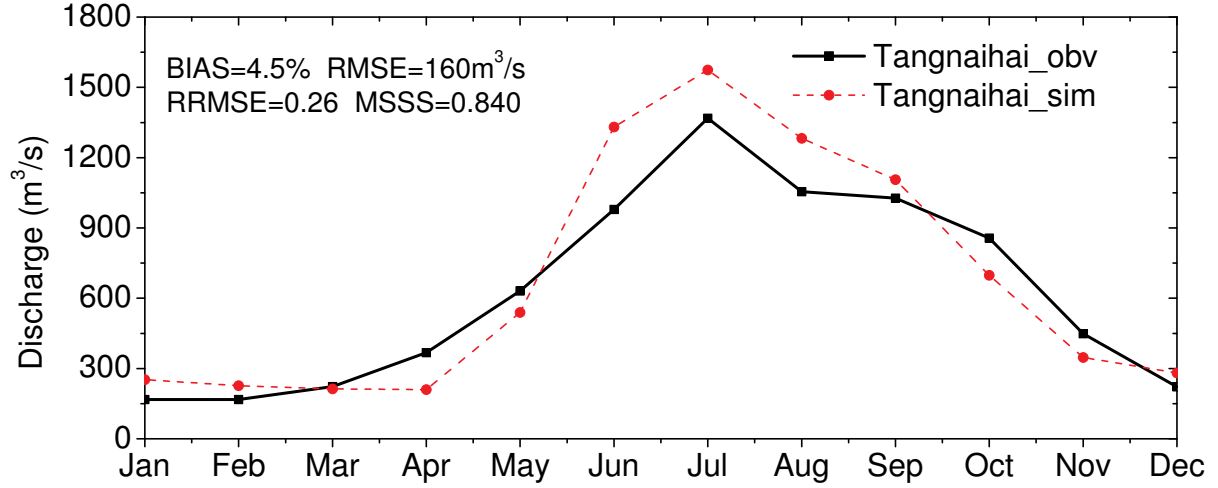


Figure 5.7: Simulated and observed mean monthly stream flow at Tangnaihai station.

where $\bar{x}_o = \sum x_o/N$ is the averaged value, RMSE is defined as

$$RMSE = \sqrt{\frac{1}{N} \sum (x_s - x_o)^2} \quad (5.13)$$

RRMSE is defined as

$$RRMSE = RMSE / \left(\sum x_o/N \right) \quad (5.14)$$

and MSSS is defined as (Murphy, 1988)

$$MSSS = 1 - \frac{\sum (x_s - x_o)^2}{\sum (x_o - \sum x_o/N)^2} \quad (5.15)$$

where N is the total number of time series for comparison, x_s represents the simulated value, and x_o is the observed value. A perfect fit should have MSSS value equal to one. Mean monthly simulated and observed stream flow values are shown in Figure 5.7. The BIAS, RRMSE, and MSSS were 4.5%, 0.26, and 0.840, respectively. The simulated and observed daily stream flow at Tangnaihai station is shown in Figure 5.8. The RRMSE was 0.5, and the MSSS was 0.685. Monthly and daily discharge values were finely reproduced, and the discharge simulation performed reasonably well for estimating irrigation water availability.

For validation purposes, we implemented an irrigation scheme and compared the model-estimated net irrigation water consumption to the statistical water consumption from several previous reports. Liu and Zhang (2002) reported the water consumption in the upper, middle, and lower reaches of the Yellow River basin from the 1950s to 1990s; these values may be larger than the irrigation water consumption because the statistical water consumption included industrial and residential use. Li et al. (2004) provided the net irrigation water consumption

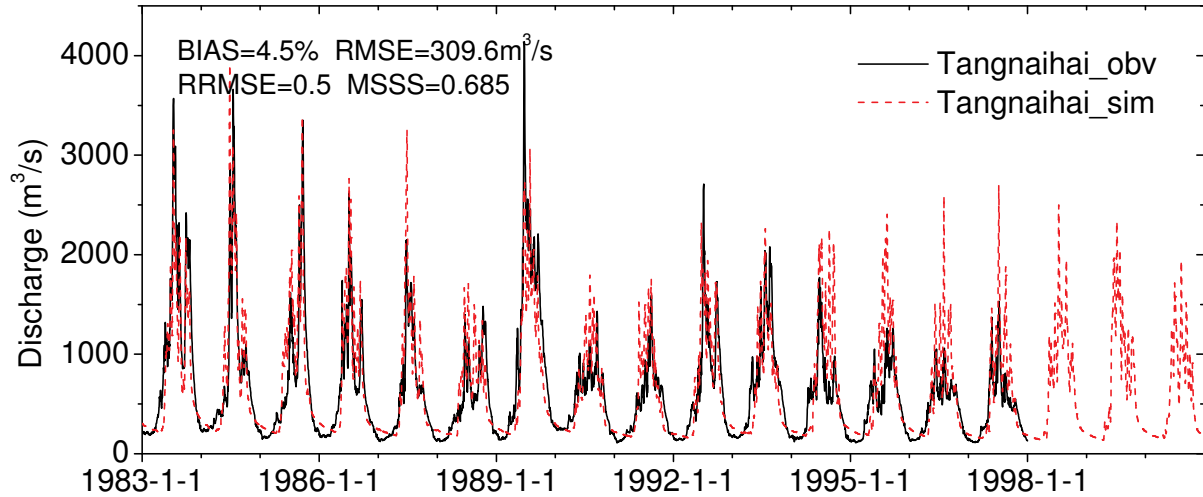


Figure 5.8: Simulated and observed daily stream flow at Tangnaihai station.

Table 5.2: Simulated and reported annual irrigation water consumption (10^9m^3)

Time period	Upper reaches ^a	Middle reaches	Lower reaches	Total
1980-1989 (reported)	12.11	6.21	11.29	29.61
1983-1989 (simulated)	8.15	7.90	11.06	27.11
1990-1995 (reported)	13.17	6.02	10.78	29.96
1990-1995 (simulated)	6.88	7.98	9.63	24.49

^aThe effect of an endoric lake was not considered in the simulations.

in seven irrigation districts in the upper and middle reaches of the Yellow River basin. Table 5.2 lists the simulated and reported irrigation water consumption. The reported numbers are summarized for the 1980s and 1990s, while the simulation results are averages for the corresponding periods. The simulated water consumption values in the upper reaches are less than reported values because large amounts of water are taken into the Hetao irrigation district, where water then drains to an endoric lake and evaporates into the atmosphere (Li et al., 2004).

5.6 Analyses and Results

Model analyses were performed for a variety of modeling cases associated with natural and anthropogenic heterogeneities: case 1, no irrigation without consideration of precipitation heterogeneity; case 2, no irrigation with precipitation heterogeneity; case 3, irrigation with precipitation heterogeneity. For all the modeling cases, the same SiB2 land cover data from the USGS Global Land Cover Characterization dataset were used, along with the same vegetation characteristics, such as LAI and FPAR, and related soil optical properties. Possible vegetation status variety because of irrigation was not accounted for in the model. The discharge at the

Table 5.3: Mean annual runoff (R), evaporation (E) for the various case (mm year⁻¹)

Subdivisions	Precipitation	Obv.		case 1		case 2		case 3	
		R	E	R	E	R	E	R	E
Up TNH	483	173	310	140	344	174	309	178	305
TNH-LZ	416	88	327	79	336	108	307	83	332
LZ-QTX	316	-61	377	21	295	22	294	-63	379
QTX-TDG	240	-56	296	15	225	15	225	-23	264
TDG-LM	395	18	377	50	345	61	334	32	363
LM-SMX	523	42	481	80	443	114	409	64	459
SMX-HYK	601	86	515	97	504	144	457	46	555

upstream Tangnaihai station was used to calibrate the precipitation heterogeneity parameters a , b , and c in equation 5.11. For cases accounting for precipitation heterogeneity in this study, $a = b = 4$ was used.

Table 5.3 summarizes the effects of precipitation and anthropogenic subgrid variability on the mean annual water balance components of the Yellow river basin. Without considering precipitation heterogeneity, the runoff contribution was underestimated. The simulated runoff contributions were less than observed contributions in the mountainous subdivision Up TNH. The runoff contribution was well simulated by considering precipitation heterogeneity. The runoff contributions were always positive values in the cases without an irrigation scheme. This result contradicts the observed negative runoff contributions in arid regions, such as for subdivisions LZ-QTX and QTX-TDG. These results suggest that the negative runoff contribution cannot be simulated by only considering the natural heterogeneity. This constructive model shortcoming can be eliminated by taking anthropogenic heterogeneity into account. With an irrigation scheme, the simulated annual runoff contributions in subdivisions LZ-QTX and QTX-TDG were -63 mm and -23 mm, corresponding to the observed contributions of -61 mm and -56 mm, respectively. The negative runoff contribution was modeled with the irrigation scheme. This result also indicates that irrigation water withdrawals have changed the pattern of the hydrological cycle in the Yellow River basin.

Figure 5.9 shows the effects of precipitation heterogeneity on runoff simulations. The simulated total runoff for case 1 in which precipitation was spatially uniform over a large grid cell was much less than that of case 2 in which the precipitation heterogeneity was considered. The annual total runoff was 81 mm for case 1 and 101 mm for case 2. The simulated total runoff differences were caused by the surface runoff differences. The annual surface runoff was 20 mm and 43 mm for cases 1 and 2, respectively. This result indicates that surface runoff simulations highly depend on precipitation heterogeneity.

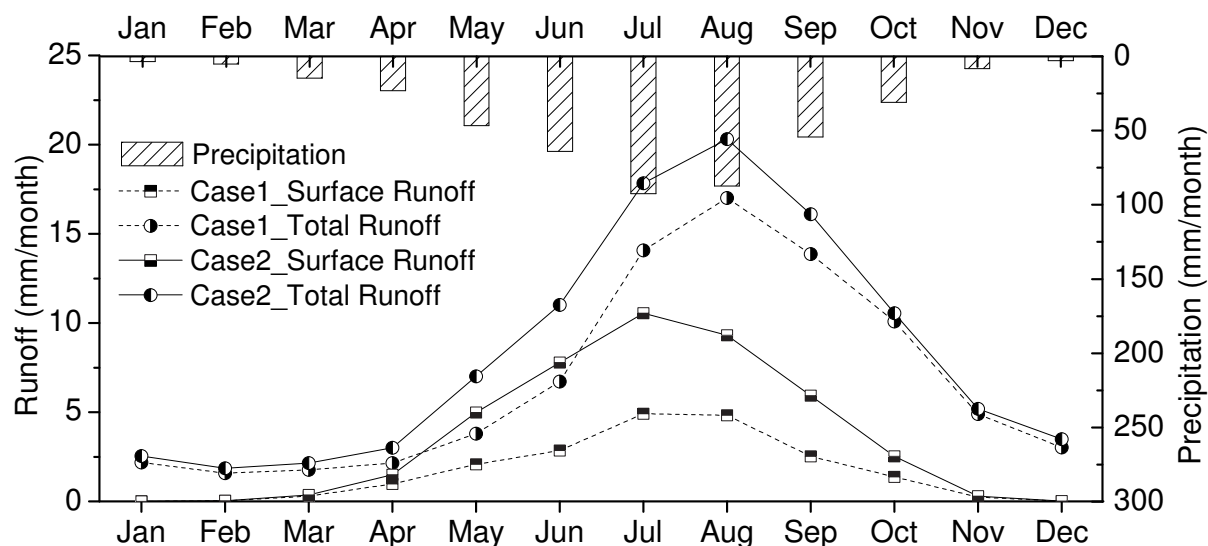


Figure 5.9: Effects of precipitation heterogeneity on runoff simulation from 1983 to 2000; (a) total runoff and (b) surface runoff in the Yellow River Basin.

Figure 5.10 shows the effects of precipitation heterogeneity and irrigation on annual stream flow along the Yellow River from upstream to downstream. Compared to the case of no irrigation with precipitation heterogeneity, discharge was underestimated for the case of no irrigation without precipitation heterogeneity. There are no large irrigation districts in the upstream reaches of the Yellow River. The observed discharge values at stations TNH and LZ were thus used to validate the model. The discharge at TNH and LZ was well simulated when the precipitation heterogeneity was taken into account. The observed discharge decreased between stations LZ and TDG. Without the irrigation scheme, the simulated discharge increased in the discharge-decrease zone, although the increase was very small. The decreasing discharge along the main stem of the river was simulated well when irrigation was taken into account. These results show that annual discharge at station HYK decreased 41% because of irrigation. The anthropogenic influence was prominent downstream from station LZ.

In Figure 5.11, spatial distributions of water balance components associated with irrigation are shown at a 10×10 -km spatial resolution. Figure 5.11a shows the irrigation water shortage (%) in each grid cell. The irrigation water shortage was calculated from the irrigation water withdrawals to the irrigation water requirements. The water shortage was small in grid cells near the main river stem or inside irrigation districts. Figure 5.11b gives the irrigation water withdrawal distribution (mm month^{-1}) per unit grid cell area. The largest irrigation water withdrawals occurred in the grid cells in irrigation districts with high irrigation fractions. Figure 5.11c shows the spatial differences between simulated evaporation with and without the irrigation scheme. Evaporation increased in the irrigation districts and grid cells with high ir-

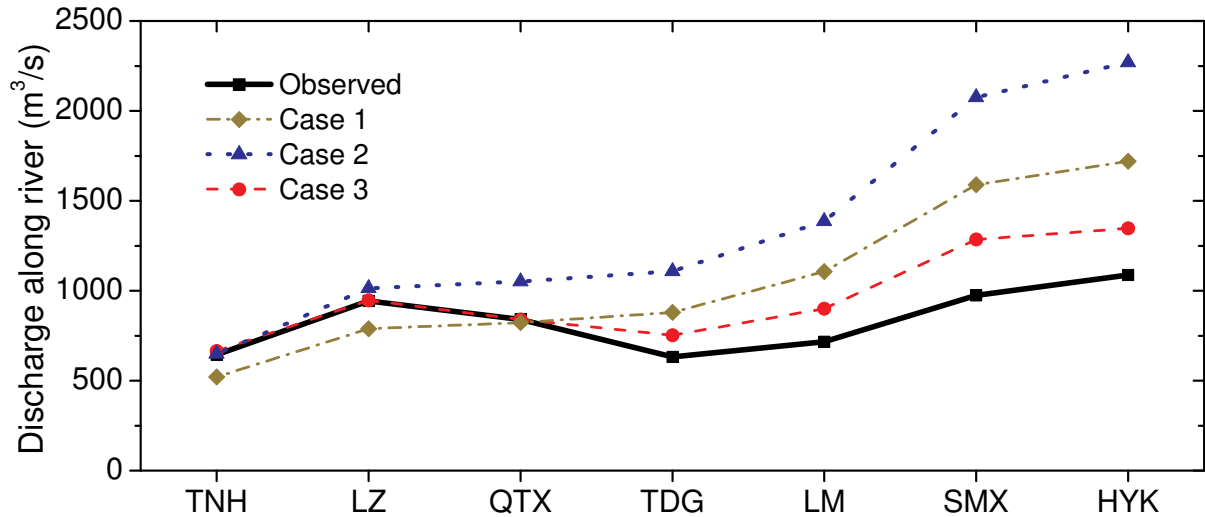


Figure 5.10: Effects of natural and anthropogenic heterogeneities on annual stream flow along the Yellow River from upstream to downstream.

rigation fractions. Within the simulation period, evaporation increased 25 mm year^{-1} because of irrigation in the Yellow River basin. Runoff spatial differences between simulated evaporation with and without the irrigation scheme are shown in Figure 5.11d. Total runoff decreased because of irrigation; however, larger runoff occurred in the grid cells in irrigation districts because flood irrigation becomes return flow and contributes to runoff. Note that all the values in Figure 5.11 are mean values over their respective grid cells and would have been much larger if reported as values per unit irrigated area.

Figure 5.12a shows the simulated surface soil wetness (soil moisture to saturated soil moisture) at the top 2-cm soil layer from the ground surface without the irrigation scheme in the Yellow River basin. The surface soil wetness was lower in the upstream area of the river basin where the annual precipitation was small. The surface soil wetness was higher in the lower stream area, which has a semi-humid climate. Figure 5.12b shows how simulated surface soil wetness changed with the irrigation scheme. The surface soil wetness increased because of irrigation water withdrawals, especially in the irrigation districts and high-irrigation areas. Over the Yellow River basin and the study period, the surface soil wetness increased 5.6% because of irrigation. The surface soil wetness increased 11.2% in the grid cells of the irrigation districts and also increased 11.1% in the grid cells where the irrigation fraction was larger than 30%.

The average change in the latent heat flux in the Yellow River basin due to irrigation was 2.0 W m^{-2} , or 7.8%, from 1983 to 2000. The latent heat flux increased more in the peak irrigation season from June to August (JJA). The averaged latent heat flux change for the basin

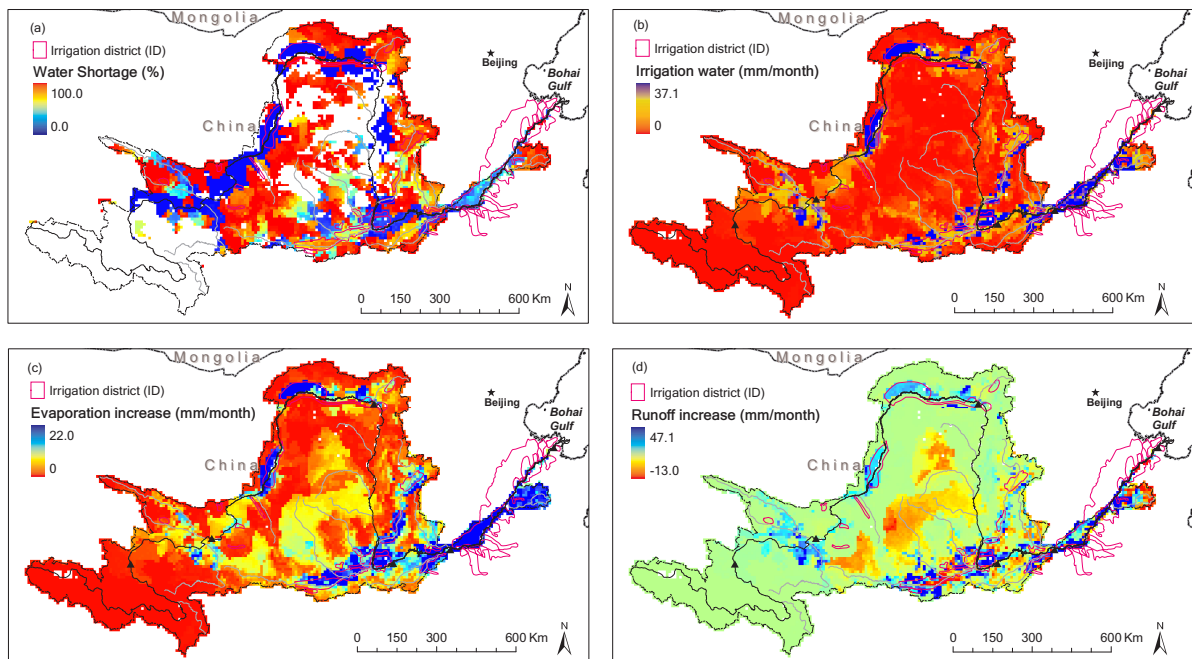


Figure 5.11: Spatial effects of irrigation on water balance components in the Yellow River basin; (a) water shortage in a grid cell with an irrigated area, (b) irrigation water withdrawal, (c) evaporation change, (d) runoff change.

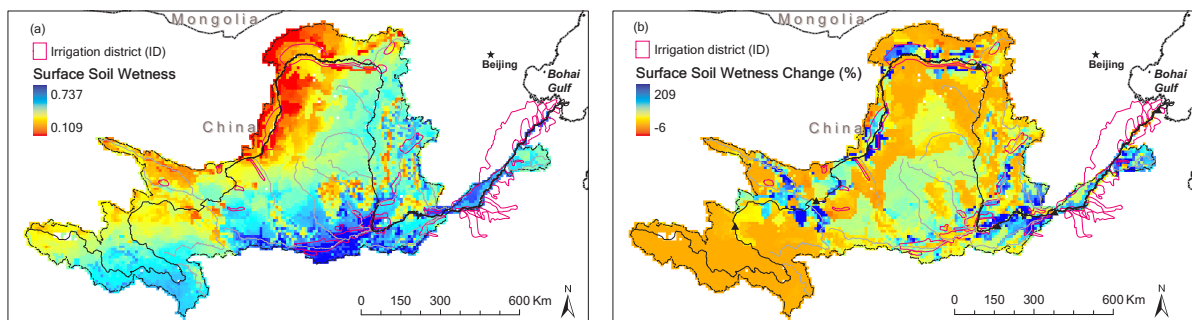


Figure 5.12: Simulated surface soil wetness (top 2 cm) without irrigation in the Yellow River basin (a), and simulated surface soil wetness change (%) with irrigation (b).

was 3.3 W m^{-2} in JJA. Figure 5.13 shows the peak irrigation season changes in ground surface temperature, canopy temperature, latent heat flux, and sensible heat flux for each grid cell in the Yellow River basin. The ground surface temperature and canopy temperature decreased because of irrigation. The latent heat flux (or evapotranspiration) increased when irrigation was taken into account, while sensible heat flux decreased with irrigation. Again, the largest effects can be seen in cells of the irrigation districts or for areas with a high percentage of irrigation by area, i.e., the middle and lower reaches of the Yellow River.

Table 5.4 shows the changes in energy components averaged over the river basin, the grid cells in the irrigation districts, and the grid cells where the irrigation fraction was larger than 30%. Decreases of ground surface temperature and canopy temperature were small over the basin, having values of 0.1 K and 0.06 K, respectively. However, averaged over irrigation districts, irrigation caused ground surface temperature and canopy temperature to decrease by 0.32 K and 0.23 K, respectively. The ground surface temperature and canopy temperature decreased 0.4 K and 0.31 K, respectively, over the grid cells where the irrigation fraction was larger than 30%. The maximum change in ground surface temperature and canopy temperature is shown in a grid cell with an irrigation fraction of 65.5%, where the ground surface temperature and canopy temperature decreased 1.6 K and 1.2 K, respectively. The latent heat flux increases over the grid cells in the irrigation districts and in the grid cells with greater than 30% irrigated area were 11.2 W m^{-2} and 15.5 W m^{-2} , or 3.5 and 4.8 times the average increase over the basin. The maximum change in latent heat flux reached 43.3 W m^{-2} , or 13.3 times the mean value. The sensible heat flux decreases over the grid cells in the irrigation districts and the grid cells with greater than 30% irrigated area were 7.7 W m^{-2} and 10.2 W m^{-2} , or 3.1 and 4.1 times the average decrease over the basin. The maximum change in sensible heat flux reached 37.8 W m^{-2} , or 15.1 times of the mean value. These results indicate that irrigation causes lower surface temperatures, higher evapotranspiration, larger latent heat flux, and smaller sensible heat flux in the Yellow River basin. The lower surface temperatures and higher evapotranspiration resulting from human activities imply that the near-surface atmosphere will be cooler and moister over irrigated areas than over nonirrigated areas.

5.7 Discussions

We evaluated the effects of natural and anthropogenic heterogeneity on hydrological simulation using a distributed biosphere-hydrological (DBH) model system. The model system is a continuous-time spatially distributed model, integrating hydrological processes and vegetation-

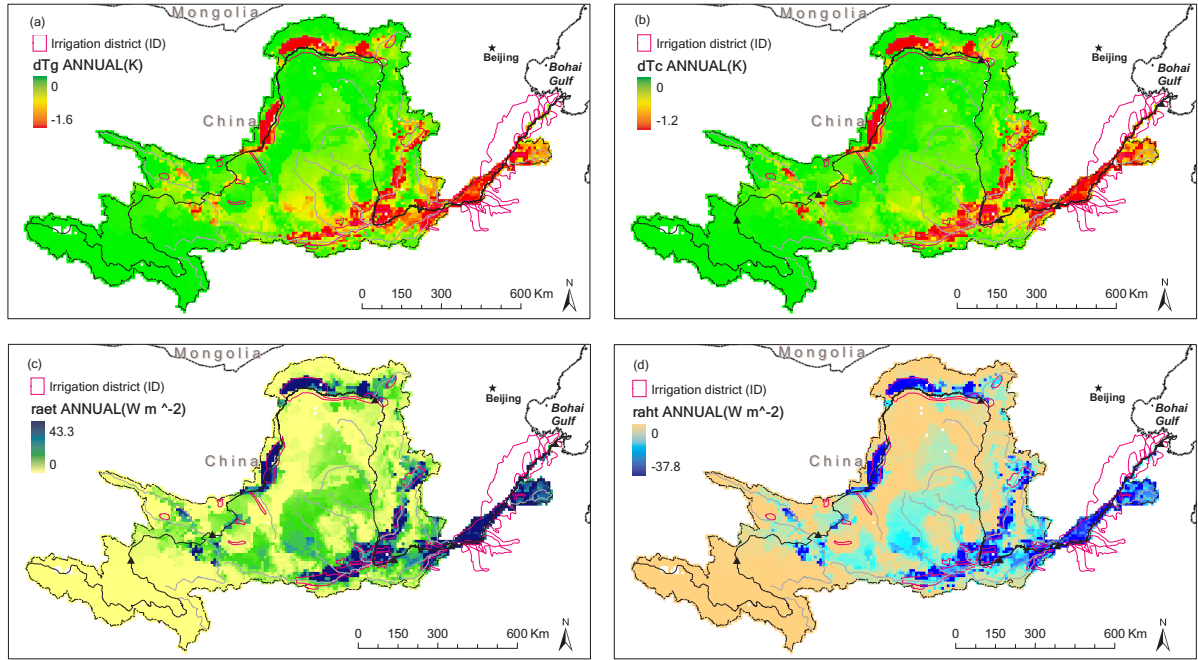


Figure 5.13: Spatial effects of irrigation on energy balance components (a) changes in ground surface temperature dT_g , (b) changes in canopy temperature dT_c , (c) changes in latent heat fluxes $raet$, and (d) changes in sensible heat fluxes $raht$ in the peak irrigation season (JJA).

Table 5.4: Changes in energy components in peak irrigation season JJA

Item	Avg.	ID ^a	IF ^b	Max.	Min.
Ground surface temperature dT_g (K)	-0.1	-0.32	-0.4	0.0	-1.6
Canopy temperature dT_c (K)	-0.06	-0.23	-0.31	0.0	-1.2
Latent heat fluxes $raet$ ($W m^{-2}$)	3.3	11.2	15.5	43.3	0.0
Sensible heat fluxes $raht$ ($W m^{-2}$)	-2.5	-7.7	-10.2	0.0	-37.8

^aAveraged for the irrigation district grid cells.

^bAveraged for grid cells in which the irrigation fraction is larger than 30%.

atmosphere transfer processes at the river basin scale. It represents the roles of topography, land cover characteristics and human activities in the hydrological cycle with the use of spatially distributed parameters of elevation, land use, land cover, and vegetation condition derived from satellite data, atmospheric forcing from ground observation network, and statistical soil properties and irrigated area from surveys.

The DBH model system was used to physically model the relationships of evaporation water demand, soil moisture deficit, and water availability. Precipitation variability was used to evaluate the effect of natural heterogeneity in the hydrological cycle. Runoff simulation could be improved by taking precipitation heterogeneity into account. However, the negative runoff contribution in the semi-arid region could only be simulated by considering anthropogenic heterogeneity. Tang (2003, 2006), Hu et al. (2004), Tang et al. (2004), and Tang et al. (2006a,b) reported the negative runoff contribution by human activities in a hyper-arid area in Central Asia. The DBH model system can physically simulate the phenomenon and promote the understanding on hydrological regime in arid area. Irrigation water withdrawals were estimated based on the model-predicted soil moisture. The irrigation water was considered to be withdrawn from the river, and no reservoir was included. Because a reservoir could store water for irrigation purposes, the irrigation water withdrawals may have been underestimated. The irrigation scheme gave priority to the upstream area. That is, upstream areas could extract river water without considering the needs of downstream areas. This does not agree with the integrated water management in the Yellow River basin, which is based on water allocation rules along the river main stem. The irrigation scheme assumed that irrigation water was extracted from the river and used for crops. The direct use of groundwater was not considered because of data unavailability. Localized water use and water waste such as water consumption from an endoric lake were also not taken into account. However, our results indicate that the method yields a reasonable approximation of the overall impact of irrigation in terms of the behavior of the hydrological system.

As this study has shown, both natural and anthropogenic heterogeneities are important factors in hydrological simulations. Precipitation variability and anthropogenic irrigation affect large-scale distributed hydrological patterns in different ways. Runoff, especially surface runoff, will increase over the whole river basin when considering the precipitation variability within grid cells. Anthropogenic heterogeneity caused by irrigation processes will increase evaporation and possibly induce negative runoff in intensively cultivated areas. The effects of anthropogenic heterogeneity are localized, centralized, and related to the intensity of human activities.

5.8 Summary

In this chapter, the DBH model system is evaluated with applications. Validation of DBH model with the daily time step is an advantage in comparison with other distributed hydrological models for macro scale basins, which are usually validated only with monthly and annual time steps. The flood peak can be reproduced and validated using the DBH model system. Then, the DBH model system is used to investigate the effects of natural and anthropogenic heterogeneities in hydrological simulation has been described. The Yellow River basin of China was selected as the study area because of the various climatic, topographic conditions and intensive human activities in the basin. The precipitation variability and partial irrigation within grid cells were used to demonstrate the effects of natural and anthropogenic heterogeneities in the hydrological cycle, respectively. The river flow pattern, i.e. discharge along river main stem, was used to observe the effects. The water and energy components effects by irrigation are presented. The results show both precipitation variability and anthropogenic irrigation affect hydrological patterns. Surface runoff will increase with considerations of precipitation variability. Evaporation will increase because of irrigation. The effects of anthropogenic irrigation are related to the intensity of irrigation.

Chapter 6

Long Term Change of Hydrological Cycles in the Yellow River Basin

6.1 Introduction

The Yellow River, regarded as the "Mother River of China", is the main surface water source of northwest and north China. There were 107 million residents and 12.6 million hectares cultivated land in the watershed, representing 8.6% and 13.3% of the national total, respectively (Yellow River Commission, 1999). It originates in the northern foothills of the Tibetan Plateau and empties into the Bohai Bay. The river length is 5464 km with a basin area of 752,443 km². The watershed area is as large as 794,712 km² if the endoric inner flow area is included. Most of the basin's area is arid or semi-arid.

The upper reach of the Yellow River drains over half of the total basin area and extends from the river's origin to the Hekouzhen gauging station. The middle reach, covering 46 percent of basin area and providing an additional 43 percent of the total runoff, begins at the Hekouzhen gauging station. From there the river begins its "great bend" to the south into and through the Loess Plateau. The lower reach of the Yellow River starts at Huayuankou station and forms one of the most unique river segments in the world. The sediment transported from the middle reach begins to settle as the river spills onto the flat North China Plain, producing a consistently aggrading bed and a naturally meandering and unstable channel. In the lower reach, the runoff into the river channel is small because the elevation of the riverbed is higher than the land surface behind artificial levees. In addition, there are large irrigation districts in the lower reach, which are located outside the watershed and channeled river water (Fu et al., 2004; Chen et al., 2002).

Since the completion of a large irrigation project in 1969, the lower Yellow River has increasingly suffered from the phenomenon of drying up. The drying up phenomenon, i.e., zero-flow in sections of the river channel, has occurred more and more often during the last 30 years. The duration of the drying up in the main course and the zero-flow distance from the river mouth increased rapidly in the 1990s. Moreover, the flow in the primary tributaries in the middle reaches of the river also dried up subsequently (Liu and Zheng, 2004). The Yellow River drying up has been a hot topic in hydrology study in China, attracting focus from many researchers.

Many researches were done to analysis the monthly or annual river flow observations and check the statistical relationship between river flow and climatic observation or measured data related to human activities. Fu et al. (2004) and Yang et al. (2004a) analyzed the hydro-climatic data trends of the Yellow River basin for the last several decades. They found the trend for precipitation was not significant while runoff has decreased. The river basin has become increasingly warmer. They suggested land use, land cover change, including agricultural activities, deforestation/forestation, urbanization, mining industry are major factors resulting the observed runoff reduction. Xia et al. (2004) checked river section water balance with an observed data set and developed a renewability indicator (α) to assess the water renewability in the Yellow River basin. The analysis showed that the renewability of water resources in the Yellow river had a significant declining trend since the 1950s. In the 1990s, the renewability indicator in the downstream reach was reduced to the worst situation. Xu (2005a) proposed a quantitative index (I_{rr}) of river flow renewability based annual measured river flow and discussed the influencing factors with a drainage area in the middle reach region of the Yellow River. They found the annual natural river flow decrease in the last half century. The river flow renewability in the study area has been found to decline significantly with time. The river flow renewability index was positively correlated to the annual precipitation, and negatively correlated to the annual air temperature. There is close, negative correlation between I_{rr} and area of soil and water conservation measures. Liu and Zheng (2004) detect trends associated with hydrological cycle components by analyzing the monthly precipitation and river discharge observations in an upper reach station and a lower reach station. They found there was only surface runoff decreasing trend in the upper reach station and there were significant decreasing trends in natural runoff, surface runoff and groundwater runoff. They suggested that increasing water resources development and utilization is the most important factor in causing the frequent drying up in the main course of the Yellow River. Xu (2005b) used a multiple regression equation to estimate the change in water fluxes to the sea caused by the changes in precipitation, air

temperature, water diversion and consumption, erosion, and sediment control measures based on annual data. They showed the contribution of water diversion and consumption to the variation in annual water flux to the sea is 41.3%, that of precipitation is 40.8%, that of temperature is 11.4%, and that of erosion and sediment control measures is 6.5%. Liu et al. (2003) estimated renewal times for several reaches in the middle and lower sections of the Yellow River basin based on observed stream flow data from the 1990s. They found the renewal times are shortest during the May-October period and annual renewal times tend to decrease from the middle to lower reaches. Huang and Zhang (2004) investigated the hydrological responses to soil conservation practices based on the observed river discharge in a tributary catchment of the Yellow River basin. They found a clear decreasing trend in annual surface runoff and baseflow volume because of conservation measures. Seasonal runoff also showed a decreasing trend with the greatest runoff reduction occurring in summer and minimum reduction in winter. Chen and Mu (2000) considered the large amount of water use for sand transport in the Yellow River and reported that the runoff reduction is much less significant than the sand reduction caused by soil conservation. Chen and Mu (2000) concluded that the soil conservation could slacken the river drying up because the save water in the sand transport water use.

Several studies were performed to investigate the land use/land cover change in the Yellow river basin. Wang et al. (2001) presented eco-environmental degradation and causal analysis in the source region of the Yellow River. Feng et al. (2005) provided the classification and evaluation information of the land degradation in the source region of the Yellow River. Sun et al. (2001) analyzed the relationship between the fractional vegetation cover change and rainfall in the Yellow River Basin with Pathfinder NOAANDVI data set. Yang et al. (2002) detected vegetation cover change over last 20 years in the Yellow River Basin.

Some researches analyzed the human and natural factors responsible for the Yellow River drying up phenomenon and suggested some countermeasures to mitigate the phenomenon. Liu and Zhang (2002) analyzed the hydro-climatic data and statistical data related to human activities and concluded that: the natural water resource shortage and its uneven distribution played a important role in the drying up; water development along the river course is the main direct reason of the drying up; the limited ability to regulate flows and lack of unified control and management of hydraulic engineering projects are the reasons that caused the drying up. Liu and Zhang (2004) showed the contribution of climate change, human activities to the actual water flow reduction in the upper reaches is 75% and 25%, respectively. The contribution of climate change, human activities to the actual water flow reduction in the middle reaches is 43% and 57%, respectively. Chen and Mu (2000) concluded the major reason for drying up is

water diversion increase in middle and lower reaches. And the second reason is the serious soil loss in the middle reaches requiring large amount of water to carrying sediment.

Although there are many studies that target on the Yellow River basin and analyze the statistical relationship among hydro-climatic observations, few studies were performed to investigate the physical water cycle processes in the Yellow River basin. Yang et al. (2004b) attempted a distributed hydrological approach in the Yellow River basin. In the hydrological approach, evapotranspiration was simulated in an empirical way and the energy flux and human activity effects were no taken into account. Mo et al. (2004) presented a process-based distributed model to simulate the temporal and spatial variation of evapotranspiration in a tributary basin in the middle reach of the Yellow River. They coupled energy and water flux in the Soil-Vegetation-Atmosphere Transfer (SVAT) processes and compared the estimated evapotranspiration with precipitation minus discharge at the outlet. However, the topography and river routing were not considered in the study. Some researches, such as Russell and Miller (1990) and Nijssen et al. (2001), used Macroscale Hydrological Models (MHMs) to link global atmospheric models and water resource systems on large spatial scales and long timescales. The energy exchange at the atmosphere-land surface interface is usually based on physical principles, while the runoff generation mechanisms tend to be more conceptual in most MHMs. The global simulations could provide a dataset of runoff estimates and accompanying components of the land surface hydrological cycle, such as evapotranspiration, soil moisture storage in the Yellow River basin. The MHMs did not consider the human activities and was usually validated at the river mouth. The spatial resolution is too coarse for water management purpose. The vertical and lateral water fluxes should be coupled to represent the connections among hydrological components in a fine resolution. In order to describe the dynamic mechanisms of the water cycle, study is urgently needed on the Soil-Vegetation-Atmosphere Transfer, runoff generating and absorbing processes in the large basin scale. The coupled study of energy and water transfer processes will improve the understanding of the physical mechanisms between climate change, human activities and the hydrological pattern in the continental scale river basin. That will give a scientific base to interpret the Yellow River drying up phenomenon. Liu et al. (2001) summarized the research on the mechanism of hydrological cycle in the Yellow River basin and pointed out the scarcity of study on physically-based hydrological simulation with the use of remote sensing data and ground observations.

In this study, we used a distributed hydrological model which couple SVAT, runoff generating and absorbing processes, and human activities into one comprehensive hydrological model system to analysis the physical connections between climatic, vegetation condition change and

hydrological cycle change in the Yellow river basin. First, we briefly introduce the distributed biosphere-hydrological (DBH) model system and the data preparation for the model simulation. Then, the methodology to represent physical connections between climate, vegetation condition change and hydrological cycle change is described. The climate, vegetation change tendency and the corresponding hydrology change is shown to analysis the reasons for the Yellow River drying up phenomenon.

6.2 Data and Methodology

6.2.1 Data Analysis

The hydro-climatic data is obtained from the China Meteorological Administration (CMA) and the Hydrological Bureau of the Ministry of Water Resources of China (Information Center of Water Resources, 1950-1990). The data set includes daily precipitation, mean temperature, maximum and minimum temperatures, mean surface relative humidity, sunshine duration, cloud amount, and river discharge from 1960 to 2000. The vegetation condition index leaf area index (LAI) was obtained from Myneni et al. (1997). The LAI data set is available with monthly temporal frequency and 16×16 km spatial resolution from 1982 to 2000. The hydro-climatic and vegetation condition change in the Yellow River basin was detected and documented in Section 3.3.

6.2.2 Methodology

The distributed biosphere-hydrological (DBH) model is used to represent physical connections between climate, vegetation condition and hydrological cycle. The DBH model embeds a biosphere model into a distributed hydrological scheme, representing both topography and vegetation conditions in a mesoscale hydrological simulation (Tang et al., 2006). In the DBH model, Multidisciplinary developments in geophysical science are used to prompt a radical improvement of hydrological simulation. These geophysical advances include the new insights into heat flux in the Soil-Vegetation-Atmosphere Transformation (SVAT) processes by meteorologists, progress in getting reliable land surface information from satellite by remote sensing scientists, and developments of Geographic Information System (GIS) technique to extract topographic variables from Digital Elevation Model (DEM). A irrigation scheme is incorporated in the DBH model to estimated human activity effects on the hydrological cycle using the Global Map of Irrigated Areas (Siebert et al., 2005). The observed climate data give a control simulation in the Yellow River basin from 1960 to 2000. The vegetation parameters before 1980s are un-

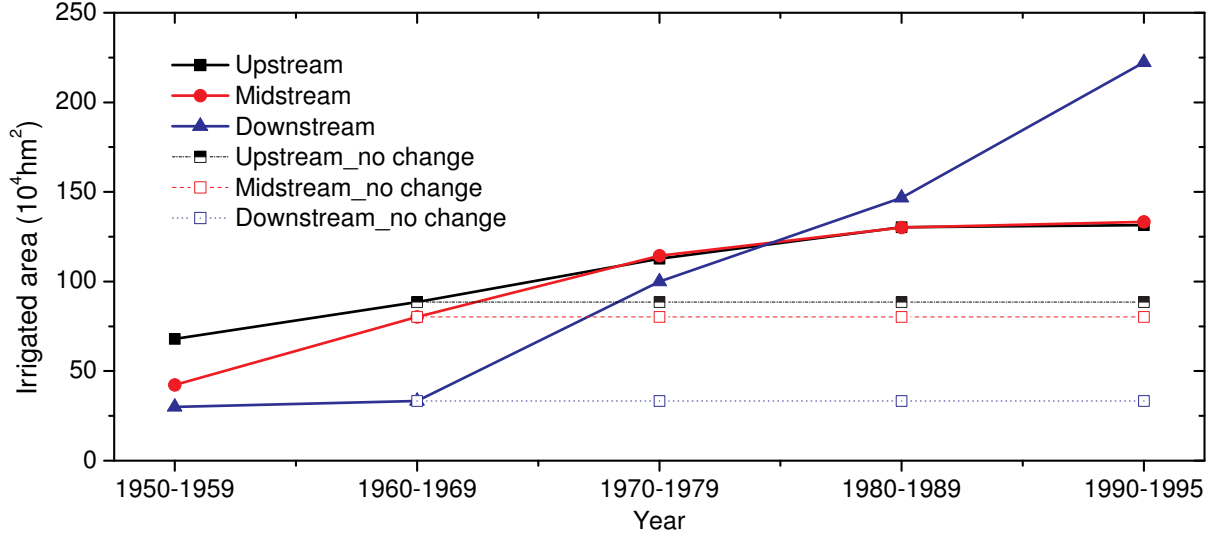


Figure 6.1: Irrigated area in the Yellow River basin.

available from satellite dataset and use the data in 1982. The irrigated area from the Global Map of Irrigated Areas is based on the investigation in 1990s. The total irrigated area in the entire river basin from the 1960s is available from literatures (Liu and Zhang, 2002; Yang et al., 2004a; Xia et al., 2004) and distribution of the irrigated area is estimated from the Global Map of Irrigated Areas with geometric proportion scale method. Figure 6.1 shows the irrigated area in the Yellow River basin.

Several scenarios are performed with the DBH model system to evaluate effects of climate, vegetation change and human activity on hydrology cycle. The observed climate, vegetation condition and irrigated area data shows strong change tendency in specific region of the river basin. The non-climate change, non-vegetation change and non-irrigation change scenarios are shown to investigate the effects of climate change, vegetation change and irrigated area change to hydrological cycle in the Yellow River basin. The linear trend is removed from the forcing data set to simulate non change scenarios. The time series data without tendency is

$$Y'_i = Y_i - (mX_i + b) + \bar{Y} \quad (6.1)$$

where \bar{Y} is expected mean value, m and b is the linear least squares regression slope and interception, X_i is time number, Y_i is the time series data before removing tendency, and Y'_i is the time series data after removing tendency. The remove trend method is detailedly documented in Appendix C.4.2. The climate data before and after remove tendency are shown in figure 6.2. The climate conditions in the 1960s are used as the reference conditions, i.e., the

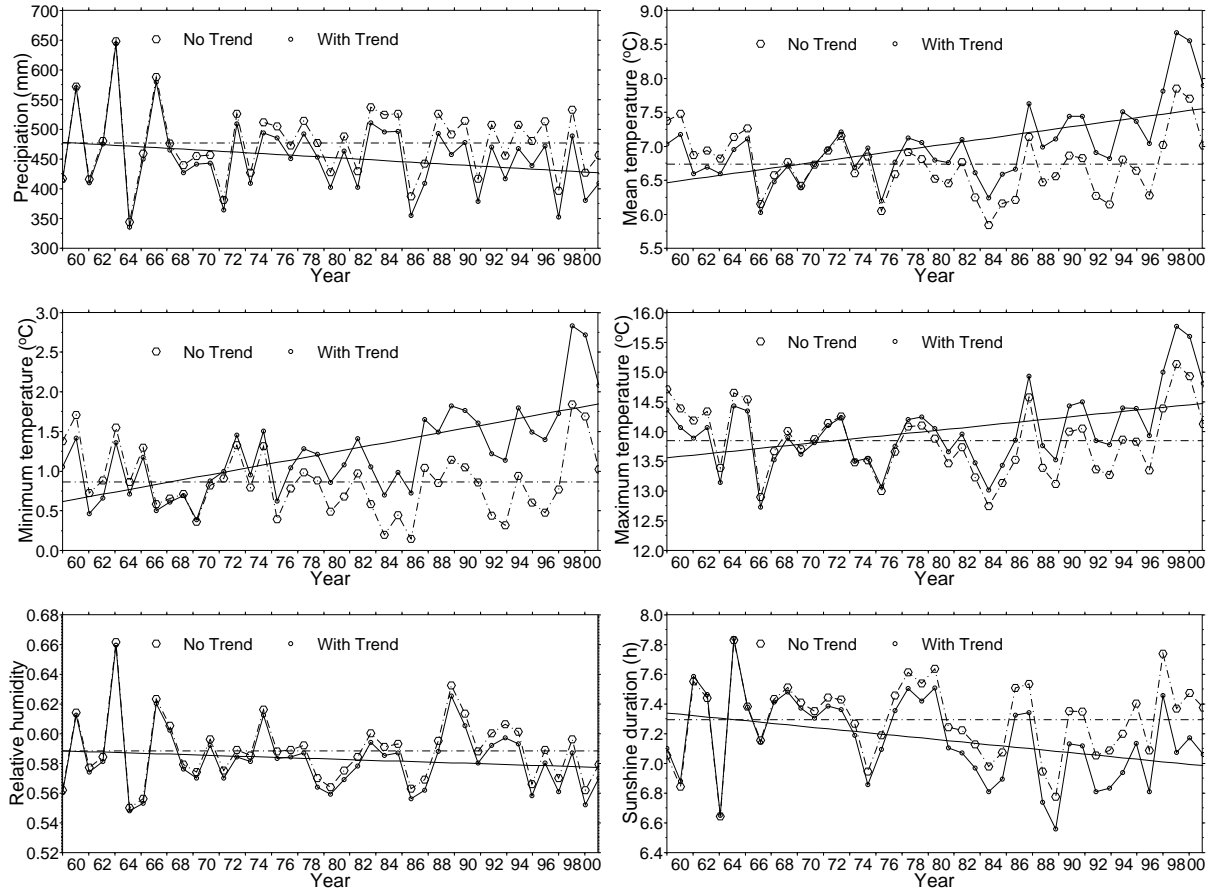


Figure 6.2: Climate data with and without linear tendency.

mean values of the data without tendency equal to the mean values in the 1960s before removing tendency. The irrigated area in the 1960s is used in the non-irrigation change scenarios (Figure 6.1). The vegetation data (LAI and FPAR) are available only from the 1980s. The data is linearly extended to the 1960s. Since the vegetation change is a slowly process, the linear extension is thought to be suited. The vegetation data with and without tendency are shown in figure 6.3.

The scenarios are 1) S1, control simulation with most realistic climate, vegetation condition and irrigated area data, 2) S2, non-climate change simulation using the climate data without linear trend, 3) S3, non-vegetation change simulation using the vegetation data without linear trend, 4) S4, non-irrigation change simulation using the irrigated area data without linear trend, 5) S5, stable simulation using the climate, vegetation conditions, and irrigated area data of the 1960s without linear trend, 6) and S6, stable simulation with climate conditions repeating the data in the 1960s. The difference between S5 and S6 is to investigate the effects of climate pattern, not the linear tendency to the hydrological components. With the DBH model system, the contributions of the climate change, vegetation condition change, and

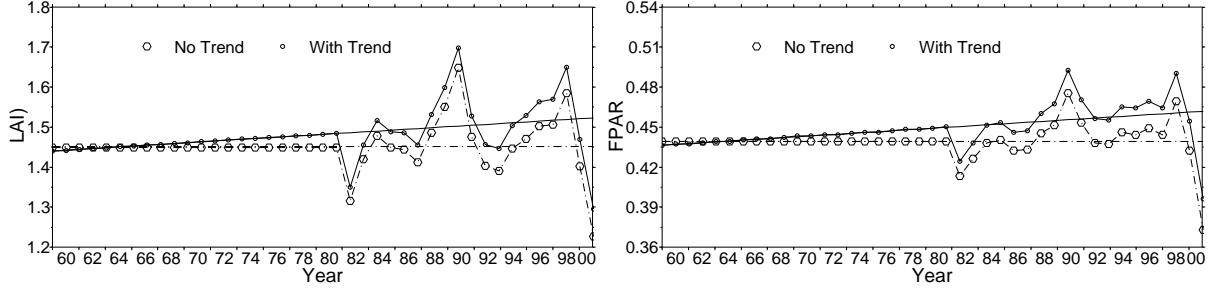


Figure 6.3: Vegetation data extension and the data with/without linear tendency.

irrigated area change to hydrological cycle change are investigated.

Based on the simulated results, the linear regression model was used to analyze the trend magnitude of simulated hydrological components. The regression weight was calculated as:

$$\beta = \frac{n \sum_{i=1}^n t_i y_i - \sum_{i=1}^n t_i \sum_{i=1}^n y_i}{n \sum_{i=1}^n (t_i)^2 - (\sum_{i=1}^n t_i)^2} \quad (6.2)$$

where n is the time series number, t_i is the time number, and y_i is the data value at the time t_i . The trend magnitude during the study period was then estimated from the regression weight:

$$\Delta Y = \beta \cdot T \quad (6.3)$$

where T is the span of time during the study period.

The effects of climate, vegetation, irrigation and all these changes to simulated hydrological components are describe with the linear regression model. The contribution of climate, vegetation, irrigation and all these change is calculated as:

$$\Delta Y_k = \frac{n \sum_{i=1}^n t_i (y_i^1 - y_i^k) - \sum_{i=1}^n t_i \sum_{i=1}^n (y_i^1 - y_i^k)}{n \sum_{i=1}^n (t_i)^2 - (\sum_{i=1}^n t_i)^2} \cdot T \quad (6.4)$$

where $k = 2, 3, 4, 5, 6$ denotes the time series related to S2, S3, S4, S5, S6, y_i^1 is the time series results of control simulation S1. The difference between S5 and S6 is used to estimate the change magnitude of the simulated hydrological components caused by the climate pattern.

6.3 Results and Analysis

Figure 6.4 shows the observed and simulated discharge in S1, control simulation at main stem gauges from 1960 to 2000. In most of the gauges, the simulated discharge agree with observed one well, with BIAS less than 10% and MSSS larger than 0.5. The river discharge shows large decreasing trend, especially at the lower reach gauges such as Sanmenxia, Huanyuankou and Lijin. Sharp decrease is observed at the Lijin gauge, implying the strong runoff absorbing between Huanyuankou and Lijin gauge.

The reported and simulated water withdrawals in S1, control simulation from 1960 to 2000 at upper, middle, and lower reaches of the Yellow River are shown in figure 6.5. The water withdrawals are well reproduced by the control simulation. Both reported and simulated water withdrawals show that the water withdrawals in upper and middle reaches have small change during the study period. The water withdrawals in lower reaches increase nearly five times from the 1960s to the 1990s. This indicates the lower reaches water withdrawals have larger impact to the hydrological change in the Yellow River than that of the upper and middle reaches.

Figure 6.6 shows the runoff, evapotranspiration, water withdrawals and ground surface temperature change in the sub-basins of the Yellow River from 1960 to 2000 with S1, control simulation. Runoff decreases over most part of the river basin. Large runoff decrease is detected over the Loess Plateau, corresponding to the precipitation decrease in that region. The simulated evapotranspiration also shows decreasing trend over the Loess Plateau. The decrease magnitude is in the same order of the runoff decrease. It suggests the decreasing precipitation over the Loess Plateau has made the hydrological cycle slow down in that region. Increase tendency of evapotranspiration was detected at the Qingtongxia-Hetao irrigation district, the middle reaches irrigation districts and lower reaches irrigation districts. The large evapotranspiration in lower irrigation districts indicate the human activities have alerted the hydrologic components in that region. The water withdrawals increase over most of the river basin. Largest increase of water withdrawals also occurs at the lower reaches. The ground surface temperature increases over the upper and middle reaches, corresponding to the warning of the river basin. The ground surface temperature increase over Tibetan Plateau and Qingtongxia-Hetao district may caused by the observed air temperature increase. The global warning has affected the regional climate, at least in these parts of the Yellow River basin. Large ground surface temperature also detected over the Loess Plateau. It implies the less precipitation and less evapotranspiration have caused the temperature increase over the Loess Plateau. Small increase of air temperature is detected in the low reaches and part of the middle

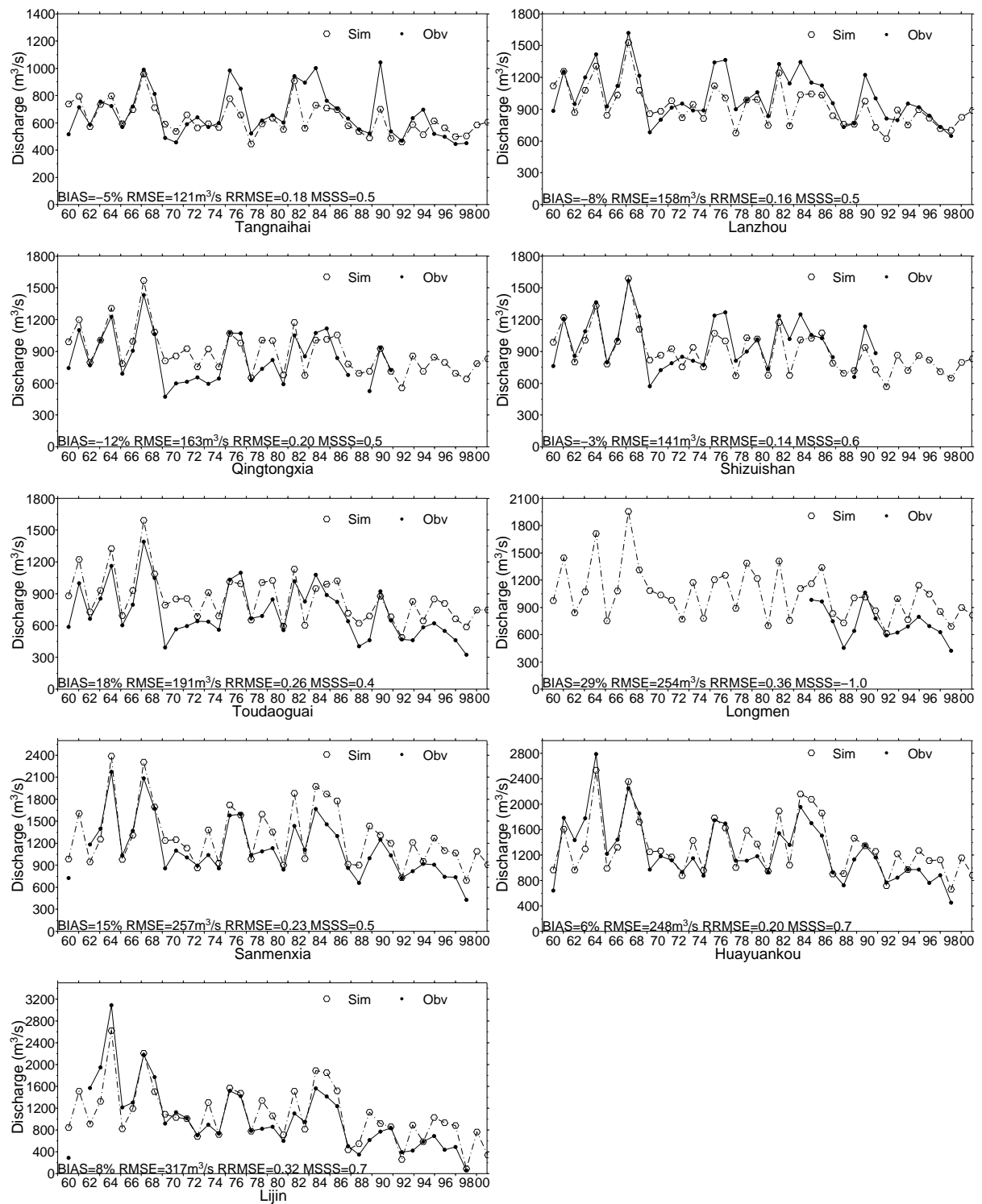


Figure 6.4: Observed and simulated discharge in S1, control simulation at main stem gauges.

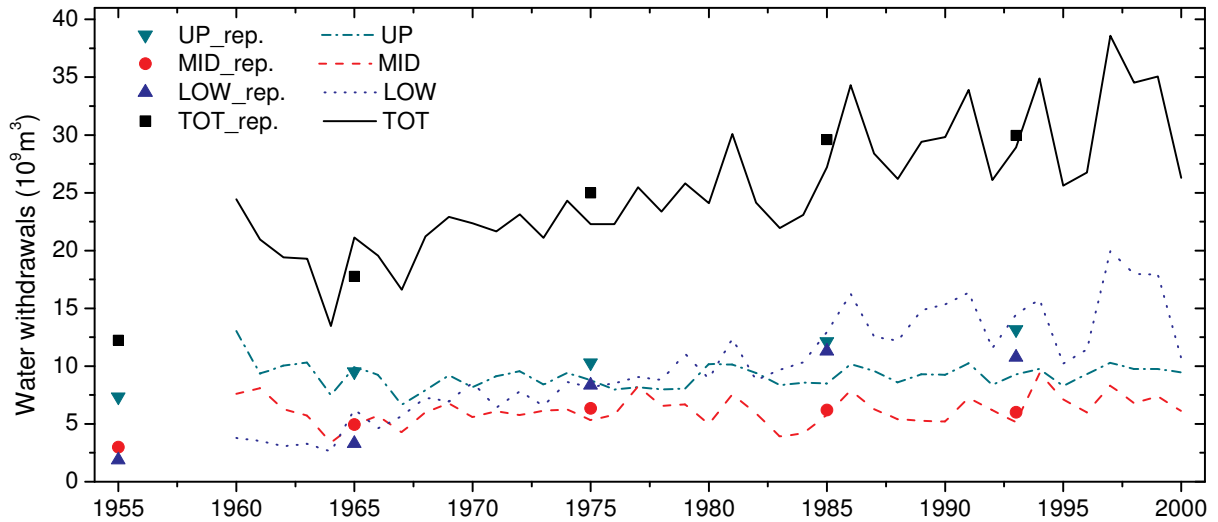


Figure 6.5: Reported and simulated water withdrawals in S1, control simulation at upper, middle, and lower reaches of the Yellow River.

reaches, but the simulated ground surface temperature gives decrease trend, implying the large water withdrawals has made more water be vaporized into atmosphere and cooled the ground in the low reaches. The hydrological components has alerted by many possible factors. The possible contributions of the alteration will be analyzed below with the scenario results.

The simulated sensible heating ($W s^{-2}$) and canopy assimilation flux ($10^{-8} mol m^{-2} s^{-1}$) are shown in figure 6.7. Decrease tendency of sensible heating flux is detected over the Qingtongxia-Hetao irrigation district, the middle reaches irrigation districts and lower reaches irrigation districts. Large sensible heating flux decrease at the lower reach irrigation districts, confirming the large water withdrawals cool the ground in the low reaches. Canopy assimilation rate decreases in the sub-basins without irrigation districts. Canopy assimilation rate increases at the sub-basins with large irrigation districts such as Qingtongxia-Hetao irrigation district, the middle reaches irrigation districts and lower reaches irrigation districts. Canopy assimilation rate alteration might be caused by the irrigation and vegetation recovery in irrigation districts and vegetation degradation outside of irrigation districts. Human activity is alerting the assimilation pattern of the Yellow River basin.

Figure 6.8 shows the climate linear change contribution to the alteration of the hydrological components in the Yellow River basin from 1960 to 2000. Runoff decreases over most part of the river basin, accompanying with the precipitation decrease pattern. Extensive runoff decrease according to climate change occurs over the Loess Plateau. The runoff decrease should respond to the precipitation decrease in that region. Runoff increases according to climate change in the lower reaches, implying the climate becomes wet in the North China Plain. As

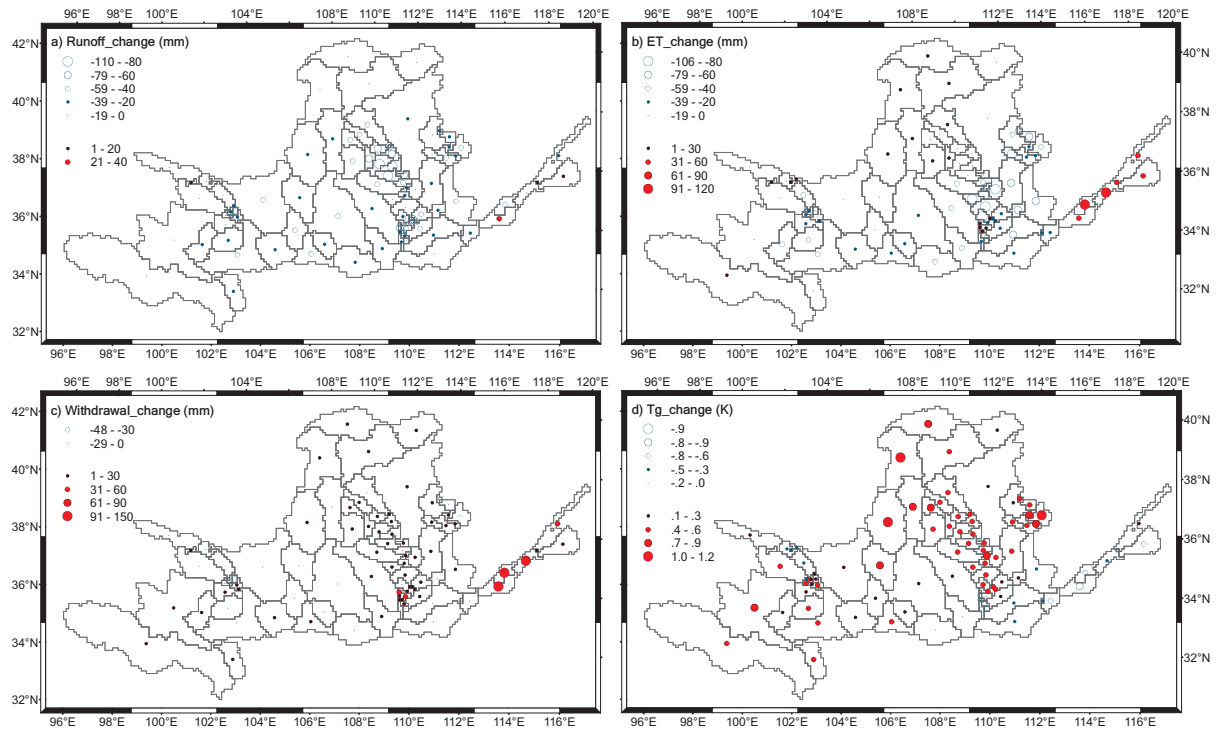


Figure 6.6: Simulated changes from 1960 to 2000 with S1, control simulation: a) Runoff change, b) Evapotranspiration change, c) Water withdrawals change, and d) Ground surface temperature change.

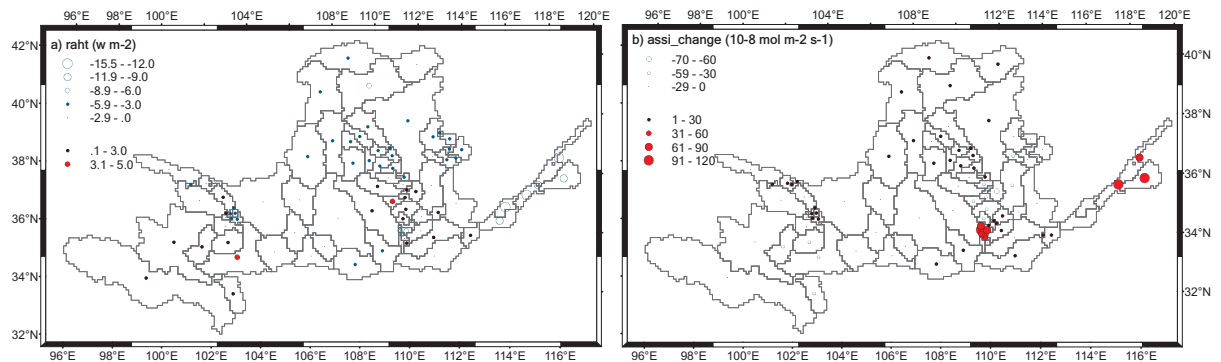


Figure 6.7: Simulated a) sensible heating and b) canopy assimilation flux changes from 1960 to 2000 with S1, control simulation.

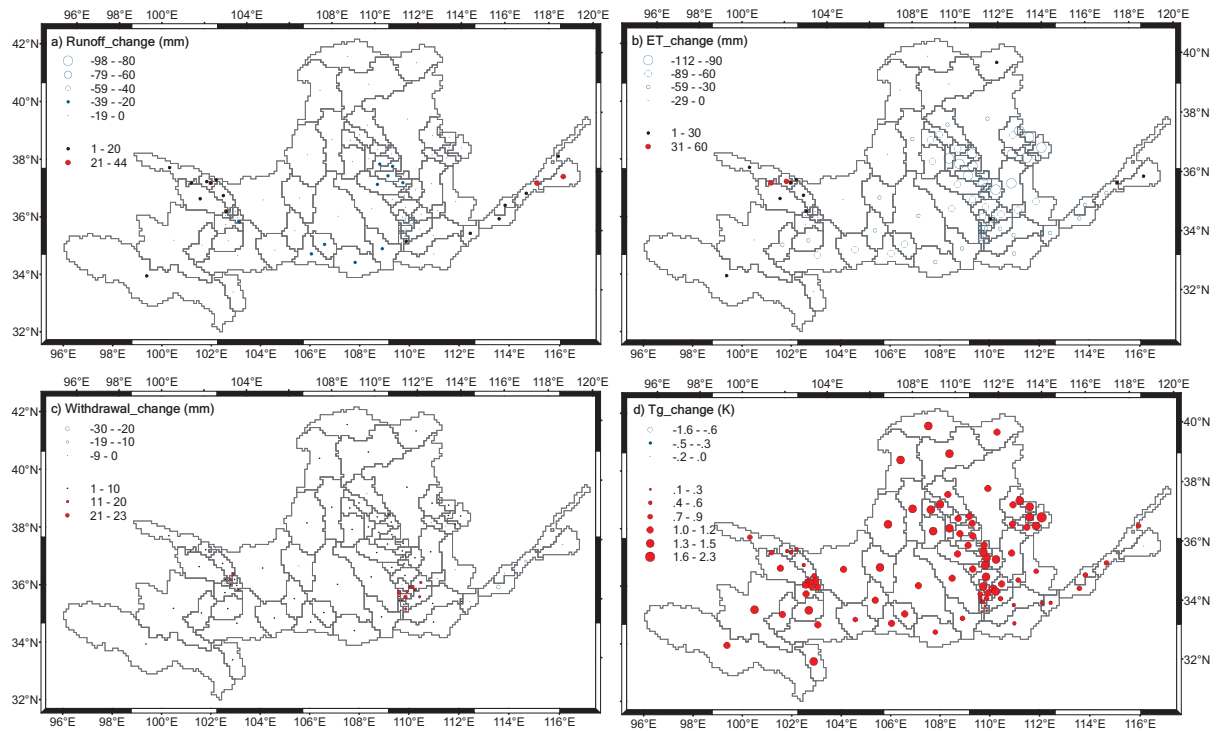


Figure 6.8: Simulated changes contributed from climate linear change: a) Runoff change, b) Evapotranspiration change, c) Water withdrawals change, and d) Ground surface temperature change.

climate changing, evapotranspiration decreases over most part of the river basin. Extensive evapotranspiration decrease occurs over the Loess Plateau, indicating less precipitation makes the soil moisture stress and decrease the evaporation. Because of the less precipitation, water withdrawals from river channel increase in the sub-basins with irrigation districts over the Loess Plateau. Water withdrawals decrease a little because of climate change, confirming the climate becomes wet in the North China Plain. Ground surface temperature increases with climate change over the entire river basin. The ground surface temperature change tendency is consistent with the observed air temperature increase over the river basin, indicating that the global warming is alerting regional climate.

Figure 6.9 gives the contribution of vegetation condition change to the alteration of the hydrological components in the Yellow River basin from 1960 to 2000. Runoff decreases over most part of the river basin. The runoff decrease is consistent with vegetation condition recovery over the whole basin. Large runoff decrease occurs in the sub-basin with irrigated area such as lower reaches irrigation districts. Evapotranspiration increases as the vegetation condition change. In the irrigated area where the vegetation condition recovers much, the evapotranspiration significantly increases. More irrigation water withdrawals is needed as the

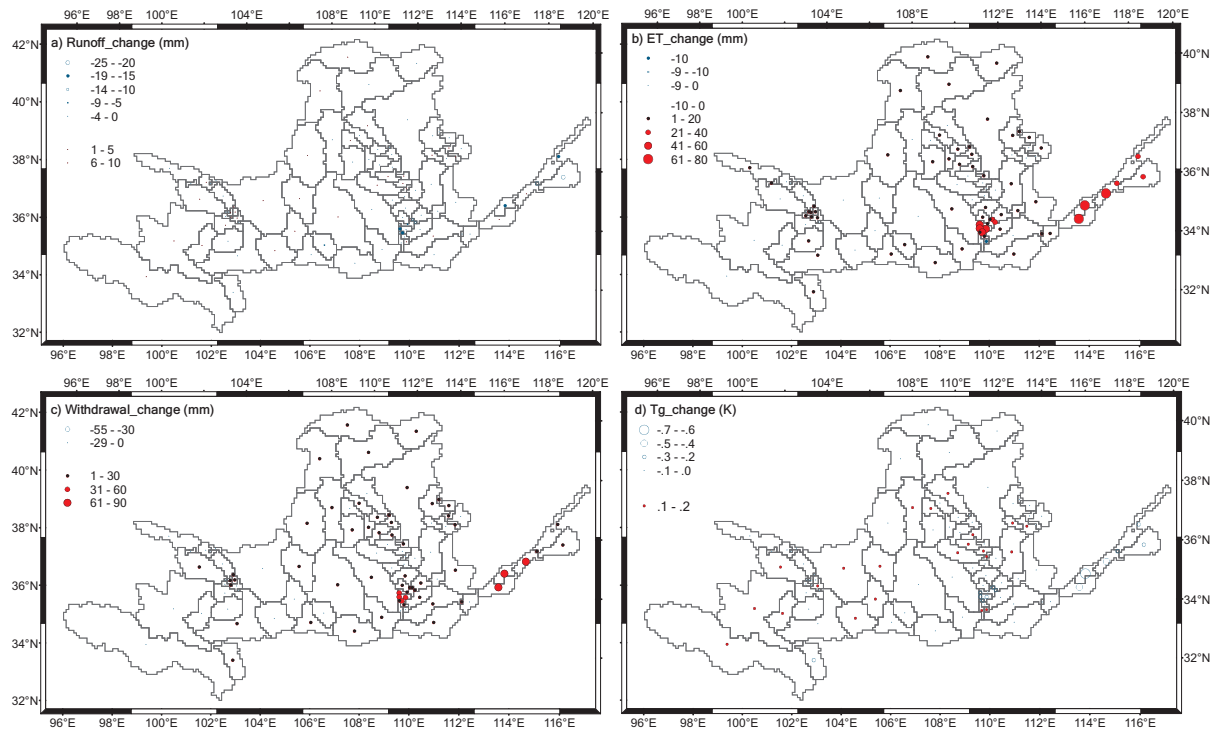


Figure 6.9: Simulated changes contributed from vegetation change: a) Runoff change, b) Evapotranspiration change, c) Water withdrawals change, and d) Ground surface temperature change.

total biosphere mass increase. The large increase of water withdrawals still occurs at the lower reach irrigation districts. The change of ground surface temperature is small responding to the vegetation condition alteration over the entire river basin. However, the ground surface temperature can decrease more than 0.5 K in the sub-basins with intensively cultivation.

The contributions of irrigation area change to the alteration of the hydrological components in the Yellow River basin from 1960 to 2000 are shown in figure 6.10. General, runoff increases, evapotranspiration increases, and irrigation water withdrawals increases with the same pattern in the river basin according to irrigated area increase. The runoff increase is because of the irrigation return flow will increase with more irrigation water withdrawals. The alterations of hydrological components are small in the upper and middle reaches as expected with smaller change of irrigated area. Larger changes occur in the lower reaches where the irrigated area in the 1990s is more than five times of that in the 1960s. The change of ground surface temperature is small responding to the irrigated area alteration over the entire river basin.

Figure 6.11 gives the total contributions of simulated changes, i.e. change of climate, vegetation, and irrigated area, to the hydrological components. The climate, vegetation and irrigated area change makes the runoff and evapotranspiration decreases over the Loess Plateau.

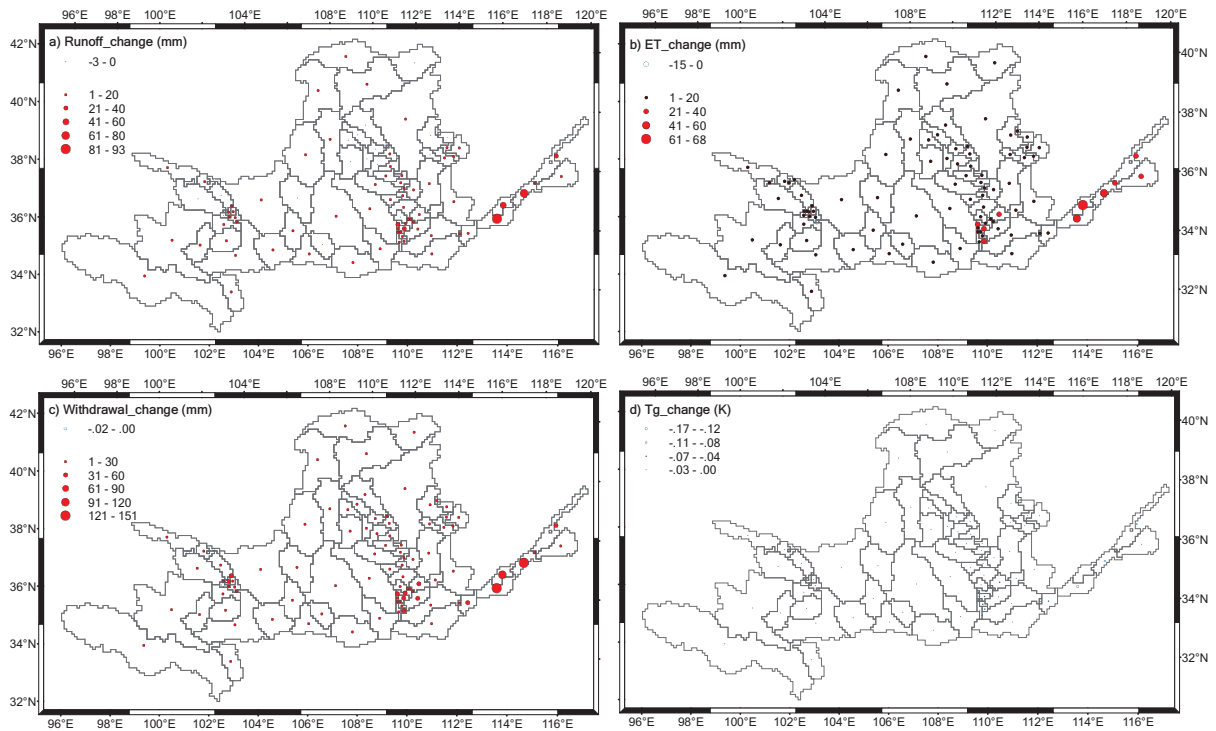


Figure 6.10: Simulated changes contributed from irrigation area change: a) Runoff change, b) Evapotranspiration change, c) Water withdrawals change, and d) Ground surface temperature change.

Comparing with figure 6.8 to figure 6.10, the contributions of climate change dominate the runoff and evapotranspiration change in the Loess Plateau. Runoff and evapotranspiration increases over Tibetan Plateau and low reaches North China Plain. The increases are contributed by both climate change and human activity. Water withdrawal has increased over the entire river basin. The changes of water withdrawals are mainly caused by the irrigated area increase and the accompanying vegetation condition increase. Climate change over the Loess Plateau makes more irrigation water withdrawals required. Ground surface temperature increases over most parts of the river basin. The changes of ground surface temperature are dominated by the climate change. An interesting phenomenon is found in the ground surface temperature in the lower reaches. On one aspect, climate change makes the ground temperature increases with the global warming; on the other aspect, human water withdrawals and vegetation recovery make the ground temperature decrease. The effects to ground temperature are canceled with the climate change and human activities in the low reaches. Comparing with figure 6.11 with figure 6.6, the contribution to runoff decrease from climate linear change, vegetation and irrigation change is less than the simulated runoff decrease in the control simulation over the Loess Plateau. The runoff decrease over the Loess Plateau is partly contributed by the climate

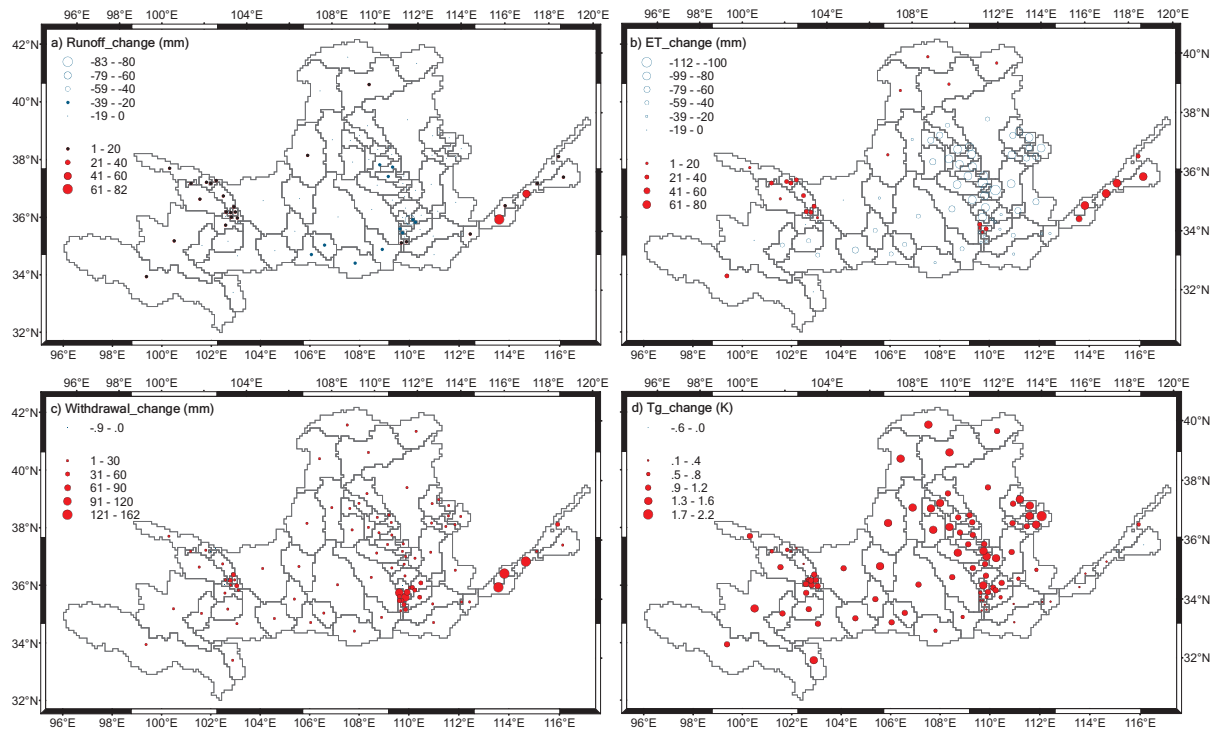


Figure 6.11: Simulated changes contributed from climate linear change, vegetation and irrigation change: a) Runoff change, b) Evapotranspiration change, c) Water withdrawals change, and d) Ground surface temperature change.

pattern change according to S6.

Table 6.1 shows the contributions to discharge change from climate linear change (C), vegetation change (V), irrigation change (I) and the climate pattern change (S6-S5). At the river mouth Lijin station, the control simulation shows nearly 1000 m³/s decrease during the study period. About 30% of the decrease is contributed by the climate pattern change and 70% is contributed by the linear changes of climate condition, vegetation and irrigation. Among the 70% contribution by linear changes, about 15% is contributed by the linear climate conditions change, 15% by the vegetation change, and 70% by the irrigation change. At the Huayuankou station, about half of the discharge decrease is caused by the climate pattern change and the other half is contributed by the linear changes. Among the half part of the contributions, about half is because of linear climate change, 10% is because of vegetation change and 40% is because of irrigation change. The different proportion shows the large irrigation change contribution between Huayuankou and Lijin station. The result agrees with the large water withdrawals at Huayuankou-Lijin section to the outside of the river basin. The vegetation change could be caused by both human activity and climate change. Taking into account of Huayuankou-Lijin section, the discharge decrease at Lijin station is mainly caused by the irrigation (about 50%),

Table 6.1: Simulation contributions of annual discharge change along river main stem (m^3/s)

Station	Obv.	S1	Climate (C)	Veg. (V)	Irr. (I)	C/V/I	S6-S5
Tangnaihai	-145	-181	0	4	-1	1	-76
Lanzhou	-324	-342	-19	6	-18	-30	-132
Qingtongxia	-133	-359	-30	5	-38	-60	-155
Shizuishan	-100	-358	-33	5	-39	-64	-160
Toudaoguai	-372	-377	-39	-9	-62	-100	-157
Longmen	-296	-452	-70	-17	-69	-144	-237
Sanmenxia	-733	-597	-166	-31	-94	-275	-343
Huayuankou	-895	-620	-170	-40	-113	-305	-356
Lijin	-1388	-959	-116	-116	-463	-668	-327

and the discharge decrease caused by direct irrigation is about 40% . Before the Huayuankou station, the discharge change is mainly caused by the climate change (about 75%), and the effects of direct irrigation is about 20%. The large linear climate change contribution occurs at the Toudaoguai-Sanmenxia section, where the Loess Plateau is, responding to the precipitation decrease in this region. Large climate pattern contributions are observed at the before Lanzhou section and the Toudaoguai-Sanmenxia section, suggesting that not only linear climate condition but also climate pattern has induced in the river drying up. Besides the lower reaches, larger irrigation contribution has found in the Tangnaihai-Qingtongxia section, Toudaoguai-Shizuishan section, and Longmen-Sanmenxia section, corresponding to the Qingtongxia irrigation district, the Hetao irrigation district and the Weihe irrigation district, respectively.

The tendency of annual hydrological components gives an overview of the possible reason for the Yellow River drying up. The hourly time step simulation provides a way to investigate the drying up in fine time scale. Figure 6.12 shows the simulated and observed drying days at the river mouth Lijin station. The river flow is recognized as drying when the discharge is less than minimum flow $10 \text{ m}^3/\text{s}$. An additional scenario is run based on the S1 without irrigation scheme. The S1 scenario without irrigation give zero drying days for the entire simulation period, indicating the Yellow River will not dry in the natural situation without human activities. The scenario S1 to S5 can assemble into two groups: irrigation change group (G1) includes scenarios S1, S2, S3, non-irrigation change group (G2) includes scenarios S4 and S5. With irrigation change group shows rapid increase of drying days, while the non-irrigation change group gives modest increase. The difference of drying days between G1 and G2 became large from the early 1970s, when the irrigated area was rapidly increasing. In the G2, the difference of drying days between S4 and S5 became large from the 1980s, implying the contribution to drying days from climate change and vegetation change became large in the 1980s and the 1990s. Even the irrigation area and climate condition are kept as the 1960s,

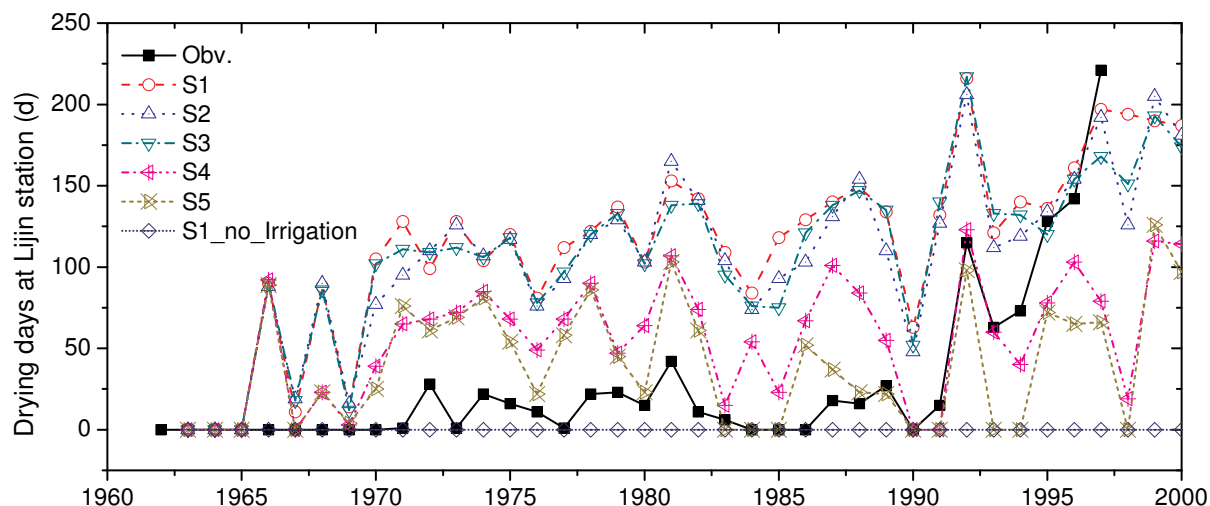


Figure 6.12: Simulated and observed drying days at the Lijin station.

the scenario S5 shows larger drying days than the observations in the 1970s. The reservoir is not considered in the simulations. It implies that the Yellow River would have zero-flow at downstream without reservoir operations even the irrigation level is kept in the relative lower level as the 1960s. The reservoirs, which release for irrigation and also release environment flow in the low flow season, make more stream flow consumption for irrigation on one hand and help to keep environment flow and counter zero-flow on the other hand.

6.4 Conclusions and Discussions

With a distributed biosphere-hydrological (DBH) model system, the hydro-climate connections in the Yellow River are simulated to describe the inner mechanisms of the Yellow River drying up phenomenon. The runoff and evapotranspiration decrease over the Loess Plateau is dominated by the contribution of climate change. The ground temperature increase is found over the most of the river basin, indicating the global warming effect. Irrigation and vegetation change affect special parts of the river basin and induce larger evapotranspiration and larger water withdrawals. The intensively affected area by irrigation and vegetation change is the irrigation districts especial Weihe irrigation district and low reaches irrigation districts. Vegetation recovery in the irrigation area significant decreases runoff and cools the ground. The climate change is dominated in the upper and middle reaches, but human activities are dominated in the lower reaches of the Yellow River basin. Nearly half of the river discharge at the river mouth is affected by climate change and half by human activities. The linear climate change contributes to the water consumption, but the climate pattern change is more important than the linear

climate change. In the upper and middle reaches, the climate pattern change contributes half of the runoff decrease. Some researchers think the water renewability in the Yellow River basin decrease is because soil and water conservation measures make the land surface situation change (Xia et al., 2004; Xu, 2005a; Huang and Zhang, 2004; Chen and Mu, 2000). It can be argued that the water renewability might be caused by the climate pattern change in the Tibetan Plateau and the Loess Plateau.

The climate change dominantly contributes to the annual water resource in the upper and middle reaches. However, the river channel flow is more significantly affected by the irrigation water withdrawals. The flow drying days at the river mouth station became large from the early 1970s, when the irrigated area was rapidly increasing. The contribution to drying days from climate change and vegetation change became large in the 1980s and the 1990s. The results also imply that the Yellow River would have zero-flow at downstream without reservoir operations even the irrigation level is kept in the relative lower level as the 1960s. The reservoirs, which release for irrigation and also release environment flow in the low flow season, make more stream flow consumption for irrigation on one hand and help to keep environment flow and counter zero-flow in the river channel on the other hand.

6.5 Summary

A distributed biosphere-hydrological (DBH) model system is used to simulate the hydro-climate connections in the Yellow River and to describe the mechanisms of the Yellow River drying up phenomenon. The model simulations are designed to interpret the mechanisms among climate system, human society and hydrological system based on the data analysis results from nontraditional data which have proposed the possible connection among climate, land cover, human activity and hydrology response. Several scenarios are performed to investigate the hydrological response to climate system, land cover, and human irrigation. These scenarios include S1) control simulation with most realistic climate, vegetation condition and irrigated area data, S2) non-climate change simulation using the climate data without linear trend, S3) non-vegetation change simulation using the vegetation data without linear trend, S4) non-irrigation change simulation using the irrigated area data without linear trend, S5) stable simulation using the climate, vegetation conditions, and irrigated area data of the 1960s without linear trend, and S6, stable simulation with climate conditions repeating the data in the 1960s. The results show that climate change is dominated in the upper and middle reaches, but human activities are dominated in the lower reaches of the Yellow River basin. The river discharge at

the river mouth nearly half is affected by climate change and half by human activities. The linear climate change contributes to the water consumption, but the climate pattern change is more important than the linear climate change. The river channel flow is more significantly affected by the direct irrigation water withdrawals than by the climate change. The reservoirs are believed to make more stream flow consumption for irrigation, at the same time, our results demonstrate the reservoirs help to keep environment flow and counter zero-flow in the river channel.

Chapter 7

Conclusions and Recommendations

Hydrology includes the study on water movement among the atmosphere, land, surface water and groundwater. Hydrological models are simplified, conceptual representations of a part of the hydrological cycle. The development of hydrological models has been in the direction from the first generation empirical and lumped model to the second generation distributed model during the last decades. Recently, with the advances in nontraditional datasets, new tools, and a better understanding of the connection between hydrology and the rest of the climate system, hydrological research is undergoing an important, fundamental change in the direction of the science. The new (third) generation hydrological models are directed to incorporate the advanced land surface schemes to understand the response of hydrological cycle to the change of biosphere, human society and climate system. This research gives a comprehensive approach of the third generation hydrological model. A distributed biosphere-hydrological model was developed by taking into account the interdisciplinary advances in biosphere, atmosphere, and remote sensing. The model hopefully will increase our understanding of the interaction between hydrology and other earth system and human society. Current available information from nontraditional data is extracted to improve physical hydrological and biospheric simulation. The nontraditional data firstly makes it possible to fully distributed representation of spatial variations. The effects of spatial heterogeneity on hydrological response can be presented by the new generation model. A comprehensive model application shows the hydrological response to climate change, vegetation change and human activity.

7.1 Summary of the Research

7.1.1 Information from Nontraditional Data

The data processing module provide the essential distributed data for the new generation model. The information from nontraditional data sources is firstly combined into one simulation system. Analyses have been done to the new information from nontraditional sources by comparing with traditional observations and checking the data continuity and tendency. The commonly used nontraditional data from satellite remote sensing are compared with traditional ground meteorological observations. The correlation relationship between nontraditional and tradition data are examined. The hydro-climate change, vegetation change, and human activity in the Yellow River basin are investigated using the data from variant sources. The potential connections among climate, land cover, human activity and hydrology response are probed.

7.1.2 Distributed Biosphere-Hydrological Model

A new generation hydrological model, distributed biosphere-hydrological (DBH) model system, is developed in this study. The model is based on the one dimensional representation of land surface processes including biosphere feature with the lateral water distribution related to catchment geomorphological properties and human activity. The one dimensional land surface processes are presented with a soil-vegetation-atmosphere transfer scheme, the revised simple biosphere model (SiB2). The SiB2 is physiologically reactive to atmospheric conditions and the type, density and health of the vegetation will be prescribed as function of season and location. The vegetation condition data is made available from satellite remote sensing. The river routing scheme is used to describe the lateral water distribution. The river flow path is decided according to geomorphological properties extracted from digital elevation model (DEM) and digit watershed information. The watershed is divided into a number of flow intervals along the flow path. River section is assigned to each flow interval, and the runoff flows to the river section and then is lead to the watershed outlet following river network. A simple irrigation scheme is incorporated to estimate human water withdrawals from the river network. The irrigation is based on the surveyed irrigated area and the predicted soil moisture. Irrigation started when the soil moisture was below the wilting point level and continued until soil moisture reached the field capacity level.

The new generation model contains three main model modules (1. soil-vegetation-atmosphere transfer scheme, 2. river routing scheme, and 3. irrigation scheme) and one data processing module which translates nontraditional data for model modules. The soil-

vegetation-atmosphere transfer module modifies a biosphere model to calculate the transfer of energy, mass and momentum between the atmosphere and the surface of the earth, representing spatial variations including topography, land use, soil properties, rainfall, snow, air temperature, radiations. The river routing module uses the kinematic wave method to solve the mass flow in the river network. The irrigation scheme provide the irrigation water requirement and water withdrawals. The data processing module analyzes and validates the input data from nontraditional datasets, and extract useful information for the model modules.

7.1.3 Effects of Heterogeneity on Hydrological Response

The effects of natural and anthropogenic heterogeneity on a hydrological simulation are evaluated using the new generation distributed biosphere-hydrological model. The effects of two kinds of variability, the precipitation variability and the variability of irrigation redistributing runoff, are investigated representing the effects of natural and anthropogenic heterogeneity on hydrological response, respectively. With consideration of precipitation variability, the observed rainfall is assumed to be spatially distributed in each grid cell with a simple exponential area-amount relationship. Otherwise, the rainfall is assumed to be uniform in one grid cell. Land use was partitioned into an irrigation part and nonirrigation part for each grid cell based on the information from global dataset. The variability of irrigation redistributing runoff is represented with the implement of the irrigation scheme. Three simulation cases, i.e. no irrigation without consideration of precipitation heterogeneity, no irrigation with precipitation heterogeneity, and irrigation with precipitation heterogeneity, are performed to evaluate the effects.

7.1.4 Comprehensive Model Application

The new generation model is used to describe the dynamic mechanisms between climate change, human activities and the hydrological pattern in the continental scale river basin. The Yellow River drying up phenomenon is initiated as the study target. The data analysis results from nontraditional data have proposed the possible connection among climate, land cover, human activity and hydrology response. The model simulations then interpret the inner mechanisms among these earth systems. Several scenarios are performed to investigate the hydrological response to climate system, land cover, and human irrigation. These scenarios include S1) control simulation with most realistic climate, vegetation condition and irrigated area data, S2) non-climate change simulation using the climate data without linear trend, S3) non-vegetation change simulation using the vegetation data without linear trend, S4) non-irrigation change

simulation using the irrigated area data without linear trend, and S5) stable simulation using the climate, vegetation conditions, and irrigated area data of the 1960s without linear trend.

7.2 Conclusions

Advances of nontraditional data from variant sources make it possible to analyze climatic and anthropogenic effects on hydrological cycle. The remote sensing observations could present land transformation such as vegetation condition and land cover change, which should account for the strong, often dominant influence of humanity, rather than directly represent the human activity. The agreement between nontraditional data and traditional ground-observed data suggests that spatial distributions of land characteristics and climatic features can be captured by nontraditional tools. Analyzes of hydro-climatic observations and vegetation data imply the potential hydrological responses to climate change, vegetation change and human activities. For the case study in the Yellow River basin, results indicate that the Loess Plateau, the Tibetan Plateau, and the irrigation districts are suggested as precipitation, temperature, and human activities "hot spots" of the Yellow River drying up, respectively.

A new generation hydrological model, DBH model, is developed and validated. It can be concluded that the hydrological model with biosphere processes can be used for hydrological simulation in continental scale river basins. The new hydrological model is a continuous-time spatially distributed model, integrating hydrological processes and soil-vegetation-atmosphere transfer processes at the river basin scale. It can represent vegetation state and phenology with the assistance from satellite remote sensing data, and geomorphological characteristics using digital elevation model. The DBH model system, which hopefully will increase our understanding of land surface hydrology, can be used to represent the land surface exchanges of moisture/energy, model the spatial interactions and lateral redistribution of moisture over complex terrain, and assess the effects of human activity on the hydrology cycle. The proposed model is intended to be as physically, biologically, and hydrologically realistic as possible.

The new generation hydrological model can demonstrate the effects of natural and anthropogenic heterogeneity on a hydrological simulation. Runoff was underestimated if rainfall was placed spatially uniformly over large grid cells. Accounting for precipitation heterogeneity improved the runoff simulation. However, the negative runoff contribution cannot be simulated by only considering the natural heterogeneity. This constructive model shortcoming can be eliminated by accounting for anthropogenic heterogeneity caused by irrigation water withdrawals. Irrigation leads to increased evapotranspiration and decreased runoff, and surface soil

moisture in irrigated areas increases because of irrigation. Simulations performed for the Yellow River basin indicated stream flow decreases of 41% due to irrigation effects. The latent heat flux in the peak irrigation season (June, July, August: JJA) increased 3.3 W m^{-2} with a decrease in the ground surface temperature of 0.1 K for the river basin. The maximum simulated increase in the latent heat flux was 43 W m^{-2} , and the ground temperature decrease was 1.6 K in the peak irrigation season.

The distributed biosphere-hydrological (DBH) model system is used to simulate the hydro-climate connections in the Yellow River and to describe the mechanisms of the Yellow River drying up phenomenon. The results show that climate change is dominated in the upper and middle reaches, but human activities are dominated in the lower reaches of the Yellow River basin. The runoff and evapotranspiration decrease over the Loess Plateau is dominated by the contribution of climate change. The intensively affected area by irrigation and vegetation change is the irrigation districts especial Weihe irrigation district and low reaches irrigation districts. The river discharge at the river mouth nearly half is affected by climate change and half by human activities. The linear climate change contributes to the water consumption, but the climate pattern change is more important than the linear climate change. The river channel flow is more significantly affected by the direct irrigation water withdrawals than by the climate change, which dominantly contributes to the annual water resources change. The reservoirs are believed to make more stream flow consumption for irrigation, at the same time, our results demonstrate the reservoirs help to keep environment flow and counter zero-flow in the river channel.

7.3 Suggestions for Future Research

The emergence of new technology and substantial amounts of data in nontraditional forms promotes land surface hydrological modeling. The new generation hydrological model described in this study exhausts the optimum use of current potentially highly valuable data. Further data collection efforts would continuously benefit research on land surface hydrology. The nontraditional data are mainly from remote sensing in the form of spectral data related to land surface variables. These data usually are not able to be used directly for hydrological purposes. The hydrological variables must be inferred from available nontraditional data with the aid of retrieval or data processing algorithms. Data assimilation can produce data that are directly useful for hydrological models. Hydrologists should improve communications with data maker community to use source data from satellites, meteorological analyses, and analyses of surface

survey work.

Data on the chemical composition of water can be used for modeling water flow paths. Chemical tracer data help define surface, subsurface, and groundwater flows and help define hydrograph separation. Many type tracers have been used to understand hydrological and geochemical processes. These tracers include stable isotopes, radiogenic isotopes, and chlorofluorocarbons. Chemical traces can provide information on flow of water, its origin, source, and flow paths. The transport processes of chemical traces could be incorporated into the third generation hydrological model and improve flow path simulation.

Further, the model can extend to simulate hydrological cycle over the global land surface with the assistance of global datasets. The model would couple with other components of the earth system models to make an entire water cycle simulation among ocean-land-atmosphere. The ocean-land-atmosphere model system will explore, establish and quantify the variability and predictability of Earth's climate and hydrological variations, and harvest this predictability for societal beneficial predictions.

With the consideration of climate, biosphere, land surface hydrology and human activity, the new generation hydrological model has potentially great societal benefits. The new generation model, which intensively uses the global dataset, can extend to continent and globe to evaluate the impact of climate change. The model can and should provide the scientific knowledge required to address contemporary global issues such as natural disaster prevent, food security, human health, and economic development. Further work should address to the reduction of the uncertainties of prediction and analysis so that managers and policy makers can more effectively use the results. Some attentions can be paid to the development of comprehensive expert systems including hydrology, ecosystem, environment, and society. The development of the new generation hydrological model will offer an opportunity that will provide great benefits both for science and for society as a whole.

Appendix A

Green-Ampt Model

A.1 Derivation of Green-Ampt Model

The infiltration flux can be estimated from Darcy's equation.

$$q_i = -K_s \frac{dh}{dz} = -K_s \frac{(\psi_f + z_f) - (H_p + 0.)}{z_f - 0.} = -K_s \frac{\psi_f + z_f - H_p}{z_f} \quad (\text{A.1})$$

where, H_p is the depth of ponding (m); K_s is saturated hydraulic conductivity (m/s); q_i is infiltration flux (m/s) and is negative; ψ_f is soil suction at wetting front in negative pressure head (m). The cumulative depth of infiltration F_i (m) is $F_i = z_f(\theta_s - \theta_i)$. Rearrange the equation above and get:

$$z_f = \frac{F_i}{\theta_s - \theta_i} \quad (\text{A.2})$$

The infiltration flux q_i is equal to the infiltration rate f_i , the first derivative of F_i with respect to time. Substitute equation (A.2) into Darcy's equation.

$$q_i = f_i = \frac{dF_i}{dt} = -K_s \left(\psi_f + \frac{F_i}{\theta_s - \theta_i} - H_p \right) \frac{\theta_s - \theta_i}{F_i} \quad (\text{A.3})$$

Assume ponding depth H_p is small relative to the other terms and the equation (A.3) simplifies to the Green-Ampt infiltration rate equation.

$$f_i = \frac{dF_i}{dt} = -K_s \left(\psi_f \frac{\theta_s - \theta_i}{F_i} + 1 \right) \quad (\text{A.4})$$

Separate variables in equation (A.4).

$$\frac{1}{\psi_f \frac{\theta_s - \theta_i}{F_i} + 1} dF = -K_s dt \quad (\text{A.5})$$

Integrate equation (A.5).

$$F_f - (\theta_s - \theta_i)\psi_f \ln \left[1 + \frac{F_f}{(\theta_s - \theta_i)\psi_f} \right] + K_s t_f = 0 \quad (\text{A.6})$$

F_f is an implicit function of t_f . Notice the original form of Green-Ampt equations can be written as :

$$t = \frac{F_f - (\theta_s - \theta_i)\psi_f \ln \left[1 + \frac{F_f}{(\theta_s - \theta_i)\psi_f} \right]}{K_s} \quad (\text{A.7})$$

$$f = K_s \left[1 + \frac{(\theta_s - \theta_i)\psi_f}{F_f} \right] \quad (\text{A.8})$$

where, F_f , f , and ψ_f are positive rather than negative as in equations (A.6).

If rainfall intensity is constant (i) and eventually exceeds infiltration rate, then at some moment the surface will become saturated and ponding when the infiltration rate equals the precipitation rate. The depth infiltrated at that moment (F_s) is given by setting $f = i$ in equation (A.8) and solving for:

$$F_s = \frac{(\theta_s - \theta_i)\psi_f}{i/K_s - 1} \quad (\text{A.9})$$

The time of ponding is given by $t_s = F_s/i$.

Assuming rainfall intensity is constant at one time step (time step length is dtt , s), the minimum rainfall intensity i_m which will cause overland runoff will fit the equation:

$$\frac{(\theta_s - \theta_i)\psi_f}{i_m(i_m/K_s - 1)} = dtt \quad (\text{A.10})$$

Solve the equation (A.10) and get the rainfall intensity i_m :

$$i_m = \frac{K_s}{2} \left[1 + \sqrt{1 + 4 \frac{(\theta_s - \theta_i)\psi_f}{K_s dtt}} \right] \quad (\text{A.11})$$

A.2 Green-Ampt Infiltration

In order to calculate the infiltration, the Green-Ampt model equation must be solved for each time step in the hyetograph. As illustrated in the Figure A.1, three cases should be considered in which the infiltration rates at times $t_1(t)$ and $t_2(t + dt)$ are denoted by $f_1 = f(t_1)$ and $f_2 = f(t_2)$ respectively, and the rainfall intensity i is assumed to be constant during the time step. If the rainfall intensity exceeds the infiltration capacity of the soil throughout the study time step ($f_2 < f_1 < i$), ponding must occur for the entire time step. If the infiltration capacity f_1 exceeds the rainfall intensity at the beginning of the time step but this changes before the

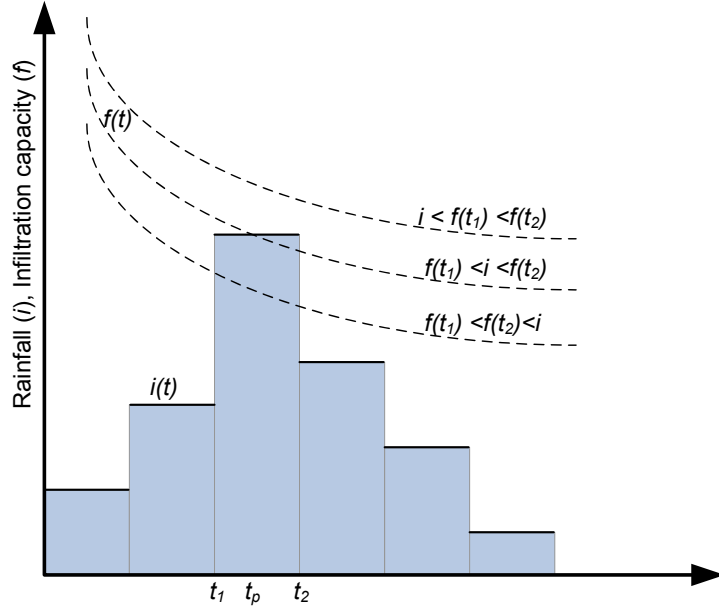


Figure A.1: Use Green-Ampt model to estimate infiltration.

time step is completed. Ponding will start during the time step. If the rainfall infiltrates for the entire time step, no ponding occurs. The solution algorithm can be summarized as follows:

The infiltration capacity f_c is set according to the soil moisture content.

$$f_c = K_s \left[1 + \frac{\psi_a - \psi_s}{L_f} \right] \quad (\text{A.12})$$

where, L_f is the soil depth (m), soil suction ψ_a is the function of averaged soil moisture content.

i) If $i_t > f_{t_1}$,

$$F_{t_2} = F_{t_1} + K \cdot dt + (\theta_s - \theta_i) \psi_f \ln \left[\frac{F_{t_2} + (\theta_s - \theta_i) \psi_f}{F_{t_1} + (\theta_s - \theta_i) \psi_f} \right] \quad (\text{A.13})$$

The overland flow R_o is:

$$R_o = i - \frac{F_{t_2} - F_{t_1}}{dt} \quad (\text{A.14})$$

ii) If $i_{t_1} \leq f_{t_1}$, assume all the rainfall infiltrates during time step. The accumulated infiltration is estimated as:

$$F_{t_2} = F_{t_1} + i \cdot dt \quad (\text{A.15})$$

and the infiltration rate is:

$$f_{t_2} = K_s \left[1 + \frac{(\theta_s - \theta_i) \psi_f}{F_{t_2}} \right] \quad (\text{A.16})$$

iii) If $i_t \leq f_{t_1}$, the assumption that all the rainfall infiltrates during time step is true.

The overland flow R_o is:

$$R_o = 0 \quad (\text{A.17})$$

If $i_t > f_{t_2}$, ponding will start during the time step. The infiltration before ponding is estimated as equation (A.9). The volume required to cause surface ponding to occur is given by $t_p = (F_s - F_{t_1})/i$. Then:

$$F_{t_2} = F_{t_1} + K \cdot (dtt - t_p) + (\theta_s - \theta_i)\psi_f \ln \left[\frac{F_{t_2} + (\theta_s - \theta_i)\psi_f}{F_{t_1} + (\theta_s - \theta_i)\psi_f} \right] \quad (\text{A.18})$$

The overland flow R_o is:

$$R_o = i_t - \frac{F_{t_2} - F_{t_1}}{dtt} \quad (\text{A.19})$$

Appendix B

Numeric Solutions

B.1 Water Fluxes Underground

The water balance equations of three soil layers are:

$$\frac{\partial W_1}{\partial t} = \frac{Q_{01} - Q_{12}}{\theta_s D_1} \quad (\text{B.1})$$

$$\frac{\partial W_2}{\partial t} = \frac{Q_{12} - Q_{23}}{\theta_s D_2} \quad (\text{B.2})$$

$$\frac{\partial W_3}{\partial t} = \frac{Q_{23} - Q_{3g}}{\theta_s D_3} \quad (\text{B.3})$$

where Q_{01} is vertical water infiltration from ground into the first soil layer(m/s), Q_{12} is vertical water exchange between the first and the second soil layer(m/s), Q_{23} is vertical water exchange between the second and the third soil layer(m/s). D_1, D_2, D_3 is the vertical thickness of the first, second, and third soil layer, respectively. W_1, W_2, W_3 is soil moisture wetness fraction of the three soil layers. The finite-difference form of above equation can be written as:

$$W_{1,t+\Delta t} = W_{1,t} + \frac{Q_{01} - Q_{12}}{\theta_s D_1} \delta t \quad (\text{B.4})$$

$$W_{2,t+\Delta t} = W_{2,t} + \frac{Q_{12} - Q_{23}}{\theta_s D_2} \delta t \quad (\text{B.5})$$

$$W_{3,t+\Delta t} = W_{3,t} + \frac{Q_{23} - Q_{3g}}{\theta_s D_3} \delta t \quad (\text{B.6})$$

The momentum equation 4.16 for the three soil layers can be:

$$Q_{12} = K_{12} \left[\frac{\partial \psi_{12}}{\partial Z_{12}} + 1 \right] \quad (\text{B.7})$$

$$Q_{23} = K_{23} \left[\frac{\partial \psi_{23}}{\partial Z_{23}} + 1 \right] \quad (\text{B.8})$$

$$Q_{3g} = K_{3g} \left[\frac{\partial \psi_{3g}}{\partial Z_{3g}} + 1 \right] \quad (\text{B.9})$$

Considering the boundary condition, the boundary condition of the top soil layer is water flux and the lower boundary condition is the ground water table, we have $Q_{01} = 0$ and $W_{g,t+\Delta t} = W_{g,t} = 1$. Equation B.4, B.5 and B.6 are substituted into equation B.7, B.8 and B.9 to get:

$$\begin{aligned} Q_{12} &= K_{12} \left[\frac{\frac{\partial \psi_{12}}{\partial W_{12}} (W_{1,t+\Delta t} - W_{2,t+\Delta t})}{(D_1 + D_2)/2} + 1 \right] \\ &= K_{12} \left[\frac{\partial \psi_{12}}{\partial W_{12}} \frac{2}{D_1 + D_2} \left(W_{1,t} - W_{2,t} + \frac{-Q_{12}}{\theta_s D_1} \delta t \right. \right. \\ &\quad \left. \left. - \frac{Q_{12} - Q_{23}}{\theta_s D_2} \delta t \right) + 1 \right] \end{aligned} \quad (\text{B.10})$$

$$\begin{aligned} Q_{23} &= K_{23} \left[\frac{\frac{\partial \psi_{23}}{\partial W_{23}} (W_{2,t+\Delta t} - W_{3,t+\Delta t})}{(D_2 + D_3)/2} + 1 \right] \\ &= K_{23} \left[\frac{\partial \psi_{23}}{\partial W_{23}} \frac{2}{D_2 + D_3} \left(W_{2,t} - W_{3,t} + \frac{Q_{12} - Q_{23}}{\theta_s D_2} \delta t \right. \right. \\ &\quad \left. \left. - \frac{Q_{23} - Q_{3g}}{\theta_s D_3} \delta t \right) + 1 \right] \end{aligned} \quad (\text{B.11})$$

$$\begin{aligned} Q_{3g} &= K_{3g} \left[\frac{\frac{\partial \psi_{3g}}{\partial W_{3g}} (W_{3,t+\Delta t} - W_{g,t+\Delta t})}{D_{3g}} + 1 \right] \\ &= K_{3g} \left[\frac{\partial \psi_{3g}}{\partial W_{3g}} \frac{1}{D_{3g}} \left(W_{3,t} + \frac{Q_{23} - Q_{3g}}{\theta_s D_3} \delta t - 1 \right) + 1 \right] \end{aligned} \quad (\text{B.12})$$

Set $d_{12} = \frac{\partial \psi_{12}}{\partial W_{12}} \frac{2}{D_1 + D_2}$, $d_{23} = \frac{\partial \psi_{23}}{\partial W_{23}} \frac{2}{D_2 + D_3}$ and $d_{3g} = \frac{\partial \psi_{3g}}{\partial W_{3g}} \frac{1}{D_{3g}}$. The equations could be reformed as:

$$\begin{cases} a_1 Q_{12} + b_1 Q_{23} + \quad = d_1 \\ a_2 Q_{23} + b_2 Q_{12} + c_2 Q_{3g} = d_2 \\ a_3 Q_{3g} + b_3 Q_{23} + \quad = d_3 \end{cases} \quad (\text{B.13})$$

where

$$\begin{cases} a_1 = 1 + \frac{K_{12} d_{12} \delta t}{\theta_s} \left(\frac{1}{D_1} + \frac{1}{D_2} \right) \\ a_2 = 1 + \frac{K_{23} d_{23} \delta t}{\theta_s} \left(\frac{1}{D_2} + \frac{1}{D_3} \right) \\ a_3 = 1 + \frac{K_{3g} d_{3g} \delta t}{\theta_s} \frac{1}{D_3} \end{cases} \quad (\text{B.14})$$

$$\begin{cases} b_1 = -\frac{K_{12}d_{12}\delta t}{\theta_s} \frac{1}{D_2} \\ b_2 = -\frac{K_{23}d_{23}\delta t}{\theta_s} \frac{1}{D_2} \\ b_3 = -\frac{K_{3g}d_{3g}\delta t}{\theta_s} \frac{1}{D_3} \end{cases} \quad (\text{B.15})$$

$$c_2 = -\frac{K_{23}d_{23}\delta t}{\theta_s} \frac{1}{D_3} \quad (\text{B.16})$$

$$\begin{cases} d_1 = K_{12}[1 + (W_{1,t} - W_{2,t}) d_{12}] \\ d_2 = K_{23}[1 + (W_{2,t} - W_{3,t}) d_{23}] \\ d_3 = K_{3g}[1 + (W_{3,t} - 1) d_{3g}] \end{cases} \quad (\text{B.17})$$

Resolve the equation B.13, we get:

$$\begin{cases} Q_{12} = \frac{a_2a_3d_1 - b_3c_2d_1 - a_3b_1d_2 + b_1c_2d_3}{a_1a_2a_3 - a_3b_1b_2 - a_1b_3c_2} \\ Q_{23} = \frac{a_1a_3d_2 - a_3b_2d_1 - a_1c_2d_3}{a_1a_2a_3 - a_3b_1b_2 - a_1b_3c_2} \\ Q_{3g} = \frac{a_1a_2d_3 - b_1b_2d_3 - a_1b_3d_2 + b_2b_3d_1}{a_1a_2a_3 - a_3b_1b_2 - a_1b_3c_2} \end{cases} \quad (\text{B.18})$$

B.2 River Flow

The momentum equation to govern the river flow is the Manning's equation. The Manning's equation gives the relationship between river flow speed and the river bed roughness together with the wetting section. The rectangular river section shape is assumed. Then, the cross sectional wetting area $A = B \cdot h$ (m^2) and the wetting perimeter $P = B + 2h$ (m). The river flow speed V is:

$$V = \frac{Q}{A} = \frac{R^{2/3}S_r^{1/2}}{n} \quad (\text{B.19})$$

where $R = A/P$. The Manning's flow speed with a roughness value of 0.12 is shown in figure B.1a. For a rectangular river section, the Manning's flow speed with a slope $S_r = 0.007$ is shown in figure B.1b. The river flow speed is almost decided by the river water depth h rather than the river width B after the river width is larger than 300 m. The discharge estimated from the Manning's equation is shown in figure B.2a. The slope $S_r = 0.007$ and roughness value of 0.12 is assumed in the figure B.2b.

The kinematic equations are solved by nonlinear explicit finite difference method. The finite difference form of the equation 4.25 is derived by the backward difference scheme as:

$$\frac{Q_{i+1}^{j+1} - Q_i^{j+1}}{\Delta x} + \frac{A_{i+1}^{j+1} - A_{i+1}^j}{\Delta t} = \frac{q_{i+1}^{j+1} - q_{i+1}^j}{2} \quad (\text{B.20})$$

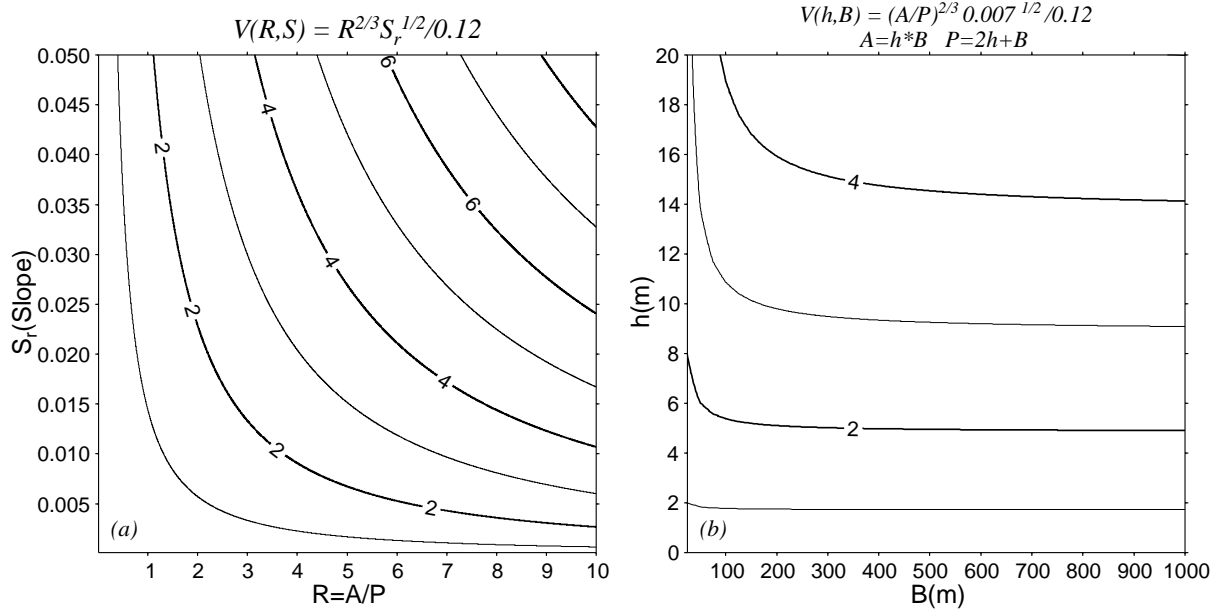


Figure B.1: Flow speed estimated from the Manning's equation.

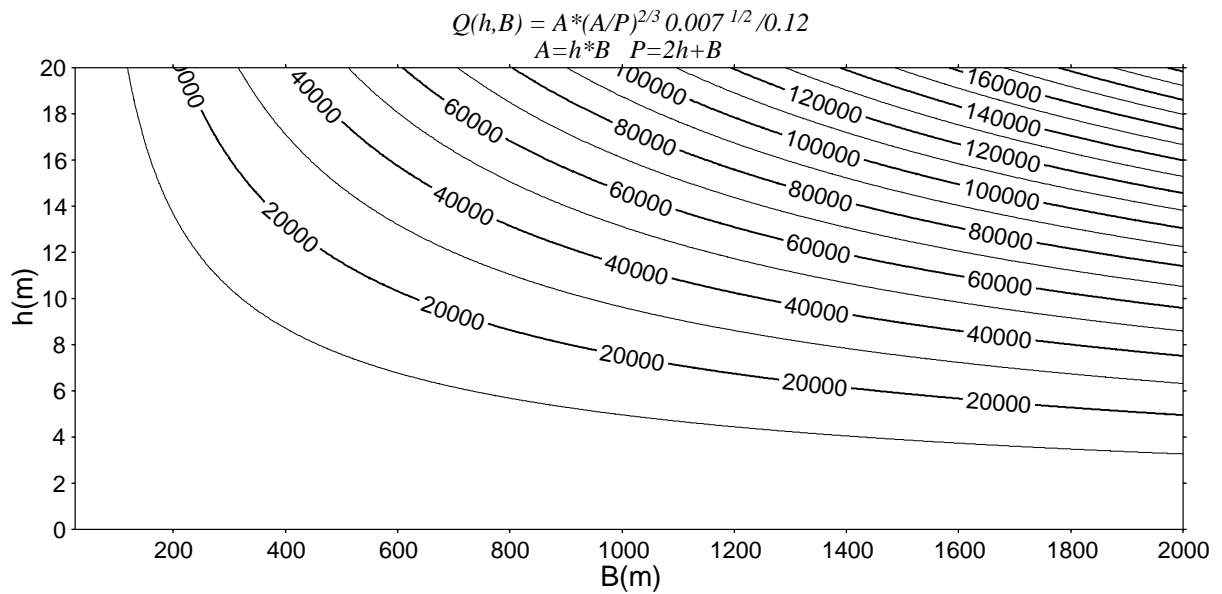


Figure B.2: Discharge estimated from the Manning's equation with a rectangular river section.

where $A_{i+1}^{j+1} = \alpha(Q_{i+1}^{j+1})^\beta$ and $A_{i+1}^j = \alpha(Q_{i+1}^j)^\beta$. The equation can be expressed in the form:

$$\frac{\Delta t}{\Delta x} Q_{i+1}^{j+1} + \alpha (Q_{i+1}^{j+1})^\beta = \frac{\Delta t}{\Delta x} Q_{i+1}^j + \alpha (Q_{i+1}^j)^\beta + \Delta t \left(\frac{Q_{i+1}^{j+1} - Q_{i+1}^j}{2} \right) = C \quad (\text{B.21})$$

where, C is the known item. Move the right side of the equation to left side, we get:

$$f(Q_{i+1}^{j+1}) = \frac{\Delta t}{\Delta x} Q_{i+1}^{j+1} + \alpha (Q_{i+1}^{j+1})^\beta - C = 0 \quad (\text{B.22})$$

Solving the equation using Newton's method with iterations $k = 1, 2, \dots$

$$(Q_{i+1}^{j+1})_{k+1} = (Q_{i+1}^{j+1})_k \frac{f(Q_{i+1}^{j+1})_k}{f'(Q_{i+1}^{j+1})_k} \quad (\text{B.23})$$

where $f'(Q_{i+1}^{j+1})_k$ is the derivative of the function $f(Q)$:

$$f'(Q_{i+1}^{j+1})_k = \frac{\Delta t}{\Delta x} + \alpha\beta (Q_{i+1}^{j+1})_k^{\beta-1} \quad (\text{B.24})$$

The criterion for the iterative process is:

$$\left| f(Q_{i+1}^{j+1})_{k+1} \right| < \varepsilon_e \quad (\text{B.25})$$

where ε_e is the error criterion.

Appendix C

Data Processing

C.1 Map Projections

Map projections are attempts to portray the surface of the earth or a portion of the earth on a flat surface. Some distortions of conformal, distance, direction, scale, and area always result from this process. Some projections minimize distortions in some of these properties at the expense of maximizing errors in others. Some projections are attempts to only moderately distort all of these properties. No projection can be simultaneously conformal and area-preserving.

Most map projections can be at least partially visualized geometrically as being projected onto one of three surfaces: the cylinder, the cone, and the plane. The cylindrical map projections can be visualized geometrically as having a cylinder wrapped around the Earth: after the map points are projected, the cylinder is cut lengthwise and rolled out as a flat plane. A conic projection can be visualized as placing a cone over the Earth, with the cone's peak (apex) along the polar axis of the Earth, and the cone's surface touching the Earth along constant latitude. Azimuthal projections can be visualized as mapped to a plane that is tangent to the surface of the Earth. If the plane is tangent to the north or south pole, the projection is polar. Several map projections is introduced and used in the DBH model system.

C.1.1 Geographic

Geographic is not a map projection. The Geographic Reference System consists of latitude and longitude. This system treats the globe as if it were a sphere or spheroid. The sphere is divided into equal parts called degrees. For longitude, it is angle made by the plane of a meridian passing through a given point on the Earth's surface and the plane of the (prime) meridian passing through Greenwich, England, east or west to 180 (positive if the point is east,

or negative if it is west). For latitude, it is angle made by a perpendicular to a given point on the surface of a sphere or ellipsoid representing the Earth and the plane of the Equator (positive if the point is north of the Equator, negative if it is south). Other map projections use latitude and longitude values to reference parameters such as the central meridian, the latitude of the true scale and the latitude of origin. The latitude and longitude values are used as reference coordinate when resample the map among different map projection in the DBH model system.

C.1.2 Lambert Azimuthal Equal Area Projection

The Lambert Azimuthal Equal-Area projection is an Azimuthal map projection. Not only is this projection equal-area, with, of course, the azimuthal property showing true directions from the center of the projection, but its scale at a given distance from the center varies less from the scale at the center than the scale of any of the other major azimuthals. The Lambert Azimuthal Equal Area projection is the default working projection in the DBH model system. The HYDRO1k dataset use the projection. Spatial data in other map projection should be projected to the default projection and used by the DBH model system.

The Lambert Azimuthal Equal Area projection has transformation equations:

$$x = k' \cos \phi \sin(\lambda - \lambda_0) \quad (\text{C.1})$$

$$y = k' [\cos \phi_1 \sin \phi - \sin \phi_1 \cos \phi \cos(\lambda - \lambda_0)] \quad (\text{C.2})$$

where, ϕ_1 is the standard parallel, λ_0 is the central longitude, and

$$k' = \sqrt{\frac{2}{1 + \sin \phi_1 \sin \phi - \cos \phi_1 \cos \phi \cos(\lambda - \lambda_0)}} \quad (\text{C.3})$$

The inverse formulas are:

$$\phi = \sin^{-1} \left(\cos c \sin \phi_1 + \frac{y \sin c \cos \phi_1}{\rho} \right) \quad (\text{C.4})$$

$$\lambda = \lambda_0 + \tan^{-1} \left(\frac{x \sin c}{\rho \cos \phi_1 \cos c - y \sin \phi_1 \sin c} \right) \quad (\text{C.5})$$

where,

$$\rho = \sqrt{x^2 + y^2} \quad (\text{C.6})$$

$$c = 2 \sin^{-1}(\rho/2) \quad (\text{C.7})$$

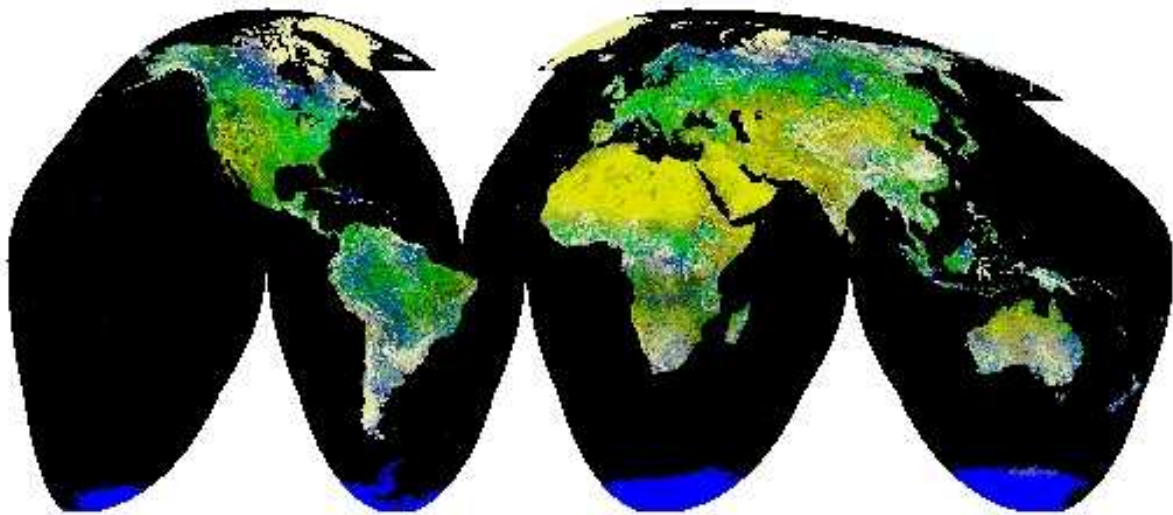


Figure C.1: Global AVHRR data with the Interrupted Goode Homolosine projection.

The scale of Lambert Azimuthal Equal Area projection is true only at the center in all directions and decreases with distance from the center along radii, increases with distance from the center in a direction perpendicular to radii.

C.1.3 Interrupted Goode Homolosine Projection

The Interrupted Goode Homolosine projection (Goode's) is an interrupted, pseudocylindrical, equal-area, composite map projection that can present the entire world on one map. The Goode Homolosine projection is a merging of the Mollweide and Sinusoidal projections. Global land masses are presented with their areas in proper proportion, with minimal interruption, and minimal overall distortion. Vector and raster data in the Goode's projection are available to the spatial data community from a variety of sources. One of these sources is the U.S. Geological Survey's (USGS) EROS Data Center (EDC). The Global Land 1-kilometer Advanced Very High Resolution Radiometer (AVHRR) imagery of the world land cover is provided with the Interrupted Goode Homolosine projection.

Steinwand (1994) described about the Interrupted Goode Homolosine projection. A Global AVHRR data example is provide by USGS (Figure C.1). The remote sensing CLAVR, NDVI, LAI, FPAR data derived from NOAA/NASA Pathfinder AVHRR use the Goode's projection. The ancillary latitude and longitude files, which can be used to extract data, are provide together with the datasets.

C.1.4 Data Resampling

The spatial data should work with same map projection in the DBH model system. The data in different map projection should be resampled to the same map projection before it can be handling in numeric simulation. Resampling is the process of determining new values for cells in an output grid that result from applying some geometric transformation to an input grid. The input grid may be in a different coordinate system, at a different resolution, or may be rotated with respect to the output grid.

Data resampling between the Interrupted Goode Homolosine projection (source) and the Lambert Azimuthal Equal Area projection (target) is included in the DBH model system. The resampling method is described in this section. The strategy is shown in figure C.2. First, the Geographic 'projection', i.e. latitude and longitude, of the map under output projection is calculated. For the case to convert the Goode's projection to the Lambert projection, the map extend under Lambert projection is decided and the latitude and longitude of each grids is calculated. The grid cell is divided into several, e.g. $N \times N$, sub-grids. The latitude and longitude of the center of the sub-grids are projected to the source map with the Goode's projection. The data values from the source map are averaged as the data values under the target projection. This method is not limited in the conversion between the Lambert Azimuthal Equal Area projection and the Interrupted Goode Homolosine projection. It is a universal method for the conversion between any projection and geometric transformation.

C.2 Point-Surface Interpolation

Spatially distributed estimates of meteorological data are becoming increasingly important as inputs to spatially explicit landscape, regional, and global models. Estimates of meteorological values such as temperature, precipitation, and evapotranspiration on rate are required for a number of landscape scale models, including hydrological, ecological, and land surface modeling. Interpolation is a procedure used to predict the values of cells at locations that lack sampled points. It is based on the principle of spatial autocorrelation or spatial dependence, which measures degree of relationship/dependence between near and distant objects. There are two categories of interpolation techniques: deterministic and geostatistical. Deterministic interpolation techniques create surfaces based on the surrounding measured values or on specified mathematical formulas that determine the smoothness of the resulting surface. Geostatistical interpolation techniques get surfaces based on statistical models that include autocorrelation (statistical relationships among the measured points). Only the deterministic interpolation

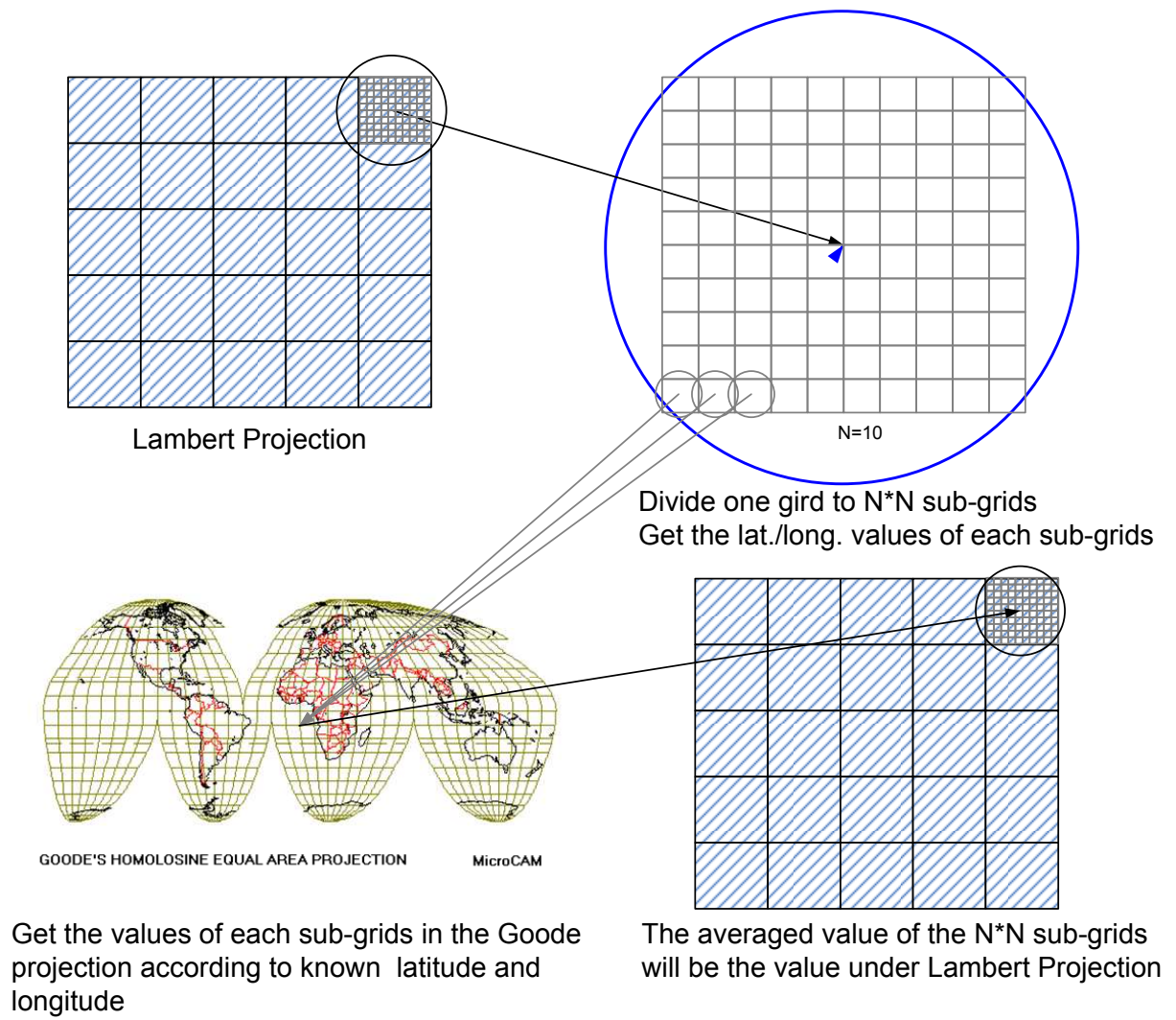


Figure C.2: Data resampling process.

techniques are used in the DBH model system.

C.2.1 Thiessen Polygons

Thiessen polygon method, in mathematics a Voronoi diagram method, defines area of influence around a point that polygon boundaries are equidistant from neighboring points. The Thiessen polygons have the property to contain only one measurement and to have a geometry that will include all the data points that are closer to the measurement than to any other measurement. Isolated observations will therefore have polygons that will be larger than those associated to clustered data. When the grid cell size is much less than the averaged distance between stations, a nearest station method would get the similar results as the Thiessen polygon method. The nearest station method is used. First, seek the nearest station to the grid cell. The value of the nearest station is then assigned for the interest grid cell.

C.2.2 Thin Plate Splines

The thin plate spline is the two-dimensional analog of the cubic spline in one dimension. It is the fundamental solution to the biharmonic equation, and has the form

$$U(r) = r^2 \ln r \quad (\text{C.8})$$

Given a set of data points, a weighted combination of thin plate splines centered about each data point gives the interpolation function that passes through the points exactly while minimizing the so-called "bending energy." Bending energy is defined here as the integral over R^2 of the squares of the second derivatives,

$$I[f(x, y)] = \int \int_{R^2} \left[\left(\frac{\partial^2 f}{\partial x^2} \right)^2 + 2 \left(\frac{\partial^2 f}{\partial x \partial y} \right)^2 + \left(\frac{\partial^2 f}{\partial y^2} \right)^2 \right] dx dy \quad (\text{C.9})$$

The name "thin plate spline" refers to a physical analogy involving the bending of a thin sheet of metal. In the physical setting, the deflection is in the z direction, orthogonal to the plane. In order to apply this idea to the problem of coordinate transformation, one interprets the lifting of the plate as a displacement of the x or y coordinates within the plane. Thus, in general, two thin plate splines are needed to specify a two-dimensional coordinate transformation.

C.2.3 Inverse Distance Weighted Method

This inverse distance weighted (IDW) interpolation method is based on the following assumptions: if a nearer grid cell is located to a station, the more similar is the value of the grid cell to the observed value in close distance. IDW is a deterministic estimation method where values at unsampled points are determined by a linear combination of values at known sampled points. Distance-based weighting methods have been used to interpolate climatic data (Legates and Willmott, 1990). In estimating each grid point using IDW method, eight nearest stations regardless direction and distance are used to contribute to a grid point estimation and form the distance weighting function (Piper and Stewart, 1996). Weights for the eight stations were determined in a two-stage process following New et al. (2000). All stations were first weighted by distance from the grid point (Jones et al., 1997; New et al., 2000):

$$w_k = (e^{-x/x_0})^m \quad (\text{C.10})$$

where x is the distance from the grid point of interest, x_0 is the correlation decay distance, m is parameters between 1 and 8. A value of 4 for m was suggested by New et al. (2000). The second component of the distance weight was determined by the directional (angular) isolation of each the eight selected stations:

$$\alpha_k = \frac{\sum_{l=1}^8 w_l [1 - \cos \theta(k, l)]}{\sum_{l=1}^8 w_l} \quad : \quad l \neq k \quad (\text{C.11})$$

where $\cos \theta(k, l)$ is the angular separation of station k and l , and w_l is the distance weight at station l . The angular-distance weight is then calculated from:

$$W_k = w_k(1 + \alpha_k) \quad (\text{C.12})$$

C.2.4 Comparison of Interpolation Methods

The three interpolation methods, TS, TPS, and IDW method, are performed and the precipitation results are compared. Figure C.3 shows the annual mean precipitation from 1960-2000 in the Yellow River basin with the three interpolation method. The thin-plate splines interpolation was found to be unsuitable because there were considerable undershoot and overshoot in the edge of the study area with poor station control. Thiessen polygon interpolation employ a limited number of data points in the estimation of grid point values and take no account of station distance. The IDW method was recommended in the Yellow River considering the

weather station density. It should be noted that data measurement accuracy, data density, data distribution, and spatial variability had the greatest influence on interpolation accuracy. The recommendation is not an endorsement of the IDW method. The DBH model system provides three different interpolation methods for reference.

C.3 Extract Geomorphological Properties

The geomorphology of the catchment, or quantitative study of the surface landform, is widely used in hydrological modeling. Several studies are done to analyze the hydrological response to geomorphological properties.

Field studies have demonstrated that areas of surface saturation tend to be found at the bottom of hillslopes and in convergent hollow areas or swales associated either with soils of low hydraulic conductivity or areas of low slope (Beven and Wood, 1983). Beven and Kirkby (1979) assumed that at any point in the catchment, down slope flow per unit width of slope, q_b , is related to saturation deficit S_b by:

$$q_b = R_b \alpha_b = K_{0b} \tan \beta_b \exp(-S_b/m_b) \quad (\text{C.13})$$

where saturation deficit S_b is defined as the storage deficit below full saturation due to soil drainage alone and excluding the additional deficits that would result from evapotranspiration. $K_{0b} \tan \beta_b$ is the transmission capacity of the soil profile at full saturation, and $\tan \beta_b$ is the local surface slope angle. R_b is a steady input rate, and α_b is the upslope area draining past that point per unit width of slope or contour length. Assuming the soil is homogeneous and of uniform depth, the K_{0b} and m_b are constant. A distribution of item $\ln(\alpha_b/\tan \beta_b)$ is used to predict the dynamic response of the contributing are for which saturation deficit is less than 0.

A Compound Topographic Index (CTI), often referred to as the steady state wetness index, is a function of the upstream contributing area and the slope of the landscape(Moore et al., 1991). It integrates both landform position and context through an index defined as:

$$CTI = \ln(A_s/\tan \beta_b) \quad (\text{C.14})$$

where A_s is upstream contributing area.

The geomorphological properties can be quantitated from DEM map with the assistant of General Information System (GIS). The flow direction and flow accumulation method is briefly described.

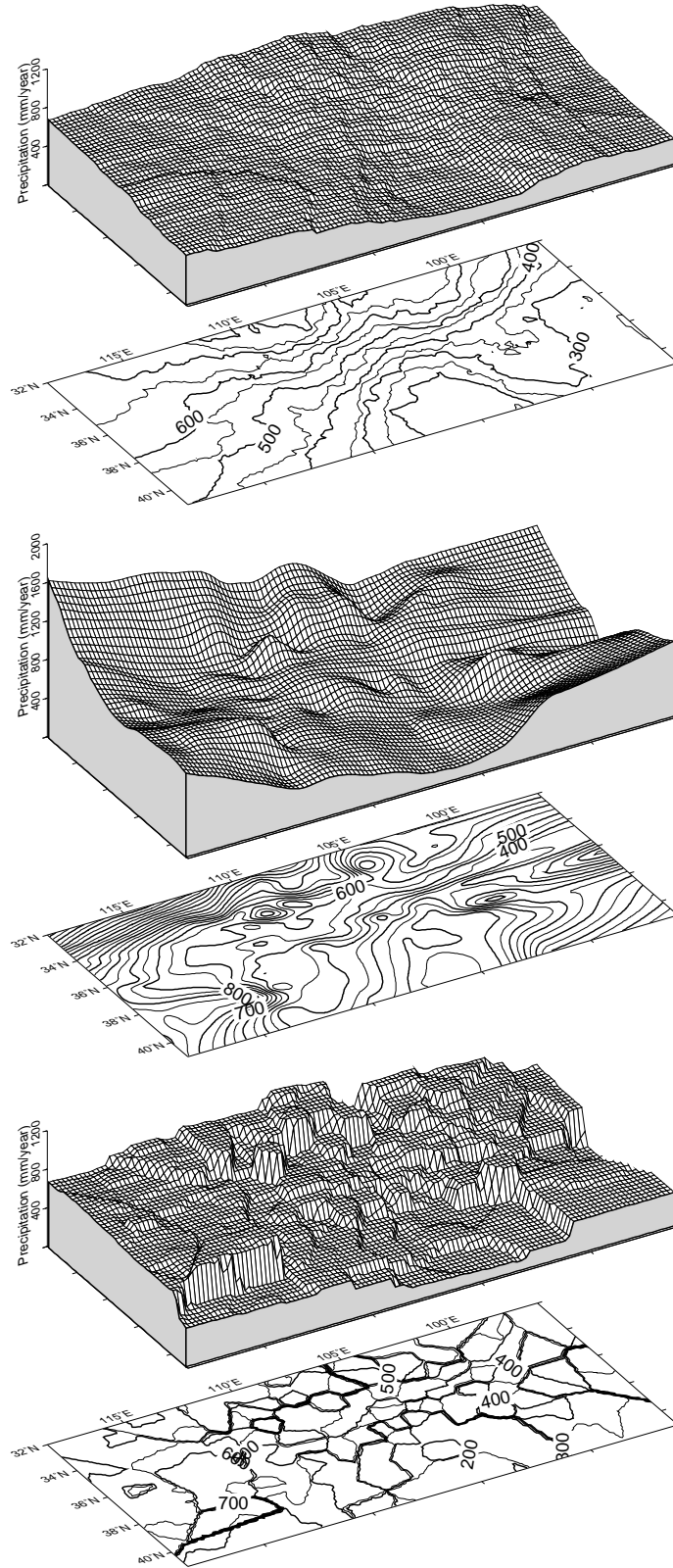


Figure C.3: Interpolation results with IDW (upper), TPS (middle), and TS (lower) method.

C.3.1 DEM Derivative Map

Flow Direction Map

The flow direction data layer defines the direction of flow from each cell in the DEM to its steepest down-slope neighbor. This is calculated as (Jenson and Domingue, 1988):

$$Slope_d = dz/d \quad (C.15)$$

where dz is altitude change, distance d is determined between cell centers. Therefore, if the cell size is 1, the distance between two orthogonal cells is 1, and the distance between two diagonal cells is $\sqrt{2}$. If the descent to all adjacent cells is the same, the neighborhood is enlarged until a steepest descent is found.

Flow Accumulation Map

Assuming homogeneous raining in a region, flow accumulation determines how much rain has fallen within a given watershed. Flow accumulation would then represent the amount of rain that would flow through each cell, assuming that all rain became runoff and there was no interception, evapotranspiration, or loss to groundwater. This could also be viewed as the amount of rain that fell on the surface, upslope from each cell. The flow accumulation data defines the amount of upstream area draining into each cell. It is essentially a measure of the upstream catchment area.

The results of flow accumulation can be used to create a stream network by applying a threshold value to select cells with a high accumulated flow. The flow accumulation map is used in the DBH model system to decide upstream area and judge the river main stem and tributaries.

Flow Length Map

Flow length is the upstream or downstream distance along a flow path for each cell. In DBH model system, the flow length map means the downstream distance to river outlet along the flow direction map. Along the flow direction map, the flow length should be difference from the real river length which is downstream distance along the realistic river path.

C.3.2 Topologically Coding System Based on DEM

Delineation of river basins is an indispensable step if GIS technology is to be used to support river basin planning. Watershed managers often need to understand how engineering applications in one part of a watershed might affect the water usage in another part of the watershed. This implies knowledge of the topological relationships between different parts of the watersheds, i.e. knowing which part (sub-basin) receive flow from or drain to a given part (sub-basin). This knowledge is also very important in hydrological simulation. The topological relationships inside watershed are indispensable to lead the runoff to the outlet with the consideration of the runoff lag time.

Such knowledge on topological relationships inside watershed can be obtained with the DEM derivative flow direction, flow accumulation and flow length map etc. The Pfafstetter Coding system is a methodology for assigning river basin code based on the topology of the land surface (Pfafstetter, 1989; Verdin and Verdin, 1999). The system is hierarchical, and river basins are delineated from junctions on a river network. The Pfafstetter system is designed to exploit features of the base-10 numbering system that mirror these basin characteristics: the ordinal nature of digit values from one through nine, and their binary trait of being alternately odd or even. The ordinal value of a digit indicates relative upstream/downstream position, while a digit's parity indicates network position on or off the main channel (Verdin and Verdin, 1999).

For the Level 1 sub basins, the seeking for the junctions of the sub-basins starts from the outlet grid with the flow direction and flow accumulation map. First, decide the upstream grids from the surround grids according to the flow direction map. Then, check the flow accumulation value of the upstream grids. The upstream grid which has the largest accumulation value is recognized as riverway main stem, other upstream grids are taken as tributary grids. Seeking along the flow direction map until reach the edge of the river basin, the main stem grids with top four largest accumulation values are recorded. These grids are the junctions of the sub-basins and are the partition of the sub-basins, coded as sub-basin 2, 4, 6, and 8 from downstream to upstream. The interbasins between the four sub-basins are codes as interbasin 1, 3, 5, 7, and 9 from downstream to upstream.

Further subdivision is carried out to obtain a Level 2 set of Pfafstetter basins based on the level 1 sub basins. Within each Level 1 basin, or interbasin, main stem and tributary are identified using the same method. The tributary are then sorted by flow accumulation value, and the four largest numbered 2, 4, 6, and 8, going from downstream to upstream along the

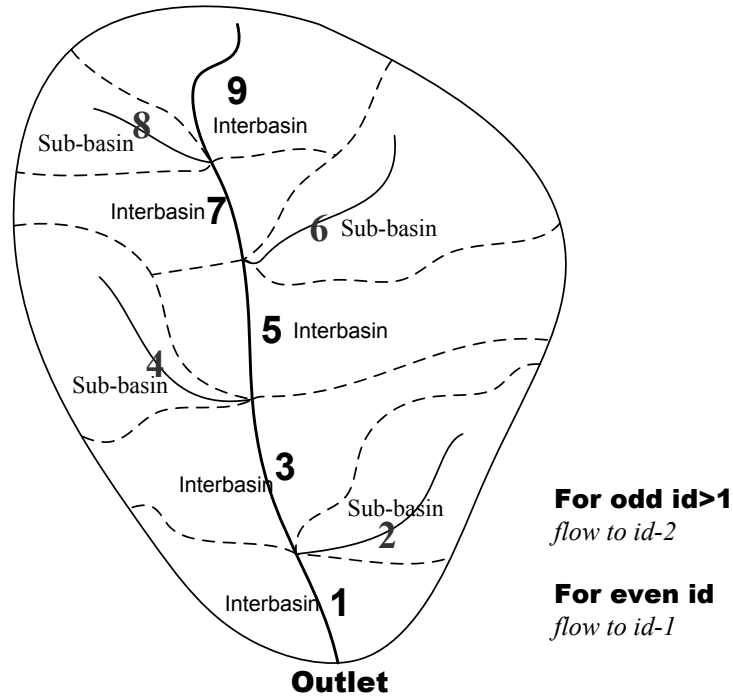


Figure C.4: Sample subdivisions of a sub-basin and an interbasin.

main stem. The corresponding drainage areas are derived using the flow direction map, and all grids are given the second Pfafstetter digit. Pfafstetter Level 2 code is shown in the figure C.5.

This subdivision process can be repeated over and over to obtain successively finer subdivisions of basins and interbasins. The process is ultimately limited by the spatial resolution of the DEM employed. This becomes evident when it is no longer possible to identify four tributaries within a basin or interbasin. In the case of the impossibility to identify four tributaries, the basin number at that level is numbered as zero in the DBH model system. Figure C.6 shows sample subdivisions of Pfafstetter Level 3, in which the Pfafstetter identification numbers with zero digit shows that it is no longer possible to identify four tributaries within a basin or interbasin. For example, the Pfafstetter code '370' shows the Level 1 code of '3', Level 2 code of '7', and Level 3 code of '0'. The Level 3 code of zero means the second subdivision sub-basin '37' is no longer possible to identify four tributaries. The same situation occurs in the sub basin with the Pfafstetter code '610', '910' etc.

Pfafstetter code numbers which end with an even digit represent basins, and numbers that end with an odd value represent interbasins. Upstream-downstream dependency between grids can be inferred by examining and comparing the topological information carried by the identification numbers. Simple rules to check digits with tests of "odd" or "even", and "less

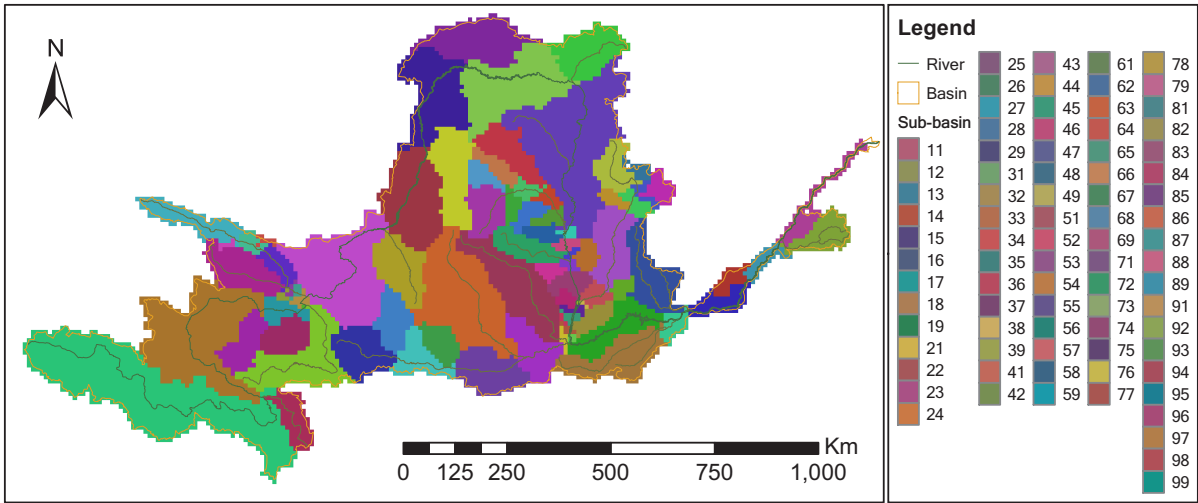


Figure C.5: Sample subdivisions of Pfafstetter Level 2.

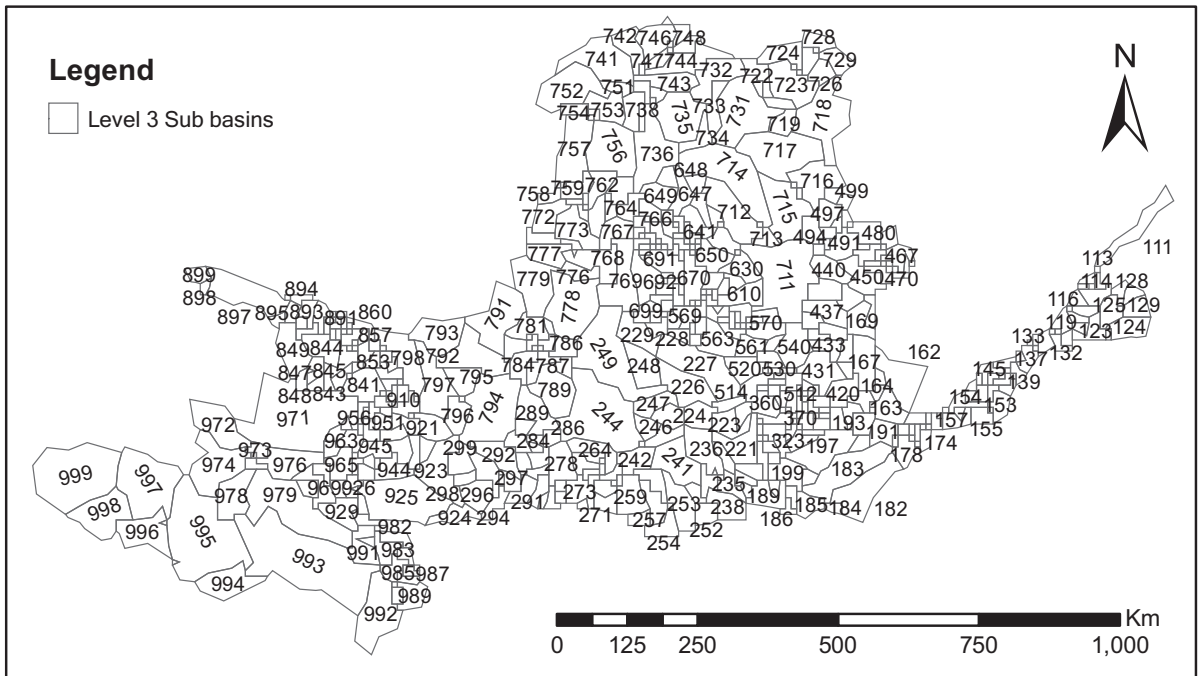


Figure C.6: Sample subdivisions of Pfafstetter Level 3.

than” or ”greater than”, can quickly identify areas of interest for a particular investigation. The river routing scheme in the DBH model system traces through the entire river basin according to the Pfafstetter identification numbers and performs the one-dimension land surface model in the grids from upstream to downstream.

C.4 Time Series Analysis

Time series is an ordered sequence of values of a variable at equally spaced time intervals. The analysis of time series is based on the assumption that the successive data values represent consecutive measurements taken at equally spaced time intervals. The time series analysis is different from the analyses of random samples of observations that are discussed in the statistical context following random orders. Time series analysis accounts for the fact that data points taken over time may have an internal structure (such as autocorrelation, trend or seasonal variation) that should be accounted for. One of the main goals of time series analysis is to identify the nature of the phenomenon represented by the sequence of observations. Most time series patterns can be described in terms of two basic classes of components: trend and seasonality. The trend is a general systematic linear or (most often) nonlinear component that changes over time and does not repeat. The seasonality repeats itself in systematic intervals over time. Considering the climate change is a slow process with long systematic interval, the DBH model system only analyzes the trend.

C.4.1 Trend Detection

If the trend is monotonous (consistently increasing or decreasing), the trend can be detected with typical automatic detect techniques. Many monotonous time series data can be adequately approximated by a linear function. The linear regression model was used to estimate the trend magnitude. The fitting function is:

$$y = mx + b \tag{C.16}$$

where the regression weight m was calculated as

$$m = \frac{N \sum_{i=1}^N x_i y_i - \sum_{i=1}^N x_i \sum_{i=1}^N y_i}{N \sum_{i=1}^N x_i^2 - \left(\sum_{i=1}^N x_i \right)^2} \tag{C.17}$$

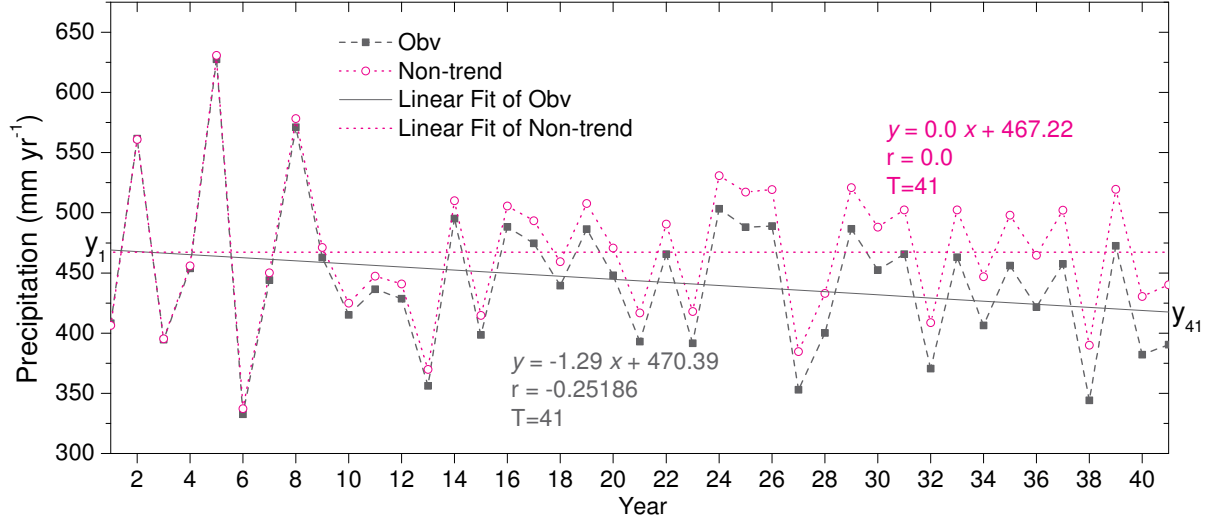


Figure C.7: Trend detection with annual precipitation in the Yellow River basin, 1960-2000.

where N is the span of time during the study period, x_i is the time number, and y_i is the data value at the time x_i . And b is

$$b = \frac{1}{N} \left(\sum_{i=1}^N y_i - m \sum_{i=1}^N x_i \right) \quad (\text{C.18})$$

The correlation coefficient r is

$$r = \frac{N \sum_{i=1}^N x_i y_i - \sum_{i=1}^N x_i \sum_{i=1}^N y_i}{\sqrt{\left[N \sum_{i=1}^N x_i^2 - \left(\sum_{i=1}^N x_i \right)^2 \right] \left[N \sum_{i=1}^N y_i^2 - \left(\sum_{i=1}^N y_i \right)^2 \right]}} \quad (\text{C.19})$$

An example of linear regression model is shown in figure C.7. The statistical significance of the annual trends is evaluated using the Students t-test (Haan, 1977). The significance of a correlation coefficient is tested with

$$t = \frac{r}{\sqrt{(1-r^2)/(N-2)}} \quad (\text{C.20})$$

where t is distributed approximately for t-test with degrees of freedom $df = N - 2$. The non-directional test is then performed with the t-ratio and the degrees of freedom. A significance level of 5% is recommended for usual trend test. The trend magnitude during the study period was estimated from the regression weight:

$$\Delta y = m \cdot N \quad (\text{C.21})$$

In figure C.7, $\Delta y = y_1 - y_{41}$. The relative trend magnitude was represented as:

$$\Delta y' = 100 \cdot N \cdot \Delta y \left/ \sum_{i=1}^N y_i \right. \quad (\text{C.22})$$

C.4.2 Remove Trend Method

The purpose to remove trend is to get a non-linear trend time series. The time series without linear trend is used in non-climate change, non-vegetation change, and non-irrigated area change scenarios. The mean annual precipitation in the Yellow River basin is analyzed in this section as an example. The trend is detected with the linear regression model described in Section C.4.1. The mean value of the non-linear trend time series should be given. If we set the mean value of the non-linear trend time series is the mean precipitation in the 1960s,

$$\overline{y''} = \sum_{i=1}^{10} y_i / 10 \quad (\text{C.23})$$

where $\overline{y''}$ is the mean precipitation in the 1960s. The non-linear trend time series is

$$y_i'' = y_i - (mx_i + b) + \overline{y''} \quad (\text{C.24})$$

The non-trend annual precipitation time series is shown in figure C.7. The same remove trend processes are performed in a point daily precipitation time series. The mean daily precipitation in the first year is set as the mean value the non-linear trend time series. The results are shown in figure C.8.

The remove trend method is simple and can work on the annual or monthly time series. It might not work for daily time series with the data range limitations. Figure C.8 shows the example to remove linear trend from point precipitation time series. The non-trend precipitation time series could be negative value after the simple remove trend method. It is necessary to prevent negative precipitation while keeping the non-linear trend characteristics. The non-linear trend time series with the value limitation y_{lim} is

$$y_i^o = y_i'' - \alpha_o [y_i - (mx_i + b)] \quad (\text{C.25})$$

$$\alpha_o = \frac{y_{min} - y_{lim}}{y_{min} - \overline{y''}} \quad (\text{C.26})$$

where y_{min} is the minimum value of non-linear trend time series y_i'' , y_{lim} is the value limitation and is zero for precipitation data. The non-linear trend time series with the values greater than

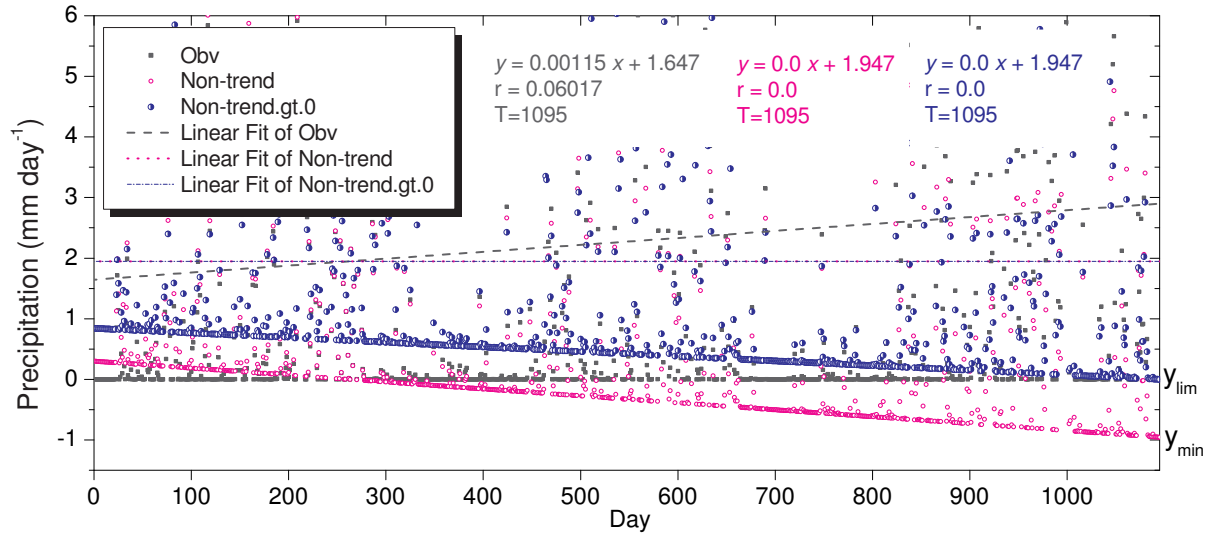


Figure C.8: Remove trend with daily precipitation.

the limitation zero is shown in figure C.8.

Bibliography

- Abbott, M. B., Bathurst, J. C., Cunge, J. A., O'connell, P. E., Rasmussen, J., 1986a. Introduction to the European Hydrological System - Systeme Hydrologique Europeen, SHE, 1: History and Philosophy of a Physically-Based, Distributed Modelling System . J. Hydrol. 87 (1/2), 45–59.
- Abbott, M. B., Bathurst, J. C., Cunge, J. A., O'connell, P. E., Rasmussen, J., 1986b. An introduction to the European Hydrological System - Systeme Hydrologique Europeen, SHE, 2: structure of a physically-based, distributed modelling system. J. Hydrol. 87 (1/2), 61–77.
- Abdulla, F. A., Lettenmaier, D. P., 1997. Development of regional parameter estimation equations for a macroscale hydrologic model. J. Hydrol. 197, 230–257.
- Acrement, G. J., Schneider, V. R., 1989. Guide for Selecting Roughness Coefficients of Natural Channels and Flood Plains. U.S. Geological Survey Water-Supply Paper 2339. Washington, DC: U.S. Government Printing Office.
- Agbu, P. A., James, M. E., 1994. The NOAA/NASA Pathfinder AVHRR Land Dataset Users Manual. Goddard Distributed Active Archive Center Publications, GCDG, Greenbelt, MD, USA.
- Allen, J. C., 1976. A modified sine wave method for calculating degree days. Environ. Entomol. 5, 388–396.
- Allen, R. G., Pereira, L. S., Raes, D., Smith, M., 1998. Crop Evapotranspiration: Guidelines for Computing Crop Water Requirements. FAO Irrig. and Drain. Paper 56. FAO, Rome.
- Alley, W. M., Healy, R. W., LaBaugh, J. W., Reilly, T. E., Jun. 2002. Flow and storage in groundwater systems. Science 296, 1985–1991.
- Ambroise, B., Beven, K., Freer, J., 1996. Toward a generalization of the TOPMODEL concepts: Topographic indices of hydrological similarity. Water Resour. Res. 32 (7), 2135–2146.

- Andersen, J., Refsgaard, J. C., Jensen, K. H., 2001. Distributed hydrological modelling of the Senegal River Basin - model construction and validation. *J. Hydrol.* 247, 200–214.
- Anderson, J. R., Hardy, E. E., Roach, J. T., Witmer, R. E., 1976. A Land Use and Land Cover Classification System for Use with Remote Sensor Data. Tech. rep., U.S. Geological Survey Professional Paper, Washington.
- Angström, A., 1924. Solar and terrestrial radiation. *Q. J. R. Meteorol. Soc.* 50, 121–126.
- Arora, V. K., Boer, G. J., 1999. A variable velocity flow routing algorithm for GCMs. *J. Geophys. Res.* 104, 30965–30980.
- Avissar, R., Pielke, R. A., 1989. A parameterization of heterogeneous land surfaces for atmospheric numerical models and its impact on regional meteorology. *Mon. Weather Rev.* 117 (10), 2113–2136.
- Avissar, R., Schmidt, T., 1998. An evaluation of the scale at which ground-surface heat flux patchiness affects the convective boundary layer using large-eddy simulations. *J. Atmos. Sci.* 55 (16), 2666–2689.
- Band, L. E., Patterson, P., Nemani, R., Running, S. W., 1993. Forest ecosystem processes at the watershed scale: incorporating hillslope hydrology. *Agric. For. Meteorol.* 63, 93–126.
- Band, L. E., Peterson, D. L., Running, S. W., Coughlan, J., Lammers, R., Dungan, J., Nemani, R., 1991. Forest ecosystem processes at the watershed scale: Basis for distributed simulation. *Ecol. Model.* 56, 171–196.
- Baskerville, G. L., Emin, P., 1969. Rapid estimation of heat accumulation from maximum and minimum temperatures. *Ecology* 50 (3), 514–517.
- Bathurst, J. C., Wicks, J. M., O’Connell, P. E., 1995. The SHE/SHESED basin scale water flow and sediment transport modelling system. In: Singh, V. P. (Ed.), *Computer Models of Watershed Hydrology*. Water Resources Publications, LLC, Highlands Ranch, CO, pp. 563–594.
- Beven, K., Wood, E. F., 1983. Catchment geomorphology and the dynamics of runoff contributing areas. *J. Hydrol.* 65, 139–158.
- Beven, K. J., 1995. Chapter 18: TOPMODEL. *Computer models of watershed hydrology*, V. P. Singh, ed. Water Resources Publications, Littleton, Colo.

- Beven, K. J., Kirkby, M. J., 1979. A Physically Based, Variable Contributing Area Model of Basin Hydrology. *Hydrological Sciences Bulletin* 24 (1), 43–69.
- Bonan, G. B., Levis, S., Kergoat, L., Oleson, K. W., May 2002. Landscapes as patches of plant functional types: An integrating concept for climate and ecosystem models. *Glob. Biogeochem. Cycle* 16 (2), 5.1–5.18.
- Boucher, O., Myhre, G., Myhre, A., 2004. Direct human influence of irrigation on atmospheric water vapour and climate. *Clim. Dyn.* 22, 597–603.
- Boyle, J. S., May 1998. Evaluation of the Annual Cycle of Precipitation over the United States in GCMs: AMIP Simulations. *J. Clim.* 11, 1041–1055.
- Brubaker, K. L., Entekhabi, D., 1996. Analysis of feedback mechanisms in land-atmosphere interaction. *Water Resour. Res.* 32, 1343–1358.
- Brunt, D., 1932. Notes on radiation in the atmosphere. *Quart. J. Roy. Meteor. Soc.* 58, 389–418.
- Brutsaert, W., 1975. On a derivable formula for long-wave radiation from clear skies. *Water Resour. Res.* 11, 742–744.
- Burrough, P. A., 1986. *Principles of Geographical Information Systems for land resources assessment*. Oxford University Press, New York.
- Carlson, T. N., Ripley, D. A., 1997. On the relation between NDVI, fractional vegetation cover, and leaf area index. *Remote Sens. Environ.* 62, 241–252.
- Cesaraccio, C., Spano, D., Duce, P., Snyder, R. L., 2001. An improved model for determining degree-day values from daily temperature data. *Int. J. Biometeorol.* 45, 161–169.
- Chen, J., Mu, X., 2000. Tendency, causes and control measures on Yellow River dry up. *Journal of natural resources* 15 (1), 31–35 (in Chinese).
- Chen, J. M., Chen, X., Ju, W., Geng, X., 2005. Distributed hydrological model for mapping evapotranspiration using remote sensing inputs. *J. Hydrol.* 305, 15–39.
- Chen, J. Y., Tang, C. Y., Sakura, Y., Kondoh, A., Shen, Y. J., 2002. Groundwater flow and geochemistry in the lower reaches of the Yellow River: a case study in Shandong Province, China. *Hydrogeol. J.* 10 (5), 587–599.
- Childs, E. C., 1971. Drainage of groundwater resting on a sloping bed. *Water Resour. Res.* 7 (5), 1256–1263.

- Choudhury, B. J., Golus, R. E., 1988. Estimating soil wetness using satellite data. *Int. J. Remote Sens.* 9 (7), 1251–1257.
- Chow, V. T., 1959. *Open-channel Hydraulics*. McGraw-Hill: New York.
- Clapp, R. B., Hornberger, G. M., 1978. Empirical equations for some soil hydraulic-properties. *Water Resour. Res.* 14, 601–604.
- Cosby, B. J., Hornberger, G. M., Clapp, R. B., Ginn, T. R., 1984. A statistical exploration of the relationships of soil moisture characteristics to the physical properties of soils. *Water Resour. Res.* 20, 682–690.
- Crawford, N. H., Linsley, R. K., 1966. *Digital Simulation in Hydrology: Stanford Watershed Model IV*. Stanford Univ., Palo Alto, Calif., Tech. Rep. No. 39.
- de Wit, C. T., Goudriaan, J., van Laar, H. H., 1978. *Simulation of Assimilation, Respiration and Transpiration of Crops*. Center for Agricultural Publishing and Documentation, Wageningen, The Netherlands.
- Deardorff, J. W., Apr. 1978. Efficient prediction of ground surface temperature and moisture, with inclusion of a layer of vegetation. *J. Geophys. Res.* 83, 1889–1904.
- Desborough, C. E., Pitman, A. J., 1998. The BASE land surface model. *Global Planet. Change* 19, 3–181.
- Dickinson, R. E., Henderson-Sellers, A., Kennedy, P. J., Wilson, M. F., 1986. Biosphere-atmosphere Transfer Scheme (BATS) for the NCAR Community Climate Model. NCAR Tech. Note NCAR/TN-387+STR. National Center for Atmospheric Research, Boulder, CO.
- Döll, P., Siebert, S., 2002. Global modeling of irrigation water requirements. *Water Resour. Res.* 38, 8.1–8.10.
- Doorenbos, J., Pruitt, W. O., 1977. *Guidelines for Predicting Crop Water Requirements*. FAO Irrig. and Drain. Paper 24. FAO, Rome.
- Dutta, D., 1999. *Distributed Modelling of Flood Inundation and Damage Estimation*. the University of Tokyo, Tokyo, Japan, Ph.D. thesis.
- Easterling, D. R., Horton, B., Jones, P. D., Peterson, T. C., Karl, T. R., Parker, D. E., Salinger, M. J., Razuvayev, V., Plummer, N., Jamason, P., Folland, C. K., Jul. 1997. Maximum and minimum temperature trends for the globe. *Science* 277 (5324), 364–367.

- Engel, V. C., Stieglitz, M., Williams, M., Griffin, K. L., 2002. Forest canopy hydraulic properties and catchment water balance: observations and modeling. *Ecol. Model.* 154, 263–288.
- Entekhabi, D., Asrar, G. R., Betts, A. K., Beven, K. J., Bras, R. L., Duffy, C. J., Dunne, T., Koster, R. D., Lettenmaier, D. P., McLaughlin, D. B., Shuttleworth, W. J., van Genuchten, M. T., Wei, M.-Y., Wood, E. F., Oct. 1999. An agenda for land surface hydrology research and a call for the second international hydrological decade. *Bull. Amer. Meteorol. Soc.* 80 (10), 2043–2058.
- Entekhabi, D., Eagleson, P. S., 1989. Land surface hydrology parameterization for atmospheric general circulation models including subgrid scale spatial variability. *J. Clim.* 2 (8), 816–831.
- ESRI, 1992. *Cell Based Modeling With GRID*. ESRI, Inc., Redlands, California.
- FAO, 1995. *Digital Soil Map of the World and Derived Soil Properties*. CD-ROM, Land and Water Digital Media Series No. 7, Food and Agriculture Organization of the United Nations, Rome.
- Feng, J. M., Wang, T., Qi, S. Z., Xie, G. W., 2005. Land degradation in the source region of the Yellow River, northeast Qinghai-Xizang Plateau: classification and evaluation. *Environ. Geol.* 47 (4), 459–466.
- Fu, G., Chen, S. L., Liu, C. M., Shepard, D., 2004. Hydro-climatic trends of the Yellow River basin for the last 50 years. *Clim. Change* 65 (1-2), 149–178.
- Gadgil, S., Sajani, S., 1998. Monsoon precipitation in the AMIP runs. *Climate Dyn.* 14, 659–689.
- Gao, X., Sorooshian, S., 1994. A stochastic precipitation disaggregation scheme for GCM applications. *J. Clim.* 7, 238–247.
- Ghan, S. J., Liljegren, J. C., Shaw, W. J., Hubbe, J. H., Doran, J. C., 1997. Influence of subgrid variability on surface hydrology. *J. Clim.* 10, 3157–3166.
- Giorgi, F., 1997a. An approach for the representation of surface heterogeneity in land surface models. Part I: theoretical framework. *Mon. Weather Rev.* 125 (8), 1885–1899.
- Giorgi, F., 1997b. An approach for the representation of surface heterogeneity in land surface models. Part II: validation and sensitivity experiments. *Mon. Weather Rev.* 125 (8), 1900–1919.

- Giorgi, F., Avissar, R., 1997. Representation of heterogeneity effects in Earth system modeling: experience from land surface modeling. *Rev. Geophys.* 35 (4), 413–438.
- Gleick, P. H., Nov. 2003. Global freshwater resources: Soft-path solutions for the 21st century. *Science* 302, 1524–1528.
- Gordon, L. J., Steffen, W., Jonsson, B. F., Folke, C., Falkenmark, M., Johannessen, A., 2005. Human modification of global water vapor flows from the land surface. *Proc. Natl. Acad. Sci. U. S. A.* 102, 7612–7617.
- Goward, S. N., Markham, B., Dye, D. G., Dulaney, W., Yang, J., 1991. Normalized difference vegetation index measurements from the Advanced Very High Resolution Radiometer. *Remote Sens. Environ.* 35, 257–277.
- Grist, J., Nicholson, S. E., Mpolokang, A., 1997. On the use of NDVI for estimating rainfall fields in the Kalahari of Botswana. *J. Arid Environ.* 35 (2), 195–214.
- Haan, C., 1977. *Statistical Methods in Hydrology*. Iowa State University Press, Ames, IA.
- Haddeland, I., Lettenmaier, D. P., Skaugen, T., 2005. Effects of irrigation on the water and energy balances of the Colorado and Mekong river basins. *J. Hydrol.* 324, 210–223.
- Hager, W. H., 1984. A simplified hydrological rainfall-runoff model. *J. Hydrol.* 74, 151–170.
- Hansen, J., Lebedeff, S., Nov. 1987. Global trends of measured surface air temperature. *J. Geophys. Res.* 92, 13345–13372.
- Holben, B. N., 1986. Characteristics of maximum-value composite images for temporal AVHRR data. *Int. J. Remote Sens.* 7 (11), 1417–1434.
- Hornberger, G. M., Boyer, E. W., 1995. Recent advances in watershed modelling. *Rev. Geophys. Suppl.* 33, 693–697.
- Horton, R. E., 1939. Analysis of runoff-plat experiments with varying infiltration capacity. *Trans. Am. Geophys. Union* 20, 693–711.
- Hou, Y. T., Campana, K. A., Mitchell, K. E., Yang, S. K., Stowe, L. L., 1993. Comparison of an experimental NOAA AVHRR cloud dataset with other observed and forecast cloud datasets. *J. Atmos. Ocean. Technol.* 10, 833–849.

- Hu, H. P., Tang, Q. H., Lei, Z. D., Yang, S. X., 2004. Runoff-evaporation hydrological model for arid plain oasis I: the model structure. *Shuikexue Jinzhan/Advances in Water Science* 15 (2), 140–145, (in Chinese).
- Huang, M., Zhang, L., 2004. Hydrological responses to conservation practices in a catchment of the Loess Plateau, China. *Hydrol. Process.* 18, 1885–1898.
- Hutchinson, M. F., 1995. Interpolating mean rainfall using thin-plate smoothing splines. *Int. J. Geogr. Inf. Syst.* 9 (4), 385–403.
- Hutchinson, M. F., Gessler, P. E., 1994. Splines - more than just a smooth interpolator. *Geoderma* 62 (1-3), 45–67.
- Hutjes, R. W. A., Kabat, P., Running, S. W., Shuttleworth, W. J., Field, C., Bass, B., da Silva Dias, M. A. F., Avissar, R., Becker, A., Claussen, M., Dolman, A. J., Feddes, R. A., Fosberg, M., Fukushima, Y., Gash, J. H. C., Guenni, L., Hoff, H., Jarvis, P. G., Kayane, I., Krenke, A. N., Liu, C. M., Meybeck, M., Nobre, C. A., Oyebande, L., Pitman, A., Pielke Sr, R. A., Raupach, M., Saugier, B., Schulze, E. D., Sellers, P. J., Tenhunen, J. D., Valentini, R., Victoria, R. L., Vörösmarty, C. J., 1998. Biospheric aspects of the hydrological cycle. *J Hydrol.* 212-213, 1–21.
- HYDRO1k Team, 2003. Web page of the HYDRO1k Elevation Derivative Database. Tech. rep., Available at <http://edcdaac.usgs.gov/gtopo30/hydro>.
- Information Center of Water Resources, 1950-1990. Hydrological Year Book (in Chinese). Bur. Hydrol., Beijing.
- Jackson, R. D., Slater, P. N., Pinter, P. J., 1983. Discrimination of growth and water stress in wheat by various vegetation indices through clear and turbid atmospheres. *Remote Sens. Environ.* 13 (3), 187–208.
- James, M. E., Kalluri, S. N. V., Nov. 1994. The Pathfinder AVHRR land data set: An improved coarse resolution data set for terrestrial monitoring. *Int. J. Remote Sens.* 15 (17), 3347–3363.
- Jenson, S. K., Domingue, J. O., 1988. Extracting topographic structure from Digital Elevation Data for Geographic Information System analysis. *Photogramm. Eng. Remote Sens.* 54, 1593–1600.

- Jia, R., 1997. Development of Distributed Hydrological Model Incorporation Surface Flow Interactions and its Application in Large Tropical Catchments. the University of Tokyo, Tokyo, Japan, Ph.D. thesis.
- Jiménez, J. I., Alados-Arboledas, L., Castro-Diez, Y., Ballester, G., 1987. On the estimation of long-wave radiation flux from clear skies. *Theor. Appl. Climatol.* 38, 37–42.
- Jones, P. D., Osborn, T. J., Briffa, K. R., 1997. Estimating sampling errors in large-scale temperature averages. *J. Clim.* 10 (10), 2548–2568.
- Justice, C. O., Townshend, J. R. G., Holben, B. N., Tucker, C. J., 1985. Analysis of the phenology of global vegetation using meteorological satellite data. *Int. J. Remote Sens.* 6 (8), 1271–1318.
- Kaiser, D. P., Oct. 1998. Analysis of total cloud amount over China, 1951–1994. *Geophys. Res. Lett.* 25, 3599–3602.
- Kimball1, J. S., Running, S. W., Nemani, R., 1997. An improved method for estimating surface humidity from daily minimum temperature. *Agric. For. Meteorol.* 85, 87–98.
- Koster, R. D., Suarez, M. J., 1992a. A comparative analysis of two land surface heterogeneity representations. *J. Clim.* 5, 1379–1390.
- Koster, R. D., Suarez, M. J., 1992b. Modeling the land surface boundary in climate models as a composite of independent vegetation stands. *J. Geophys. Res.* 97, 2697–2715.
- Lakshmi, V., Apr. 2004. The role of satellite remote sensing in the Prediction of Ungauged Basins. *Hydrol. Process.* 18, 1029–1034.
- Lau, K.-M., Sud, Y., Kim, J. H., Oct. 1996. Intercomparison of hydrologic processes in AMIP GCMs. *Bull. Amer. Meteor. Soc.* 77, 2209–2228.
- Legates, D. R., Willmott, C. J., 1990. Mean seasonal and spatial variability in global surface air temperature. *Theor. Appl. Climatol.* 41, 11–21.
- Leung, L. R., Ghan, S. J., 1998. Parameterizing subgrid orographic precipitation and surface cover in climate models. *Mon. Weather Rev.* 126 (12), 3271–3291.
- Li, C., Yang, D., Ni, G., Hu, H., 2004. Simulation of irrigation water consumption in the Yellow River basin using a distributed hydrological model. In: *Proceedings of the Second*

- International Conference on Hydrology and Water Resources in Asia Pacific Region. APHW, Singapore.
- Liang, X., Lettenmaier, D. P., Wood, E. F., Burges, S. J., Jul. 1994. A simple hydrologically based model of land surface water and energy fluxes for general circulation models. *J. Geophys. Res.* 99, 14415–14428.
- Liang, X., Xie, Z., 2001. A new surface runoff parameterization with subgrid-scale soil heterogeneity for land surface models. *Adv. Water Resour.* 24, 1173–1193.
- Lighthill, M. H., Whitham, G. B., 1955. On kinematic waves, I. Flood movement in long rivers. *Proc. R. Soc. London* 229, 281–316.
- Liu, C., Zhang, X., 2004. Causal analysis on actual water flow reduction in the mainstream of the Yellow River. *Acta. Geographica. Sinica.* 59 (3), 323–330 (in Chinese).
- Liu, C. M., Zhang, S. F., 2002. Drying up of the Yellow River: its impacts and counter-measures. *Mitigation and Adaptation Strategies for Global Change* 7 (3), 203–214.
- Liu, C. M., Zheng, H. X., 2004. Changes in components of the hydrological cycle in the Yellow River basin during the second half of the 20th century. *Hydrol. Process.* 18 (12), 2337–2345.
- Liu, L. L., Yang, Z. F., Shen, Z. Y., 2003. Estimation of water renewal times for the middle and lower sections of the Yellow River. *Hydrol. Process.* 17, 1941–1950.
- Liu, S., Zhang, S., Liu, C., 2001. Advances on the research into the mechanism of hydrological cycle in Yellow River catchment. *Acta. Geographica. Sinica.* 20 (3), 257–265 (in Chinese).
- Liu, X. D., Chen, B. D., 2000. Climatic warming in the Tibetan Plateau during recent decades. *Int. J. Climatol.* 20 (14), 1729–1742.
- Loveland, T. R., Reed, B. C., Brown, J. F., Ohlen, D. O., Zhu, Z., Yang, L., Merchant, J. W., 2000. Development of a global land cover characteristics database and IGBP DISCover from 1 km AVHRR data. *Int. J. Remote Sens.* 21 (6-7), 1303–1330.
- Loveland, T. R., Zhu, Z., Ohlen, D. O., Brown, J. F., Reed, B. C., Yang, L., Sep. 1999. An analysis of the IGBP global land-cover characterization process. *Photogramm. Eng. Remote Sens.* 65 (9), 1021–1032.
- Luo, Z., Wahba, G., Johnson, D. R., 1998. Spatial-temporal analysis of temperature using smoothing spline ANOVA. *J. Clim.* 11, 18–28.

- Mackay, D. S., Band, L. E., Jul. 1997. Forest ecosystem processes at the watershed scale: dynamic coupling of distributed hydrology and canopy growth. *Hydrol. Process.* 11, 1197–1217.
- Manabe, S., 1969. Climate and the ocean circulation I. The atmospheric circulation and the hydrology of the Earth's surface. *Mon. Weather Rev.* 97 (11), 739–774.
- Matheussen, B., Kirschbaum, R. L., Goodman, I. A., O'Donnell, G. M., Lettenmaier, D. P., Apr. 2000. Effects of land cover change on streamflow in the interior Columbia River Basin (USA and Canada). *Hydrol. Process.* 14, 867–885.
- Milly, P. C. D., Dunne, K. A., Apr. 1994. Sensitivity of the global water cycle to the water-holding capacity of land. *J. Clim.* 7, 506–526.
- Milly, P. C. D., Eagleson, P. S., 1988. Effect of storm scale on surface runoff volume. *Water Resour. Res.* 24 (4), 620–624.
- Mo, X. G., Liu, S. X., Lin, Z. H., Zhao, W. M., 2004. Simulating temporal and spatial variation of evapotranspiration over the Lushi basin. *J. Hydrol.* 285, 125–142.
- Moore, I. D., Grayson, R. B., Ladson, A. R., 1991. Digital terrain modelling: a review of hydrological, geomorphological, and biological applications. *Hydrol. Process.* 5 (1), 3–30.
- Moore, I. D., O'Loughlin, E. M., Burch, G. J., 1988a. A contour based topographic model for hydrological and ecological applications. *Earth Surf. Proc. Land.* 13, 305–320.
- Moore, I. D., Pamuska, J. C., Grayson, R. B., Srivastava, K. P., 1988b. Application of digital topographic modeling in hydrology. *Proc., Int. Symposium on Modeling Agricultural, Forest, and Rangeland Hydrology*, Publication No. 07-88, American Society of Agricultural Engineers, St. Joseph, Mich.
- Murphy, A. H., 1988. Skill scores based on the mean square error and their relationships to the correlation coefficient. *Mon. Weather Rev.* 16, 2417–2424.
- Myneni, R. B., Nemani, R. R., Running, S. W., 1997. Estimation of global leaf area index and absorbed par using radiative transfer models. *IEEE T Geosci. Remote.* 35 (6), 1380–1393.
- New, M., Hulme, M., Jones, P., Mar. 1999. Representing twentieth-century space-time climate variability. Part I: Development of a 1961-90 mean monthly terrestrial climatology. *J. Clim.* 12 (3), 829–856.

- New, M., Hulme, M., Jones, P., 2000. Representing twentieth-century space-time climate variability. Part II: development of 1901-96 monthly grids of terrestrial surface climate. *J. Clim.* 13 (13), 2217–2238.
- Ni, G., 1994. Distributed Catchment Modelling Including Efficient Subsurface Flow Simulation. the University of Tokyo, Tokyo, Japan, Ph.D. thesis.
- Niemelä, S., Räisänen, P., Savijärvi, H., 2001. Comparison of surface radiative flux parameterizations. Part I: Longwave radiation. *Atmos. Res.* 58, 1–18.
- Nijssen, B., O'Donnell, G. M., Lettenmaier, D. P., 2001. Predicting the discharge of global rivers. *J. Clim.* 14 (15), 3307–3323.
- Nilsson, C., Reidy, C. A., Dynesius, M., Revenga, C., Apr. 2005. Fragmentation and flow regulation of the world's large river systems. *Science* 308, 405–408.
- NRC, 1991. Opportunities in the Hydrologic Sciences. National Academy Press, Washington, D.C.
- Oki, T., Sud, Y. C., 1998. Design of Total Runoff Integrating Pathways (TRIP)-a global river channel network. *Earth Interactions* 2, 1–37.
- Oreskes, N., Shrader-Frechette, K., Belitz, K., Feb. 1994. Verification, validation, and confirmation of numerical models in the earth sciences. *Science* 263, 641–646.
- Ottlé, C., Vidal-Madjar, D., Girard, G., 1989. Rainfall-runoff modeling - Past, present and future. *J. Hydrol.* 105, 369–384.
- Parton, W. J., Logan, J. A., 1981. A model for diurnal-variation in soil and air-temperature. *Agr. Meteorol.* 23 (3), 205–216.
- Pfafstetter, O., 1989. Classification of Hydrographic Basins: Coding Methodology. unpublished manuscript, Departamento Nacional de Obras de Saneamento, 18 August 1989, Rio de Janeiro.
- Pielke, R. A., 2001. Influence of the spatial distribution of vegetation and soils on the prediction of cumulus convective rainfall. *Rev. Geophys.* 39, 151–178.
- Pietroniro, A., Leconte, R., 2000. A review of Canadian remote sensing applications in hydrology, 1995-1999. *Hydrol. Process.* 14, 1641–1666.

- Pietroniro, A., Leconte, R., 2005. A review of Canadian remote sensing applications in hydrology, 1999-2003. *Hydrol. Process.* 19, 285–301.
- Pietroniro, A., Prowse, T. D., Jun. 2002. Preface: Applications of remote sensing in hydrology. *Hydrol. Process.* 16, 1537–1541.
- Piper, S. C., Stewart, E. F., 1996. A gridded global data set of daily temperature and precipitation for terrestrial biospheric modeling. *Global Biogeochem. Cy.* 10 (4), 757–782.
- Pitman, A. J., Apr. 2003. The evolution of, and revolution in, land surface schemes designed for climate models. *Int. J. Climatol.* 23, 479–510.
- Pitman, A. J., Henderson-Sellers, A., Yang, Z. L., 1990. Sensitivity of regional climates to localised precipitation in global models. *Nature* 346, 734–737.
- Revfeim, K. J. A., 1997. On the relationship between radiation and mean daily sunshine. *Agr. Forest Meteorol.* 86, 181–191.
- Roerink, G. J., Menenti, M., Verhoef, W., Jun. 2000. Reconstructing cloudfree NDVI composites using Fourier analysis of time series. *Int. J. Remote Sens.* 21 (9), 1911C1917.
- Running, S. W., Coughlan, J. C., Aug. 1988. A general model of forest ecosystem processes for regional applications: I. Hydrologic balance, canopy gas exchange and primary production processes. *Ecol. Model.* 42 (2), 125–154.
- Rushton, K. R., Tomlinson, T. M., 1979. Possible mechanisms for leakage between aquifers and rivers. *J. Hydrol.* 40, 49–65.
- Russell, G. L., Miller, J. R., 1990. Global river runoff calculated from a global atmospheric general circulation model. *J. Hydrol.* 117, 241–254 (in Chinese).
- Rykiel, E. J. J., 1996. Testing ecological models: the meaning of validation. *Ecol. Model.* 90, 229–244.
- Schultz, G. A., 1993. Hydrological modeling based on remote sensing information. *Adv. Space Res.* 13 (5), (5)149–(5)166.
- Sellers, P. J., 1985. Canopy reflectance, photosynthesis and transpiration. *Int. J. Remote Sens.* 6 (8), 1335–1372.

- Sellers, P. J., Dickinson, R. E., Randall, D. A., Betts, A. K., Hall, F. G., Berry, J. A., Collatz, G. J., Denning, A. S., Mooney, H. A., Nobre, C. A., Sato, N., Field, C. B., Henderson-Sellers, A., 1997. Modeling the exchanges of energy, water, and carbon between continents and the atmosphere. *Science* 275 (5299), 502–509.
- Sellers, P. J., Meeson, B. W., Hall, F. G., Asrar, G., Murphy, R. E., Schiffer, R. A., Bretherton, F. P., Dickinson, R. E., Ellingson, R. G., Field, C. B., Huemmrich, K. F., Justice, C. O., Melack, J. M., Roulet, N. T., Schimel, D. S., Try, P. D., 1995. Remote sensing of the land surface for studies of global change: models - algorithms - experiments. *Remote Sens. Environ.* 51, 3–26.
- Sellers, P. J., Mintz, Y., Sud, Y. C., Dalcher, A., 1986. A simple biosphere model (SiB) for use within general circulation models. *J. Atmos. Sci.* 43, 505–531.
- Sellers, P. J., Randall, D. A., Collatz, G. J., Berry, J. A., Field, C. B., Dazlich, D. A., Zhang, C., Collelo, G. D., Bounoua, L., 1996. A revised land surface parameterization (SiB2) for atmospheric GCMs - Part I: model formulation. *J. Clim.* 9, 676–705.
- Seth, A., Giorgi, F., 1996. Three-dimensional model study of organized mesoscale circulations induced by vegetation. *J. Geophys. Res.* 101 (D3), 7371–7392.
- Seth, A., Giorgi, F., Dickinson, R. E., 1994. Simulating fluxes from heterogeneous land surfaces: explicit subgrid method employing the biosphere-atmosphere transfer scheme (BATS). *J. Geophys. Res.* 99, 18651–18667.
- Siebert, S., Döll, P., Feick, S., Hoogeveen, J., 2005. Global Map of Irrigated Areas Version 3.0. Johann Wolfgang Goethe University, Frankfurt am Main, Germany/FAO, Rome, Italy.
- Singh, V. P. (Ed.), 1995. *Computer Models of Watershed Hydrology*. Water Resources Publications, LLC, Highlands Ranch, CO.
- Singh, V. P., Frevert, D. K. (Eds.), 2002a. *Mathematical Models of Large Watershed Hydrology*. Water Resources Publications, LLC, Highlands Ranch, CO.
- Singh, V. P., Frevert, D. K. (Eds.), 2002b. *Mathematical Models of Small Watershed Hydrology and Applications*. Water Resources Publications, LLC, Highlands Ranch, CO.
- Singh, V. P., Woolhiser, D. A., 2002. Mathematical modeling of watershed hydrology. *J. Hydrol. Eng.* 7 (4), 270–292.

- Steinwand, D. R., 1994. Mapping raster imagery to the Interrupted Goode Homolosine projection. *Int. J. Remote Sens.* 15 (17), 3463–3471.
- Steinwand, D. R., Hutchinson, J. A., Snyder, J. P., 1995. Map projections for global and continental data sets and an analysis of pixel distortion caused by reprojection. *Photogramm. Eng. Remote Sens.* 61, 1487–1497.
- Stohlgren, T. J., Chase, T. N., Pielke Sr., R. A., Kittel, T. G. F., Baron, J. S., 1998. Evidence that local land use practices influence regional climate, vegetation, and stream flow patterns in adjacent natural areas. *Glob. Change Biol.* 4, 495–504.
- Storck, P., Bowling, L., Wetherbee, P., Lettenmaier, D., May 1998. Application of a GIS-based distributed hydrology model for prediction of forest harvest effects on peak stream flow in the Pacific Northwest. *Hydrol. Process.* 12, 889–904.
- Stowe, L. L., 1991. Cloud and aerosol products at NOAA/NESDIS. *Glob. Planet. Change* 4, 25–32.
- Stowe, L. L., Davis, P. A., McClain, E. P., 1999. Scientific basis and initial evaluation of the CLAVR-1 global clear/cloud Classification algorithm for the Advanced Very High Resolution Radiometer. *J. Atmos. Ocean. Technol.* 16 (6), 656–681.
- Stowe, L. L., McClain, E. P., Carey, R., Pellegrino, P., Gutman, G. G., Davis, P., Long, C., Hart, S., 1991. Global distribution of cloud cover derived from NOAA/AVHRR operational satellite data. *Adv. Space Res.* 11, 51–54.
- Su, Z., 2000. Remote sensing of land use and vegetation for mesoscale hydrological studies. *Int. J. Remote Sens.* 21 (2), 213–233.
- Sun, R., Liu, C., Zhu, Q., 2001. Relationship between the fractional vegetation cover change and rainfall in the Yellow River Basin. *Acta. Geographica. Sinica.* 56 (6), 667–672 (in Chinese).
- Szilagyi, J., Rundquist, D. C., Gosselin, D. C., Parlange, M. B., May 2000. NDVI relationship to monthly evaporation. *Geophys. Res. Lett.* 25 (10), 1753–1756.
- Tang, Q., 2006. Hydrological cycle representation with runoff-evaporation processes. *Earth Surf. Process. Landf.*, submitted.
- Tang, Q., Hu, H., Oki, T., 2006a. Groundwater recharge and discharge in a hyperarid alluvial plain (Akesu, Taklimakan Desert, China). *Hydrol. Process.*, accepted.

- Tang, Q., Hu, H., Oki, T., 2006b. Water balance within intensively cultivated alluvial plain in an arid environment. *Water Resour. Manag.*, submitted.
- Tang, Q., Oki, T., 2006. Daily NDVI relationship to cloud cover. *J. Appl. Meteorol.*, submitted.
- Tang, Q., Oki, T., Hu, H., 2006. A distributed biosphere hydrological model (DBHM) for large river basin. *Ann. J. Hydraul. Eng. JSCE* 50, 37–42.
- Tang, Q., Oki, T., Kanae, S., Hu, H., 2006. The influence of precipitation variability and partial irrigation within grid cells on a hydrological simulation. *J. Hydromet.*, submitted.
- Tang, Q. H., 2003. A Study of Dissipative Hydrological Model for Arid Plain Oasis. Tsinghua University, Beijing, China, Master thesis (in Chinese).
- Tang, Q. H., Tian, F. Q., Hu, H. P., 2004. Runoff-evaporation hydrological model for arid plain oasis II: the model application. *Shuikexue Jinzhan/Advances in Water Science* 15 (2), 146–150, (in Chinese).
- Tarpley, J. D., Schneider, S. R., Money, R. L., Mar. 1984. Global vegetation indices from the NOAA-7 meteorological satellite. *J. Appl. Meteor.* 23 (3), 491–494.
- Thiessen, A. H., 1911. Precipitation averages for large areas. *Mon. Wea. Rev.* 39, 1082–1084.
- Todini, E., 1988. Rainfall-runoff modeling - Past, present and future. *J. Hydrol.* 100, 341–352.
- Towner, G. D., 1975. Drainage of groundwater resting on a sloping bed with uniform rainfall. *Water Resour. Res.* 11 (1), 144–147.
- Tucker, C. J., 1979. Red and photographic infrared linear combinations for monitoring vegetation. *Remote Sens. Environ.* 8 (2), 127–150.
- Tucker, C. J., Dregne, H. E., Newcomb, W. W., Jul. 1991. Expansion and contraction of the Sahara Desert from 1980 to 1990. *Science* 253 (5017), 299–301.
- UN-SWI, 1997. Comprehensive Assessment of the Freshwater Resources of the World. United Nations and the Stockholm Water Institute, World Meteorological Organization.
- Vanshaar, J. R., Haddeland, I., Lettenmaier, D. P., Sep. 2002. Effects of land-cover changes on the hydrological response of interior Columbia River basin forested catchments. *Hydrol. Process.* 16, 2499–2520.

- Verdin, K. L., Greenlee, S. K., 1996. Development of continental scale digital elevation models and extraction of hydrographic features. In: Proceedings, Third International Conference/Workshop on Integrating GIS and Environmental Modeling, Santa Fe, New Mexico.
- Verdin, K. L., Verdin, J. P., 1999. A topological system for delineation and codification of the Earth's river basins. *J. Hydrol.* 218, 1–12.
- Verhoef, W., Menenti, M., Azzali, S., Jan. 1996. A colour composite of NOAA-AVHRR-NDVI based on time series analysis (1981-1992). *Int. J. Remote Sens.* 17 (2), 231–235.
- Vitousek, P. M., Mooney, H. A., Lubchenco, J., Melillo, J. M., 1997. Human domination of Earth's ecosystems. *Science* 277, 494–499.
- Vörösmarty, C. J., Moore, B., Grace, A. L., Gildea, M. P., Melillo, J. M., Peterson, B. J., Rastetter, E. B., Steudler, P. A., 1989. Continental-scale models of water balance and fluvial transport: An application to South America. *Global Biogeochem. Cy.* 3, 241–266.
- Vörösmarty, C. J., Sahagian, D., 2000. Anthropogenic disturbance of the terrestrial water cycle. *Bioscience* 50 (9), 753–765.
- Wang, G., Qian, J., Cheng, G., Lai, Y., 2001. Eco-environmental degradation and causal analysis in the source region of the Yellow River. *Environ. Geol.* 40 (7), 884–890.
- Wiegand, C. L., Richardson, A. J., Kanemasu, E. T., 1979. Leaf area index estimates for wheat from LANDSAT and their implications for evapotranspiration and crop modeling. *Agron. J.* 71 (2), 336–342.
- Wigmosta, M. S., Vail, L. W., Lettenmaier, D. P., 1994. A distributed hydrology-vegetation model for complex terrain. *Water Resour. Res.* 30, 1665–1680.
- Willmott, C. J., Rowe, C. M., Philpot, W. D., 1985. Small-scale climate maps - a sensitivity analysis of some common assumptions associated with grid-point interpolation and contouring. *Am. Cartographer* 12 (1), 5–16.
- Xia, J., Wang, Z. G., Wang, G. S., Tan, G., 2004. The renewability of water resources and its quantification in the Yellow River basin, China. *Hydrol. Process.* 18 (12), 2327–2336.
- Xu, J. X., 2005a. Temporal variation of river flow renewability in the middle Yellow River and the influencing factors. *Hydrol. Process.* 19 (9), 1871–1882.

- Xu, J. X., 2005b. The water fluxes of the Yellow River to the sea in the past 50 years, in response to climate change and human activities. *Hydrol. Process.* 35 (5), 620–631.
- Xu, Z. X., Takeuchi, K., Ishidaira, H., Zhang, X. W., 2002. Sustainability analysis for Yellow River water resources using the system dynamics approach. *Water Resour. Manag.* 16 (3), 239–261.
- Yang, D., 1998. Distributed Hydrologic Model Using Hillslope Discretization Based on Catchment Area Function: Development and Applications. the University of Tokyo, Tokyo, Japan, Ph.D. thesis.
- Yang, D., Herath, S., Musiake, K., 1998. Development of a geomorphology-based hydrological model for large catchments. *Ann. J. Hydraul. Eng., JSCE* 42, 169–174.
- Yang, D., Herath, S., Musiake, K., 2000. Comparison of different distributed hydrological models for characterization of catchment spatial variability. *Hydrol. Process.* 14, 403–416.
- Yang, D., Li, C., Hu, H., Lei, Z., Yang, S., Kusuda, T., Koike, T., Musiake, K., Jun. 2004a. Analysis of water resources variability in the Yellow River of China during the last half century using historical data. *Water Resour. Res.* 40 (6), W06502.
- Yang, D., Li, C., Ni, G., Hu, H., 2004b. Application of a distributed hydrological model to the Yellow River basin. *Acta. Geographica. Sinica.* 59 (1), 143–154 (in Chinese).
- Yang, D., Musiake, K., 2003. A continental scale hydrological model using the distributed approach and its application to Asia. *Hydrol. Process.* 17, 2855–2869.
- Yang, K., Huang, G. W., Tamai, N., 2001. A hybrid model for estimating global solar radiation. *Sol. Energy* 70, 13–22.
- Yang, K., Koike, T., 2005. A general model to estimate hourly and daily solar radiation for hydrological studies. *Water Resour. Res.* 41, W10403.
- Yang, S., Liu, C., Sun, R., 2002. The vegetation cover over last 20 years in Yellow River Basin. *Acta. Geographica. Sinica.* 57 (6), 679–684 (in Chinese).
- Yeh, P. J. F., Eltahir, E. A. B., 2005. Representation of water table dynamics in a land surface scheme. Part II: subgrid variability. *J. Clim.* 18, 1881–1901.
- Yellow River Commission, 1999. Some Basic Data of the Yellow River. Huang-he Bao (The Yellow River Newspaper), (in Chinese).

- YRCC (Yellow River Conservancy Commission), 1986. Assessment of the Water Resources in the Yellow River Basin (in Chinese). YRCC, Zhengzhou, China.
- YRCC (Yellow River Conservancy Commission), 1991-2000. Water Resources Bulletin of the Yellow River, Annu. Rep. (in Chinese). YRCC, Zhengzhou, China.
- Zalom, F. G., Goodell, P. B., Wilson, W. W., Bentley, W. J., 1983. Degree-Days: the Calculation and Use of Heat Units in Pest Management. Division of Agricultural and Natural Resources, University of California, Berkeley, California 94720.
- Zektser, I. S., Loaiciga, H. A., 1993. Groundwater fluxes in the global hydrologic cycle: past, present and future. *J. Hydrol.* 144, 405–427.
- Zeng, X. M., Zhao, M., Su, B. K., Tang, J. P., Zheng, Y. Q., Zhang, Y. J., Chen, J., 2002. Effects of subgrid heterogeneities in soil infiltration capacity and precipitation on regional climate: a sensitivity study. *Theor. Appl. Climatol.* 73, 207–221.
- Zhang, S. Y., Williams, T. H. L., Jan. 1997. Obtaining spatial and temporal vegetation data from Landsat MSS and AVHRR/NOAA satellite images for a hydrologic model. *Photogramm. Eng. Remote Sens.* 63 (1), 69–77.
- Zhang, Y., Rossow, W. B., Lacis, A. A., Oinas, V., Mishchenko, M. I., 2004. Calculation of radiative fluxes from the surface to top of atmosphere based on ISCCP and other global data sets: Refinements of the radiative transfer model and the input data. *J. Geophys. Res.* 109, D19105.

Vita

Personal Information

Name: Qihong TANG
Born: August 8, 1981
Hunan, China
Nationality: Chinese
Marital Status: Single

Education

- M.E. in Hydrology and Water Resources, Jul 2003
Institute of Hydrology and Water Resources, Tsinghua University, Beijing, China
- B.E. in Hydraulic Engineering, Jul 2001
Tsinghua University, Beijing, China

Honors and Scholarships

- MEXT Scholarship, Ministry of Education, Culture, Sports, Science, and Technology of Japan (2003 - 2006)
- Shijiayang Fellowship, Tsinghua University (2001 - 2002)
- Scholarship for the Excellency in Community Work, Tsinghua University (1999 - 2000)
- Certificate of Excellency in Community Work, Tsinghua University (1999 - 2000)
- Excellence Studying Scholarship, Tsinghua University (1999 - 2000)
- Third Prize of Theoretical Mechanics Competition, Tsinghua University (1999)

Submitted Papers (4)

Q. Tang, T. Oki, S. Kanae, and H. Hu, *A spatial analysis of hydro-climatic and vegetation condition trends in the Yellow River Basin*, Hydrological Processes, 2006. (under review)

Q. Tang, T. Oki, S. Kanae, and H. Hu, *The influence of precipitation variability and partial irrigation within grid cells on a hydrological simulation*, Journal of Hydrometeorology, 2006. (under revision)

Q. Tang, *Hydrological cycle representation with runoff-evaporation processes*, Earth Surface Processes and Landforms, 2006. (under revision)

Q. Tang, H. Hu, and T. Oki, *Water balance within intensively cultivated alluvial plain in an arid environment*, Water Resources Management, 2006. (under review)

International refereed papers (2)

Q. Tang, T. Oki, *Daily NDVI relationship to cloud cover*, Journal of Applied Meteorology and Climatology, 2006. (accepted)

Q. Tang, *Groundwater recharge and discharge in a hyperarid alluvial plain (Akesu, Taklimakan Desert, China)*, Hydrological Processes, 2006. (accepted)

Other refereed research papers (3)

Q. Tang, T. Oki, and S. Kanae, *A distributed biosphere hydrological model (DBHM) for large river basin*, Annual Journal of Hydraulic Engineering, JSCE. 2006.

Q. Tang, F. Tian, and H. Hu, *Runoff-evaporation hydrological model for arid plain oasis II: the model application*, Shuikexue Jinzhan/Advances in Water Science, 15 (2): 146-150, 2004. (in Chinese with English abstract)

H. Hu, Q. Tang, Z. Lei, and S. Yang, *Runoff-evaporation hydrological model for arid plain oasis I: the model structure*, Shuikexue Jinzhan/Advances in Water Science, 15 (2): 140-145, 2004. (in Chinese with English abstract)

International non-refereed papers (1)

Q. Tang, H. Hu, and T. Oki, *Hydrological processes within an intensively cultivated alluvial plain in an arid environment*, Sustainability of Groundwater Resources and its Indicators (Proceedings of symposium S3 held during the Seventh IAHS Scientific Assembly at Foz do Iguaçu, Brazil, April 2005). IAHS Publ. 302, 2006.

Other non-refereed papers (2)

Q. Tang, T. Oki, and H. Hu, *NDVI value drop with cloudiness*, Proc. 2005 Annual Conf., Japan Soc. Hydrol. Water Res., Tsukuba, 246-247, August, 2005.

Q. Tang, T. Oki, and H. Hu, *A Runoff-Evaporation model for Arid Plain Oasis*, Proc. 2004 Annual Conf., Japan Soc. Hydrol. Water Res., Muroran, 194-195, August, 2004.

Oral presentation in international conferences (1)

Hydrological processes within an intensively cultivated alluvial plain in an arid environment, Sustainability of Groundwater Resources and its Indicators (Symposium S3 held during the Seventh IAHS Scientific Assembly at Foz do Iguaçu, Brazil, April 2005).

Oral presentation in other conferences (1)

A Distributed Biosphere Hydrological Model (DBHM) For Large River Basin, Discharge (International session held during the 50th conference on hydroscience and hydraulic engineering of Japan Society of Civil Engineers at Kyoto, Japan, March 2006).

Poster presentation in other conferences (2)

NDVI value drop with cloudiness, Remote Sensing (Symposium held during the 2005 Annual Conference of the Japan Society of Hydrology and Water Resources at Tsukuba, Japan, August 2005).

A Runoff-Evaporation Model for Arid Plain Oasis, Agriculture Hydrology (Symposium held during the 2004 Annual Conference of the Japan Society of Hydrology and Water Resources at Muroran, Japan, August 2004).

This dissertation was typeset with L^AT_EX 2_ε¹ by the author.

¹L^AT_EX 2_ε is an extension of L^AT_EX. L^AT_EX is a collection of macros for T_EX.